

METHANE PRODUCTION FROM CO-ELECTROLYSIS PRODUCTS APPLYING A MICROCHANNEL REACTOR

Zur Erlangung des akademischen Grades eines
DOKTORS DER INGENIEURWISSENSCHAFTEN

von der KIT-Fakultät für Chemieingenieurwesen und Verfahrenstechnik des
Karlsruher Instituts für Technologie (KIT)
genehmigte

DISSERTATION

von

Dipl.-Ing. Michael Belimov

Tag der mündlichen Prüfung: 13. November 2020

Erstgutachter: Prof. Dr. Peter Pfeifer

Zweitgutachter: Prof. Dr. Thomas Turek

Abstract

This PhD thesis comprises the development of a polytropic microstructured methanation unit for conversion of CO/CO₂ mixtures. As part of the MINERVE Power-to-Gas project, conducted from 2012-2015, the developed reactor contributes to transformation of electrical surplus energy into chemical energy by using methane.

The theory focuses on the examination of thermodynamic equilibria, methane formation mechanisms, catalyst degradation and kinetics. From a technological point of view, microreactors were identified as a promising tool due to the possibility of precise temperature control, which is key in the highly exothermic methanation reaction.

The experimental procedure encompasses the catalyst behavior under variation of H₂/C-ratio, temperature and concentrations of CO and CO₂. Under CO methanation conditions, strong deactivation of the commercial Ni catalyst was observed, while almost no catalyst degradation was encountered under pure CO₂ methanation conditions. The assumption of deactivation by coke was supported with surface carbon and BET-surface decrease. Preferential methanation of CO was observed in CO/CO₂-mixtures with deactivation of catalyst being similar to that under CO conditions.

Two microstructured packed bed reactors were developed showing few novelties in respect to temperature control and pressurized operation of both cooling and reaction zones. It could be shown, that the methanation of CO/CO₂-mixture is possible in one step by controlling the temperature of the reactor to a certain degree while evaporating the cooling water. Due to strong exothermicity of the methanation reaction, a partial overheating of the catalyst took place in both reactors, however, was clearly below adiabatic temperature rise. The hot spot occurrence pointed to heat transfer resistances either in the packed bed or the metal housing. The Prototype 2 showed superior performance compared to Prototype 1 due to additional cooling zone. The idea is filed as an international patent and a scaled-up version is successfully utilized in industrial application for methane generation. An extensive CFD study of Prototype 1 revealed the proper fluid distribution in the cooling zone and the positive effect of fins on heat transfer rate. Besides, valuable information could be extracted by using parameter variation in the packed bed and in the metal housing to determine the heat transfer bottleneck of the system, which could be narrowed to the separating metal wall.

In the final chapter, a few literature models in respect to porosity, flow and heat conductivity distribution in packed beds were discussed, which served as a benchmark to successfully validate the presented meshing strategy using CFD. Ideal plug-flow behavior, as in case of microreactors, was found for packed beds, even at low d_t/d_p -ratios, regarding flow and mass transport in the laminar and transition regions. Pronounced heat transfer issues could occur in the wall areas for $Re < 100$.

Acknowledgement

“Difficult roads often lead to beautiful destinations” by Zig Ziglar eloquently reflects my journey of around three and a half years at the Institute for Micro Process Engineering (KIT). Various challenges have been faced, hurdles taken and successes celebrated.

First and foremost, I am deeply grateful to Prof. Dr.-Ing. Peter Pfeifer, who played a key role in my professional career by giving me this demanding, yet thrilling research topic. I appreciated his help, valuable suggestions and his supporting guidance during this memorable time at IMVT. Thank you Peter, I feel privileged to have worked with you and you have taught me a lot!

My sincere thanks goes to Prof. Dr.-Ing. Dittmeyer for his valuable advice, and fruitful discussions on methanation. I cannot think of a person, who exceeds your skillset on chemical engineering.

I am thankful to all my students: Victor Camargo, Darius Zinn, David Metzger and Philipp Rech, who invested their time and energy for catalyst and reactor studies.

Excellent work was contributed by many people from the IMVT staff. Your help, knowledge and support is the corner stone of this thesis. The list of names would be long, so I keep it short - thank you!

I was fortunate to have met my doctorate colleagues Martin Siebert, Manuel Selinsek and Tim Boeltken, with whom I enjoyed spending my spare time, discussing interesting topics, drinking coffee and having fun. Not to forget the effort and help Manuel put into developing the method on meshing and simulating the packed bed using CFD.

Finally, all my gratitude and love goes to my parents, my wonderful wife Berna and my daughter Leyla. You gave me the strength, support and love to finish this work.

Contents

Contents	iii
1 Introduction	1
1.1 Background	1
1.2 Objectives & requirements of the MINERVE Project	2
1.3 Structure of this work	2
2 Theoretical fundamentals of the methanation system	5
2.1 The reaction system	5
2.1.1 General information	5
2.1.2 Catalyst system	6
2.2 Hydrogenation mechanisms	9
2.2.1 Hydrogenation mechanism of carbon monoxide	9
2.2.2 Hydrogenation mechanism of carbon dioxide	11
2.2.3 General remarks on adsorption and dissociation	13
2.3 Kinetic aspects of the CO and CO ₂ methanation	15
2.3.1 Effect of reaction conditions on the methanation reaction	15
2.3.2 Kinetic rate expressions for CO and CO ₂ methanation	19
2.3.3 Summary	22
2.4 Thermodynamic consideration	23
2.4.1 Methodology & definitions	23
2.4.2 Results of the thermodynamic analysis	26
2.4.3 Summary	31
2.5 Catalyst deactivation in methanation	32
2.5.1 General mechanisms	32
2.5.2 Fundamentals of coke formation	34
2.5.3 Catalyst regeneration and prevention of coke formation	36
2.5.4 Summary	37
3 Conventional vs microstructured reactor technology	38
3.1 State of the art	38
3.1.1 Packed bed reactor	39
3.1.2 Fluidized bed	42

3.2	Microstructured reactor technology	44
3.2.1	Fundamental aspects of process intensification	44
3.2.2	Challenges in microstructured reactors	46
3.3	Summary	49
4	Catalyst performance	50
4.1	Issues with catalyst deactivation in kinetic studies	50
4.2	Experimental tools and analysis methods	52
4.2.1	Test rig, reactor concept & online analytics	52
4.2.2	Tested catalysts	53
4.2.3	Experimental conditions	54
4.2.4	Catalyst characterization methods	55
4.2.5	Reactor modeling equations and correlations in this study	56
4.3	Experimental results	57
4.3.1	Long-term stability of the commercial Ni catalyst under CO methanation conditions	57
4.3.1.1	Heat and mass transport phenomena	57
4.3.1.2	Influence of particle size on the catalyst deactivation	58
4.3.1.3	Effect of temperature on the catalyst deactivation	59
4.3.1.4	Effect of the H ₂ /CO-ratio on the catalyst deactivation	60
4.3.1.5	Deactivation behavior during the shut-down and restart cycles	61
4.3.2	Long-term stability of the catalyst under CO ₂ methanation conditions	62
4.3.2.1	Heat and mass transport phenomena	62
4.3.2.2	Effect of temperature on the catalyst deactivation	62
4.3.2.3	Effect of the H ₂ /CO ₂ -ratio on the catalyst deactivation	66
4.3.3	Long-term stability of the catalyst and kinetics under methanation conditions of CO/CO ₂ mixtures	67
4.4	Analysis of the fresh and spent catalysts	69
4.4.1	SEM and WDS analysis of the commercial Ni catalyst	69
4.4.2	Physisorption and XRD analysis of the commercial Ni catalyst	71
4.4.3	Analysis of the self-prepared Ni/Al ₂ O ₃ catalyst	72
4.5	Comparison of the initial activity with kinetic models from literature & their thermody- namic consistency	74
4.6	Summary	77

5	Reactor development & performance tests	79
5.1	Microstructured competitor devices for methane production	79
5.2	Development of the novel microstructured reactor concept for methanation of CO and CO ₂ mixtures	81
5.3	Prototype specifications and manufacturing	85
5.4	Experimental procedure and equipment	87
5.5	Characterization of the Prototype 1	90
5.5.1	Heat transfer experiments in absence of reaction	90
5.5.2	Reaction experiments	92
5.5.2.1	Dynamic behavior of the reaction system	92
5.5.2.2	Steady-state temperature profiles in methanation of CO/CO ₂ mixtures using gas cooling	94
5.5.2.3	Evaporation cooling in the microreactor	95
5.6	Characterization of the Prototype 2	99
5.6.1	Methanation of CO/CO ₂ mixtures	99
5.6.1.1	On the temperature control under CO ₂ methanation conditions	101
5.7	Summary	102
6	CFD analysis of the microstructured prototype	105
6.1	Motivation	105
6.2	Methodology	106
6.3	Results	108
6.3.1	Geometry and mesh generation	108
6.3.2	Validation of the model - Conjugate heat transfer	109
6.3.3	CFD analysis of the cooling zone	110
6.3.3.1	Flow distribution	110
6.3.3.2	Influence of fins on heat transfer capability	111
6.3.4	CFD analysis of the reaction zone	113
6.3.4.1	Influence of the packed bed heat conductivity on the hot spot formation	113
6.3.4.2	Determination of the effective packed bed heat conductivity by comparing CFD simulation and reaction experiments	116
6.3.4.3	Identification of the heat transfer bottleneck	117
6.3.4.4	Simulation of the reactor using CFD with kinetic reaction models	119
6.4	Summary	122

7	Understanding the micro packed bed	124
7.1	Fundamentals	124
7.1.1	Porosity	124
7.1.2	Flow distribution	126
7.1.3	Heat transfer	128
7.2	CFD study of a resolved packed bed	133
7.2.1	Introduction	133
7.2.2	Methodology	134
7.2.3	The Mark and Separate Meshing approach (MSM) for packed bed description . .	138
7.2.4	Results obtained with the MSM approach	141
7.2.4.1	Heat transfer on a single sphere	141
7.2.4.2	Packed bed meshes for the CFD study	142
7.2.4.3	Contact points	143
7.2.4.4	Local porosity	144
7.2.4.5	Fluid flow profile	144
7.2.4.6	Pressure drop	146
7.2.4.7	Heat transfer	146
7.2.4.8	Chemical reaction	148
7.3	Summary	150
8	Summary	152
9	Zusammenfassung	156
	Symbols and abbreviations	161
	References	166
	List of Figures	182

1 Introduction

1.1 Background

The trend towards sustainability and environmental protection motivates European countries to gradually substitute their fossil and nuclear energy sources with clean and renewable energy carriers. Exemplarily, 31.6% of Germany's gross electricity consumption was generated from renewables in 2015 and is expected to grow to 40-45% by 2025 [1]. Although, wind farms (13.3%) and photovoltaics (6.5%) contribute to green electricity production largely [1], their seasonal, daily or even weather-dependent energy production leads to a mismatch between energy generation and consumption. A promising solution offers the so-called Power-to-Gas (PtG) process which converts electrical to chemical energy by creating storable compounds like hydrogen or methane as final products. In 2012, the MINERVE PtG project was funded by KIC InnoEnergy and aimed to offer a solution for efficient, locally- and time-dependent storage of electrical excess energy. The process consists of four major steps as visualized in Fig. 1.1: "Green" energy from wind farms and solar power plants is used for hydrogen production by electrolysis of water. However, MINERVE was supposed to go a step further with regard to efficiency and to co-reduce water and CO₂ by electric energy in a Solid Oxide Electrolysis Cell (SOEC), i.e. to perform a co-electrolysis at high temperature. According to literature studies, this was the first attempt worldwide to improve the PtG process by three major advantages. First, to utilize renewable energy to directly reduce CO₂ instead of generation of CO by other processes like reverse water-gas shift with additional hydrogen. Second, by applying the reaction heat of the subsequent methanation of CO and H₂ for feeding the SOEC with steam. Third, to apply microstructured reactor technology known for its high degree of process intensification. The resulting synthetic natural gas rich mixture is followed by an optional purification and upgrading step prior to be delivered to a customer. Methane as an energy carrier can be transported through the well-developed gas network for decentralized energy generation and used to store large amount of energy via the gas grid [2].

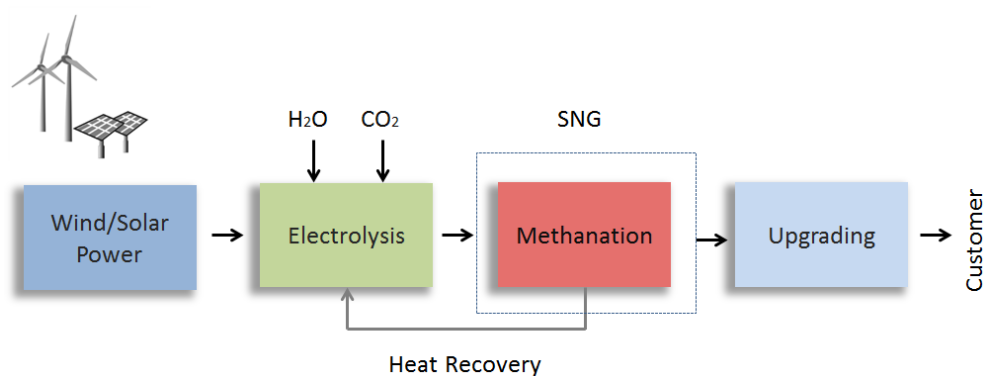


Figure 1.1: Schematic representation of the MINERVE PtG project (2012-2015).

1.2 Objectives & requirements of the MINERVE Project

This work focuses on the development of the microstructured methanation unit. Compared to conventional reactor technology, miniaturization of heat and mass transport distance can lead to a high degree of process intensification. In the highly exothermic methanation reaction, the primary goals are superior temperature control, less byproduct formation due to narrow residence time distribution and better handling of thermodynamic constraints. Moreover, compactness and portability of microreactors could be a key element in flexible and decentralized methane production.

Following boundary conditions are given for the microreactor development in the scope of the MINERVE project. The first aspect concerns the syngas composition and throughput provided by the SOEC for methanation. Due to a moderate conversion of CO_2 to CO via co-electrolysis, the SOEC output syngas contains around 10% CO , 7% CO_2 with hydrogen content close to the stoichiometric H_2/C -ratio and the total volumetric flow of $1 \text{ Nm}^3/\text{h}$. The targeted gas composition may also contain steam, which can be used if benefits are gained in the methanation unit, otherwise it can be removed by condensation.

The SOEC operates at the elevated pressure of 6 bar, which is also applied to methanation and allows benefits in respect to thermodynamics and catalysis.

To further optimize the MINERVE PtG process, the heat release due to strongly exothermic methanation reaction is used to generate superheated steam for the SOEC feed. Preferentially, this step should happen in the microreactor to reduce the peripheral process units.

1.3 Structure of this work

In order to develop a microreactor prototype suitable for the MINERVE project, an analysis and understanding of multiple research fields are required due to the considerable complexity of the matter (Fig. 1.2).

Fundamentals of the reaction system

Information on the reaction system and underlying mechanisms for methane production are summarized to understand the results of the reactor experiments. Therefore, possible methanation catalysts, appropriate hydrogenation mechanisms and kinetic models are examined. The analysis of the thermodynamic equilibrium is conducted, being a fundamental part of the reactor design. The catalyst deactivation mechanisms and possible regeneration methods are discussed.

Technological aspects

Typical conventional reactor systems for methane generation are analyzed regarding their benefits and

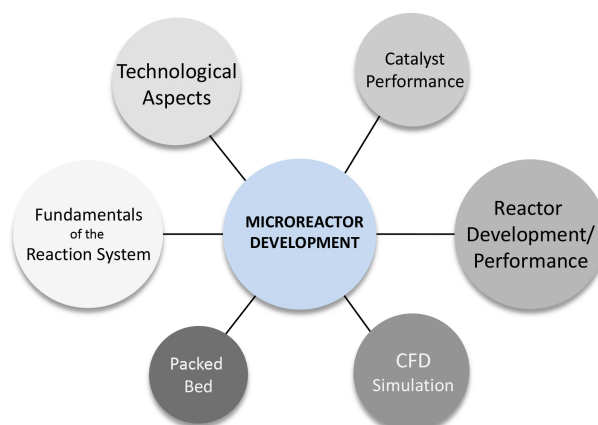


Figure 1.2: “Microreactor Development” as major goal of this thesis and the spectrum of further research fields required for accomplishment.

drawbacks. In comparison, the choice of microstructured devices for this particular task is discussed and challenges are highlighted.

Catalyst performance

This aspect covers the understanding of a suitable catalyst under short contact-time methanation conditions and includes the influence of several important parameters like H_2/C -ratio and temperature on stability under relevant methanation conditions using CO and CO_2 , but also their mixtures. Post-analysis of the spent catalyst is conducted to elucidate the deactivation causes. Finally, the obtained results are used to adapt literature reaction models and to identify suitable literature kinetic rate expressions.

Reactor development/performance

This aspect is motivated through the development of the innovative reactor concept while examining already patented technologies. Based on previous experience and constraints prescribed by the MINERVE project, two possible solution concepts are presented. The prototypes are examined regarding temperature control under methanation conditions and their main performance, strengths and weaknesses are discussed.

CFD simulation

A comprehensive insight into the mass and heat transport phenomena in the developed device is given. After validation of the model, thermal effects in the cooling and reaction zones with the focus on hot spot formation are examined. By applying different boundary conditions, the heat transfer bottleneck is uncovered and recommendations for optimization of future devices are given.

Packed bed

The final aspect of this thesis is devoted to a brief introduction to the description of the packed bed by focusing on porosity and heat conductivity distribution. An alternative meshing approach for packed beds is presented, allowing quick and non-complicated geometry generation for CFD analysis. The collected results allow a deeper understanding of the micro packed beds.

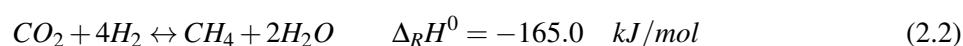
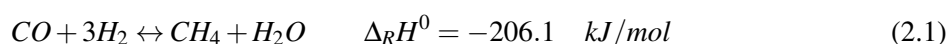
2 Theoretical fundamentals of the methanation system

This chapter gives a brief introduction into the methanation system. Reaction equations and known catalyst systems, hydrogenation mechanisms and kinetic characteristics are discussed. Insights into the reaction system are given based on thermodynamic analysis as general conditions for further work. Finally, known problems of the catalyst system, i.e. deactivation mechanisms are discussed.

2.1 The reaction system

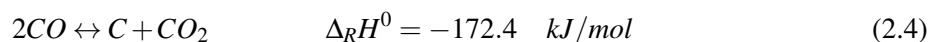
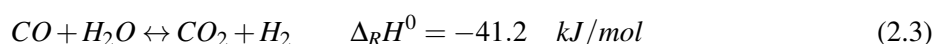
2.1.1 General information

The heterogeneously catalyzed methanation reaction was described first by P. Sabatier and J. P. Senderens in 1902 [3]. Thereby, one mole of carbon monoxide reacts in presence of three moles of hydrogen over a metallic catalyst and forms one mole of methane and water (Eq. 2.1). Methane is also formed by hydrogenation of carbon dioxide (2.2).



Both reactions are strongly exothermic with -206 (Eq. 2.1) and -165 kJ/mol (Eq. 2.2) and are limited by thermodynamic equilibrium. Hence, the effect of initial gas composition, temperature and pressure is crucial for desired system performance and is discussed in Chapter 2.4.

Besides the hydrogenation of CO and CO₂, several side reactions can occur. The most important are, however, the water-gas shift (WGS) (Eq. 2.3) and the Boudouard (Eq. 2.4) reactions.



The WGS reaction is a slightly exothermic equilibrium reaction. It describes the transformation of CO in presence of water to CO₂ and hydrogen, and is often used for adjustment of a desired H₂/C-ratio in technical conversion processes of coal or biomass. According to literature, this reaction plays a key role in the methanation reaction system and is examined extensively in the course of kinetic studies (see Chapter 2.3).

The Boudouard reaction describes the decomposition of CO to solid carbon while releasing CO₂. The resulting carbon contributes to catalyst degradation considerably (see Chapter 2.3 and 2.5) and plays a major role in industrial applications [4].

2.1.2 Catalyst system

The methanation of CO and CO₂ is catalyzed by metals of group VIII, by molybdenum (group VI) and by silver (group I). The activity of the metals, determined by Fischer, Tropsch and Dilthey [5] varies according to sequence in 2.5:

$$Ru > Ir > Rh > Ni > Co > Os > Pt > Fe > Pd \quad (2.5)$$

A similar order was also determined by other groups, e.g. Vannice [6]. Unanimously, ruthenium was determined as the most active for the methanation system followed by Rh, Ir, Fe and Ni. According to modern surface chemistry, the metal order follows the Brønsted-Evans-Polanyi relation, which describes the relationship between activation energy/reactivity of the molecule to its chemisorption energy on the metal surface. Fig. 2.1 shows the activity of different MgO-supported catalysts at methanation conditions (CO content <1 vol. % 550 K, 1 bar) as a function of chemisorption energy of CO in dissociated state. The so-called Volcano diagram, shows maximum at approx. -1.2 eV. At low dissociative adsorption energy, the dissociation rate of CO is the rate-limiting step. This applies for rhenium and iron metals. At higher dissociative adsorption energy, the system is limited by intermediate/product desorption due to strong covalent bonding. This is the case for nickel, rhodium, iridium, platinum and palladium. This behavior is also known as Sabatier-principle [8]. The peak in the Volcano curve represents the most suitable active metal for the methanation system and is characterized by an optimum in the adsorption and desorption rates which are likely on ruthenium and cobalt metals.

Although these metals seem to be the most suitable catalysts, nickel is widely spread in industrial ap-

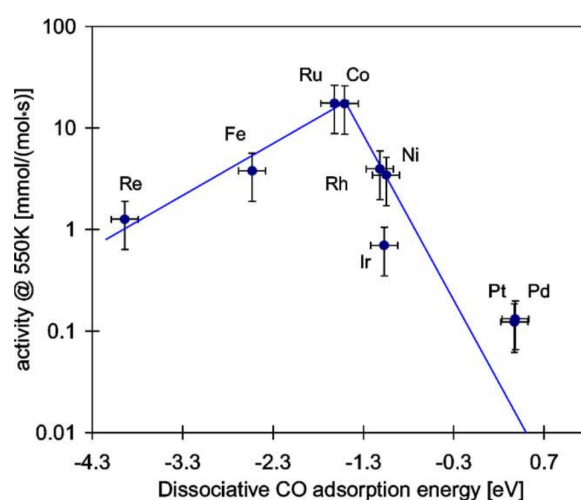


Figure 2.1: Activity of different supported transition metals as a function of the reaction energy for dissociative CO chemisorption [7].

plications due to its low cost and relatively good catalytic properties. It is very active and shows good selectivity to methane [9]. Yet, it is prone to deactivation by sulfur poisoning, likely forms nickel carbonyls ($\text{Ni}(\text{CO})_4$), carbides (Ni_3C) and also carbon [10].

Ruthenium is the most active metal and shows less deterioration than nickel due to, e.g. coking at lower temperatures [11; 12]. The drawbacks are attributed to its high market price and higher hydrocarbon formation at higher pressures and low H_2/C -ratios [13].

Further other metals like iron produce oxygenated compounds and olefins; Cobalt produces mainly alkanes with a high fraction of gasoline hydrocarbons [14]. Molybdenum and tungsten suffer from low selectivity to methane, are prone to deactivation and are therefore less spread in industry [15].

For additional information about metals and their characteristics, a comprehensive overview is given by Mills and Steffgen [16].

Besides active metal, the contribution of the carrier material to the overall performance of the catalyst is significant. Panagiotopoulou et al. [17] studied CO methanation on ruthenium at temperatures between 170-470°C and found that activity varied according to sequence 2.6.

$$\text{TiO}_2 > \text{Al}_2\text{O}_3, \text{CeO}_2 > \text{YSZ} > \text{SiO}_2 \quad (2.6)$$

They show that the turnover frequency of CO on TiO_2 -supported Ru is 1-2 orders of magnitude higher than that on SiO_2 or Y-stabilized Zirconia (YSZ), whereas CeO_2 and Al_2O_3 supported catalysts exhibit intermediate performance. Similar work was conducted by Vannice et al. [18] who examined the effect of support materials for Ni systems (Tab. 2.1). Under methanation conditions at 205°C and atmospheric pressure, they show that the titania supported Ni exhibits much greater activity, better stability and shows less nickel carbonyl formation compared to alumina and silicon dioxide. However, the selectivity towards higher hydrocarbons almost doubles in comparison to titania and silicon oxide supported Ni. Worst per-

Table 2.1: Activity of Ni catalyst on different supports for the methanation reaction [18].

Catalyst	$\frac{\text{Moles CO converted}}{\text{g Ni}}$	$\frac{\text{Moles CO converted}}{\text{g Catalyst}}$
1.53 % Ni/ TiO_2	8.35	0.11
10 % Ni/ TiO_2	22.8	2.28
5 % Ni/ η - Al_2O_3	3.44	0.17
8.8 % Ni/ η - Al_2O_3	1.63	0.14
42 % Ni/ α - Al_2O_3	0.21	0.09
16.7 % Ni/ SiO_2	0.21	0.09
20 % Ni/graphite	0.064	0.013
Ni – powder	0.032	0.032

formance is observed using graphite as support, or pure nickel powder.

The presented metals and their interaction with different support materials give a rough idea which catalyst may be suitable for a particular methanation system and conditions. However, commercial catalysts are very complex in nature and are mainly composed of several active metal and support components. Exemplarily, the MCR-2X catalyst manufactured by Haldor Topsøe is composed of Ni and Mo which are supported on $ZrO_2-Al_2O_3$ basis to survive high temperature conditions. The other, MCR-4 uses a more conventional Ni-MgO- Al_2O_3 formulation [19].

A comprehensive overview of the commercial catalyst formulations, dominantly patents, can be found in the study of Ross [19].

2.2 Hydrogenation mechanisms

The mechanistic consideration of the methanation process according to elementary steps is crucial for understanding the system and its mathematical description. With the development of modern spectroscopy methods (Mass Spectroscopy, Auger-Electron-Scattering etc.), especially the isotopic labeling method, deeper insights into the surface reaction processes are possible. Although the final mechanism is still unclear, the number of unknowns is narrowed to a manageable extent in literature.

2.2.1 Hydrogenation mechanism of carbon monoxide

Since the discovery of the reaction, the methanation models can be categorized into two groups based on CHO_H-surface complex and carbide (Carbide Theory) as intermediates. Both theories were acknowledged and developed in parallel (see Tab. 2.2).

Methanation via CHO_H-complex

The first model assumes an oxygen containing surface complex as precursor, which is adsorbed in the enol form (CHO_H) [22]. The idea is apparently adapted from Fischer-Tropsch synthesis since Storch et al. [20] and Kummer and Emmett [22] discuss an activated CHO_H-complex which could contribute to chain growth via water condensation from higher alcohols. Vlasenko and Yuzefovich [29] assume that the CHO_H-intermediate could also be the initial step for methane formation, which is later examined by other researchers, e.g. Vannice [6]. The mechanistic steps proposed by Vannice [6] include the molecular adsorption of CO and H₂ forming the CHO_H surface complex. Its hydrogenation in the next step to CH₃ finally yields CH₄ and water. The rate-determining step is proposed as hydrogenation of the CHO_H-complex due to a C-O bond scission. The rate equations derived on the steps proposed by Vannice [6] yield a convincing accordance with experimental data. However, the existence of the proposed complex is not verified [29].

Table 2.2: Categorization of few significant literature works focusing on the particular methanation models.

CHO _H -complex		Carbide model and its modification	
Storch et. al. 1951	[20]	Craxford & Rideal 1939	[21]
Kummer and Emmett 1953	[22]	Araki & Ponc 1976	[23]
Blyholder and Neff 1962	[24]	Goodman et al. 1979	[25]
Eidus 1967	[26]	Happel, Cant & Bell 1982	[27; 28]
Vlasenko and Yuzefovich 1969	[29]	Darensbourg et al. 1985	[30]
Baldwin and Hudson 1971	[31]	Fujita et al. 1991	[32]
Vannice 1975	[6]	Alstrup 1994	[33]
		Otarod et al. 1997	[34]
		Andersson et al. 2007	[35]

Methanation via surface carbide - The Carbide Theory

The origin of the Carbide model lies in the Fischer-Tropsch synthesis and is proposed by Fischer and Tropsch, later refined by Craxford and Rideal in 1939 [21]. The theory states that the surface carbide is formed by disproportionation of molecularly chemisorbed CO, whereby CO₂ is released. The products, e.g. methane, or higher hydrocarbons are obtained via hydrogenation of CH₂ groups [21]. The idea is supported by the work of Araki and Ponec [23] to a great extent, who used isotopic labeling of CO to show the feasibility of the surface carbide formation. By introducing the syngas mixture over a clean nickel film (H₂/CO=5, 250°C), CO₂ and CH₄ production is observed (Fig. 2.2). Due to preferential production of CO₂ over CH₄, disproportionation of CO into solid carbon according to Boudouard reaction could be feasible (Eq. 2.4). For this reason, the authors also conducted an experiment, in which labeled ¹³CO was dissociated on the Ni film and evacuated the experimental chamber afterwards. Syngas mixture containing ¹²CO was introduced and the products were traced with a mass spectrometer. According to Fig. 2.3, ¹³CH₄ is produced directly after introduction of hydrogen. The ¹²CH₄ and ¹²CO₂ are formed after an induction period of around 20 min. This observation is an indication that methane is formed from carbide on the surface rather than carbon from gas phase CO and that surface carbide does not form gaseous CO₂.

Therefore, the authors propose the mechanism scheme for CO hydrogenation according to Eqns. in 2.7. Hydrogen and CO are adsorbed in dissociated state on the surface site represented by an asterisk (*).

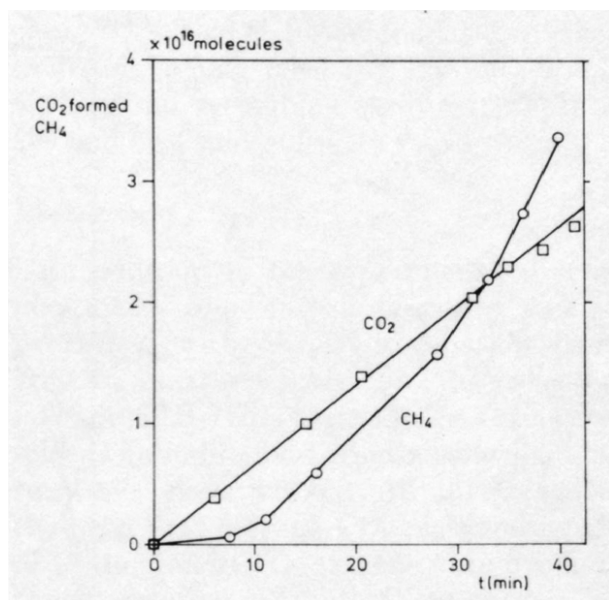


Figure 2.2: Number of CH₄ and CO₂ molecules formed during CO disproportionation in presence of H₂ as a function of time (H₂/C=5, 250°C).

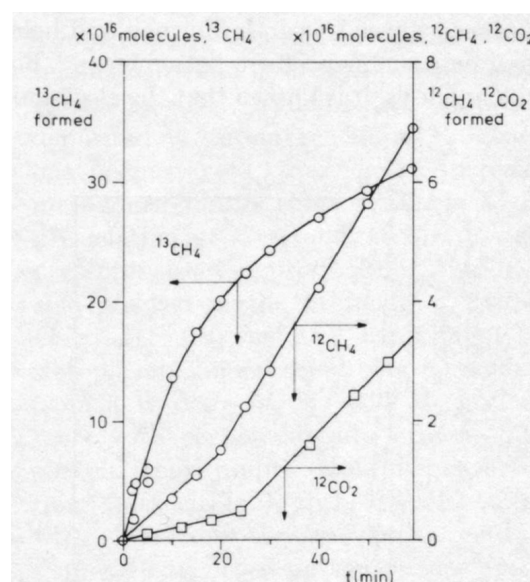
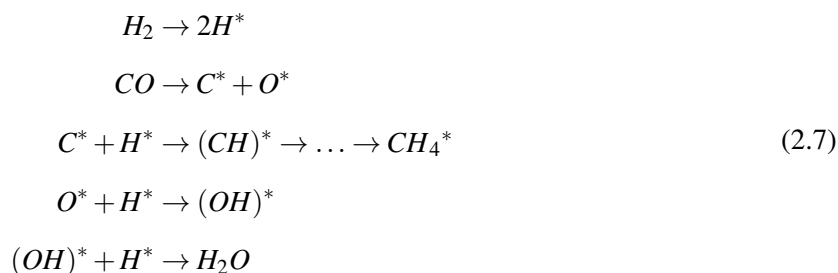


Figure 2.3: Methane and CO₂ formation after presaturation of Ni film with ¹³C and flushing the reaction chamber with ¹²CO/H₂ syngas as a function of time.



Adsorbed C is hydrogenated step-wise to methane while remaining surface oxygen is subsequently hydrogenated to water. According to the authors, the dissociation of CO likely is the rate-limiting step towards methane formation.

The Carbide model is supported by other researchers, who detected adsorbed C, CH, CH₂, CH₃ on the catalyst surface [25; 27; 28]. However, the rate-determining step is still a matter of discussion.

Further modifications of the Carbide model are proposed since the assumption of the one-step dissociation of CO into C* and O* led to unprecise description of some experimental data on Ni/SiO₂ catalysts. Coenen et al. [36] assume that the dissociation step of CO could happen via a COH-complex ($CO^* + H^* \leftrightarrow COH^*$), which could be decomposed into surface carbide and water in a next step ($COH^* + H^* \leftrightarrow C^* + H_2O$). Interestingly, this issue was already mentioned by Craxford and Rideal [21], yet not considered by Araki and Ponec [23].

2.2.2 Hydrogenation mechanism of carbon dioxide

The hydrogenation of CO₂ differs to that of CO in many ways. For example, methanation of CO₂ shows higher selectivities towards CH₄ up to 100% [37], starts at considerably lower temperatures with approx. 50°C (CO-meth. 130°C) [38], and shows noticeably lower activation energies with 60-80 kJ/mol below 400°C ($E_{A,CO-meth} > 100$ kJ/mol) [39]. In addition, up to 1.5 less surface carbon is formed compared to CO methanation conditions [40].

As in the case of CO methanation, two main theories on hydrogenation can be found in literature (Tab. 2.3). The model including the assumption of oxygenated surface complex as an intermediate received little attention and was abandoned in the 1980s. The idea is first proposed by Medsforth in 1923 [41] and includes the reaction of the adsorbed CO₂ with dissolved hydrogen to bis-hydroxycarbene which is transformed to methanal. The latter produces methanol, observed in the experiments, which is believed to decompose to methylen and CO in parallel. The recombination of two methylen ions results in CH₄ [30]. Due to lack of relevance, the model is not discussed further.

The second model, proposed by Solymosi et al. [40] in 1980, is greatly acknowledged up to now. The

Table 2.3: Literature categorization of the CO₂ hydrogenation mechanisms.

CO as intermediate		Oxygenated surface complex as intermediate	
Falconer and Zagli 1980	[37]	Medsforth 1923	[41]
Solymsi, Iizuka et al. 1981	[38; 40]	Vlasenko and Yuzevovich 1969	[29]
Weatherbee and Bartholomew 1982	[42]	Mills Review 1974	[16]
Peebles and Goodman 1983	[43]		
Henderson and Worley 1984	[44],		
Darensbourg et al. Review 1985	[30]		
Prairie et al. 1991	[45]		
Gupta et al. 1994	[46]		
Liotta et al. 1996	[47]		
Marwood et al. 1997	[48]		
Lapidus et al. 2006	[49]		
Panagiotopoulou et al. 2009	[17]		
Jacquemin et al. 2010	[50]		
Beuls et al. 2012	[39]		
Westermann et al. 2015	[51]		

group examined the methanation of CO₂ on ruthenium catalyst at 25-300°C using transient IR spectroscopy. First, they show that carbon dioxide is decomposed into surface carbide, being an important intermediate. The procedure is similar to that of Araki and Ponec [23] examining the CO methanation mechanism. A H₂/CO₂ mixture is fed over the catalyst. After evacuation of the reaction chamber and removal of the adsorbed CO₂, hydrogen is introduced leading to methane formation. Furthermore, introduction of O₂ instead of H₂ results in CO₂ formation, proving the existence of surface carbon.

The route from CO₂ to CH₄ is shown in Fig. 2.4. Starting with the adsorption, Solymsi et al. [40] suggest the formation of formate ion and adsorbed CO in parallel reaction from adsorbed CO₂. The formate ion is proposed to form on metal. However, due its migration to the support material, it is believed to contribute less to CO* formation. The adsorbed CO decomposes in the following step to surface carbon and oxygen. The surface carbon is believed to react quickly either to methane by a step-wise hydrogenation or to age by forming a less reactive carbon species C^x. The formation of the CO* was proposed as the rate-limiting step. Since the model of Solymsi et al. [40] includes the same route towards methane starting from CO* as the CO methanation model, the question about lower activation energy requires explanation. According to authors, the surface concentration of CO* and hence C* are identified as key elements. They suggest that due to 1.5 times lower amounts of accumulated C*, faster hydrogenation to CH₄ at equivalent temperatures occurs.

Further modification of the model is suggested by Henderson and Worley [44], who propose an additional step including CO₂ dissociation on the surface by forming metal carbonyl hydride being the most important intermediate. Hence, the dissociation is believed to be hydrogen assisted. The authors do not

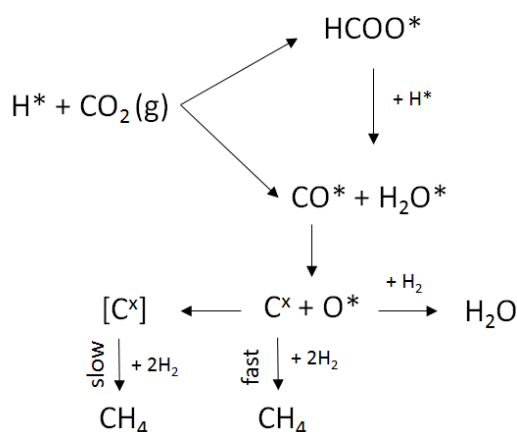


Figure 2.4: Hydrogenation model of CO_2 to CH_4 according to Solymosi et al. (adapted from [40]).

make any statements about the rate-limiting step but agree with Peebles and Goodman [43] that there is an influence between C^* formation and its removal by hydrogen. Gupta et al. [46], however, propose the CO dissociation into surface carbide must be the rate-limiting step. Furthermore, they propose a metal carbonyl being a direct precursor for C^* formation, which formation is dependent on the reaction conditions.

From here, it becomes obvious that different metals, supports and reaction conditions influence the system to a great extent leading to no consensus about the universal reaction route.

2.2.3 General remarks on adsorption and dissociation

In the previously presented hydrogenation models, adsorption and dissociation of the reactants are assumed as the first steps and are often simplified to $AB(\text{g}) \rightarrow AB^* \rightarrow A^* + B^*$. However, the underlying processes are highly complex in nature. For better understanding of the methanation mechanism, few remarks on adsorption of H_2 , CO, CO_2 are given in the following.

Hydrogen

It is well established that hydrogen is adsorbed on transition metals by a dissociative mechanism $>25^\circ\text{C}$ [27]. The process is accompanied by electron transfer from the surface to the hydrogen atoms which leads to negative charge. The metal surface is charged positively [29]. According to Goodman et al. [52], the adsorption of H_2 on Ni is structure “insensitive”, that is, the crystallography of the metal has a negligible influence on adsorption/desorption enthalpy. The presence of impurities blocks the dissociation and the capacity of the surface to adsorb hydrogen [52].

The behavior of hydrogen in the course of methanation process on Ni(111) was investigated by, e.g. Johnson et al. [53] by using isotope labeled molecules. They could show that bulk hydrogen successfully

participates in the hydrogenation of CH_3 to methane, whereas surface hydrogen remains non-reactive. This is explained with the required orientation of the deuterium atom for sp^3 hybridization, which reacts instantly with CH_3 to CH_3D .

Carbon monoxide

The adsorption and activation of CO is a very complex process leading to misconceptions in the mechanistic examination of the methanation process. A review by Vlasenko and Yuzefovich [29] summarizes the results from IR-spectroscopy up to the year 1969, which reveals, that at lower temperatures $<80^\circ\text{C}$, pure carbon monoxide is chemisorbed on nickel in five different forms, e.g. linear, or bridged with different levels of adsorption strengths and reactivity potentials. As a consequence, it is concluded that a molecular complex based on the CO molecule is an important intermediate. However, the literature also indicates that molecularly chemisorbed CO is not reactive [23]. On the contrary, other groups observed dissociative adsorption of CO on nickel producing CO_2 due to Boudouard reaction [23; 52].

Supported by DFT calculations, Andersson et al. [35] examined adsorption and dissociation of CO on Ni surfaces. They show that on certain surfaces, no dissociation is possible due to lower desorption energy (approx. 1.2 eV) compared to dissociation energy (1.5-1.6 eV), pointing to the fact that CO dissociation is structure sensitive. They suggested that the dissociation process takes place predominantly on steps, rather than on terraces. Furthermore, they found that the presence of hydrogen lowers the dissociation energy of CO to approx. 1.02-1.08 eV, which makes the hydrogenation of CO via a dissociated state plausible.

Carbon dioxide

Regarding CO_2 , the adsorption is influenced by the same parameters as the CO adsorption. So, dissociation of CO_2 molecules does not take place below 300 K. However, dissociation is induced in presence of hydrogen [44]. The activation is proposed to happen via a metal carbonyl [44; 46].

2.3 Kinetic aspects of the CO and CO₂ methanation

The methanation system has been extensively studied in literature since the 1960s and a lot of information on kinetics has been published. The main trends are summarized and the effects of the most important parameters, e.g. temperature, concentration and pressure elucidated. Finally, few kinetic rate expressions are presented being applicable to the constraints of the MINERVE project.

2.3.1 Effect of reaction conditions on the methanation reaction

The influence of the CO concentration on the measured reaction rate is shown in Fig. 2.5. Herwijnen et al. [54] found that at very low CO concentrations, the rate correlates linearly with the W/F_{CO} -ratio implying zero order kinetics (Fig. 2.5 on the left). However, by plotting the rate as a function of CO concentration, the rate reveals a strongly non-linear character in respect to CO partial pressure (Fig. 2.5 on the right). At low CO concentration values in the ppm range, the rate of methane formation increases significantly and shows a remarkable concentration sensitivity. However, a maximum is reached quickly, which is attributed to surface blockage by the CO molecules, forcing hydrogen to compete for remaining active sites [54]. This trend seems to continue with further increasing concentration of the CO leading to a complete surface blockage and drop of the reaction rate towards zero [54]. The observation is supported by studies of Baerns et al. [55].

Besides carbon monoxide, hydrogen is found to have a pronounced effect on the methanation rate. Fig. 2.6 on the left shows the rate of methane formation at 223°C as a function of CO and H₂ partial pressures measured by Klose and Baerns [55]. Hydrogen clearly enhances the methanation rate with increasing concentration and does not show any retarding effects. Higher concentrations also allow to shift the maximum of the methanation rate towards higher carbon monoxide concentrations. The

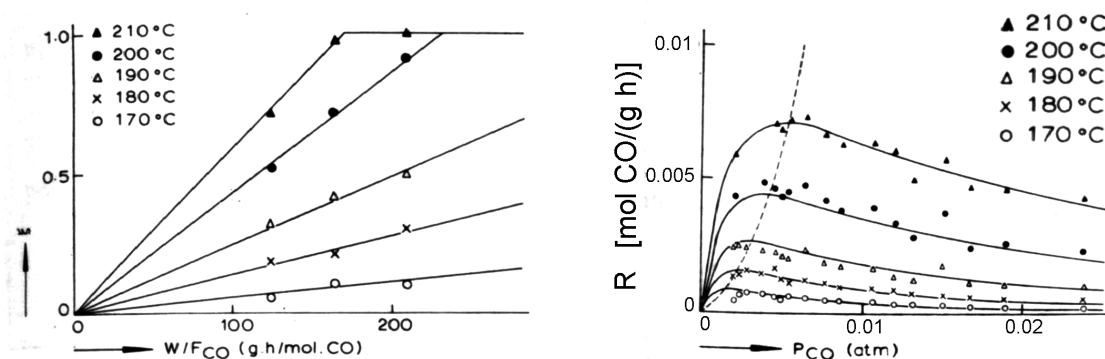


Figure 2.5: Conversion of CO as a function of W/F_{CO} ($x_{CO}=0.0065\%$) (left) and initial rate of methanation of CO (right) on Ni/Al₂O₃ at different temperatures [54].

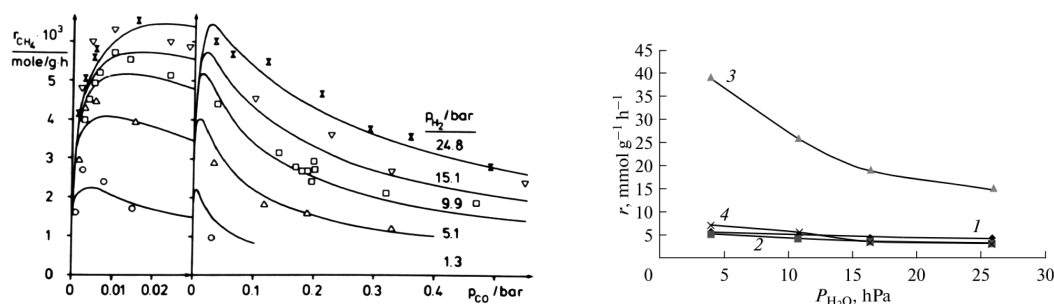


Figure 2.6: Rate of methane formation at 496 K as a function of CO and H_2 partial pressures (left) [55] and dependence of the reaction rate on the partial pressure of H_2O at 220°C and $p_{\text{H}_2}=200$ hPa and $p_{\text{CO}}=6$ hPa on different catalysts: 1) Ni/TiO₂, 2) Ni/Al₂O₃, 3) Ni-CaO/Al₂O₃ and 4) Ni-Ce₂O₃/Al₂O₃ (right) [15].

effect is only studied in the ppm range of CO [55].

The influence of water on the methanation rate is ambiguous. Some groups report a retarding effect on CO conversion [15; 56] (Ni catalyst, $230\text{--}322^\circ\text{C}$), whereas other groups could not see any effects at all (Ni catalyst, $180\text{--}284^\circ\text{C}$) [55; 57]. A recent work by Kopyscinski et al. [58] reveals the effect of water in a wider temperature range between 280 and 360°C and steam concentrations up to 20% on a commercial Ni catalyst. They showed that H_2O influence is temperature dependent and exhibits a retarding effect on CO conversion up to 300°C with a positive influence above 300°C . However, above 300°C , CO is not exclusively converted to methane but also to CO_2 , which is a clear evidence for the importance of water-gas shift reaction [58].

The retarding/enhancing effect of water on the methanation reaction is not only temperature but also partial pressure [57] and catalyst/support dependent [15] (Fig. 2.6 on the right). Loc et al. [15] show that TiO₂ supported Ni is seriously inhibited by the water vapour, whereas Al₂O₃ supported Ni exhibits lower activity and is less sensitive to water addition.

Another significant aspect of the methanation reaction is its temperature sensitivity and is expressed in terms of activation energy E_A . Generally, the reaction rate is enhanced with higher temperatures (see Fig. 2.5 on the left and right) under negligible thermodynamic limitations. According to Vannice and Garten [18], the activation energy of the CO methanation rate varies with catalyst system as shown in Tab. 2.4. They could observe that some catalyst metals exhibited lower activation energies, e.g. Pt and Ir which were in the range $70\text{--}85$ kJ/mol, whereas other metals, e.g. Ru, Fe, Ni, Co and Rh showed

Table 2.4: Turnover number, activation energy and exponential coefficients of the methanation reaction on different active metals (adapted from [18]).

Catalyst	TON @255°C ×10 ³	E_A [$\frac{kJ}{mol}$]	X	Y	A [$\frac{molecules}{sites \cdot sec}$]
5% Ru/Al ₂ O ₃	181	101.2	1.60	-0.60	5.7×10^8
15% Fe/Al ₂ O ₃	57	89.1	1.14	-0.05	2.2×10^7
5% Ni/Al ₂ O ₃	32	104.6	0.77	-0.31	2.3×10^8
2% Co/Al ₂ O ₃	20	113.0	1.22	-0.48	9.0×10^8
1% Rh/Al ₂ O ₃	13	100.4	1.04	-0.20	5.2×10^7
2% Pd/Al ₂ O ₃	12	82.4	1.03	0.03	1.2×10^6
1.75% Pt/Al ₂ O ₃	2.7	69.9	0.83	0.04	1.6×10^4
2% Ir/Al ₂ O ₃	1.8	70.7	0.96	0.10	1.4×10^4
4.75% Pd/SiO ₂	0.32	112.5	0.71	0.15	2.0×10^6
0.5% Pd/H-Y Zeolite	5.9	88.7	0.84	0.30	5.7×10^5

$$r_{CH_4} = A \cdot \exp(-E_A/(RT)) \cdot p_{H_2}^X p_{CO}^Y$$

values in the range 95-115 kJ/mol. In addition, the turnover numbers vary significantly despite similar activation energies as in case of alumina supported Rh and Ru. This phenomenon is explained with the capability of the metal to promote CO and H₂ dissociation and has already been covered in Chapter 2.1.2 using the Volcano-plot.

The influence of the support material on the activation energy was also examined by Vannice and Garten [18], who found that Al₂O₃ supported Pd has lower activation energy of 82 kJ/mol compared to H-Y Zeolite with 89 kJ/mol and SiO₂ with 113 kJ/mol. This fact emphasizes the relevance of metal-support interaction during catalysis.

Besides, the support material is also found to determine the side product formation, e.g. coke, which is covered in Chapter 2.5.

The methanation of CO₂ in the syngas mixtures requires a special attention with regards to the tasks in this thesis. The reason for this is that CO₂ conversion to methane is inhibited by the presence of CO to a considerable extent [17; 39; 59]. CO is methanated first, followed by a subsequent conversion of CO₂. This phenomenon is explained with strong adsorption coefficient of CO over CO₂ (see also Chapter 2.2.3). Fig. 2.7 shows a conversion-temperature plot for methanation of CO and CO₂ mixtures at different space velocities on Ru_{0.5%}/Al₂O₃ catalyst [17]. Pangiotopoulou et al. [17] observed that the inhibition of CO₂ methanation is strongly temperature dependent. No CO₂ co-conversion takes place below 300°C but increases steadily above 300°C. In parallel, CO conversion can drop. This effect is supposed to be attributed to reverse water-gas shift reaction which produces CO from CO₂. Hence, it is proposed that methane formation happens via transformation of CO₂ to CO and subsequent

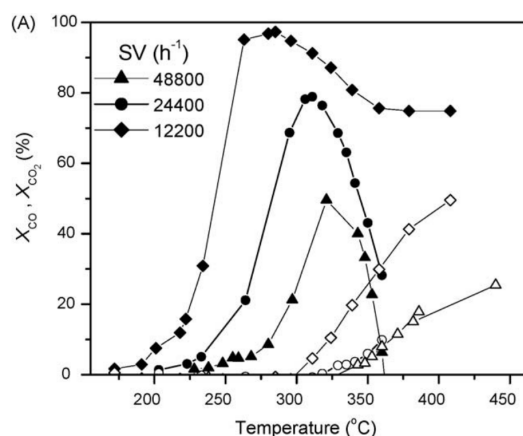


Figure 2.7: Conversion of CO and CO₂ as function of temperature and space velocity on a Ru/Al₂O₃ catalyst [17].

hydrogenation of CO [56; 58].

Another observation is that the presence of CO₂ does neither affect CO conversion, nor the formation of water or methane [56; 58]. Furthermore, the addition of CO₂ to the syngas does not have any effect on the population of adsorbed CO, suggesting that CO₂ methanation reaction deviates from that of CO [60].

The influence of the total pressure on the overall reaction rate is typically not examined in kinetic studies. One reason could be low influence on the reaction rate, as it is shown by the work of Schoubye [57]. By conducting the variation of H₂/CO-ratio at different pressures, he found that the CH₄ rate is clearly a function of the H₂/CO-ratio. Yet, the relation did not change with the increasing pressure. He proposes the relation $r_{CH_4} \propto p_{tot}^{0.15}$ indicating that the highest acceleration of the rate can be achieved in the lower pressure range, whereas negligible change occurs at higher pressures. Nevertheless, side reactions may be sensitive to absolute pressure (See Chapter 2.4).

2.3.2 Kinetic rate expressions for CO and CO₂ methanation

In general, the complexity of the kinetic rate models has developed from simple empirical to very complex expressions and has been strongly influenced by advances in surface science. For narrow temperature or concentration range, an empirical power-law rate expression (Eq. 2.8) can describe the experimental data sufficiently.

$$r_i = A \cdot \prod_{i=1}^n p_i^{j_i} = k_0 \cdot e^{-\frac{E_A}{RT}} \cdot \prod_{i=1}^n p_i^{j_i} \quad (2.8)$$

The reaction rate takes into account the temperature influence of the pre-exponential factor k_0 using the Arrhenius relation and the influence of the reactant partial pressures in power with a designated constant j_i . Exemplarily, the pre-exponential factors, activation energies and the reaction orders of CO and H₂ on different catalysts for carbon monoxide methanation are summarized in Tab. 2.4. The obvious scattering in pre-exponential factors leads to the assumption that the simple model are not capable to capture the entire range [18] leading to more sophisticated approaches, e.g. Langmuir-Hinshelwood-Hougen-Watson (LHHW) models [61]. The formulation is based upon elementary steps involving adsorption (Langmuir-isotherm), dissociation, reaction, desorption and eventually other relevant steps. The rate for a simple $A + B \leftrightarrow S$ reaction and its generalized form is shown in Eq. 2.9.

$$r_i = \frac{k_{rds} N_T K_i \dots (p_A p_B - p_C / K_{eq})}{(1 + K_A p_A + K_B p_B + K_C p_C + \sum K_j p_j)^n} = \frac{\text{rate factor} \cdot \text{driving force}}{\text{inhibition term}} \quad (2.9)$$

The numerator consists of the rate-determining step k_{rds} , number of participating active sites N_T and the driving force, i.e. how far the reaction is from thermodynamic equilibrium. The denominator can be regarded as inhibition term, which includes the adsorption of all components among others components which do not participate but physisorb on the surface. The advantage of such models is that they allow to study single reaction steps while narrowing down the rate-limiting processes. Besides, they are valid in a broader concentration and temperature range [61].

The Langmuir-Hinshelwood models and their modifications for methanation of CO, CO₂ and their mixtures started in the 1980s and have been summarized in several PhD works [62; 63; 64; 65; 66] and reviews [9; 16]. Despite a great number of kinetic rate expressions in the literature, only few of them are applicable for the MINERVE project. The requirements are: The rate equation must be valid for high concentrations of carbonaceous species and should take into account the methanation of CO and CO₂ in parallel, as they are the main components from the electrolysis cell. In addition, the rate must be valid in a wide temperature range between 250 and 600°C, since heat recovery in the reactor at higher temperature niveaus is pursued. Table 2.5 shows the kinetic rate equations for methanation of CO/CO₂ mixtures with appropriate validity range regarding temperature and concentration and are briefly discussed in the following.

Xu & Froment

The kinetic model given by Xu and Froment [67] is designed for steam-reforming of methane and a set of coefficients are also provided for the reverse reactions. The kinetic experiments were performed in a tubular reactor, operated in integral mode, using Ni_{15.2%}/MgAl₂O₄ catalyst ($d_p=180-250 \mu\text{m}$). Prior to kinetic measurements, the catalyst was aged under steam reforming conditions for 70 h. Regarding elementary steps in the model, adsorption of all reactants on the surface is assumed. Dissociation of CO₂ to CO* and O* is considered as a key rate-determining step (RDS) in the CO₂ activation resulting in adsorbed CO* and O* and has been already described by Solymosi et al. [40]. The second RDS includes hydrogen assisted activation of CO₂ with H* to CHO* and O*. The third RDS is assumed as CHO* formation from CO* and H*. Subsequent hydrogenation of CHO* species produces methane. Obviously, the proposed model comes close to the Carbide model, but deviates in some details. No surface carbide C* is assumed, which contradicts the Carbide theory. However, subsequent hydrogenation of CH₂* to CH₄, being a part of the Carbide model, is included.

Kopyscinski

The kinetic model proposed by Kopyscinski et al. [58] is based on CO methanation and water-gas shift reactions. The experiments were performed in a spatially resolved plate reactor, which was wall-coated with nickel/alumina (50 wt.%) catalyst. The reaction system was examined between 280-360°C and 1 bar while varying the concentration of carbon monoxide and dioxide between 0-14% and 0-10%, respectively.

The rate equations are based upon a Langmuir-Hinshelwood approach and take into account the recent know-how about mechanisms on methanation of CO and CO₂. The conversion of CO₂ into methane is assumed to happen via CO according to water-gas shift. The authors come to conclusion that the models with rate-limiting steps a) $C^* + H^* \rightarrow CH^* + *$, b) $CH^* + H^* \rightarrow CH_2^* + *$ and c) $COH^* + H^* \rightarrow CH^* + OH^*$ yield all the best fit to experimental data. The advantage of this model, compared to that of Xu and Froment, is the proper reflection of the local concentrations due to spatial resolution. Unfortunately, the equilibrium constant of the steam reforming is not considered, which makes the model invalid at temperatures above 360°C.

Zhang

Zhang et al. [56] performed methanation of CO/CO₂ mixtures in a tubular milli fixed bed reactor on a commercial Ni catalyst (50 wt.%) in the temperature range between 250-360°C and at pressure of 3 bar. The rate equations of Xu and Froment [67] are adopted neglecting the equation for methanation of CO₂. It is assumed that the consumption of CO₂ happens via the reverse water-

Table 2.5: Overview of the examined rate expressions for CO and CO₂-methanation from literature.

Rate expression	Catalyst	Reactor type	Validity range	Source
CO/CO₂-methanation				
$r_1 = \frac{k_1}{p_{H_2}^{2.5}} (p_{CH_4} p_{H_2O} - \frac{p_{H_2}^3}{K_1}) / (DEN)^2$	Ni/MgAl ₂ O ₄	TR	300-400°C, <10 bar	[67]
$r_2 = \frac{k_2}{p_{H_2}} (p_{CO} p_{H_2O} - \frac{p_{H_2} p_{CO_2}}{K_2}) / (DEN)^2$				
$r_3 = \frac{k_3}{p_{H_2}^{3.5}} (p_{CH_4} p_{H_2O}^2 - \frac{p_{H_2}^4 p_{CO_2}}{K_3}) / (DEN)^2$				
$DEN = 1 + K_{CO} p_{CO} + K_{H_2} p_{H_2} + K_{CH_4} p_{CH_4} + \frac{K_{H_2O} p_{H_2O}}{p_{H_2}}$				
$r_{SMR} = \frac{k_{SMR}}{p_{H_2}^{2.5}} (p_{CH_4} p_{H_2O} - \frac{p_{H_2} p_{CO}}{K_{SMR}}) / (DEN)$	Ni comm. 50 wt.%	TR	275-360°C, <5 bar	[56]
$r_{WGS} = \frac{k_{WGS}}{p_{H_2}} (p_{CO} p_{H_2O} - \frac{p_{H_2} p_{CO_2}}{K_{WGS}}) / (DEN)$				
$DEN = 1 + K_{CO} p_{CO} + K_{H_2} p_{H_2} + K_{CH_4} p_{CH_4} + \frac{K_{H_2O} p_{H_2O}}{p_{H_2}}$				
$r_{MET} = \frac{k_1 K_C p_{CO}^{0.5} p_{H_2}^{0.5}}{[1 + K_C p_{CO} + K_{OH} p_{H_2O} p_{H_2}^{-0.5}]^2}$	Ni/Al ₂ O ₃ 50 wt.%	SRMR	280-360°C, 0-14 vol.% CO, 2 bar	[58]
$r_{WGS} = \frac{k_2 (K_\alpha p_{CO} p_{H_2O} - \frac{p_{CO_2} p_{H_2}}{K_{eq}})}{p_{H_2}^{0.5} (1 + K_C p_{CO} + K_{OH} p_{H_2O} p_{H_2}^{-0.5})}$				
CO₂-methanation				
$r_{MET} = \frac{k_p p_{CO_2}^{0.5} p_{H_2}^{0.5} (1 - \frac{p_{CH_4} p_{H_2O}}{p_{CO_2} p_{H_2}^{1.5} K_{eq}})}{(1 + K_{OH} \frac{p_{H_2O}}{p_{H_2}^{0.5}} + K_{H_2} p_{H_2}^{0.5} + K_{min} p_{CO_2})^2}$	NiAl(O) _x	TR	H ₂ /C=0.25-8, 250-340°C, <15 bar	[68]

gas shift converting the resulting CO to methane in the following as suggested by Kopyscinski et al. [58].

Koshany

Koshany et al. [68] performed pure CO₂ experiments at temperatures between 250-340°C in a plug-flow reactor on a NiAl(O)_x catalyst. Prior to experiments, the catalyst was aged for approx. 320 h at 380°C. A Langmuir-Hinshelwood-Hougen-Watson kinetic rate expression is derived taking into account the thermodynamic equilibrium. The authors examined two mechanisms. In the first, CO* is decomposed into surface carbon C* and O* according to the theory of Solymosi et al. [40] after dissociation of CO₂ into CO* and O*. In the second, CO* is hydrogenated to formyl CHO*, which releases O* in the next step and hydrogenated to CH₄ in the following. The authors concluded that the second model via formyl formation fit the experimental result best.

The named kinetic rate expressions are used as a reference for the kinetic studies obtained in this work in Chapter 4.

2.3.3 Summary

The methanation reaction is greatly influenced by CO, H₂ and temperature. Due to the poisonous nature of CO, the reaction rate is inhibited at larger partial pressures, whereas the opposite is true for hydrogen. The reaction is highly temperature sensitive and exhibits high activation energy between 80-100 kJ/mol, which in return is influenced by the catalyst and support material. The addition of CO₂ to syngas leads to preferential methanation of CO due to the strong adsorption of CO on the common methanation catalysts. The effect of water vapour is ambiguous and depends on the catalyst system and temperature range. The influence of total pressure on the methanation rate is beneficial at lower and less pronounced at higher pressures.

Only few kinetic models can be selected according to constraints of the MINERVE project from literature. Their comparison with the kinetic data obtained in this work is given in Chapter 4.

2.4 Thermodynamic consideration

Thermodynamic analysis of the methanation system is imperative for further kinetic catalyst studies and reactor development. The influence of temperature, concentration and pressure on the system performance and byproduct formation is discussed.

2.4.1 Methodology & definitions

Thermodynamic study allows the calculation of equilibrium constants, reaction heat and equilibrium composition. The latter is of major interest and can be calculated in several ways. In the stoichiometric approach, the equilibrium constant is calculated according to Eq. 2.10 using the Gibbs energy (Eq. 2.11).

$$\log K = -\Delta G_R / RT \quad (2.10)$$

$$\Delta G_R = \Delta H_R - T \Delta S_R \quad (2.11)$$

The Gibbs energy is a function of temperature, reaction enthalpy and entropy, which requires integration of the latter variables in case non-standard conditions are used. The equilibrium composition can be obtained by applying the mass action law. This, however, requires the exact knowledge of the reactions and their stoichiometry [69]. For complex problems, the method is less suitable [70].

The more advanced approach is based on minimization of the Gibbs energy of the system (non-stoichiometric) and has several advantages. The reactants and possible products are specified without further information about the chemistry behind it. The distribution is governed by the minimum of the Gibbs energy of the system. Furthermore, this method predicts the interaction of reacting and non-reacting species properly and can be applied to multiphase systems [71; 72]. The mathematical formulation of the minimization function G_{sys} can be written as follows (Eq. 2.12) [72]:

$$G_{sys} = \sum_{j=1}^S G_j^0 n_j^C + \sum_{j=S+1}^C \sum_{l=1}^P G_{jl} n_{jl} \quad (2.12)$$

P is the number of phases, while C is the number of chemical species and S the number of condensed species. The condensed species are generally solid and do not distribute amongst other phases. The system is valid once it satisfies the mass balance according to Eq. 2.13.

$$b_k = \sum_{j=1}^S m_{jk} n_j^C + \sum_{j=S+1}^C \sum_{l=1}^P m_{jl} n_{jl} \quad \text{with } k = 1, \dots, E \quad (2.13)$$

Thereby, b_k is the number of atoms of element k , m_{jk} is the number of atoms of element k in the component j and E is the number of elements [72].

For pure species, G_j is equal to the chemical potential μ_j and can be written for gaseous species as a function of μ_j^0 , activity a_j and temperature T (Eq. 2.14).

$$\mu_j = \mu_j^0 + RT \ln a_j = \mu_j^0 + RT \cdot \ln \left(\frac{n_j}{\sum_i n_i} \cdot \frac{P}{P_{ref}} \right) \quad (2.14)$$

Assuming the ideal gas behavior, the activity can be rewritten as a function of the mole number of the component j related to the total number of moles in the system including the total and reference pressures.

For the calculation of the solid carbon amount, carbon is assumed in its most stable form, graphite, with the chemical potential of 0 J/mol. This may seem inappropriate, since reactive carbon species (amorphous carbon) in the methanation process are formed. The increased activity, however, is attributed to kinetic effects [53], leading to a less reactive form during the aging process [40] and finally to non-reactive graphite.

The objective function is minimized in respect to $\frac{n_j}{\sum_i n_i}$ using the built-in MATLAB function “fmincon” yielding mole amounts of each species, i.e. the final equilibrium composition.

The presented calculations were performed using standard chemical potentials of the components as functions of temperature which are obtained from literature [73].

In the framework of the thermodynamic study, the conversion of the species j is calculated using the mole amount in the system according to Eq. 2.15.

$$X_{j,Eq} = \frac{F_{j,0} - F_{j,Eq}}{F_{j,0}} \quad (2.15)$$

Where $F_{j,0}$ is the initial and $F_{j,Eq}$ the equilibrium mole amounts. Due to non-stoichiometry, the equilibrium selectivity from CO (Eq. 2.16) and CO₂ (Eq. 2.17) to CH₄ are defined as the ratio between the produced methane and the sum of all carbonaceous components being formed from CO or CO₂ [71].

$$S_{CO,CH_4,Eq} = \frac{F_{CH_4,Eq}}{F_{CH_4,Eq} + F_{CO_2,Eq} + F_{C_s,Eq}} \quad (2.16)$$

$$S_{CO_2,CH_4,Eq} = \frac{F_{CH_4,Eq}}{F_{CH_4,Eq} + F_{CO,Eq} + F_{C_s,Eq}} \quad (2.17)$$

The equilibrium yield is calculated according to Eq. 2.18 [71].

$$Y_{j,Eq} = \frac{F_{j,Eq}}{\sum_j N_j F_{j,0}} \quad (2.18)$$

The mole amount of the component j is referred to the sum of the initial moles of all carbonaceous components, where N_j describes the number of C-atoms in the component j .

2.4.2 Results of the thermodynamic analysis

Equilibrium constants and Gibbs free energy

The equilibrium constants and Gibbs energy are examined as a function of temperature for a given set of reactions. Fig. 2.8 on the left shows thermodynamic equilibrium constants, evaluated using Eq. 2.10, for CO (R1) and CO₂ (R3) methanation, but also for plausible parallel reactions like CH₄ formation due to reverse dry reforming of methane (R2), water-gas shift (R4), Boudouard reaction (R5) and methane cracking (R6). The equilibrium constants of the favored reactions which produce methane (R1, R2 and R3) show very high values with 10²⁰-10³⁰ at low temperatures supporting the idea of methane as the favored product. However, the tendency towards CH₄ is decreased with increasing temperature and reverse reactions play a major role at temperatures above 600°C. Besides methane producing reactions, Boudouard reaction (R5) exhibits extremely high equilibrium constant values. The feasibility of Boudouard reaction occurrence is supported by the Carbide theory which requires carbon formation as the major important step for further hydrogenation to methane [23]. The decomposition of methane (R6) is unlikely below 550-600°C due to the negative equilibrium constant. Hence, industrial applications target this temperature range. This is often reached by dilution of the feed gas with cooled recycle gas [74; 75]. Temperatures above 550-650°C, which can be encountered in industrial reactors [75], may lead to coke deposition due to CH₄ cracking.

Fig. 2.8 on the right reveals the feasibility of the proposed reaction set by Gao et al. [71] in terms of the Gibbs energy. The negative of the Gibbs energy implies that the reactions R1-R5 are physically feasible below 600°C. Positive values imply that the reverse processes may become possible.

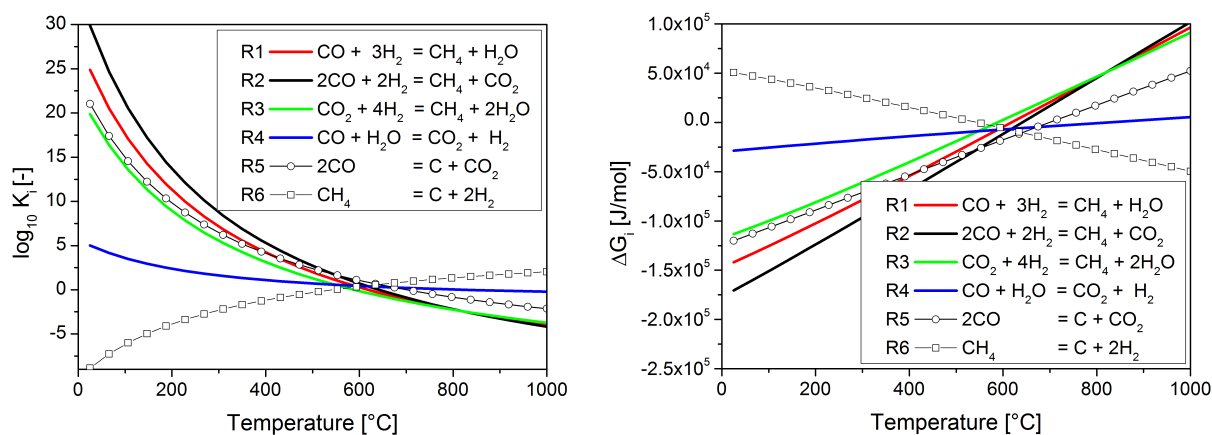


Figure 2.8: Equilibrium constants (left) and Gibbs energy (right) for possible reaction set R1-R6 as a function of temperature in the range 25-1000°C.

Thermodynamic equilibrium composition

The analysis is performed using the minimization of the Gibbs function, taking into account the gaseous species CO, CO₂, H₂, H₂O, CH₄, N₂ and graphitic carbon C in the solid phase. The thermodynamic equilibrium composition is examined in Fig. 2.9 A) using an initial syngas mixture with 10% CO, 7% CO₂ at the stoichiometric H₂/C-ratio of 3.4 in the temperature range between 200 and 800°C (1 bar). Obviously, the system shows a strong non-linear dependence with temperature. High concentrations of methane, low amounts of CO and CO₂, as well as side products are obtained below 400°C. This issue was already reflected by the high equilibrium constants of the main reactions. The extent of water formation is not discussed further, however, more water is formed alongside with methane. The reason for this lies in the Sabatier reaction which produces water in the stoichiometry of 2 compared to methane. The obtained concentration profiles in Fig. 2.9 A) are also representative for slightly different conditions as discussed later in the parametric study. The conversion of both species CO and CO₂ is considered in Fig. 2.9 B) and 2.9 C) separately. In case of CO (Fig. 2.9 B), conversion higher than 95% is obtained below 450°C which drops sharply above 500°C and becomes negative above 650°C. The decrease in H₂O and methane in parallel (Fig. 2.9 A) at temperatures higher than 500°C is a clear indicator for the reverse process, i.e. methane steam reforming. Regarding selectivity from CO to CH₄, a significant decrease at temperatures higher than 300°C is obvious. The reason lies in the increased production of CO₂ due to water-gas shift reaction of CO with formed water as can be seen from Fig. 2.9 A). Another major side product taking influence on the selectivity is the graphitic carbon which occurs between approx. 490 and 620°C (see Fig. 2.9 A) and can be mainly attributed to the Boudouard reaction. The contribution of carbon deposition from methane cracking is also feasible due to positive

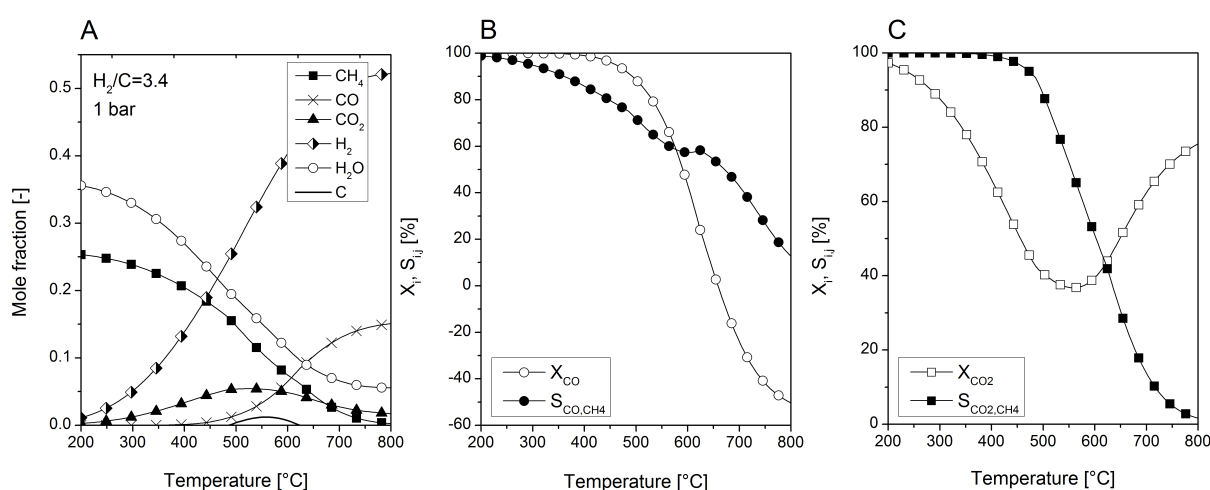


Figure 2.9: Thermodynamic equilibrium composition as a function of temperature (A) and conversion/selectivity as function of temperature for CO (B) and CO₂ (C) in the mixture containing 10% CO, 7% CO₂, H₂/C=3.4 at 1 bar (N₂ as remainder).

equilibrium constant at temperatures $>500^{\circ}\text{C}$. However, the extent of the contribution is unclear. At temperatures higher than 650°C , coke seems to be regasified. The issue concerning coke formation and its removal will be discussed later.

The conversion of CO_2 and selectivity to methane in Fig. 2.9 C) show a completely different behavior compared to CO methanation. The CO_2 conversion is up to 30% lower than that of CO below 350°C . This fact could be attributed to potential CO_2 production due to water-gas shift reaction. According to the selectivity curve, the route from CO_2 to methane is preferred below 450°C , while at higher temperatures CO production due to reverse water-gas shift or carbon gasification via reverse Boudouard reaction takes place.

Methane yield

By knowing the drawbacks of the system regarding temperature effects on the conversion and selectivity, the question arises which parameters affect the methane yield and how the reaction conditions can be optimized. One of the most important parameters concerns the H_2/C -ratio. In the conventional methanation processes based on coal or biomass gasification, this ratio is governed by the gasifier, whereas in the MINERVE project, the H_2/C -ratio is governed by the Solid Oxide Electrolysis Cell. The decision about the best H_2/C -ratio for the methanation system is answered in Fig. 2.10 A) by evaluating its effect on the methane yield. First, the methane yield is a clear function of temperature and shows similar trends as the CO/CO_2 conversion (Fig. 2.9 B and C) at all H_2/C -ratios. The yield is maximized at lower temperatures and decreases with the onset of the steam reforming of methane above approx. $500\text{--}600^{\circ}\text{C}$. The role of hydrogen excess is clearly beneficial for the system, but may be discussed later with regards to methane purity in different applications. Best performance is obtained with H_2/C -ratio of 5.4 leading to maximum yield below 500°C . Even higher hydrogen contents allow maximum yields beyond 500°C . However, such large ratios are less significant for application. By lowering the hydrogen content, as depicted in the stoichiometric case, the yield is clearly decreased down to 80% below 500°C due to potential CO_2 production. At an even lower hydrogen to carbon ratio of 3, additionally coke starts to form at temperatures higher than 450°C as side product (see later). The choice of the hydrogen content depends on the requirements of the final gas composition but also on the applied technology. High H_2/C -ratios are favorable for the methane yield. However, the residual hydrogen in the final product gas requires an additional cleaning step. Low H_2/C -ratios may produce less hydrogen residue, but pollute the final product gas with CO_2 and enhance the risk of coke formation.

The effect of pressure on the methane yield is depicted in Fig. 2.10 B) ($\text{H}_2/\text{C}=3.4$). In general, a positive effect on the methane yield is observed with increasing pressure in the entire temperature range. Below 250°C , methane yield is barely pressure sensitive independent of the H_2/C -ratio. A pronounced

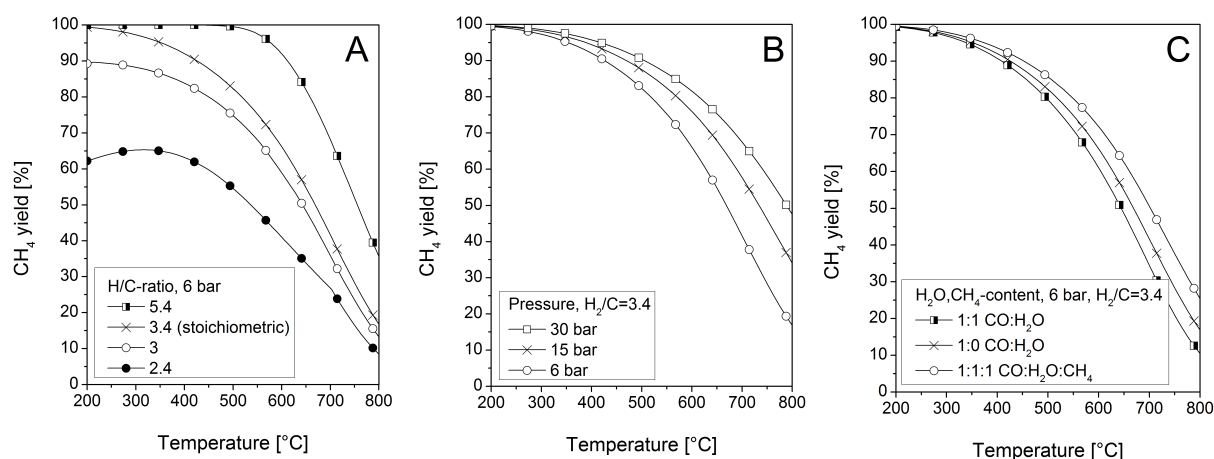


Figure 2.10: Influence of H₂/C-ratio A), pressure B) and addition of water and methane C) to the mixture containing initially 9% CO and 6% CO₂ (N₂ as remainder).

improvement with approx. 10 percentage points (p.p.) of methane yield takes place above 500°C and becomes especially important in the adiabatic packed bed reactors. In case of defined temperature control ($T < 450^\circ\text{C}$), which holds for microreactors, low pressurization guarantees high product quality already. Absence of additional compression makes the microreactor technology interesting also from an economical point of view.

The effect of steam and methane addition is depicted in Fig. 2.10 C) for the reason that it is a common practice to recirculate methane rich product gas in conventional applications to lower the maximum temperature (see Chapter 3.1). The initial gas composition is assumed to contain 9% CO, 9% CH₄, 9% H₂O, 6% CO₂ and 51% H₂ with N₂ as a remainder. According to thermodynamic calculation, the content of steam and methane has a slight positive effect on the methane yield. Below 500°C the effect is negligible. The addition of steam seems to inhibit ΔY_{CH_4} slightly. Summarized, the effect of methane and water gas addition has a negligible effect on the methane yield. However, the contribution of steam is remarkable with regards to kinetics and becomes relevant in terms of byproduct formation as described in the following.

Coke as side product

The significance of coke formation in methanation processes is indisputable. Therefore, the effect of H₂/C-ratio, steam content and the total pressure is examined in Fig. 2.11. The amount of hydrogen in the feed has a huge potential to prevent coke formation with increasing H₂/C-ratio (Fig. 2.11 A). Exemplarily, the carbon yield can be reduced from approx. 15% to 2.5% by increasing the H₂/C-ratio from 2.4 to 2.7 at 400°C. The increase to a stoichiometric ratio of 3.4 results in absence of graphitic carbon at 6 bar in the entire temperature range.

Another interesting fact concerns the deposition of coke from the species CO and CO₂. The component

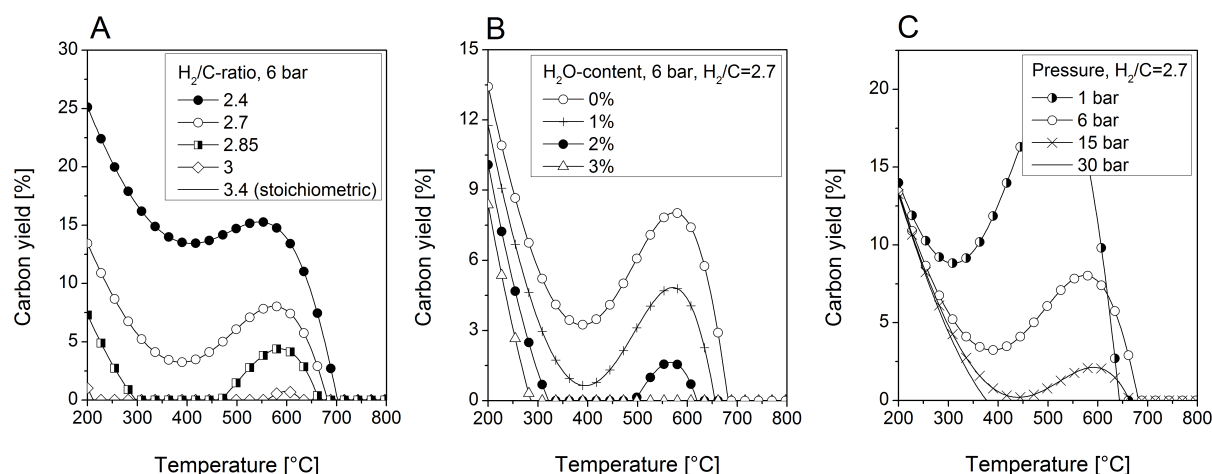


Figure 2.11: The effect of H_2/C -ratio A), steam content B) and pressure C) on the coke formation (10% CO , 7% CO_2 , N_2 as remainder)

CO_2 , depending on the H_2/C -ratio, forms coke at lower temperatures less than $350^\circ C$. The coke deposition resulting from CO solely happens in the temperature window between 450 and $700^\circ C$. This was obtained by evaluating of the equilibrium composition of pure H_2/CO and H_2/CO_2 mixtures and is not shown here. As consequence, the coke-free operation in the methanation process of $H_2/CO/CO_2$ mixtures narrows the temperature window with decreasing H_2/C -ratio. Under these conditions, precise temperature control is key for preventing catalyst damage by coke formation.

The addition of steam in conventional technology to counteract the carbon formation is analyzed in Fig. 2.11 B) by using H_2/C -ratio of 2.7 and a total system pressure of 6 bar. Surprisingly, even small amounts of water in the range of a few percent have a tremendous impact on the carbon deposition probability. Comparing to the effect of H_2/C -ratio, two percent of either hydrogen or steam lead to the similar effect on carbon deposition at high temperature. However, steam barely affects the coke deposition due to CO_2 decomposition below $300^\circ C$, while hydrogen does. Steam usage becomes interesting if partial recirculation of the product gas is realized. The steam generation due to reaction eliminates external steam generation and reduces the carbon probability at high methane yield. Finally, the effect of pressure on the carbon yield is studied using a fictitious H_2/C -ratio of 2.7 in Fig. 2.11 C), i.e. at high carbon formation probability. As in case of water, the effect of pressure leads to a carbon yield decrease caused by the CO decomposition which takes place above approx. $350^\circ C$. The carbon region which is caused due to CO_2 decomposition remains unaffected. Apparent improvement can be achieved by increasing the pressure from 1 to 6 bar. Thus, pressure can be effectively used as a supplementary tool for reducing carbon formation in feeds where sub-stoichiometric H_2/C -ratios may occur from time to time.

2.4.3 Summary

The thermodynamic study allows valuable insights into the methanation system. The non-stoichiometric approach based on the minimization of the Gibbs energy is a suitable tool for equilibrium composition calculation in complex multiphase systems. Applied to the methanation system containing CO and CO₂ at 1 bar with the H₂/C-ratio of 3.4, general characteristics are revealed. It is found that the conversion of CO/CO₂ and selectivity to methane are maximized at lower and inhibited at higher temperatures. The conversion of CO is generally higher than that of CO₂. However, opposite trends are observed regarding the selectivity to methane due to the importance of water-gas shift.

The possibility of influencing methane yield using primary parameters like H₂/C-ratio, pressure, steam and methane in the feed is carefully examined. In contrast to steam/methane addition and pressure variation, the significance of the H₂/C-ratio on methane yield is high. A study on the thermodynamically possible coke formation shows that both CO and CO₂ could contribute to coke formation at characteristic temperatures. Depending on the gas composition, CO leads to coke at higher temperatures above 400°C. The coke deposits due to CO₂ decomposition can occur rather at lower temperatures less than 300°C. The possibility for inhibiting coke formation is studied in terms of H₂/C-ratio, water content and pressure variation. Hydrogen and water, at small amounts <3 vol.%, are found to decrease coke formation probability considerably. However, opposed to hydrogen, steam influences the coke formation only at higher temperatures. This result is in-line with common praxis, i.e. recirculation of the steam containing product gas. The same applies for pressure which has a clearly beneficial effect for methanation applications.

It would be misleading to state that the lowest possible temperature is best from methane yield basis, since the system represents a complex optimization problem regarding optimal conversion, selectivity and yield. Reactor size would also increase with lowering the temperature. Furthermore, the possibility of nickel carbonyl formation on nickel (catalyst and reactor material) is very high below 250°C. Thus, a definite and precise temperature control is required for the optimal solution of the methanation system. Temperatures should lie between 300 and 450°C, which is a challenge with regards to the fast kinetics of the methanation system.

2.5 Catalyst deactivation in methanation

Catalyst deactivation is a serious problem in industrial applications and also concerns the methanation reaction. This section briefly summarizes the most common deactivation mechanisms while analyzing their causes and elucidating the consequences for the methanation reaction system.

2.5.1 General mechanisms

According to common literature on deactivation [76; 77], the catalyst degradation is based on mechanical, thermal and chemical deactivation processes, which can be further narrowed down to poisoning, sintering/evaporation, leaching, fouling and attrition (Fig. 2.12). Often, the processes occur in parallel and cannot be considered separately.

Poisoning

This category encompasses the blocking of the catalyst surface by formation of covalent bonds between an undesired chemical compound (impurity) and the active catalyst site. Thereby, the adsorption strength of the poisonous compound exceeds that of the reactants resulting in surface inaccessibility for the reactants [77]. Strong poisons in methanation processes are hydrogen sulfides, which are encountered in syngas mixtures obtained from biological sources by, e.g. gasification of coal or biomass [78]. According to Gardener et al. [79], sulphur poisoning on Ni/Al₂O₃ reduces the dissociation of

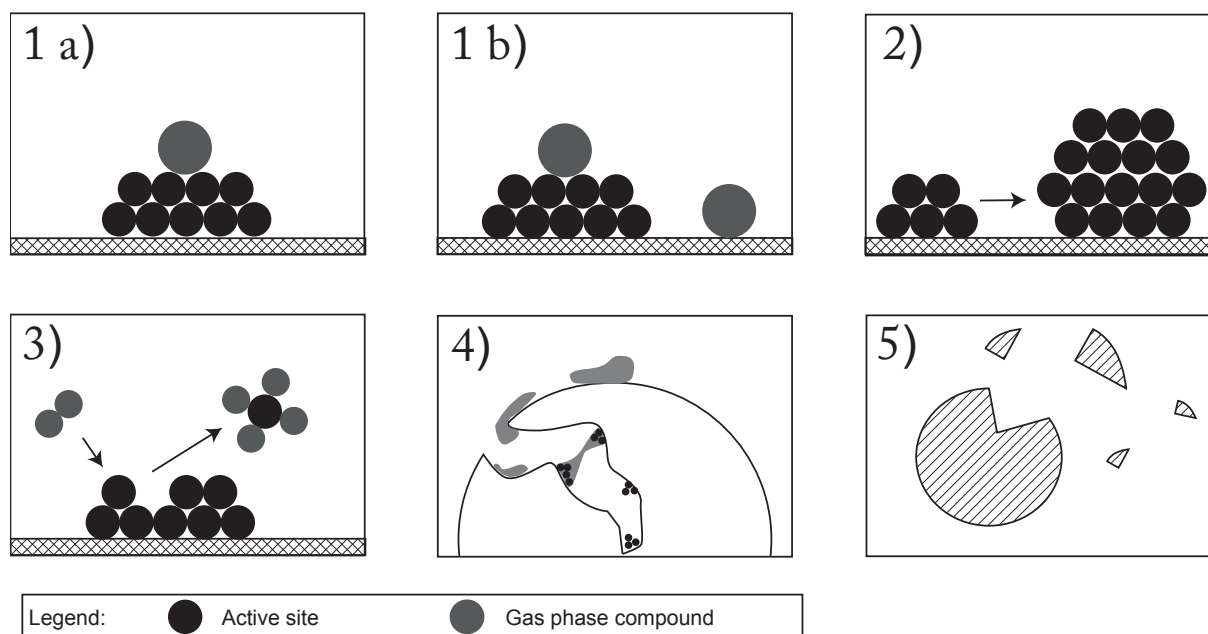


Figure 2.12: Five deactivation mechanisms: 1a) Selective poisoning, 1b) Non-selective poisoning, 2) Sintering 3) Leaching/Corrosion 4) Fouling 5) Attrition (adapted from [77]).

hydrogen drastically while CO adsorption is lowered by approx. 50% on a completely sulphur poisoned catalyst. The lack of dissociated hydrogen on the surface leads to decreased hydrogenation rates of the carbonaceous intermediate from CO and favors finally carbon accumulation. Hence, sulfur induces a fouling process by coke, which is explained later.

In the present work, the syngas is produced by the SOE-Cell which requires clean CO₂ and water as feed. Hence, the poisoning of the catalyst by sulfur in the methanation unit is not considered in this work.

Sintering

Sintering is often referred to the loss of the active surface via structural modification of the catalyst and is a thermally induced process [80]. The process is not only restricted to the active metal phase but may also concern the material support. The sintering of the active sites takes place via crystallite and atomic migration [81], which broadens the crystallite size distribution and lowers the catalytic active surface. Since crystallite migration requires movement of the entire entity, atomic migration is governed by the detachment of single atoms and their movement. Sintering kinetics of Ni-supported catalysts in hydrogen rich environments were studied by Bartholomew et al. [81; 82], who found that surface collapse of Al₂O₃ was dominantly contributing to active site sintering below 650°C, whereas crystallite growth dominated at temperatures larger than 650°C. The extent of sintering was shown in terms of the total Ni surface, which decreased in steady-state by approx. 5% at 650°C and more than 30% at 750°C in pure hydrogen.

Leaching

The leaching stands for loss of catalytic phases by forming of volatile compounds, e.g. carbonyls, nitrosyls, oxides, sulfides or halides [83]. In the methanation process, nickel carbonyl formation Ni(CO)₄ is of interest in case Ni-based catalysts are used. Like other chemical reactions, the formation of Ni(CO)₄ is a chemical process where Ni reacts with CO to gaseous Ni(CO)₄. The rate of formation was analyzed by, e.g. Goldberger and Othmer [84] by passing CO over reduced nickel powder at temperatures below 100°C. They found that the rate of Ni(CO)₄ depends linearly on the CO surface coverage. The rate of formation was found to pass through a maximum at 75°C for all examined total pressures, followed by a decline at higher temperatures. The decreasing formation rate at higher temperatures was explained with a faster decomposition of nickel carbonyl on the active site. The drawbacks resulting from nickel carbonyl formation on engineering level were discussed by Shen et al. [85], who found that in “unsafe” operation regime, the volatilization and decomposition processes result in Ni-flux from smaller to larger crystallites. As a consequence, crystallite growth takes place. By reducing the temperature, a more dramatic phenomenon was observed leading to nickel content downstream the packed bed and Nickel

loss from the system. Good stability of alumina supported Ni catalyst was observed above 250°C at methanation conditions [85]. Nickel carbonyl is highly toxic, thus, syngas temperatures should always be above 250°C in presence of nickel catalyst.

Attrition

Attrition belongs to the mechanical degradation of the catalyst caused by internal or external forces leading to disruption. This phenomenon is applicable to all reaction systems and is ubiquitous in many reactor types. For example, attrition occurs in packed and fluidized beds. In conventional catalyst beds, the pellets have to stand the pressure from the weight of the packing which can exceed several tons. In addition, supplementary forces are caused by thermal expansion or shrinkage of the reactor and catalyst volume [77] leading to high or uneven pressure drop, flow maldistribution and undesired behavior of the reactor [4].

In fluidized beds, the formation of the fine particles represents a more serious problem and leads to a considerable catalyst loss [77; 86]. This kind of degradation also concerns catalyst in the form of wall coating, as they are encountered in microreactors resulting in cracking and detachment from the wall [87]. In this thesis, the packed bed microreactor system is investigated. As the bed height is low in this case, attrition may be negligible from weight contributions, but could still occur due to temperature effects.

Fouling

Fouling considers all phenomena involving deposition of a substance on the catalyst, e.g. dust or ash [77]. In the methanation system, fouling by coke deposition represents a serious problem and was examined by a number of groups. Due to its significance, also encountered in this work, the origin of coke, likelihood of formation and prevention methods are presented in the following section.

2.5.2 Fundamentals of coke formation

What is coke and how does it occur? The “coke” is not a well-defined term in literature and encompasses all kinds of carbonaceous substances precipitating to the catalytic surface, which originate from a catalytic decomposition process of, e.g. CO, CO₂, CH₄ or saturated/non-saturated hydrocarbons [10]. The carbon formation in the methanation process, as encountered in this work, is due to CO/CO₂ transformation and has been extensively discussed and summarized in several reviews [10; 76; 80]. Here, a brief summary is given to elucidate the complexity of this topic.

Origins & morphology

The coke formation resulting from CO or CO₂ is believed to proceed via adsorption and subsequent decomposition to surface carbon C* and oxygen O*. This assumption is the basis of the Carbide theory in methane formation (see Chapter 2.2). For adsorption phenomena, please refer to Ch. 2.2.3. Although, the decomposition to C* seems to be simple, the resulting surface carbon is highly complex in structure and is strongly influenced by the system parameters like temperature, pressure and gas phase composition. In general, three main types of carbon can occur on a catalyst particle: Amorphous, crystalline or coke dissolved in the metal [88]. The amorphous structures are products of single chemisorbed carbon atoms, which undergo hydrogenation and form meta-stable “fluffy” entities [89]. Different hydrogenation states of carbon, e.g. C*, CH_x and CH₄ according to Carbide theory and the effect of the rate-limiting step (see Chapter 2.2) are corresponding this hydrogenation of meta-stable carbon. As was shown by McCarthy and Wise [88], the reactivity of atomic (α) and amorphous (β) carbon species on an alumina-supported Ni catalyst is relatively high and results in methane formation at lower temperature of 450 to 650 K. Crystalline species in the form of graphite are not reactive at lower temperatures, however, can be gasified with hydrogen at temperatures >800 K [88]. McCarthy and Wise could also show that the aging of the α type carbon resulted in gradual transformation to β which was further converted to graphite.

Besides the surface carbon formation, saturation of the metal with carbon leads to the nickel carbide NiC₃ phase. The phase composition is governed by the carbon solubility, metal properties, temperature and can be obtained from phase diagrams [90]. This type of carbon is the main cause for the metal dusting effect [90; 91] (see Chapter 3.1.1) and carbon filaments growth [92].

Carbon formation and loss of catalytic activity

Carbon accumulation leads to different geometrical forms which determine the way of the catalyst deactivation. According to Nolan et al. [93] carbon can accumulate on surfaces as layers/shells or grow as filaments/whiskers. In case of layers, encapsulation of the active sites leads to their physical inaccessibility and catalytic loss of activity as consequence (Fig. 2.13 A). The filaments or whiskers were examined by Baker et al. [92]. They propose that the decomposed carbon on the crystallite surface diffuses through the particle and segregates on the opposite site forming a tube or a whisker. Thereby, the crystallite is detached from the support with progressing filament growth. This process is called “tip-growth” [92] (Fig. 2.13 B). In case of the “root/bottom-growth”, the crystallite stays attached to the support surface [92]. According to Nolan et al. [93], hydrogen presence is imperative for whisker formation. Its absence results in layered encapsulation. A further key parameter is the temperature leading to whiskers below 500°C and layered carbon formation at higher temperatures [95], leading to the assump-

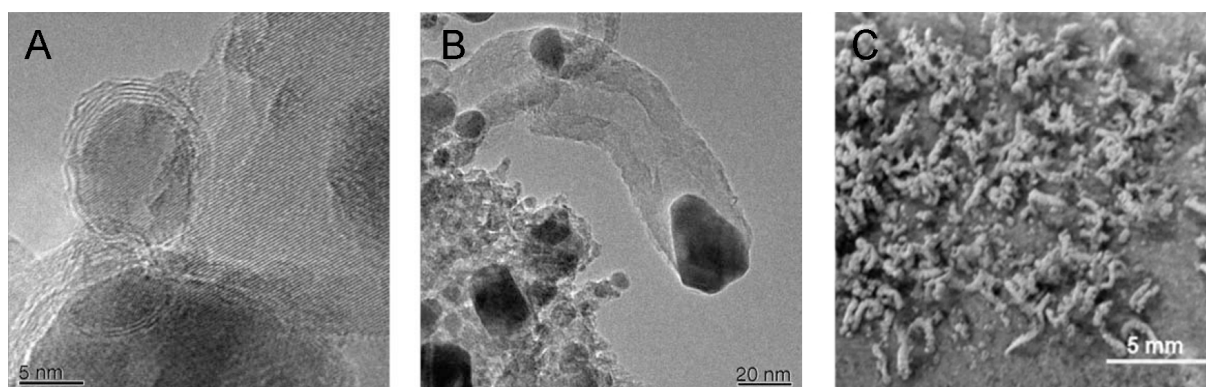


Figure 2.13: TEM images of carbon deposition on a $\text{Ni/MgAl}_2\text{O}_4$ catalyst via encapsulation of the catalyst A), whisker formation on the catalyst B) [94] and whisker formation on the reactor material Inconel 693 at 650°C C) [90].

tion that whisker carbon is less stable from a thermodynamic point of view. Whisker/nanotube growth leads to the loss of the metal-support interaction and active material loss. Furthermore, the growth of the whiskers inside the pores of the catalyst pellet may also destroy its structure, leading to attrition [10]. It has also to be mentioned that filaments can also be observed on the reactor material walls as shown in Fig. 2.13 C) resulting from the metal dusting process (see Chapter 3.1.1). Detailed studies of this phenomenon are discussed extensively in nanotube science and can be found in the appropriate literature.

2.5.3 Catalyst regeneration and prevention of coke formation

Carbon formation cannot be prevented completely, but its formation can be delayed [76]. In general, the prevention takes place either by modifying the catalyst properties or the process parameters, e.g. temperature or gas composition. On the catalyst level, the acidic support material, e.g. $\gamma\text{-Al}_2\text{O}_3$ promotes coke formation, whereas less acidic MgO or SiO_2 reduces its formation [10]. Better coke resistance of the catalyst is also observed by adding alkali promoters to reduce the acidity of the alumina support. However, according to the study of Chen et al. [96] only Na and K yield better coke resistance on an $\text{Ni/Al}_2\text{O}_3$ amongst Ca, Mg, K, Ni and Li. A further study by Huang and Richardson [97] reveals that the loss of activity may be encountered if the alkali amount is too high or too low. A maximum in TOF is detected at 0.3 wt.% in Na exceeding that of non-promoted catalyst by a factor of 6.

Other optimization methods involve a) alloying of the nickel with Pt, Co, Ru or Mo [98; 99] and b) adjustment of the crystallites size [100; 101] to enhance hydrogenation and thus resistance towards coke. The discussion of these aspects would go beyond the scope of this work and can be found in the appropriate literature.

On the process level, the extension of the catalyst life time can be done by adjusting H_2/C -ratio, H_2O

concentration, temperature, pressure and can be quantified using thermodynamic equilibria (see Chapter 2.4). Furthermore, removal of poisons, e.g. H_2S and non-saturated hydrocarbons promote better catalyst stability (see Chapter 2.5.1).

Since the catalyst fouling by carbon deposition is a matter of time, the removal of coke is necessary and is successfully applied in the industry by gasification of the solid C with e.g. O_2 , CO_2 , H_2 and H_2O [4; 76]. The reason for this procedure is clear, however, the consequences for the catalyst have to be kept in mind. According to Rostrup-Nielsen [4], hydrogen and steam can be applied for fresh coke depositions which are gasified at around 500°C . Oxygen or air are used for aged coke and temperatures up to 700°C are required [99]. Obviously, high temperatures and the choice of the gasification agent, especially hydrogen, can result in sintering phenomena as described previously. Moreover, the gasification reaction can be accompanied by several transport limitations, e.g. through pore network [4] or through carbon saturated Ni crystallites [102], which implies that the total removal of coke is difficult. An interesting phenomena during regeneration of the Ni catalyst in a fluidized bed with air is observed by Moeller et al. [99] in the scope of the BI-Gas project. Up to 7% of Ni is lost during the regeneration process, which is explained with the detachment of the Ni crystallite due to tip-growth of the whiskers. By burning off the carbon, Ni crystallites were automatically removed as fine particles. Hence, the authors conclude that multiple regeneration steps would lead to a steady decrease of the Ni content, reducing the performance of the reactor, and recommend no more than 2-3 regeneration cycles.

2.5.4 Summary

The deactivation of the methanation catalyst may result from several causes, which can be categorized in mechanical, thermal and chemical degradation processes. Although many of them can be avoided by a proper reactor design (temperature control for preventing sintering or leaching phenomena) or process design (purification of the feed from poisons), the other forms of deactivation are more sophisticated. In the methanation reaction, carbon is supposed to be the most important intermediate which can be hydrogenated to methane but also lead to serious fouling problems. Carbon, depending on the reaction conditions, may exhibit different hydrogenated states and can grow as layer or whisker. To counteract the fouling process, several groups suggest optimization of the catalyst systems with respect to modification of the active metal and support material. In case coke formation is inevitable, several important aspects regarding the regeneration procedure are discussed. It is shown that gasifying the coke at higher temperatures may partially restore the catalyst activity. However, sintering phenomena and active metal removal due to whisker burn-off may occur. In this thesis, the influence of the reactor properties and reaction conditions will be in focus. Catalyst modification is not in the scope.

3 Conventional vs microstructured reactor technology

Based on the knowledge from the previous chapter and understanding the most important aspects regarding kinetic mechanisms, thermodynamic equilibrium and catalyst deactivation, this chapter focuses on the reactor technology. The conventional methods are briefly presented, since methanation has a long history and lessons learned can be applied for design of advanced technologies. Finally, novel reaction engineering solutions are presented for methanation reaction using microstructured technology.

3.1 State of the art

First large-scale applications for synthetic natural gas (SNG) production evolved in the energy and oil crisis in the 1970s and provided an additional energy source aside from oil [103]. Since then, many projects were established including plants for research but also for commercial purposes. The analysis of the projects conducted between 1965 and 2013, which are partially summarized in Tab. 3.1, reveals that the commercial and pilot plants are mainly restricted to two reactor types: fixed bed reactors and fluidized bed reactors. Rare concepts like three-phase methanation have already been tested in the 1970s, yet gained less popularity [78]. Novel reactor technologies, e.g. structured honeycombs or microstructured reactors for methanation have been objects of research starting from the late 2010s.

In the following, the conventional technology and the knowledge behind it is briefly examined.

Table 3.1: Methanation process developments from 1965-2013 partially adapted from [105].

Process	Year	Stage of Devel.	Reactor Type	React. Conditions	Feed
Bi-Gas	1965	Pilot	FL, 1 Stage	40-530°C, 86 bar	Coal
Lurgi	1974	Comm.	FB, 2 stages	450°C, >18 bar	Coal
Conoco-Meth	1974	Pilot	FB, 4 Stages	n.s., 80 bar	Coal
Linde	1979	Semi-Comm.	FB, 2-3 Stages	300-750, 20 bar	n.s.
Comflux	1980/2008	Pilot	FL, 1 Stage	400-500°C, 20-60 bar	Coal, biomass
TREMP	1980	Comm.	FB, 3 Stages	300-700°C, 30 bar	Coal, biomass
HICOM	1981	Pilot	FB, 4 Stages	230-640°C, 25-70 bar	Coal
Bio-SNG	2006	Pilot	FL (Comflux)	350°C, 2-5 bar	Biomass
GoBiGas	2013	Demo	FB, 2 Stages	300-700°C, 25 bar	Biomass
Audi e-gas [104]	2013	Comm.	FB	NA	

FB: Fixed bed; FL: Fluidized bed; Pilot: Pilot plant; Comm: Commercial plant; Demo: Demonstration plant; n.s.: not specified.

3.1.1 Packed bed reactor

In most of the commercial applications, fixed bed reactors are realized as tubular reactors with several cubic meters of reactor volume. A typical representative is the tubular reactor from the TREMP™ process with approx. 0.6 m in diameter and 2.5 m in length (Fig. 3.1 on the left) [75]. The reactor volume is usually filled with several hundred kilograms of catalyst in form of hollow cylinders (Raschig rings) which generate up to 50% less pressure drop compared to spherical particles [106]. The reactant throughput depends on the plant size. Large processes like TREMP™ exhibit very high feed flows with around $2 \cdot 10^5 \text{ Nm}^3/\text{h}$ yielding finally around $36000 \text{ Nm}^3/\text{h}$ of SNG [75].

Adiabatic operation of such packed bed reactors, which is the case in many methanation applications, is caused by several factors. The most important is that the reaction is very fast and releases tremendous amounts of heat. Its removal cannot be guaranteed due to thermal packed bed properties but also due to large reactor dimensions leading to heat transport resistances. A polytropic packed bed reactor was presented by, e.g. Linde AG (Fig. 3.1 on the right) with integrated cooling possibility. A piping in the form of a coil is submerged in the catalyst bed and flushed with water producing steam during the methanation process. The reactor did not perform as expected under methanation conditions, however, was successfully applied for methanol synthesis at a later stage [107].

In adiabatic reactors or in reaction units with lack of temperature control, strong exothermicity of the methanation process can lead to enormous temperature peaks with up to 750°C (see Tab. 3.1). The extent of the overheating is governed by the thermodynamic equilibrium and depends on the reaction

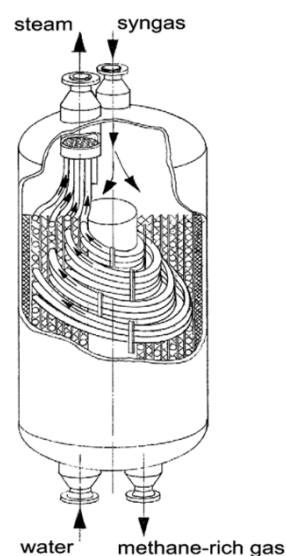


Figure 3.1: Picture of one semi-commercial reactor stage in the TREMP™ process for $200 \text{ Nm}^3/\text{h}$ of SNG product [106] (left). Linde reactor concept for isothermal operation including submerged piping coil for cooling purposes [107] (right).

conditions (see Chapter 2.4). A typical temperature profile in a large adiabatic fixed bed reactor is shown in Fig. 3.2 as a function of the reactor length. Thereby, the temperature rises at the inlet almost instantly and remains constant in the following due to thermodynamic equilibrium. This kind of operation is extremely disadvantageous for all levels of the process.

Catalyst level

On the catalyst level, extremely high temperatures lead to catalyst deterioration in mechanical, thermal and chemical nature (see Chapter 2.5). This also includes temperature related byproduct formation in the form of carbon. The effect of catalyst deactivation is captured in Fig. 3.2 as a function of the reactor length at different times on stream (TOS). With progressing activity loss of the catalyst, hot spot movement along the axial coordinate takes place. Here, the required catalyst excess for long-term operation becomes visible. The excess catalyst is also exposed to high temperatures and is altered with time on stream which makes the reactor concept less attractive. Kinetics and mass transfer phenomena, e.g. catalyst efficiency are barely of interest since the excess of the catalyst guarantees reactor behavior governed by thermodynamics.

Reactor level

On the reactor level, high temperatures in the range 450-750°C and supersaturated gaseous environments with respect to carbon result in a corrosion phenomena named as “Metal Dusting” [91]. The process can be simplified to the following steps: Carbon monoxide is decomposed on the metal surface to solid carbon and H₂O [90]. Solid carbon dissolves in the metal and forms a metal carbide phase M_xC_y. Due to thermodynamic instability, the phase decomposes into pure metal and carbon as loosely particles.

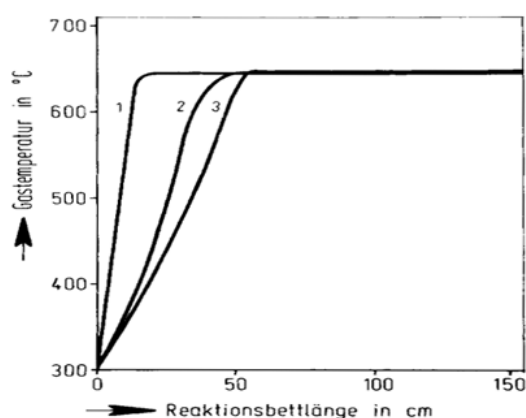


Figure 3.2: Temperature profile in the first reactor stage of the TREMPTM process as a function of the reactor length and operation time ($H/C=6$, 30 bar). The catalyst bed with the length of 2.5 m is filled with the MCR-2X catalyst which is regenerated two times after (2) 2013 h and (3) 4034 h.

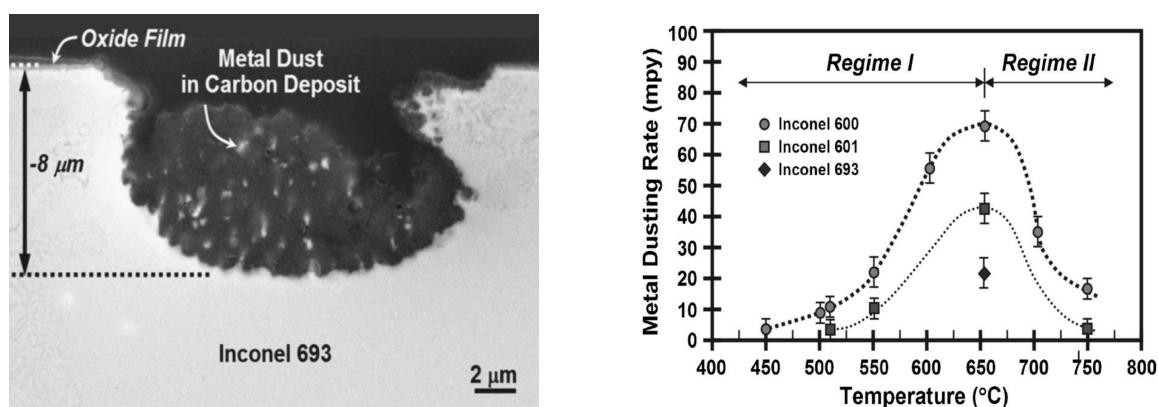


Figure 3.3: Cross-sectional SEM image of the Inconel 693 after 160h at 650°C (left) and metal dusting rate on the Ni-alloys as a function of temperature in a $H_2:CO$ -rich environment (50:50 vol.%) (right) [90].

The segregated carbon with incorporated metal dust particles is shown in Fig. 3.3 on the left. The metal dusting takes place on Fe, Ni, Mo metals and their alloys [91]. Nickel alloys containing chromium, e.g. Inconel 600 (15.5 wt.%), 601 (23.0 wt.%) and 693 (30.0 wt.%) show higher resistance due to surface oxide formation (Cr_2O_3) [90]. Fig. 3.3 on the right depicts the metal dusting rate on the Inconel alloys in a $H_2:CO$ environment (50:50 vol.%) as a function of temperature. The beneficial effect of the increasing chromium content is explained with segregation of the Cr atoms forming a thicker protective oxide layer. Another phenomenon concerns the temperature dependence of the metal dusting rate with maximum at approx. 650°C. Below the critical temperature, the carburization rate of the metal increases with temperature. At higher temperatures, this tendency is kept, however, the ability of the Cr-oxide to form continuous and defect-free layers is also increased working against the carbon penetration. The maximum rate at 650°C in the Inconel 600 produces pit depths of around 32 μm with ablation rates around 1.75 mm per year.

By applying the knowledge to the conventional adiabatic packed bed reactors, the metal dusting rate is at maximum in adiabatic reactor and requires continuous maintenance for safety reasons.

Process level

On the process level, the usage of multiple adiabatic reactors requires a sophisticated heat management and process layout to achieve high concentrations of methane in the product gas. Most of the process schemes for methanation using adiabatic fixed bed reactors, partially covered by Tab. 3.1, are extensively discussed in reviews by Kopyscinski et al. [74] and Rönisch et al. [78]. Here, a brief insight into the TREMP™ process is given, which was developed in the scope of the NFE-Project (Nukleare Fernenergie) in cooperation with Kernforschungszentrum Jülich GmbH, Rheinische Braunkohlenwerke and Haldor Topsoe in the 1980s [75]. Fig. 3.4 shows the flow sheet of the methanation plant including three adiabatic methanation units filled with MCR 2X catalyst. The feed is provided by the steam-reforming

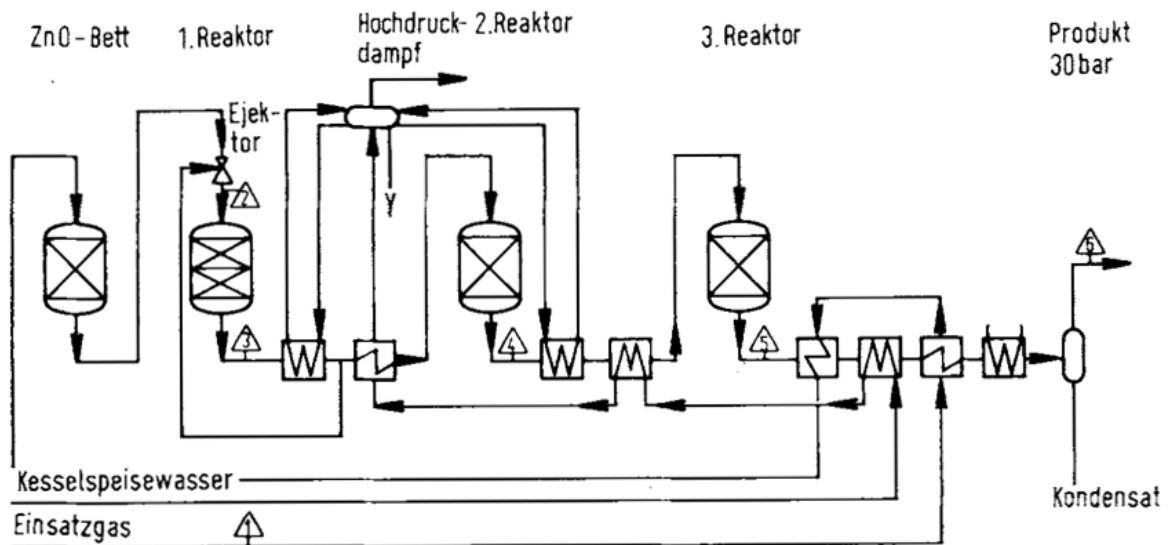


Figure 3.4: Flow diagramm of the TREMP™ process as designed during the NFE-Project in the 1980s.

unit and includes hydrogen sulfide removal in a ZnO bed. The syngas consists of 18% CO, 3% CO₂, 13% CH₄ and 66% H₂. The first step in the methanation process involves the mixing of the dry syngas with a partially recirculated product gas to obtain the ignition temperature of around 250-300°C. The recirculation step is further required to limit the temperature to max. 650°C in the first stage. The heat removal is realized via heat exchangers in between the stages, which generate superheated steam and cool down the product gas to the ignition temperature for the next reactor stage. The maximum temperature in the first, second and third stages is kept below 650, 500 and 330°C, accordingly. After removing water in the final product gas, a methane content larger 95 vol.% is achieved. The entire process consumes around 100000 Nm³/h of syngas and produces around 36200 Nm³/h of SNG. The presented scheme for the attached power plant utilizing the generated high-pressure steam would generate around 70-99 MW of electrical energy and 24-240 MW of thermal energy. For further details, refer to the original research article [75].

3.1.2 Fluidized bed

Although the fluidized bed technology seems to be very promising for highly exothermic reactions, the application of fluidized bed reactors is still limited to pilot plant scale and is not offered as a commercial solution on the market, as it is the case for the fixed bed reactors. A typical fluidized bed reactor consists of a vertical erected tube, in which the fine powdered catalyst particles in the micron range are fluidized by the feed gas. The cooling or heating is realized as in-tube bundles which are placed into the fluidized

bed. The drawback of the system is that it is far more complex than a packed bed. The fluidization regime requires minimum gas velocities to prevent undesired effects, e.g. slugging [86]. In addition, catalyst loss and attrition take place [86]. During the BI-GAS project, it could be shown that the catalyst activity decreases more rapidly compared to a fixed bed, which is explained with a more uniform exposure to reactants [99]. Benefits from this kind of technology are a better heat transfer in the fluidized bed leading to better temperature control compared to a fixed bed, and the regeneration of the spent catalyst during the operation. The most successful pilot plant was built in the cooperation of Thyssengas GmbH and University of Karlsruhe between 1975 and 1986; the COMFLUX process (Fig. 3.5 on the left). The final reactor consists of a vertical erected tube with 1 m in diameter and holds 1-3 tons of catalyst with particle size between 10 and 400 μm . The tested throughput of SNG was around 2000 Nm^3/h with a H_2/C -ratio of 3. High CO conversion in one reactor unit greater than 99% was achieved, while the axial reaction temperature could be kept nearly isothermal and clearly below 500°C [74].

A modification of the fluidized bed is the replacement of the working fluid with inert liquids so that three phases are obtained. This reactor concept was realized as a pilot plant by Chem Systems Inc. in the 1970s and allows isothermal operation of the methanation process [109]. The drawbacks of such systems are high gas-liquid mass transfer resistance in the involved liquid and its degradation [108; 110]. Such systems are regarded as a viable alternative for conventional technology and are examined at the present time by KIT within Energy Lab 2.0 [111].

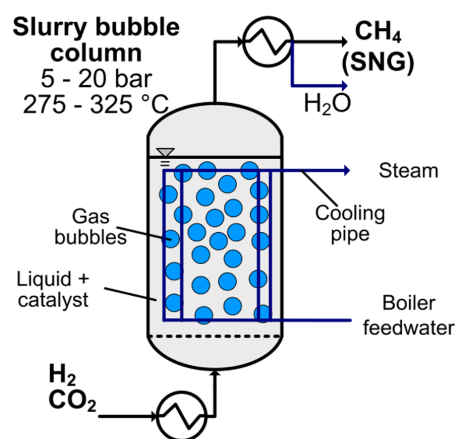


Figure 3.5: COMFLUX pilot plant for up to 20 MW_{SNG} erected by Ruhrchemie Oberhausen (Ger) [74] (left) and schematic visualization of the three-phase slurry reactor for methanation [108] (right).

3.2 Microstructured reactor technology

Although the conventional methods accomplish the task of SNG production, the packed and fluidized beds can be considered as technology lacking in efficiency and dynamics capability. At this point, microstructured reactor technology is introduced, which allows a high degree of process intensification on the reactor and process levels and can be considered as a promising solution for the extremely fast and strongly exothermic methanation reaction.

3.2.1 Fundamental aspects of process intensification

What is microstructured technology and what kind of benefits arise by conducting the methanation reaction in such devices? According to classical definition, the key feature in microstructured devices is the lateral dimension of channels or ducts which are in the sub-millimeter range (Fig. 3.6 on the left). Thereby, the characteristic lengths reach into the boundary layer [112], resulting in a considerable decrease or even disappearance of the bulk phase. As consequence, higher transfer rates of mass and heat are expected which is described in more detail later. The microstructured devices are not limited to small outer size and can achieve significant dimensions with industrially relevant throughput as shown in Fig. 3.6 on the right. This allows design of methanation modules capable to compete with medium throughput applications at pilot-plant scale.

From a geometrical point of view, miniaturization results in high specific surface area, which is defined as the ratio between the wall surface area and the volume of the unit cell according to Eq. 3.1.

$$a_v = \frac{A}{V} \quad (3.1)$$

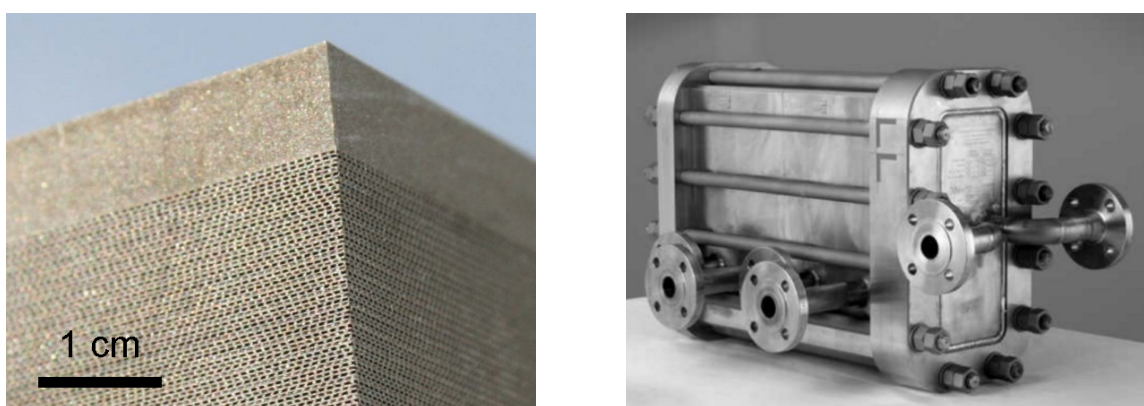


Figure 3.6: Microstructured reactor element (left) and polytropic reactor of 290 kg in weight with the total throughput capability of approx. 1700 kg/h of liquid chemicals built by KIT.

Typical values in the microstructured reactors are in the range of $20000 \text{ m}^2/\text{m}^3$, whereas conventional technology exhibits values below $1000 \text{ m}^2/\text{m}^3$ [113]. The superiority of miniaturization regarding specific area becomes beneficial for applications requiring walls as interface. For example, extremely high surface area can be achieved by wash-coating with catalyst which allows high GHSV values while keeping the pressure drop low. Regarding heat transfer, increased contact area with, e.g. heat transfer medium on the other side of the wall allows profound temperature control while conducting extremely fast and exothermic reactions in adjacent channels.

Another advantage arising from miniaturization concerns the enhancement of the mass and heat transport phenomena by conduction. The indicator for the extent of the process intensification can be expressed in terms of time scale in Eq. 3.2.

$$t = \frac{r^2}{D} \quad (3.2)$$

Thereby, the time scale t is a ratio between the transport length r in power of 2 and the diffusion coefficient D . Due to small distances in microstructures, the diffusion process can be reduced by a factor of 10^3 [114] compared to conventional technology. Similar relation can be formulated for, e.g. heat conduction by substituting the diffusion coefficient with thermal diffusivity ($a = \frac{\lambda}{\rho C_p}$) leading to superiority of microstructures regarding heat and mass transport. The intensification of the heat transport is not only achieved in the fluid phase, which can be reacting flow or cooling/heating media, but also in the solid phase. According to Fourier's law, $\dot{q} = -\lambda_s \int \frac{dT}{dx}$, extremely small transport distances (dx) allow neglecting the heat transport resistances in the construction material, which simplifies the system.

In conventional methanation technology, heat transfer takes place solely via the reactive fluid in packed bed reactors as well as the fluidized bed and need to be transferred to external or internal cooling systems, respectively.

The benefits of the intensification on the reactor level have a great impact on the entire methanation process chain. Fig. 3.7 on the left clarifies the required steps using the conventional packed bed and microstructured technology with a reasonable gas composition of 10% CO, 7% CO₂ and H₂/C-ratio of 3 at 1 bar from co-electrolysis. The conventional procedure requires at least three adiabatic reactors with intermediate cooling to achieve an acceptable methane content in the product gas (see TREMP™ process). The reason for this is the strong temperature rise in each stage, which limits the methane composition according to thermodynamic equilibrium. On the contrary, microstructured reactors with in-situ cooling of the reaction, keeping the temperature in the catalyst in a certain temperature region (polytropic), allow to reach the same product quality in a **single step** due to enhanced heat transfer capability. As a consequence, less periphery, e.g. heat exchangers and respective heat management are required decreasing the capital expenditures (CAPEX). Furthermore, less operation units decrease the plant size, promote its portability and applicability in decentralized systems.

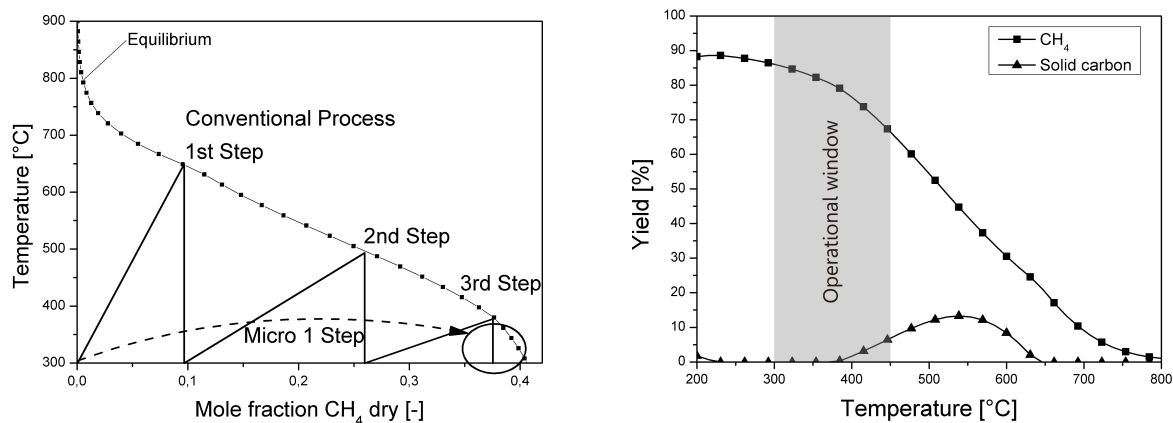


Figure 3.7: Visualization of the methanation process conducted in a conventional technology using 3 adiabatic reactors with interstage cooling and in a polytropic microstructured reactor (left). The optimum temperature regime is characterized in terms of yield of CH₄ and byproduct formation (solid carbon) (right). Initial equilibrium conditions: 10% CO, 7% CO₂, N₂ as remainder, H₂/C=3, 1 bar.

Another aspect concerns the byproduct formation and its effect on the general process. Fig. 3.7 on the right shows the equilibrium yield of methane and solid carbon as a function of temperature. The major insight is that the graphitic carbon is formed beyond 400°C and may form in the 1st and 2nd adiabatic reactors. In contrast, the formation of this species in microstructures could be prevented while maximizing the methane yield when the temperature stays in the highlighted region. This would result in longer operation times for the catalyst, reactor and the entire process. In addition, there would be no excess of catalyst accounting for deactivation required, implying the compactness of the reactor size.

Summarized, the microstructured reactor technology would allow the design of compact, portable and highly efficient reactors due to intensification of mass and heat transport phenomena and make them a perfect choice for the extremely fast and highly exothermic methanation reaction.

3.2.2 Challenges in microstructured reactors

Despite the attractiveness of the process intensification, the microstructured reactor technology encounters challenges which have to be examined carefully. This is also true for the resulting solutions involved in the design of the methanation reactor.

Fluid flow

Fluid flow in microstructures is often associated with maldistribution of the fluid (reaction mixture or heat transfer fluid) which can lower the overall performance of the device considerably. The origin of non-uniform fluid flow is primarily caused by an uneven pressure drop distribution in the device due to

fabrication tolerances of individual channels or inappropriate geometry of the, e.g. distributor, fins and channels. It is often a result of an improper design [115]. A lot of attention was paid to the geometry of the inlet manifolds of plate-fin reactors, since the inlet connector bridges the micro channels and has a direct impact on the flow [115]. Exemplarily, Fig. 3.8 on the left shows the numerical pressure drop profiles at the gas velocity of 10 m/s in a certain microstructured foil consisting of distribution chamber and microchannels. Obviously, the pressure varies in the manifold area and is clearly not uniform in all microchannels, leading to a velocity profile among the channels and, hence, a broad residence time distribution. Delsmann et al. [116] found that at gas velocities below a critical value, in this case 30 m/s (channel $w \times h \times l$: 0.4 x 0.3 x 40 mm), the flow distribution is governed by the wall friction and the relative standard deviation of the flow distribution is flow independent. At higher flows, they found that inertia started to contribute and worsened the relative standard deviation of the flow distribution linearly with gas velocity.

Another example is shown in Fig. 3.8 on the right depicting the flow profiles in an optimized geometry of a plate-fin micro heat exchanger [117]. The authors could show that below Reynolds number of 5 ($u < 0.04$ m/s), two outlets could provide good pressure loss management yielding uniform velocity profiles in the center of all microchannels. However, according to Fig. 3.8 on the right, the velocity distribution in the manifold chamber is not homogeneous and a possible maldistribution at higher Reynolds numbers could appear. Further design aspects of the manifolds and channels are summarized in a comprehensive review by Rebrov et al. [115].

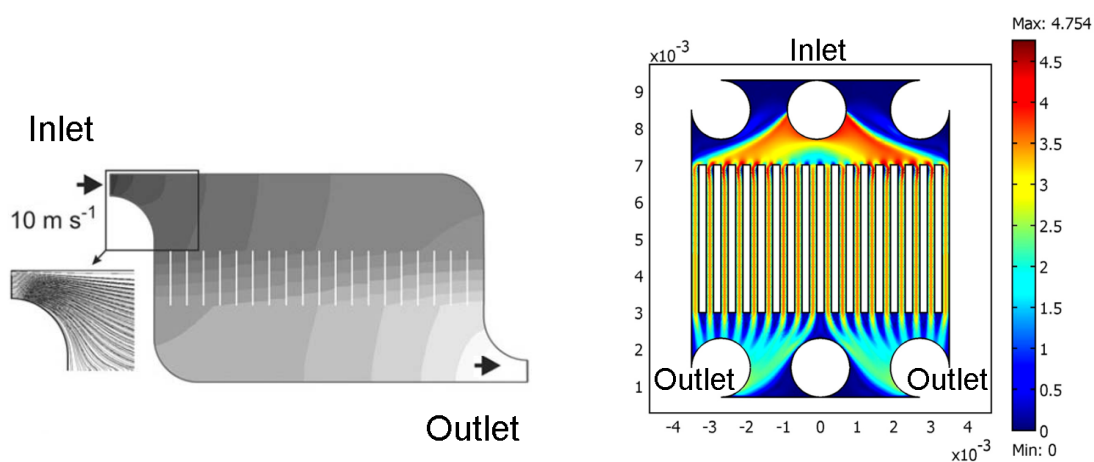


Figure 3.8: Pressure (left) [116] and velocity profile (right) [117] distribution examination in two microstructured heat exchanger geometries.

Catalyst integration & deactivation

The optimal performance of microstructured devices is obtained by tailoring the device to the characteristics of the reaction type, which determines the type and integration method of the catalyst. Catalyst integration methods in microchannels are commonly based on the idea to produce a thin catalytic layer in the micron range on the channel walls. For this reason, depending on the method, a surface roughening is performed, followed by catalyst application using, e.g. sol-gel or suspensions, finalized with the drying and calcination step. A comprehensive summary of all applicable methods in microstructures can be found in the review by Meille [87]. Transferred to the methanation system, the application of catalyst layer was successfully adopted in microreactors [58; 118; 119]. Thus it may be the ideal choice, since thin catalyst layers exhibit good heat transfer characteristics and cause negligible pressure drop allowing high throughputs. However, degradation of the catalytic activity of the catalyst was reported by many authors under CO methanation conditions (see Chapter 2.3). Assuming such scenario, the application of wash-coating methods becomes less suitable, since low catalyst amounts per reactor volume would shorten the operation time of the reactor considerably. In addition, fouling processes caused by coke could even block the reactor channels. The first issue is problematic when irreversible catalyst damage occurs and would require reproducing reactor and catalyst manufacture.

An alternative method involves the filling of the microchannels with the catalytic particles forming a packed bed. The packed bed is a complex structure exhibiting porosity, flow and heat conductivity distribution (see Chapter 7), which may complicate the system. In addition, heat transfer resistance in the packed bed and pressure drop may increase. On the contrary, the packed bed is superior in terms of catalyst integration and replacement. Furthermore, a high ratio of catalyst mass per reactor volume may allow higher throughputs compared to coating methods with identical reactor volume.

On the temperature control in microstructured reactors

In general, due to small lateral dimensions and increased specific surface, it is often assumed that hot spots arising from reaction heat are smoothed and isothermal conditions prevail. This assumption is certainly valid for most systems with moderate reaction rates or thin catalyst coating, however, may not apply to rapid reactions in packed bed arrangements such as the methanation. To this date, there is a scarce amount of works in literature, investigating the effect of the hot spot formation in microreactors for methanation. Regarding methanation, Brooks et al. [120] presented an oil cooled stainless steel microreactor for Sabatier reaction. The catalyst zone was filled with a metal felt, impregnated with Ru based catalyst. Despite a low throughput of the reactants in the range of 200 sccm with a reaction heat release of approx. 45 W, hot spot with around 20-40 K was observed. By increasing the gas velocity, the hot spot temperature was diminished, but could not be completely removed. Another valuable work

with regards to heat transfer in catalytic microreactors was done by Rebrov et al. [121] examining the oxidation of ammonia, releasing about 150 W of reaction heat, in an alumina reactor which was cooled in cross flow with air. Despite a compact geometry and high heat conductivity of the alumina housing, gradients in axial (6 K) and transverse direction between microchannels (4 K) are determined which originate from heat transfer resistance in the metal housing. Based on these findings, hot spot formation and distinct gradients may be expected using stainless steel housings and in a packed bed arrangement. However, it seems appropriate to investigate this approach since complete isothermal operation may not be required as discussed in Chapter 3.2.1.

3.3 Summary

It has been shown that conventional reactor technology for industrial methane generation can be narrowed to adiabatic packed bed and fluidized bed reactors. Packed beds dominate the industrial applications, however, have several drawbacks which arise from lack of temperature control. As a consequence, the entire process becomes complicated in terms of the process control and additional periphery. On the contrary, fluidized beds offer good temperature control and allow SNG production in one step, but are not established on the commercial level due to lack of throughput flexibility regarding fluidization and the catalyst attrition.

Amongst other new arising technologies, microreactor technology seems to be an alternative tool for rapid and highly exothermic methanation reaction. It offers enhanced heat and mass transfer due to the scale effect of the relevant structures and allows improved temperature control. Process intensification in methanation may result in many advantages on the reactor level, e.g. less catalyst deterioration due to thermal effects or less byproduct formation (coke). Further benefits are also expected on the process level by condensing the entire process into a single or maximum two steps depending on the required purity of methane, which is beneficial in the framework of methanation applying hydrogen from fluctuating renewable energy. Fewer steps make the process compact or even transportable via containers, guarantee an improved flexible or dynamic operation and thus reduce the intermediate storage requirement of hydrogen. On-site conversion of renewable energy may be feasible.

Nevertheless, microstructured reactors encounter several challenges. Many of them can be overcome by tailoring the reactor geometry to the characteristics/prerequisites of a) the applied heat transfer medium to prevent, e.g. maldistribution of fluid flow or b) the methanation system to overcome severe hot spot formation. Other challenges in methanation may not be restricted to a particular reactor geometry (e.g. poisoning species in the feed leading to catalytic loss). They must be considered on the process level. However, the latter is not focus of this thesis.

4 Catalyst performance

This chapter focuses on the characterization of a small selection of Ni catalysts as the working horse for the microreactor development based on the packed bed approach. The catalyst is tested regarding stability and activity under methanation conditions using CO, CO₂ and their mixtures, as required by the MINERVE project. Kinetic models from literature are used to assess the performance of the analyzed catalysts. Possible deactivation causes are suggested based on the ex-situ analysis of the spent catalyst.

4.1 Issues with catalyst deactivation in kinetic studies

The reasons for catalyst deactivation are manifold and are detailed in Chapter 2.5. According to the literature, several groups reported good long-term stability of the catalyst in the course of the kinetic measurements using CO or CO₂ [15; 54; 57; 58; 122], whereas other groups reported catalytic loss [55; 56; 67; 68; 123; 124; 125]. Both parties may be right, since the loss of catalyst activity may vary with reaction conditions or the catalyst system. For parameter estimation, the activity decline of the catalyst can be handled in several ways. An appropriate method seems to be an aging process conducted prior to the parameter variation in the range of several hundreds of hours [55; 67; 68]. Examining the Sabatier reaction, Koshany et al. [68] aged the catalyst under very harsh conditions, i.e. high temperatures around 380°C and gas mixture containing both reactants and products for 320 h (Fig. 4.1 on the left). Afterwards, parameter variation did not require any correction factors. In case of CO methanation, the situation is typically more complicated. According to Klose and Baerns [55], the aging procedure led to a plateau of the reaction rate after a defined time on stream (TOS) (Fig. 4.1 on the right), however, after a change of parameters, e.g. temperature, the deactivation continued. Klose and Baerns [55] corrected all further data with a reference value obtained at the plateau at TOS of approx.

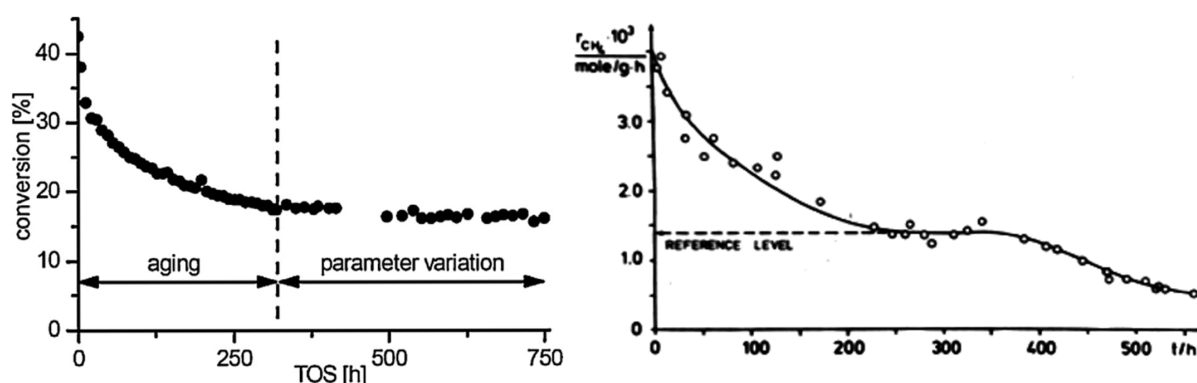


Figure 4.1: Conversion as a function of time during the aging process of the NiAlO_x catalyst under CO₂ methanation conditions [68] (left) and observed decline of reaction rate on alumina supported Ni catalyst under CO methanation conditions at 485 K (H₂/CO=48) [55] (right).

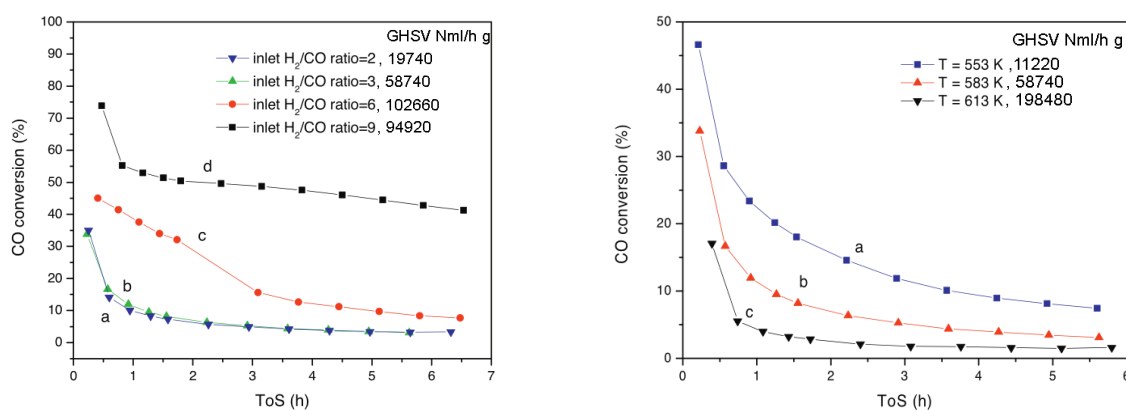


Figure 4.2: Influence of the H_2/CO -ratio (left) and temperature ($\text{H}_2/\text{CO}=3$) (right) at 583 K and 1 bar and different GHSV on conversion over TiO_2 supported Ni catalyst [123].

250 h. No constant level of activity was observed at constant parameters in the work of Zhang et al. [56] within a period of approx. 24 h. Hence, the authors considered the initial activity of the catalyst for parameter estimation. A more sophisticated way to account for activity loss is shown by Sehstedt et al. [125], who corrected the reaction rate with a function accounting for available number of active sites. From the presented cases, the extraction of the kinetic data on a deactivating catalyst is a vague undertaking. The consideration of the initial activity, as done by Zhang et al. [56], leads to higher reaction rate constants not comparable to data from aged catalysts. However, by aging a catalyst sample for each data point under continuous decline of activity would require a tremendous effort. The latter is circumvented using the method by Klose and Baerns [55], but also requires multiple repetition of a standard in the reaction condition.

Temperature and H_2/C -ratio are the most distinct parameters for the methanation system and their influence on the catalytic loss is examined by many groups [56; 123; 124; 125]. Barrientos et al. [123] could show that the catalytic degradation is enhanced with decreasing H_2/CO -ratio (Fig. 4.2 on the left). Similar trends were also observed using temperature variation (Fig. 4.2 on the right), which was explained with limitation of the hydrogenation rate above 575 K favoring the accumulation of carbon. Similar observations regarding conversion drop were obtained by several other groups [56; 124; 126] and are not discussed here further.

4.2 Experimental tools and analysis methods

The experimental details include test rig configuration, reactor concept for kinetic measurements, applied catalyst and experimental conditions. Furthermore, definitions and used literature correlations for analysis of the results are provided.

4.2.1 Test rig, reactor concept & online analytics

The flow chart of the test rig for kinetic measurements is shown in Fig. 4.3. The setup consists of gas supply, reactor unit, pressure regulation and analytics. The reactants CO, CO₂, H₂ and nitrogen, provided by Air Liquide, are dosed via MKS mass flow controllers (MFCs). For pressure regulation, a FlowServ[®] valve is used. The analytics is done on an online gas chromatograph 7890 (Agilent) including a capillary plot Q column and a mol sieve. The integrated Plot Q capillary column is 530 μm in diameter with 40 μm film thickness and has a length of 30 m. The HP-Plot mol sieve 5Å is 530 μm in diameter with 25 μm film thickness and is 15 m in length. For detection, thermal conductivity and a flame ionization detector are used. The verification of the gas flows and calibration of the MFCs are done via a soap bubble meter. Compressed air is used for tempering purposes. The preheating of the air in the flow range of 100 Nl/min to the reaction temperature is done via a microstructured heat exchanger which is equipped with 15 heating cartridges (HORST) 225 W each. Prior to disposal, the hot exhaust air is cooled down to room temperature in a double shell heat exchanger using water.

A microstructured reactor concept with integrated cooling possibility is utilized for kinetic measure-

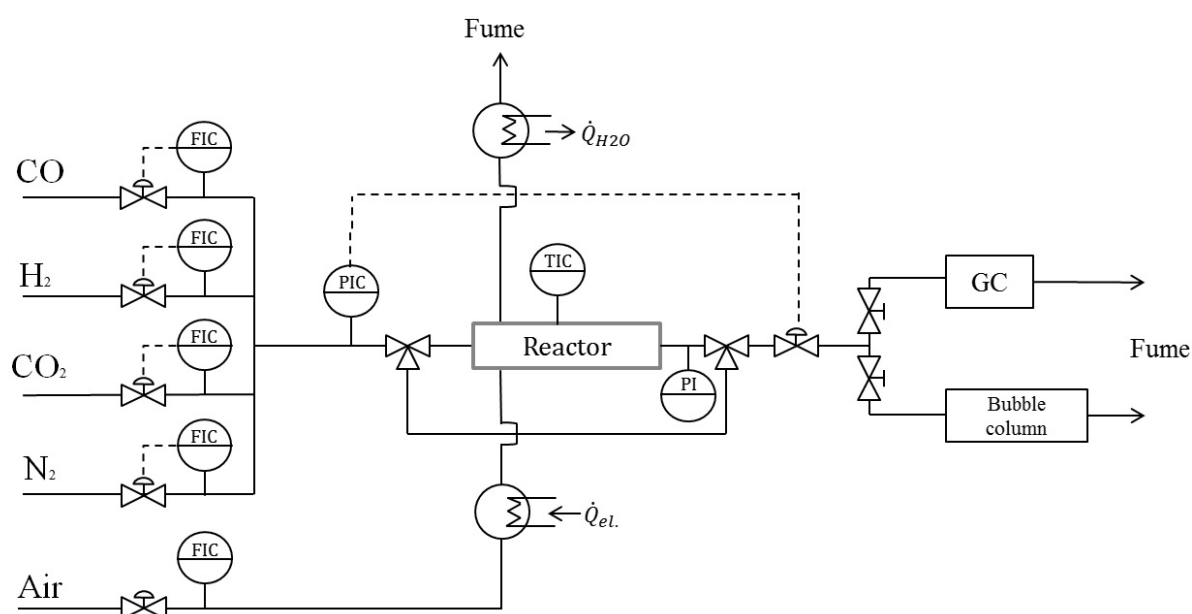


Figure 4.3: General flow chart of the test rig used for kinetic studies of the methanation reaction.

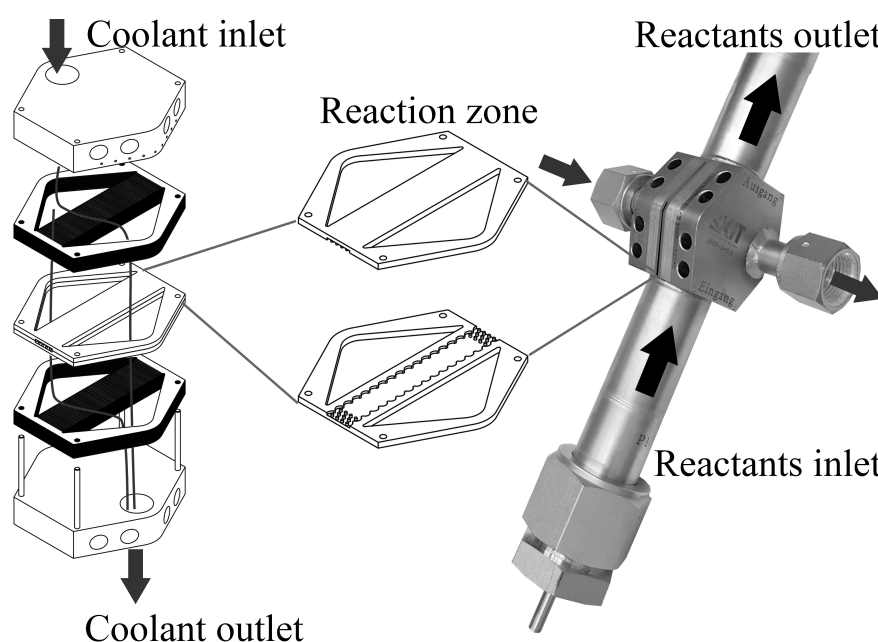


Figure 4.4: Visualization of the reactor architecture (left) and the manufactured device (right) for kinetic measurements.

ments. The manufacturing procedure is based upon stacking of microstructured foils which are bonded together by diffusion welding. Highly alloyed stainless steel FeNi32Cr21AlTi-HC is used for the reactor parts to counteract the corrosion and carburization phenomena. Fig. 4.4 on the left shows the inner architecture of the reactor. The main part consists of the reaction zone which is formed by two foils placed face to face. The machined foils form a channel of 1.5 mm in depth, 9.3 mm in width and 60 mm in length. Above and below the reaction slit, 16 x 2 foils are placed for tempering with hot air. Each thermal foil consists of 72 channels à 500 x 500 x 15000 μm (width x height x length). The whole foil stack is sandwiched between two metal plates. Four drilled holes in each plate offer the possibility to heat with heating elements. Additional 9 holes with 0.5 mm in diameter in the plates allow temperature measurement in axial direction. Metallic holders and the quartz wool ensure that the catalyst is kept in place. A photo of the device is shown in Fig. 4.4 on the right side.

4.2.2 Tested catalysts

In this study, three different catalysts are examined. The first catalyst type is a commercial Ni/Al₂O₃ with 25 wt.% of NiO. According to the data sheet the catalyst contains 5-10 wt.% of Ca. This catalyst is extensively tested under CO and CO₂ methanation conditions and their gas mixtures. Different particle sizes were obtained by crushing and sieving the pellets. The second catalyst type is a self-prepared Ni/Al₂O₃ and is tested for long-term stability under CO₂ methanation conditions only. The preparation

was done via the impregnation technique. Purified water was preheated to 70°C and Ni-containing salt, $\text{Ni}(\text{NO}_3)_2 \cdot 6\text{H}_2\text{O}$ (Merck KGaA), was dissolved. The salt loading of the solution was 2.47 g Ni-salt/(g H_2O). Support material consisting of high surface $\gamma\text{-Al}_2\text{O}_3$ provided by Alfa Aesar, in the form of cylindrical pellets (2 mm i.d. and 5 mm in length) was dried at 350°C for 5.5 h, cooled down and introduced into the Ni-solution. The suspension was stirred for 18 h and filtrated. The wet support material was dried in the oven for 12 h and calcined for 6 h at 500°C. The final catalyst exhibited loading of approx. 15 wt.% regarding NiO.

The third catalyst was provided by Benjamin Mutz from the Institute for Catalysis Research and Technology (IKFT) at KIT and is tested under CO_2 methanation conditions. The bimetallic catalyst contains a total amount of 17 wt.% NiFe (Ni/Fe=3) and is supported on Al_2O_3 .

4.2.3 Experimental conditions

All catalytic experiments are performed at the total throughput of 2.2 NI/min and 6 bar. Methanation of single CO/H_2 and CO_2/H_2 mixtures are conducted with initial concentration of carbonaceous species of 9.1 vol.%. The variation of the H_2/C -ratio is always obtained by variation of the hydrogen amount only. Nitrogen is used as remainder. The modified residence time in this study is defined as the ratio between the volumetric flow (STP) of the reactant i and the catalyst mass according to Eq. 4.1.

$$\tau_{mod,i} = \frac{\dot{V}_i}{m_{Cat}} \quad (4.1)$$

For CO methanation, the modified residence time ranges between 1221 and 3665 ml/(g min) and is governed by the catalyst amount. The residence time remains constant with 1221 ml/(g min) in all CO_2 methanation experiments.

Under methanation conditions using mixtures of CO and CO_2 , the content of CO is kept constant while the concentration of CO_2 is varied.

The examination includes different conditions, e.g. temperature, particle size and H_2/C -ratio. Tab. 4.1 gives an overview of the conducted studies with the appropriate conditions for the commercial Ni catalyst. Silicon carbide is used as diluent. The catalyst was reduced in-situ at 450°C for 15 h in all cases in hydrogen/nitrogen (volumetric flows 1:1) mixture at 6 bar prior to experiments.

A separate study is devoted to the comparison of the three catalysts under CO_2 methanation conditions. The examination of the commercial Ni, self-prepared Ni and bimetallic Ni_3Fe catalysts is performed at temperatures between 305 and 380°C at equal H_2/C -ratio of 4, τ_{CO_2} of 1221 ml/(g min) and the particle diameter of 200-300 μm . The reduction procedure was shortened in this study due to the comparison to

Table 4.1: Summary of conducted studies on the commercial Ni catalyst and according parameter variation.

Reaction / Study	T [°C]	d_p [μm]	H_2/CO [-]	H_2/CO_2 [-]
CO-Methanation				
Particle influence	360-450	50-100 up to 300-400	6	-
H_2/C influence	360	200-300	3-6	-
Temperature influence	360-400	200-300	6	-
CO₂-Methanation				
H_2/C influence	360-400	200-300	-	2-6
Temperature influence	360-400	200-300	-	2-6
CO/CO₂-Methanation				
Partial pressure variation	360	200-300	6	6-11

results of B. Mutz with the Ni₃Fe catalyst: 2h at 500°C for all three samples.

4.2.4 Catalyst characterization methods

Physisorption

The physisorption experiments are conducted with Quantachrome Z10/97-Autosorb-1-C instrument. Nitrogen is used as adsorbate. The Brunauer-Emmett-Teller model is used for the evaluation of the isotherm. The surface area is obtained with 5-point BET in the pressure range $0.5 < p/p_0 < 0.3$. The pore volume distribution is determined with the BJH method in the range $0.3 < p/p_0 < 1$.

Electron Probe Microanalyzer

A field emission electron probe microanalyzer (EPMA) JXA-8530F is utilized to examine the surface of the catalyst particles. Surface maps are obtained by wavelength dispersive spectroscopy (WDS) giving insight into elemental composition.

XRD

X-ray diffraction (XRD) analysis is performed using a PANalytical X'Pert PRO diffractometer with Ni filtered Cu-K α radiation ($\lambda = 1.54060$) at $2\Theta = 20-80^\circ$ with a step size of 0.017° (0.51 s per scan step). The catalyst powders are measured ex-situ after calcination (4 h, 500°C, 5 K/min in static air). The crystallite size is estimated using the Scherrer equation.

4.2.5 Reactor modeling equations and correlations in this study

1D Pseudo-homogeneous reactor model

For the evaluation of the literature kinetic models presented in Chapter 2.3, a pseudo-homogeneous and 1D plug-flow model is implemented in MATLAB®. The implemented mass balance in differential form is given in Eq. 4.2.

$$\frac{d\dot{F}_i}{dV_R} = \eta_{Cat} \cdot R_i \cdot \rho_{Cat} \quad (4.2)$$

Thereby, \dot{F}_i is the molar flow of the component i [mol/s], V_R is the reactor volume [m³], R_i is the net reaction rate of the component i [mol/(kg s)], ρ_{Cat} is the catalyst density per reactor volume [kg/m³] and η_{Cat} is the catalyst effectiveness factor. Ode45 solver with 4th order Runge-Kutta integration routine is used. As inlet boundary condition, initial molar flow of each component is applied. Catalyst effectiveness factor is assumed 1 if not stated otherwise.

Correlations for analysis of heat and mass transport limitations

The external mass transport limitation is estimated using the Carberry number (Eq. 4.3).

$$Ca = \frac{r_{eff}}{k_G a_v C_{i,bulk}} < \frac{0.05}{n} \quad (4.3)$$

The equation for calculation of the external mass transfer coefficient k_G is obtained from Wakao et al. [127] (Eq. 4.4).

$$Sh = \frac{k_G d_p}{D_{i,eff}} = 2 + 1.1 Re^{0.6} Sc^{1/3} \quad (4.4)$$

The definition of single parameters is given in the symbols list. The external heat transfer resistance is calculated according to the Mears criterion [128] (Eq. 4.5).

$$\Delta T_{film} = \frac{r_{eff} |\Delta_r H| d_p}{6 \alpha_p} < \frac{0.05 RT_G^2}{E_A} \quad (4.5)$$

The particle heat transfer coefficient is calculated according to Eq. 7.16 [129] (see chapter 7). The existence of possible internal mass transport limitation by diffusion is calculated according to the Weisz-Prater criterion [128] (Eq. 4.6).

$$\Phi = \frac{n+1}{2} \left(\frac{d_p}{6} \right)^2 \frac{r_{eff}}{D_{i,eff} C_{i,s}} \quad (4.6)$$

The Weisz modulus is the ratio between the observed reaction rate and the diffusion rate in the particle. For name definition of single parameters, refer to symbols list.

4.3 Experimental results

Experimental results are discussed including heat and mass transport phenomena, catalyst activity and degradation under CO and CO₂ methanation conditions and their gas mixtures.

4.3.1 Long-term stability of the commercial Ni catalyst under CO methanation conditions

4.3.1.1 Heat and mass transport phenomena

The first issue concerns the external mass transport resistance and is analyzed by using the Carberry criterion in Eq. 4.3. By assuming the reaction order of 0.5 in CO [57], the Carberry inequality is fulfilled ($Ca=0.03<0.1$) for the most harsh condition (9% CO, 2245 mol/(m³s) and 450°C) so the absence of the external mass transport phenomena can be assumed. The reaction rate is approximated using the literature kinetics given by Kopyscinski et al. [58] which is found to be in good agreement with the experimental data as shown later.

Concerning the Weisz-Prater criterion, the inequality is not fulfilled ($0.22<0.08$ [128]) for the particle size between 200-300 μm, which gives hint to possible falsification of the intrinsic reaction rates by internal diffusion processes (9% CO, 2245 mol/(m³s) [58], $n=0.5$, $D_{eff}=1E-6$ m²/s). To validate this finding, variation of the particle size is conducted while keeping the modified residence time constant. Fig. 4.5 shows the conversion plot for a constant $\tau_{mod,CO}$ of 7329 ml/(g min) at 450°C (left) and for $\tau_{mod,CO}=3665$ ml/(g min) at 380°C (right). For both examined temperatures, deactivation of the catalyst is obvious. Due to fast deterioration process, the detection of the initial conversion is difficult due to a sampling time of 10.5 min of the GC. Nevertheless, for the highest temperature of 450°C, extrapolation

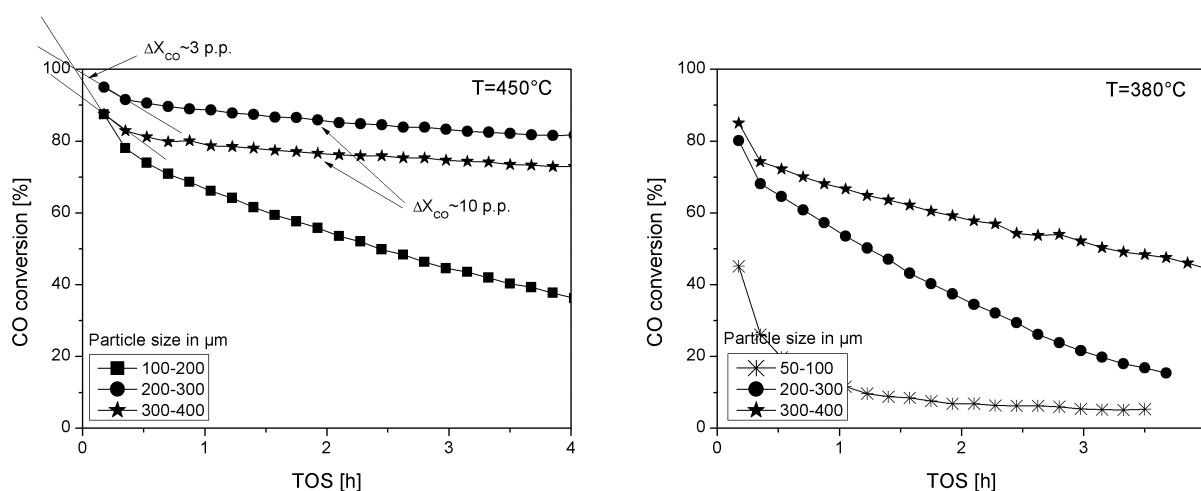


Figure 4.5: Influence of particle size on the conversion of CO at 450°C, $\tau_{mod,CO}=7329=const.$ ml/(g min) (left) and 380°C, $\tau_{mod,CO}=3665=const.$ ml/(g min) (right) at the constant H₂/CO-ratio of 6 and pressure of 6 bar.

of the first datapoints yields a conversion difference of approx. 3 p.p. between 100-200 and 200-300 μm particles. The effect of diffusion processes can be assumed, however, is not significant. For the particle size between 200-300 μm and 300-400 μm , the experimental difference in CO conversion is around 10 p.p. and gives evidence to significant distortion of the intrinsic reaction rate caused by diffusion influence and is therefore not used for further literature data comparison. No conclusion on the importance of mass transfer resistances at lower temperature of 380°C (Fig. 4.5 on the right) is possible using the extrapolation technique due to the extremely fast activity drop and the possible error. However, based on the findings at 450°C, influence of diffusion phenomena could be excluded up to 300 μm particle diameter.

For completeness, the Mears criterion is evaluated for temperatures of 380 and 450°C. For particles between 200-300 μm , the film overheating ranges between 4 and 7 K at 380°C and 10-17 K at 450°C for CO methanation (kinetic rate estimation using Kopyscinski model [58]), despite a very high heat transfer coefficient of approx. 1600 and 1360 $\text{W}/(\text{m}^2\text{K})$, respectively. This is clearly above the limit condition of 2 K and requires reconsideration of temperature effects with regard to mass transport observations above.

4.3.1.2 Influence of particle size on the catalyst deactivation

The first question to answer concerns possible deactivation causes observed in Fig. 4.5. The first clue is the shape of the conversion curve with TOS. According to Butt and Petersen [130], an asymptotic decline irrespective of temperature is characteristic for a non-uniform deactivation of the catalyst and is likely governed by a fouling process which blocks major parts of the catalyst. Pore mouth poisoning encountered in the coke accumulation process is given as an example in their study. Similar asymptotic activity decline under methanation conditions is measured by Barrientos et al. [123], Zhang et al. [56] and Brontos [124], who support the idea of coke formation as the main deactivation cause. The analysis of the spent catalyst in the present work shows that coke on the surface could be indeed one of the deactivation mechanisms. For full information refer to chapter 4.4. Sintering effects and support collapse, as studied by Bartholomew et al. [81; 82], can be excluded as the dominant deactivation, since these effects are characterized by a relatively slow activity decline of 1-10 p.p. within several hundred of hours at similar conditions.

The second question attributes to the effect of the particle size on the stability behavior of the catalyst. As presented in Fig. 4.5 on the right, small catalyst particles lose their activity faster compared to larger particles. Based on the deactivation hypothesis caused by coke, this phenomenon could be explained with the mass transport problematics governed by diffusion. In smaller particles the CO partial pressure is constant due to fast diffusion into the pores and thus higher than in larger particles. CO promotes the

rate of coke deposition in the entire particle [131; 132]. On the contrary, concentration gradients of CO in larger particles lower the coking rate which in turn might prolong the catalyst activity. However, no considerable diffusion difference exists between 50-100 and 100-200 μm particles, which indicates the presence of further mechanisms contributing to the catalyst degradation process.

4.3.1.3 Effect of temperature on the catalyst deactivation

The influence of temperature between 360 and 450°C on activity degradation and selectivity behavior for the particle size 200-300 μm is shown in Fig. 4.6 at H_2/CO -ratio of 6 and 6 bar. For better comparison reasons, the catalyst amount (catalyst to inert ratio) was varied to provide similar initial CO conversion at all temperatures while maintaining the same gas throughput. The plot reveals clearly that the catalyst stability is a function of temperature, which is poor at temperatures below 380°C, and improves at higher temperatures beyond 450°C. Assuming coke to be the main deactivation cause, the opposite is observed in the major part of literature, supported by gravimetric studies on coke deposition [79; 132] and kinetic measurements [56; 123; 124]. The findings were explained with Boudouard reaction being favored with increasing temperatures.

However, Panagiotopoulou et al. [133] suggests that the deactivation depends on the reaction pathway from CO to CH_4 and is strongly catalyst and reaction conditions dependent. For explanation, they refer to the two most widely used reaction mechanisms which are already described in Chapter 2.2. They propose that at lower temperatures less than 250°C, the dissociative adsorption of CO to surface carbide and oxygen takes place. On the one side, the formed surface carbide is hydrogenated to methane, however, contributes to catalyst fouling on the other side (Carbide model). The second reaction pathway is preferred at higher temperatures larger than 250°C and includes associative adsorption of CO. The

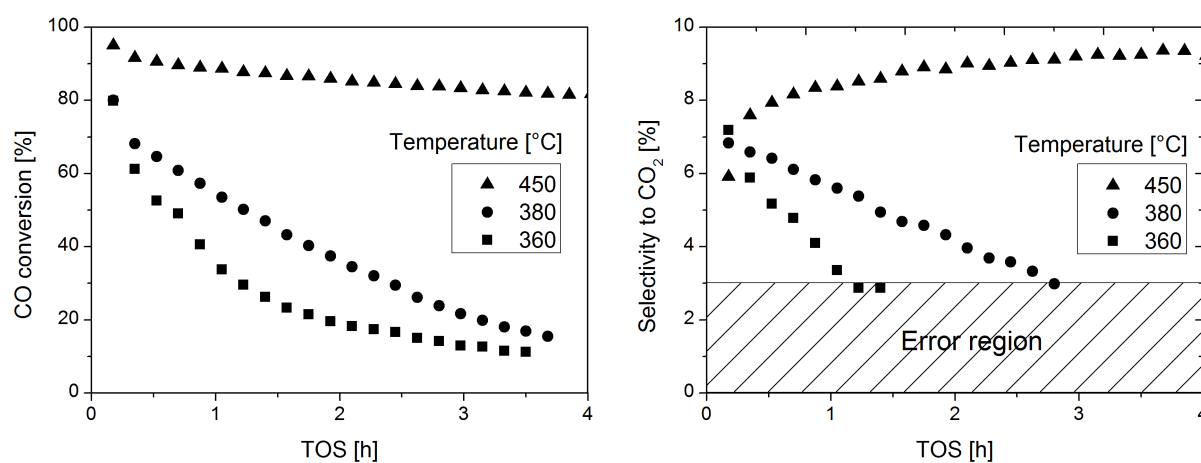


Figure 4.6: Temperature dependence of the conversion loss (left) and corresponding selectivity to CO_2 for particle size of 200-300 μm at 450, 380 and 360°C and $\tau_{\text{mod,CO}}$ of 7557, 3715 and 2438 $\text{ml}/(\text{g min})$ as a function of TOS, respectively ($\text{H}_2/\text{C}=6$, 6 bar).

methane is formed via the CHOH^* complex without the formation of surface carbide as intermediate which results in better catalyst stability. According to Sachtler et al. [134], the dissociative route is common on Ni catalyst whereas the second route is typical for noble metal catalysts like Ru.

The selectivity towards CO_2 is shown in Fig. 4.6 on the right. No other carbonaceous side products except CH_4 are detected. Higher temperatures result in higher selectivities towards CO_2 in the range of approx. 9%, which can be explained with the water-gas shift reaction. In addition, it can be assumed that additional hydrogen as product of the WGS could contribute to better catalyst stability by retarding the surface carbon accumulation.

4.3.1.4 Effect of the H_2/CO -ratio on the catalyst deactivation

The effect of the H_2/CO -ratio on the catalytic loss of the commercial $\text{Ni}/\text{Al}_2\text{O}_3$ catalyst is shown in Fig. 4.7 on the left at the temperature of 360°C , pressure of 6 bar and for the particle size between $200\text{--}300\ \mu\text{m}$. A positive effect is observed on the catalyst life time with higher hydrogen content. At this comparatively long residence time of $\tau_{\text{mod},\text{CO}} = 1166\ \text{ml}/(\text{g min})$ the initial conversion is high at all H_2/CO -ratios. However, depending on the hydrogen content, the deactivation seems to progress through the catalyst at different speed, so that eventually the conversion suddenly drops to a minimal conversion at the end of the catalytic experiment. For quantification of the degradation process, the slope at the inflection point of the individual conversion curves can be considered. For the H_2/C -ratio of 4 and 6 the deactivation rate is similar with approx. $-17\ \text{p.p./h}$. With decreasing hydrogen content, the degradation becomes more pronounced with approx. $-25\ \text{p.p./h}$. This finding is completely coherent with literature observations and thermodynamic analysis presented in Chapter 2.4.

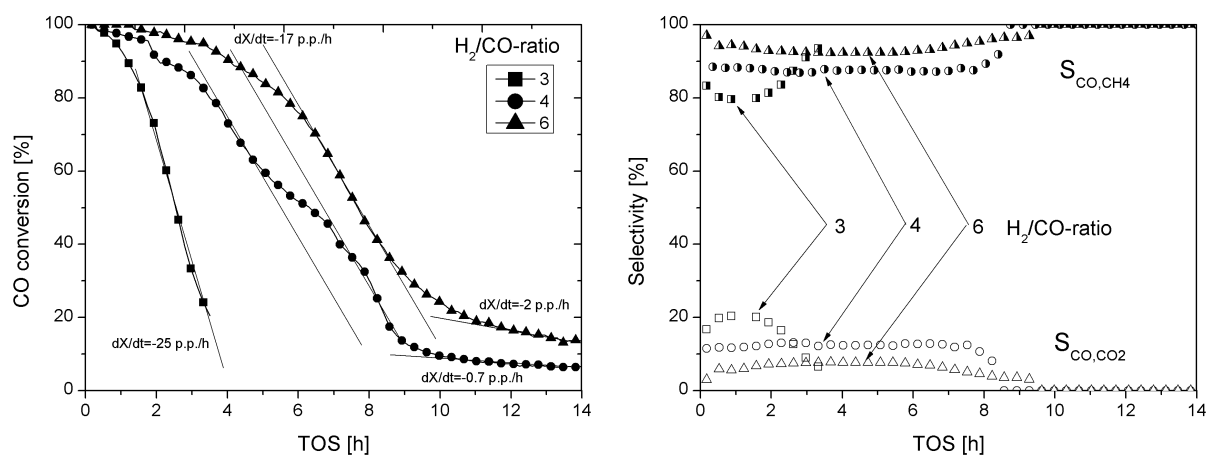


Figure 4.7: Influence of the H_2/CO -ratio on the catalytic loss of the commercial $\text{Ni}/\text{Al}_2\text{O}_3$ catalyst (left) and according selectivities towards methane and CO_2 for $T=360^\circ\text{C}$, $\tau_{\text{mod},\text{CO}}=1166\ \text{ml}/(\text{g min})$, $p=6\ \text{bar}$, $d_p=200\text{--}300\ \mu\text{m}$ (right).

With progressing TOS after approx. 8-10 hours, the activity function reaches a plateau, which is also observed by other groups [56; 123]. However, the plateau value in literature differs only slightly compared to the initial conversion value. In this work, the decrease by more than 80 percentage points is a considerable catalytic loss. This finding might be influenced by the fact that aging was not performed prior to the experiment. The deactivation rate at TOS > 10 h for the H₂/CO-ratio of 4 and 6 is calculated to -0.7 p.p./h and -2 p.p./h, respectively. These values are again similar to these measured by Zhang et al. [56], who report -0.83 to -1 p.p./h at 310°C and H₂/CO-ratio of 3 to 5.

The selectivity towards methane is found to be the highest for the H₂/CO-ratio of 6 with around 95% and very small towards CO₂ with around 5%. The decrease of the H₂/CO-ratio to 3 results in selectivity drop to methane to approx. 80%. At the same time, the selectivity towards CO₂ increases to approx. 20%.

Another characteristic phenomena is that the selectivity curve is relatively constant and nearly TOS independent. This is a hint that the fouling processes caused by coke don't lead to modifications of the metal or metal-support interaction. The selectivity values obtained at conversion values below 10% are not considered due to the error in CO₂ determination in the GC.

4.3.1.5 Deactivation behavior during the shut-down and restart cycles

Methanation coupled to renewable energy might require a shut-down and restart of the system. Several interesting phenomena are observed in such cycles concerning the deactivation behavior of small catalyst particles, which is shown in Fig. 4.8. The improved stability with increasing operation temperature has already been discussed. However, for small particles with less than 300 μm in diameter, the catalytic activity seems to be influenced in a negative manner by the reaction gas drop-out. In the experiment, shown in Fig. 4.8, the reaction gas was substituted with nitrogen at 450°C and the reactor cooled down

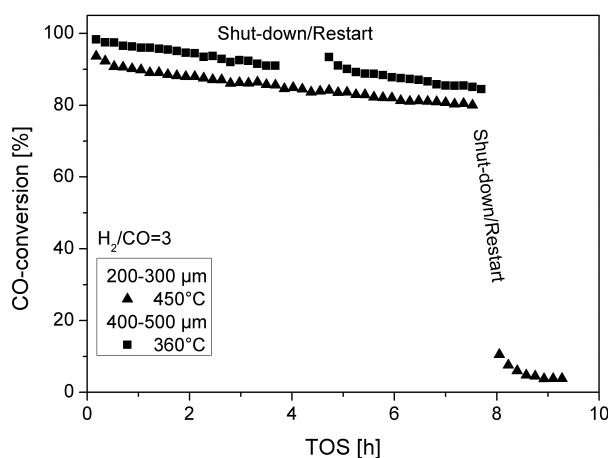


Figure 4.8: Catalytic activity after the shut-down/restart cycles under CO methanation conditions at 360 ($\tau_{mod,CO}=1166$ ml/(g min)) and 450°C ($\tau_{mod,CO}=4448$ ml/(g min)) as a function of different particle sizes.

to 300°C, to continue the catalytic experiments on the next day. After heating up the catalyst to the initial temperature of 450°C and introduction of the syngas, almost no activity was observed. No reports on this behavior under methanation conditions could be found in literature. On the contrary, larger particles of 400-500 μm with catalyst effectiveness factors in the range of 80% at 360°C remain active disregarding the shut-down/restart procedure. The explanation for this behavior could be similar to the general discussion on the dependency of deactivation on particle size. The inner particle of the size 400-500 μm diameter may be protected by large CO concentrations and thus may also resist fluctuating H_2/CO -ratio during gas drop-out for a certain time frame.

4.3.2 Long-term stability of the catalyst under CO_2 methanation conditions

The long-term stability under CO_2 methanation conditions is examined separately to reveal individual effects, before studying the stability of the catalyst under methanation conditions using CO/CO_2 mixtures.

4.3.2.1 Heat and mass transport phenomena

The external mass transfer is excluded using the Carberry number, which is determined to $2.5 \cdot 10^{-4}$ fulfilling the criterion <0.1 for $n=0.5$ and $r_{eff} = 570 \text{ mol}/(\text{m}^3\text{s})$ [68]. The influence of the internal diffusion process is excluded via the Weisz-Prater criterion fulfilling the inequality ($0.048 < 0.08$) for the conditions used in this work (9% CO_2 , $r_{eff} = 570 \text{ mol}/(\text{m}^3\text{s})$ [68], $n=0.5$, $D_{eff} = 1\text{E-}6 \text{ m}^2/\text{s}$). The Mears criterion is evaluated for the same parameters at the temperature of 360°C yielding film overheating of approx. 2.6 K which is slightly above the limit of 2 K.

Compared to CO methanation, the CO_2 reaction system suffers neither from mass transfer limitation nor from overheating of the catalyst pellets under examined conditions.

4.3.2.2 Effect of temperature on the catalyst deactivation

Commercial Ni catalyst

The long-term stability of the commercial Ni catalyst is shown in Fig. 4.9 (top) in terms of CO_2 conversion at 6 bar, $\text{H}_2/\text{C}=4$ and $\tau_{mod,\text{CO}_2} = 1237 \text{ ml}/(\text{g min})$. The catalyst is exposed to reaction mixture at 360°C, followed by a stepwise decrease and increase in temperature to analyze possible hysteresis effects. The initial period of the catalyst deactivation at 360°C shows a completely different behavior compared to that under CO methanation conditions. The degradation is slow with around -0.10 p.p./h in conversion and is practically linear with TOS. By decreasing the temperature to 328°C, the deactivation

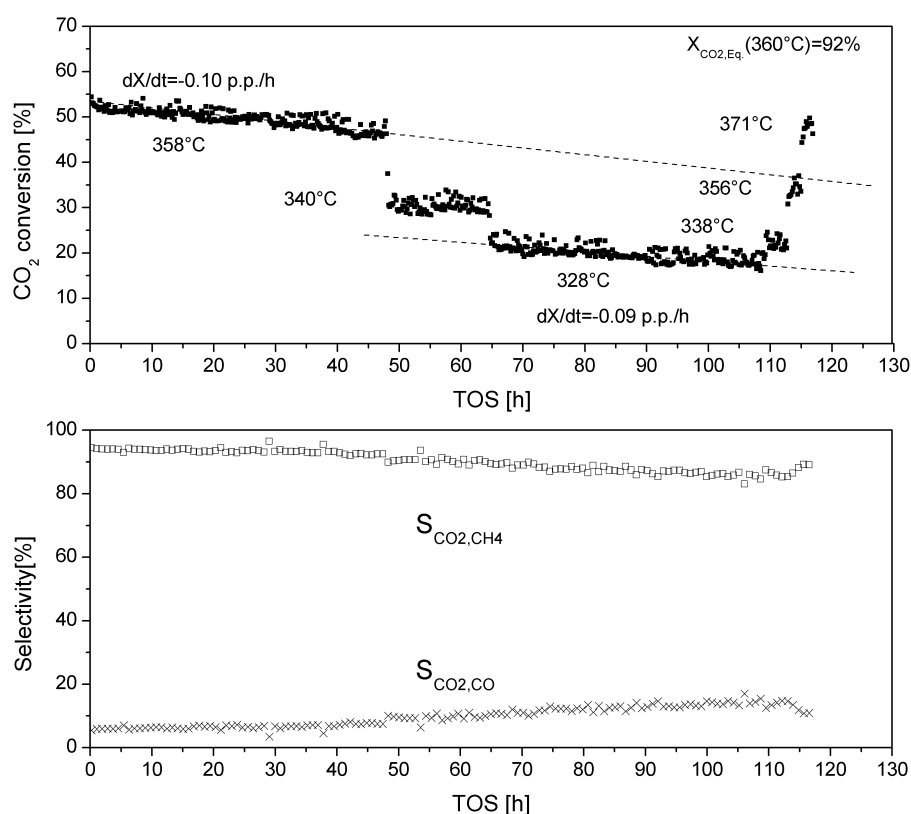


Figure 4.9: Long-term stability of the commercial Ni catalyst under methanation conditions of CO_2 in the temperature range between 328–371°C using initial gas composition of 9% CO_2 , $\text{H}_2/\text{C}=4$ at 6 bar and $\tau_{\text{mod},\text{CO}_2}=1237 \text{ ml}/(\text{g min})$.

remains nearly unchanged with a loss in conversion of around -0.09 p.p./h . The almost linear catalytic loss with TOS could be attributed to any type of deactivation mechanism [130]. The degradation due to thermal and mechanical stress can be excluded since relatively mild temperatures are applied and the packed bed is fixed in its position. Leaching was not observed under CO_2 methanation in the literature and poisoning can be excluded due to the high purity of the applied gases. As consequence, the failing of catalyst through coke accumulation seems plausible and can be explained with the mechanistic model for CO_2 methanation given by Solymosi et al. [40]. As in case of CO methanation, CO_2 is decomposed into surface carbide and oxygen. The lack of hydrogenation of the surface carbide leads to its accumulation followed by blocking of the active sites. The rate of the deactivation process points also to the fact that the step, which includes the aging/accumulation of the surface carbon, is very slow compared to the hydrogenation step [40].

Regarding extraction of kinetic data, the extrapolation to the initial conversion is justified due to linear behavior of the conversion with TOS.

CH_4 and CO are the only measurable gaseous carbonaceous species besides CO_2 (Fig. 4.9 (bottom)). The selectivity towards CH_4 is in the range of 95%. The selectivity from CO_2 towards CO is around 5%

at 360°C which increases to around 10-15% at lower temperatures of around 328°C.

According to literature, most of the authors studying the kinetics of the Sabatier reaction on Ni catalysts either did not observe CO at all [120; 135; 136], or neglected the presence of the CO species due to little amounts in the gas phase [68]. This assumption simplifies the reaction system, however, CO seems an important intermediate and is always observed under CO₂ methanation conditions not only on Ni [42; 137] but also on Ru and Ce catalysts [45; 138]. The formation of CO, observed in this work, could be explained with the model given by Solymosi et al. [40] (see Chapter 2.2), which includes the adsorption of CO₂ and its dissociation to CO* and O*. According to Weatherbee et al. [42], adsorbed CO* is in equilibrium with the CO in the gas phase. Thus, one can deduce that the accumulation of the chemisorbed CO* in this case is favored with lower temperatures implying that the rate-limiting step, which may be attributed to CO* dissociation to surface carbon and O* leads to increasing gaseous amounts of CO in the product gas. When the catalyst deactivates, the rate-determining step is getting more important which also leads to less selectivity towards methane.

Self-prepared Ni catalyst

In order to make sure that the observed effects are not influenced by any promoter effect in the commercial Ni catalyst, the self-prepared pure Ni/Al₂O₃ catalyst was tested for stability at equal conditions (6 bar, H₂/C=4 and $\tau_{mod}=1237$ ml/(g min)) for approx. 120 h. Also in this case, a linear conversion drop is obviously independent on temperatures allowing an extrapolation to higher TOS (see Fig. 4.10). In contrast to the commercial catalyst, the drop in conversion is lower. It is unclear whether alkali or earth alkali metals in the commercial catalyst are responsible for this difference. The selectivity towards methane is in the range of 95% and is comparable to that of the commercial catalyst. The selectivity towards CO is also similar to the commercial catalyst at higher temperature niveau. The main difference is that the selectivity towards CO remains constant at varying TOS and temperatures making the self-prepared catalyst a better choice for CO₂ methanation.

Fe doped Ni catalyst

The third catalyst system investigated in this study was developed with co-workers at KIT for CO₂ methanation. This bimetallic NiFe alloy (Ni₃Fe) is compared with regard to stability at previously mentioned conditions (6 bar, H₂/C=4 and $\tau_{mod,CO_2}=1237$ ml/(g min)) for approx. 95 h. Fig. 4.11 (top) shows the conversion of CO₂ as a function of TOS at temperatures between 305 and 382°C. The initial conversion at 358°C is around 73% and considerably higher than on the commercial and self-prepared Ni catalysts. Higher conversions are also obtained at lower temperatures. The trend of better activity using Fe-alloys is supported by observations in the experimental work of Tian et al. [139]. However,

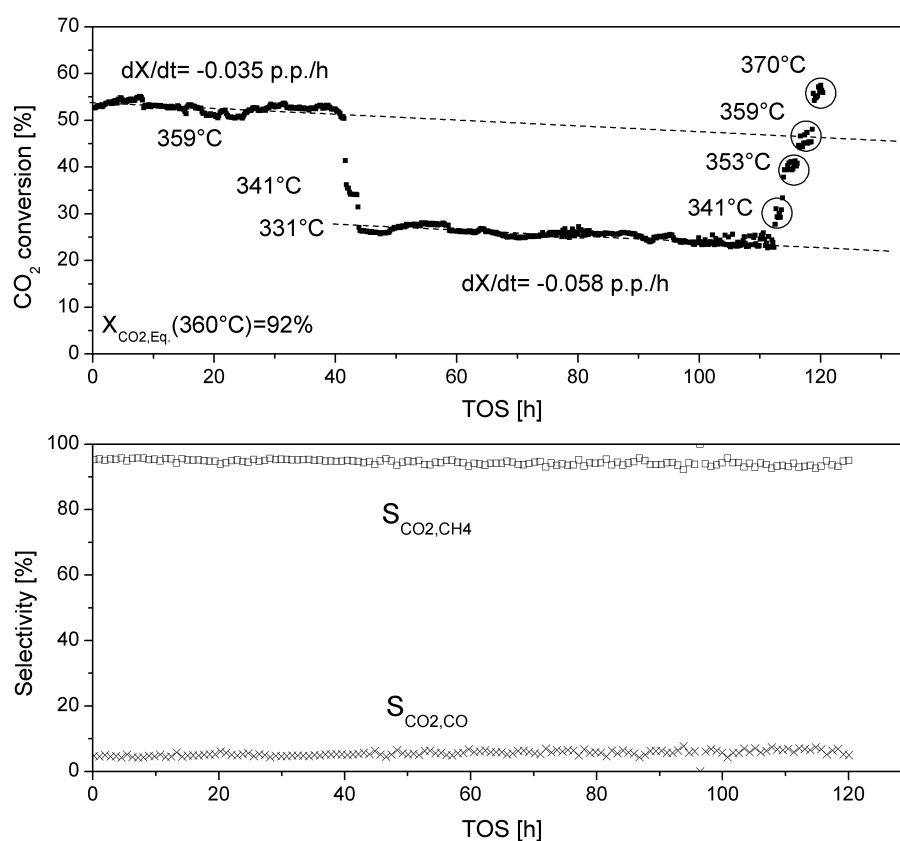


Figure 4.10: Long-term stability of the self-prepared Ni catalyst under methanation of CO₂ in the temperature range between 331–370°C using initial gas composition of 9% CO₂, H₂/C=4 at 6 bar and $\tau_{mod, CO_2} = 1237$ ml/(g min).

the comparison is difficult, since carbon monoxide is applied and the content of Fe was different in their work.

Regarding deactivation at 358°C, the loss in conversion correlates linearly with TOS and exhibits a deactivation rate of approx. -0.02 p.p./h within the first 40 h time on stream. The deactivation is comparable to that on the self-prepared Ni catalyst (-0.03 p.p./h) and up to 5 times slower than on the commercial catalyst system at equal conditions. At 305°C, the catalyst exhibits a rapid deactivation which is approx. 17 times faster compared to 358°C. The subsequent increase of temperature to 358°C shows much lower conversion implying irreversible catalyst damage. The conversion of CO₂ is 27%, compared to 70% before the operation at low temperature.

The selectivity towards methane and CO is shown in Fig. 4.11 (bottom). Obviously, the bimetallic Ni catalyst provides a superior selectivity towards methane in the range larger than 99%, which is in perfect agreement with the experimental work of Hwang et al. [140]. However, a decrease in temperature to 305°C lowers the catalyst performance also with regards to the increase of selectivity towards CO and the decrease of selectivity towards methane. The situation gets worse at prolonged TOS with a

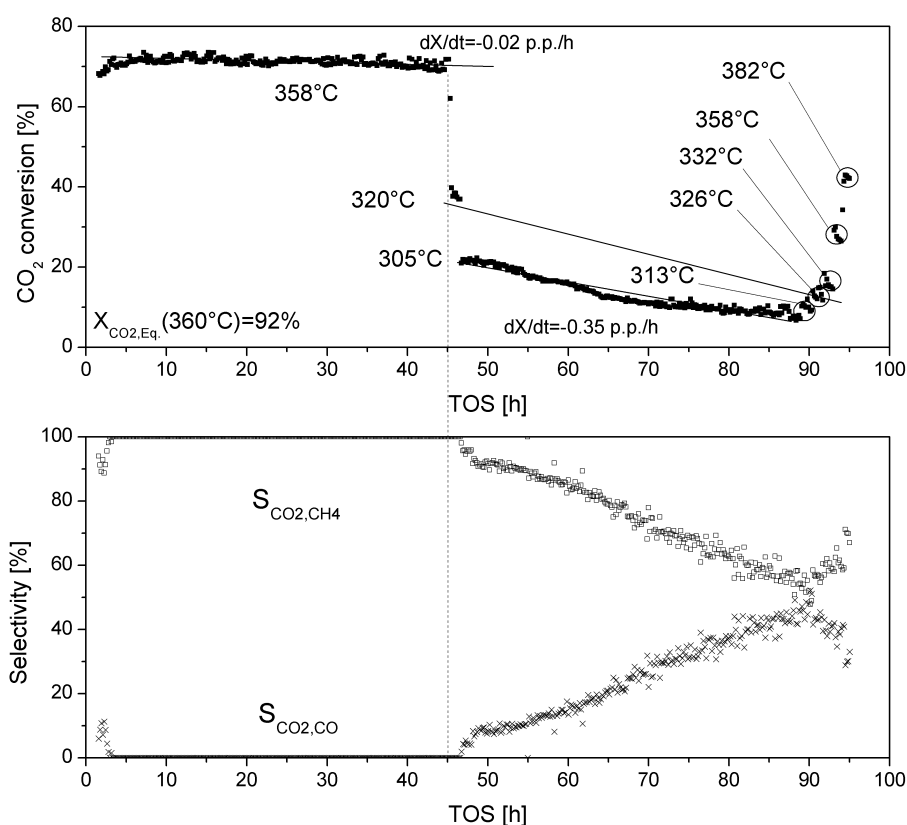


Figure 4.11: Long-term stability of the Ni-Fe bimetallic catalyst under CO_2 methanation conditions in the temperature range between 305 and 382°C using initial gas composition of 9% CO_2 , $\text{H}_2/\text{C}=4$ at 6 bar and $\tau_{\text{mod},\text{CO}_2}=1237$ ml/(g min).

selectivity towards CO of approx. 40-50% along with catalyst deactivation. Potentially, this could be explained with the mechanistic steps regarding dissociation and hydrogenation. By alloying the Ni and Fe metals, the dissociation energy barrier for CO_2 decomposition to CO^* and its further decay to C^* is accelerated in the entire temperature range according to literature. At higher temperatures, the hydrogenation step seems to be fast enough to convert the produced C^* . However, by lowering the temperature, hydrogenation may become the bottleneck of the system. As a consequence, CO^* and C^* would accumulate on the surface, which would explain the faster performance loss at a lower temperature. The accumulation of the adsorbed CO^* on the surface leads to more CO in the gas phase according to Weatherbee et al. [42], explaining the strong increase in CO selectivity. The stability studies of the Ni_3Fe catalyst including surface analysis have been published in [141].

4.3.2.3 Effect of the H_2/CO_2 -ratio on the catalyst deactivation

The ratio between the carbonaceous species and hydrogen is drastically influencing the deactivation behavior under CO methanation conditions (see Chapter 4.3.1.4). Thus, the investigation is repeated for

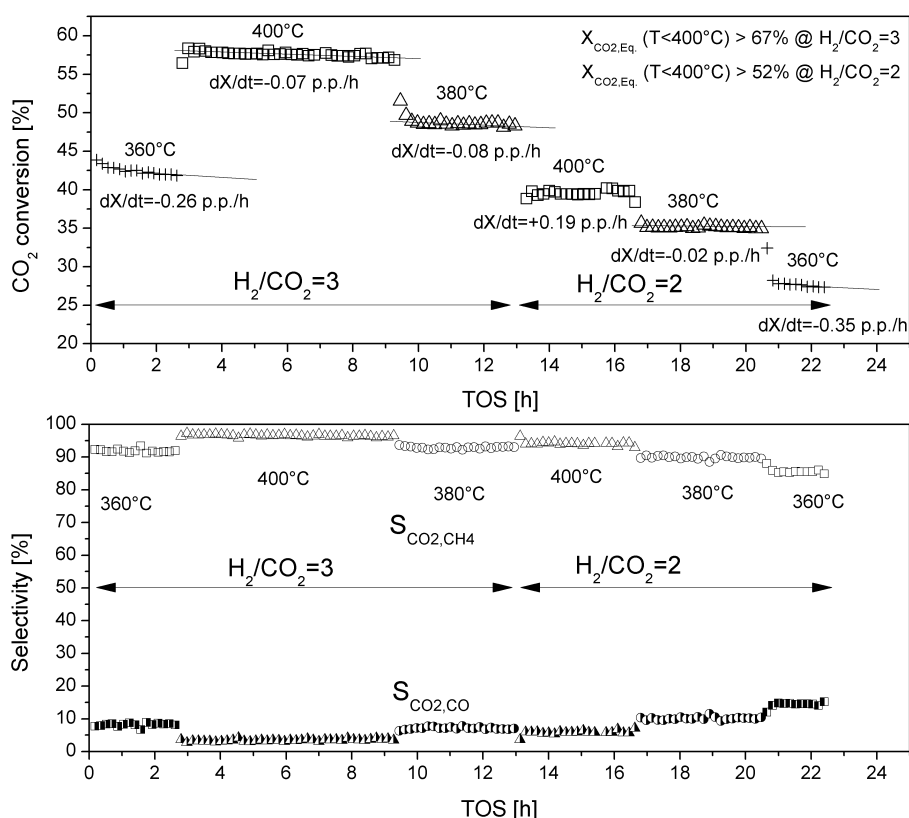


Figure 4.12: Stability test of the commercial Ni catalyst under CO_2 methanation conditions at different temperatures and H_2/CO_2 -ratios at equal $\tau_{\text{mod},\text{CO}_2}=1283 \text{ ml}/(\text{g min})$ and 6 bar.

the CO_2 methanation on a commercial Ni catalyst. Fig. 4.12 shows the CO_2 conversion as a function of TOS at H_2/CO_2 -ratio of 2 and 3 for three different temperatures of 360, 380 and 400°C at 6 bar and $\tau_{\text{mod},\text{CO}_2}$ of 1283 ml/(g min). As reported in the previous section, better stability is observed at higher temperatures along with less selectivity to CO.

At first glance, the effect of H_2/CO_2 -ratio shows no apparent effect due to only a low decrease in conversion. However, a direct comparison of H_2/CO_2 -ratios of 4 (see Fig. 4.9), 3, and 2 reveals a difference in conversion decline with -0.1, -0.26 and -0.35 p.p./h, respectively. Also, the stronger deactivation is directly correlated with selectivity to CO as a function of temperature and H_2/CO_2 -ratio. The selectivity to CO increases at lower H_2/CO_2 -ratio.

4.3.3 Long-term stability of the catalyst and kinetics under methanation conditions of CO/CO_2 mixtures

The methanation of CO/CO_2 mixtures on a commercial Ni catalyst is shown in Fig. 4.13 on the left at H_2/C -ratios of 3 and 4 at 360°C and 6 bar. For reference, conversion of CO in a $\text{CO}-\text{H}_2$ -mixture is plotted for the same conditions. The modified residence time regarding CO is kept constant ($\tau_{\text{mod},\text{CO}}=1191 \text{ ml}/(\text{g}$

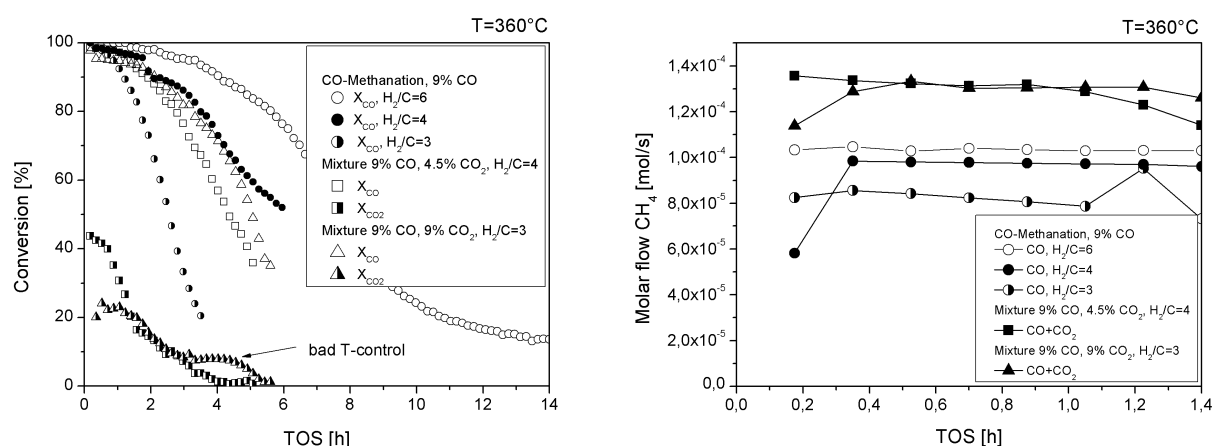


Figure 4.13: Deactivation of the commercial Ni catalyst under methanation conditions of CO/ CO_2 mixtures at H_2/C -ratios of 3 and 4 compared to activity loss under CO methanation conditions at H_2/C -ratios of 3, 4 and 6 ($\tau_{mod,CO}=1191$ ml/(g min), $\tau_{mod,CO_2}=\text{varied}$ and 6 bar).

min)) for all samples. From the kinetic point of view, several questions can be answered. Obviously, CO is converted preferentially compared to CO_2 , which is in agreement with kinetics on Ni and Ru methanation catalysts [56; 58; 133]. The addition of different amounts of CO_2 to the syngas mixture does not affect the conversion of CO while maintaining the same H_2/C -ratio. This could indicate that the methanation of CO_2 could proceed via a different hydrogenation route, see Chapter 2.2.2. However, CO could also be preferentially adsorbed compared to CO_2 so that CO_2 cannot react to intermediate CO. Another interesting aspect concerns the value of CO_2 conversion. By increasing the amount of CO_2 in the feed from 4.5 to 9%, its conversion drops to half the value. The conversion of CO_2 is thus kinetically limited and depends on the available active sites. A high conversion can only be reached if only small amounts of CO_2 are in the feed.

Nevertheless, a beneficial effect of the methanation of CO/ CO_2 mixtures can be seen from Fig. 4.13 on the right. Obviously, around 20-30% more methane could be produced compared to a single methanation of CO at the same H_2/C -ratio. However, for SNG production, an additional purification step may be required to remove the residual CO_2 .

The most interesting effect concerns the loss of activity when both CO and CO_2 are converted in parallel. The previous subchapters establish that the catalyst deactivation is considerably slower for CO_2 than for CO methanation, even at smaller H_2/C -ratios. By comparing the catalyst deactivation under pure CO-methanation conditions ($H_2/CO=6$) and a corresponding experiment where both CO and CO_2 are present ($H_2/CO=6$) (Fig. 4.13 on the left), the conversion of CO in CO/ CO_2 mixtures leads to lower catalyst life time. Hence, in the mixture case, CO_2 considerably contributes to catalyst degradation. This issue could be explained by the conversion of CO_2 to CO according to RWGS reaction. CO is an intermediate for methane formation from CO_2 .

Therefore, the definition of general H_2/C -ratio seems appropriate to conclude the severity of the catalytic degradation effects. The comparison of the activity loss at slightly understoichiometric H_2/C -ratio of 3 reveals that under methanation conditions of CO/CO_2 mixtures, better stability is achieved. According to Habazaki et al. [59], this can be explained by the shift of the equilibrium of the Boudouard reaction to the gaseous CO , counteracting solid coke production. However, this seems less plausible since the capability of the solid coke to influence the gas phase is unlikely. A better explanation is that the inhibiting impact of the CO on the CO_2 conversion yields more hydrogen for CO conversion and causes less degradation due to an increased H_2/CO -ratio.

Another phenomenon to discuss is the coupled decrease of CO and CO_2 conversions in the course of the deactivation process. Obviously, the conversion curves of both species drop asymptotically after the initiation period. This implies that the same active sites are responsible for methanation of both CO and CO_2 .

4.4 Analysis of the fresh and spent catalysts

SEM, WDS, Physisorption and XRD methods are applied to investigate the change of the catalyst and to reveal possible deactivation mechanisms.

4.4.1 SEM and WDS analysis of the commercial Ni catalyst

Two SEM images of the fresh commercial Ni catalyst with particle diameter between $200\text{--}300\ \mu\text{m}$ are shown in Fig. 4.14 at 100 (on the left) and 5000-fold (on the right) magnification. The pellets are non-spherical and exhibit platelet shape. The thickness is roughly one third of the pellet length, which leads to an overestimation of the diffusion influence calculated with the Weisz-Prater criterion. The negligible

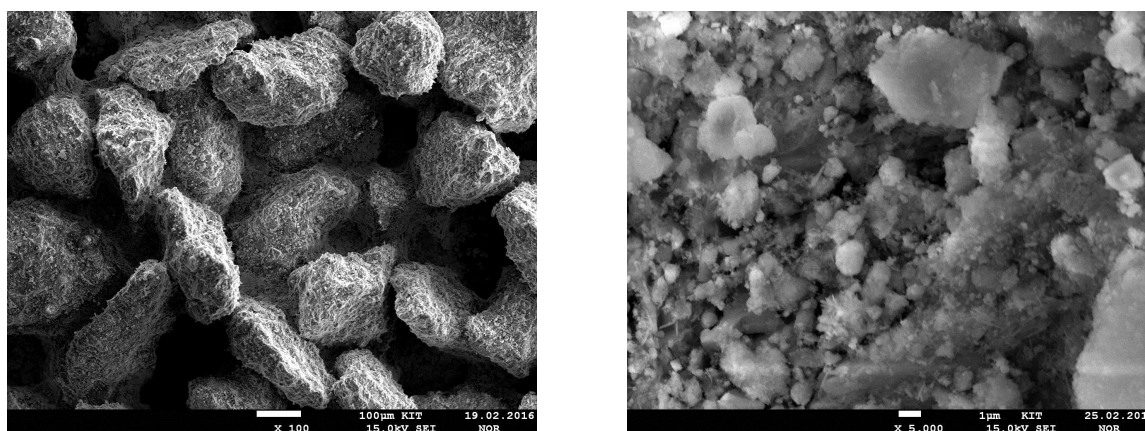


Figure 4.14: SEM images of the fresh surface of the commercial Ni catalyst at 100 (left) and 5000-fold (right) magnification.

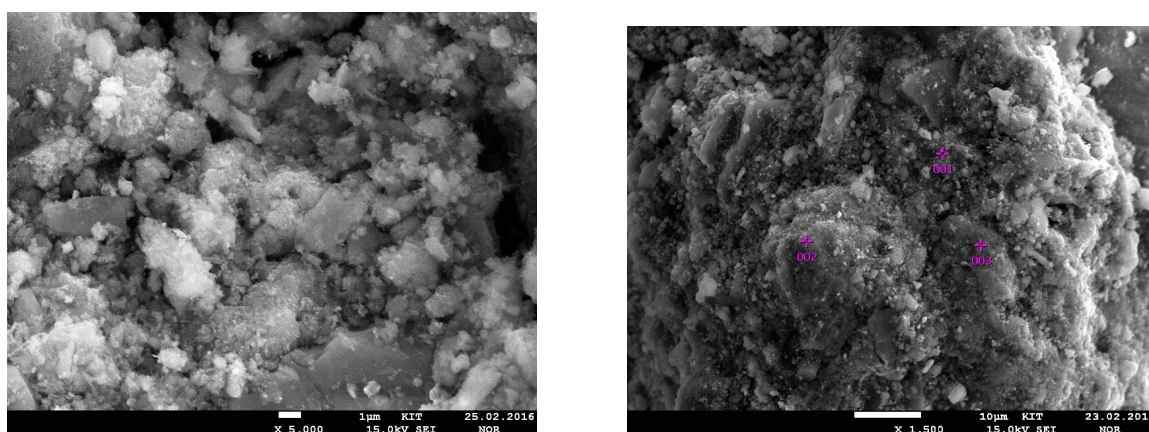


Figure 4.15: SEM images of the spent commercial Ni catalyst deactivated under CO methanation conditions at 360°C and $H_2/CO=4$ for approx. 4 h. Surface topology at 5000-fold magnification (left) and measuring points for WDS analysis (right).

difference in activity as a function of the catalyst particle size can thus be explained by the catalytic experiments. The surface topology is rough and reveals lots of smaller particles on the surface of larger particles. Examining the polished cross-section (not shown here), the catalyst particles turned out to be agglomerates consisting of several phases sticking together. Both smaller and larger particles are determined as Al_2O_3 , which contain finely distributed NiO phase.

Due to strong deactivation in the course of CO methanation experiments and obvious color change from grey to black, SEM images are acquired of the spent and completely deactivated catalyst (Fig. 4.15). The surface and topology at 5000-fold magnification (left), is similar as on the fresh catalyst. Small particles are uniformly distributed while no obvious carbon filaments or layers are visible as described in literature [10]. Supplementary surface analysis via WDS at three different spots (Fig. 4.15 on the right) reveals the presence of carbon. The detected amounts of carbon species are considerably high and range between

Table 4.2: Elemental surface distribution (mass %) on the spent commercial Ni catalyst tested under CO methanation conditions at 360°C and $H_2/CO=4$ for approx. 4 h (Samples 001-003) and under CO_2 methanation conditions at 360-400°C and $H_2/CO_2=2-3$ for 22 h (Samples 004-005).

Sample\Element	C	O	Mg	Al	Si	Ca	Ni
CO-Methanation							
001	12.49	29.83	-	24.81	0.20	3.28	29.28
002	11.20	44.76	0.07	30.26	0.10	3.44	10.08
003	12.26	37.54	-	24.48	-	1.42	24.16
CO ₂ -Methanation							
004	2.21	47.79	0.24	23.22	0.68	2.04	19.67
005	2.12	39.17	0.27	24.95	1.53	2.06	29.47
006	1.39	34.40	0.19	25.00	0.28	3.58	34.93

11 and 12 mass % (see Tab. 4.2 sample Nr. 001-003). For comparison reasons, the surface analysis is repeated on the commercial Ni catalyst operated under CO₂ methanation conditions for 22 h at sub-stoichiometric H₂/C-ratios of 2 and 3. As in case of CO methanation, no obvious optical surface changes are detected. However, a significant change in surface elements can be found (Tab. 4.2 (Sample 004-006)). According to WDS, the amount of elemental carbon deposition ranges between 1 and 3 mass % and is clearly below the values obtained under CO methanation conditions. This finding is in agreement with most of the literature and is for example described by Solymosi et al. [40], who suggest that the hydrogenation of the surface carbon must take place much faster compared to its accumulation/aging. The amount of carbon on the surface directly correlates with the deactivation behavior and may be the main deactivation cause. However, the type of the carbon, amorphous, layered or dissolved remains unclear.

4.4.2 Physisorption and XRD analysis of the commercial Ni catalyst

Physisorption analysis can be applied to gather information regarding pore size distribution and surface area of the fresh and spent catalysts. Fig. 4.16 on the left shows the differential intrusion volume as a function of the pore size of the fresh and spent catalysts tested under CO methanation conditions (360°C, H₂/CO=4, 4 h TOS) and CO₂ methanation conditions (360-400°C, H₂/CO₂=2-3, 22 h TOS). The fresh catalyst possesses monomodal micropores network with pores in the range of 4-5 nm (mean) and exhibits a BET-surface area of approx. 129.3 m²/g. After the treatment of the catalyst under CO methanation conditions, a broadening of the pore diameter distribution is obvious. The change of the mean pore diameter from 4 to 5-6 nm is relatively weak, however, the surface area is drastically reduced

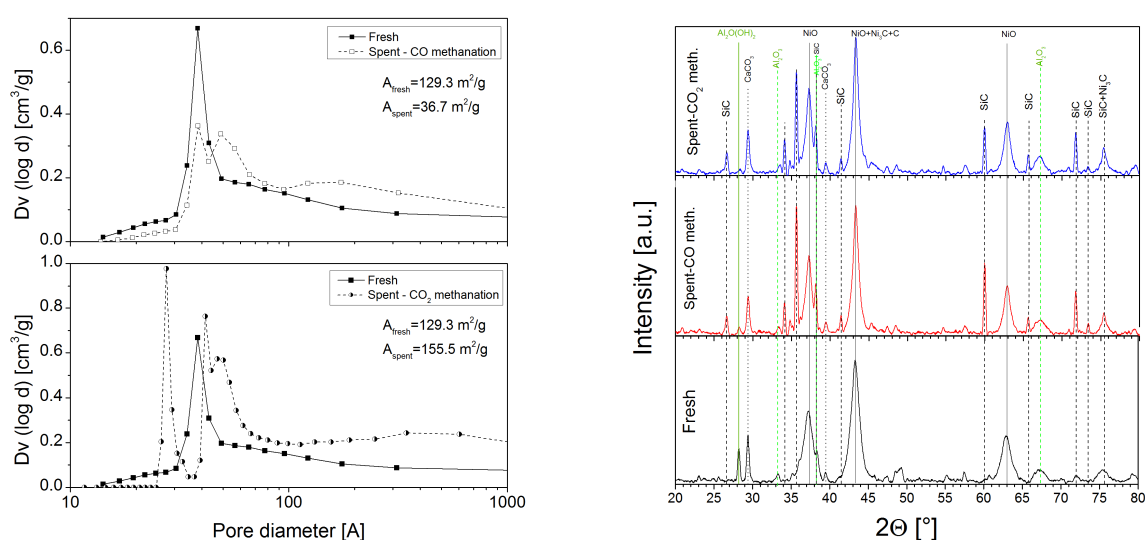


Figure 4.16: Pore size distribution (left) and XRD (right) of the fresh and spent commercial Ni catalysts.

from 129.3 to 36.7 m²/g. The change of the latter, supported by WDS and activity tests, is surely due to a fouling process caused by coke deposition.

The change of the catalyst aged under CO₂ methanation conditions is significantly different. The surface area shows a slight increase, however, is close to the value of the fresh catalyst. Regarding pore size distribution, a clear split of pore sizes is obvious while yielding peaks at 3 and 5 nm. The formation of smaller pores could be explained with thin layered carbon deposition on the pore walls. Larger pore formation could be due to possible collapse of the catalyst support by CO₂ and its hydrogenated species. The XRD analysis of the fresh and spent catalysts is shown in Fig. 4.16 on the right. Representative samples of the catalyst tested under CO methanation conditions (360°C, H₂/CO=6) and CO₂ conditions (360-400°C, H₂/CO₂=6) are oxidized at 450°C prior to XRD measurements. The fresh catalyst contains NiO (37.3°, 43.4°, 63.0°), Al₂O₃ (28.2°, 38.3°), CaCO₃ (29.5°, 39.4°), CaO (37.4) and Al₂O(OH)₂. Obviously, Al₂O(OH)₂ is used as the binder in the fresh catalyst and is decomposed to Al₂O₃ after temperature treatment. Regarding Al₂O₃, the reflexes are broad and of low intensity. The support is a low crystalline Al₂O₃/Al₂O(OH)₂ mixture, rather than high crystalline γ -Al₂O₃. The finding is in agreement with the polished cross-section of an agglomerate investigated with SEM. Since the fresh catalyst is diluted with SiC for catalytic testing, SiC could not be completely separated leading to reflexes in the spent samples at 26.5°, 34.1°, 35.7°, 38.2°, 41.4°, 60°, 65.6°, 71.8°, 73.4°, 75.4°. Conclusions regarding crystalline carbon/graphite (44.3° or 52.2°) or Ni₃C (44.4°, 51.8°, 75.5°) cannot be made due to strong overlapping with Ni, NiO and SiC signals.

The crystallites of NiO on the fresh catalyst are determined to 9.5-9.7 nm. After the reaction, a slight increase to 11.2-11.9 nm and 12.0-12.4 nm at CO and CO₂ methanation conditions took place, respectively. The influence of the sintering on activity loss could thus be neglected at given temperatures and operation times.

4.4.3 Analysis of the self-prepared Ni/Al₂O₃ catalyst

After the impregnation with nitrate solution, calcination and crushing procedures, the BET-surface of the Al₂O₃ support decreased from 234.6 to 201.6 m²/g. After the CO₂ experiments (see Fig. 4.10, 331-370°C, H₂/C=4), a further decrease to 183.2 m²/g is found. As supported by WDS measurements on the commercial catalyst, the accumulation of carbon species which contribute to the surface change, are also very likely on the self-prepared catalyst.

The fresh catalyst support has a monomodal pore-size distribution with a mean pore value of approx. 9 nm. After the impregnation the mean value shift to 7.8 nm and remain similar after the CO₂ methanation experiments.

According to XRD analysis, the crystallite size of NiO was calculated to 13.4 nm which decreased to 8.1 nm after the reaction experiments. The apparent re-dispersion would require further analysis but is not in scope of this work.

The analysis of the Fe doped Ni catalyst and discussion is performed by Benjamin Mutz and can be found in [142].

4.5 Comparison of the initial activity with kinetic models from literature & their thermodynamic consistency

In this work, the development of a kinetic model is not in scope due to a variety of available kinetic expressions for Ni catalysts from the literature. Instead, the most suitable models, selected from Chapter 2.3.2 are evaluated and compared with the obtained results.

The experimental and simulated conversions obtained under methanation conditions of CO, CO₂ and their mixtures are presented in terms of parity plot in Fig. 4.17 A), B) and C), respectively. Data obtained with commercial Ni catalyst are applied in all cases. Extrapolation to the initial conversion is used if possible (see previous chapters) for the experimental data.

CO methanation

The collection of the experimental conversion data in the course of CO methanation (Fig. 4.17 A) is strongly affected by the deactivation process of the catalyst. Especially at low reaction temperatures, the determination of the initial CO conversion is impossible. At higher temperatures, improved stability is achieved, however, overheating of the particle could be expected. In addition, the applied dilution with SiC could also lead to possible uncertainties regarding catalyst mass distribution in the bed. Nevertheless, the obtained conversions at higher temperatures (>400°C) are in acceptable agreement with the literature on kinetic models given by Kopyscinski et al. [58] and Xu and Froment [67] with an error of ± 20 p.p. Considerably higher conversions compared to experiments (up to 30 p.p.) are predicted by the model of Zhang et al. [56] and could be attributed to a higher Ni content of 50 wt.% in their work compared to this work (25 wt.% NiO). However, Kopyscinski et al. [58] also used a

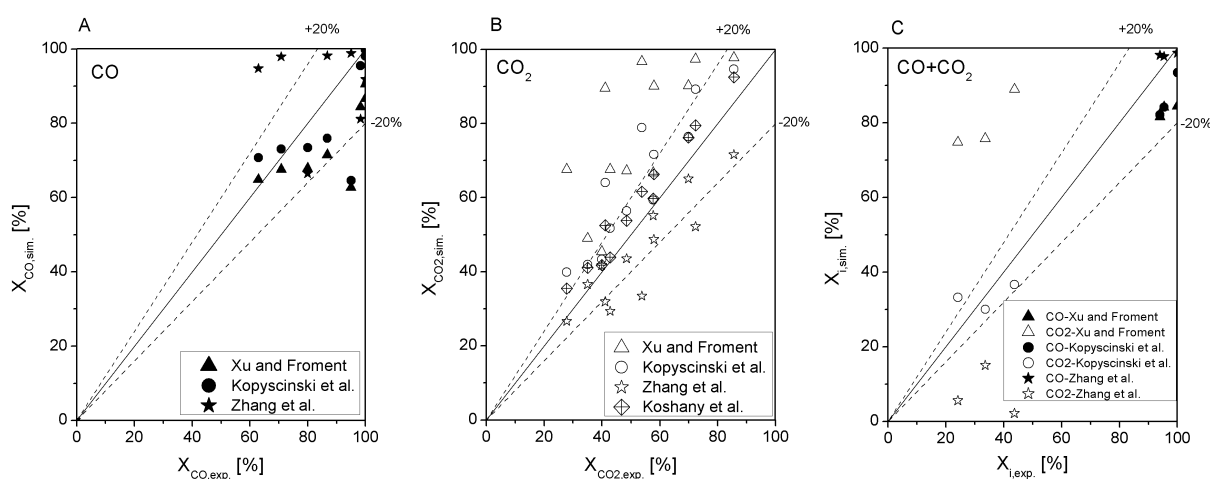


Figure 4.17: Parity plot showing experimental and simulated conversions for A) Methanation of CO, B) Methanation of CO₂ and C) Parallel methanation of CO and CO₂. For simulation, original kinetic models with according parameters are used.

commercial catalyst with a higher Ni content (50 wt.%) and applied washcoating instead of a packed bed as the catalyst integration method.

Due to the limitation of integral operation of the reactor with resulting high integral conversions of CO, the rate of CO formation is prone to large errors. This is worsened by an extremely fast deactivation at lower temperatures and fast methanation kinetics, requiring dilution with silicon carbide even in the applied microreactor. Further improvements with regards to the reactor design could be the reduction of bed length to ensure even lower residence time under higher temperature conditions while reducing the pressure drop. The pressure drop is one of the reasons why higher flow rates are not applicable in the current reactor design. The simulated reaction rates of CO given by Xu and Froment with $2118 \text{ mol}/(\text{m}^3 \text{ s})$ are clearly higher than that of Kopyscinski ($788 \text{ mol}/(\text{m}^3 \text{ s})$) and Zhang ($569 \text{ mol}/(\text{m}^3 \text{ s})$) at $\text{H}_2/\text{CO}=4$ and 350°C . Regardless of the above mentioned problems for collection of kinetic data from experiments, the rates by Zhang and Kopyscinski seem to be in the same order of magnitude and are likely representative for the obtained experimental data.

CO₂ methanation

Better stability and lower activity of the catalyst allow more freedom for kinetic data collection. As can be seen from Fig. 4.17 B), all examined models except Xu and Froment [67] describe the experimental data of the methanation on the used Ni catalyst with acceptable agreement. The $\text{Ni}_{15.2\%}/\text{MgAl}_2\text{O}_4$ catalyst applied by Xu and Froment may to be more active in the lower temperature region compared to other Ni methanation catalysts. The best match is obtained for the kinetic model designed by Koshany et al. [68] in the entire temperature regime between $360\text{--}400^\circ\text{C}$ and H_2/CO_2 -ratios of 2-6. It is used for evaluation of the Weisz-Prater criterion in Chapter 4.3.2.1 accordingly. Koshany et al. [68] did not include CO into the reaction mechanism, although it is observed in their experiments. The CO selectivity up to 10% as observed in this work may require further adjustments of the Koshany model. The models of Kopyscinski et al. [58] and Zhang et al. [56] are in better agreement with regards to concentrations of CO and CO₂. Both models neglected the Sabatier reaction and convert the CO₂ according to RWGS reaction to CO which is subsequently hydrogenated to methane.

CO/CO₂ methanation

The methanation of CO/CO₂ mixtures is probably the most complex system and is poorly investigated in the literature. The kinetic model on $\text{Ni}_{15.2\%}/\text{MgAl}_2\text{O}_4$ catalyst by Xu and Froment [67]) catalyst does not reflect the preferential methanation of CO and predicts high conversions of CO₂ which are similar to that of CO. The model of Zhang et al. [56] predicts the conversion of CO properly, however, underestimates the conversion of CO₂ slightly. The best match for the methanation of CO/CO₂ mixtures

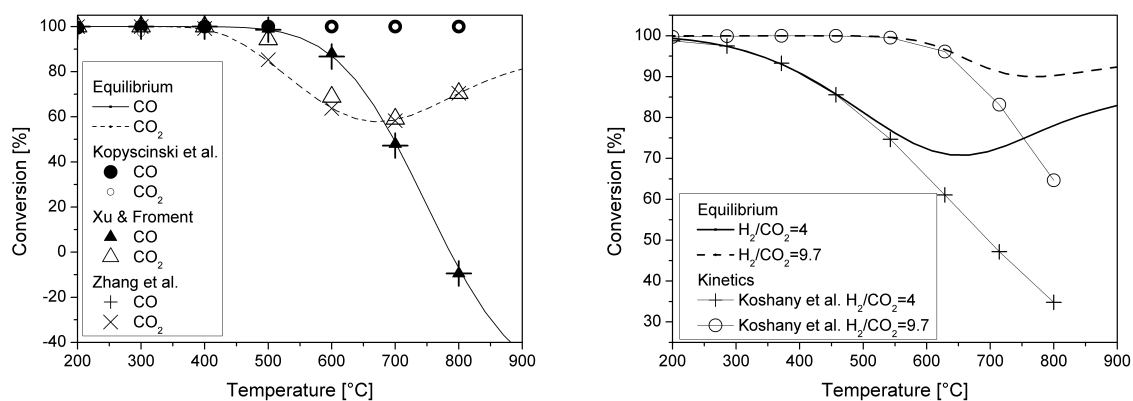


Figure 4.18: Thermodynamic consistency of the models given by Kopyscinski et al. [58], Xu and Froment [67] and Zhang et al. [56] (10% CO, 7% CO₂, H₂/C=4, 6 bar) (left) and the model by Koshany et al. [68] (7% and 15% CO₂, H₂/C=4 and 9.7) (right).

is predicted by the model of Kopyscinski et al. [58], which does not only reflect the conversion of CO and CO₂ in single gas experiments.

Apart from the fit of experimental data, the models are investigated in the following regarding their thermodynamic consistency for methanation of CO/CO₂ mixtures in the temperature range between 200 and 800°C at 6 bar. Fig. 4.18 depicts thermodynamic equilibrium conversion versus conversions predicted by the kinetic models at high residence time. The model of Xu and Froment [67] as well as its altered version, proposed by Zhang et al. [56], follow the thermodynamic equilibrium in the entire temperature range up to 800°C with negligible deviations. Unfortunately, the model of Kopyscinski et al. [58] exceeds the equilibrium above 400°C due to the absence of the equilibrium constant for the RWGS reaction at higher temperatures.

The model of Koshany et al. [68] for pure CO₂ methanation is plotted versus equilibrium conversion at different initial concentrations of 7 and 15% CO₂, H₂/C=4 and 6 bar in Fig. 4.18 on the right. Regardless the CO₂ concentration, the model is thermodynamically consistent below 600°C. Beyond 600°C, the model lacks accuracy in conversion description. One reason could be that the CO production is not captured by the model due to absence of the reverse water-gas shift reaction in the model.

4.6 Summary

Three main aspects of the catalyst are discussed in Chapter 4: The deactivation under methanation conditions, deactivation causes and comparison of the obtained kinetics with literature models. The main results are briefly summarized.

CO methanation

The CO methanation system suffers from mass and heat transport limitations at higher temperatures due to fast kinetics. The Mears criterion is not fulfilled implying overheating of the catalyst pellet at most examined temperatures and catalyst particle sizes. Mass transport limitation is most likely influencing the reaction rate and is definitely occurring at particle diameters above 400 μm .

The degradation process of the catalyst under methanation conditions of CO is found to depend on temperature, H_2/C -ratio and particle size. Better stability of the catalyst is obvious at higher temperatures which contradicts to most of the literature findings at similar conditions on Ni catalysts. The effect could be explained by a change in reaction pathway from CO to CH_4 . Hydrogen is found to be beneficial for stability and activity and this finding is coherent with literature observations. Slower deactivation of larger particles could be explained with mass transfer limitation of CO.

The post-experimental analysis of the spent catalyst exhibits a considerable decrease in BET-surface area during experimental testing. The assumption of carbon accumulation is confirmed using the surface analysis with WDS. Crystallite growth is detected with XRD, however, is excluded as the main catalyst deactivation cause.

CO₂ methanation

The long-term stability of three different catalysts is investigated: A commercial Ni catalyst, self-prepared Ni/ Al_2O_3 and a bimetallic NiFe catalysts. It is found that all catalysts possess a good stability and selectivity towards methane at higher temperatures larger than 350°C. At lower temperatures (less than 320°C), an increased selectivity towards CO is observed which correlates with a stronger deactivation rate of the catalyst. The best performance regarding activity and selectivity towards methane is obtained with the bimetallic Ni₃Fe system at temperatures higher than 350°C compared to Ni catalysts. However, quick degradation is encountered at lower temperatures (less than 320°C), which occurs alongside increasing selectivities towards CO production.

An examination of the commercial catalyst at different H_2/C -ratios demonstrates that even at low hydrogen contents in the feed, extremely low deactivation rates compared to those under CO methanation conditions are possible.

The post-analysis of the spent commercial catalyst using WDS shows that carbon accumulation occurs

and is likely the cause for the catalytic loss. The carbon surface concentration is by a factor of 5 lower compared to the value obtained under CO methanation conditions, indicating a difference in mechanistic steps for the methanation sequence between the two methanation reactions. Although, coke accumulation is observed, the BET surface change is relatively low compared to the strong specific surface decrease under CO methanation conditions.

Methanation of CO/CO₂ mixtures

Most of the literature observations are confirmed regarding kinetics in methanation of CO/CO₂ mixtures. Preferential conversion of CO takes place and the conversion is not affected when CO₂ is introduced. Methanation of such mixtures increases the methane flow rate. However, higher CO₂ conversions are only achievable when low amounts of CO₂ are added.

Regarding catalyst degradation, the deactivation curves lead to the assumption that CO is the main precursor for coke formation.

Comparison of the obtained catalyst activity with kinetic rates from the literature

The obtained kinetic data from methanation experiments are successfully compared with literature models by Xu and Froment [67], Zhang et al. [56], Kopyscinski et al. [58] and Koshany et al. [68]. All models reflected the collected data well in spite of individual drawbacks. The Kopyscinski model matches conversions obtained under methanation conditions using pure CO/H₂, pure CO₂/H₂ and as well as their mixtures with good accuracy. However, it is valid only below 400°C since no limitation by thermodynamics is considered. The Zhang model seems to fit better to the obtained results than that of Xu and Froment; both are thermodynamically consistent. In case of methanation of pure CO₂, the model of Koshany et al. [68] is the most accurate. However, the selectivity towards CO cannot be described at all.

5 Reactor development & performance tests

This chapter covers the design aspects and performance of microstructured reactor prototypes developed in the course of the MINERVE project. The reactor performance is examined from the viewpoint of temperature control under methanation conditions using CO/CO₂ mixtures. Benefits and drawbacks of the developed reactor prototypes are discussed.

5.1 Microstructured competitor devices for methane production

According to literature surveys, several microstructured reactor concepts have already been designed and used for the methane production. Their analysis provides valuable insights into the design aspects which are partially followed and developed further in this work. In the following, the most similar methanation prototypes are presented which are scalable for higher throughput of reactants. Lab-scale microreactors are not considered.

Tegrotenhuis et al. [143] patented a microchannel reactor for highly exothermic and endothermic equilibrium limited reaction systems which includes at least one of the following reactions: Selective methanation, Sabatier process, water-gas shift, etc.. The description of the reactor is given as a stack of embossed sheets bonded together. The heat transfer capability is realized by alternating the reaction and heat exchange sheets. The channels are micro sized and allow the heat transfer in co- or counter-flow. The catalyst integration is limited to washcoating methods. No information is given about cooling fluids or operation pressures.

Brooks et al. [120] suggest a microreactor for the Sabatier reaction. The reactor consists of multiple reaction slits in parallel which are millisized. The catalyst integration into the reaction channels could be done by washcoating methods. Another method is provided by filling the reaction slits with a porous

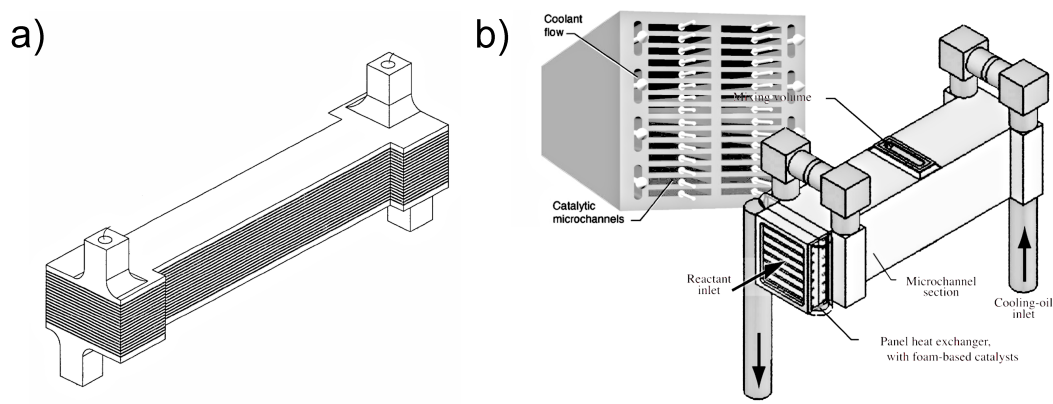


Figure 5.1: Microreactor concepts by Tegrotenhuis et al. [143] (a) and Brooks et al. [120] (b) for highly exothermic equilibrium reactions.

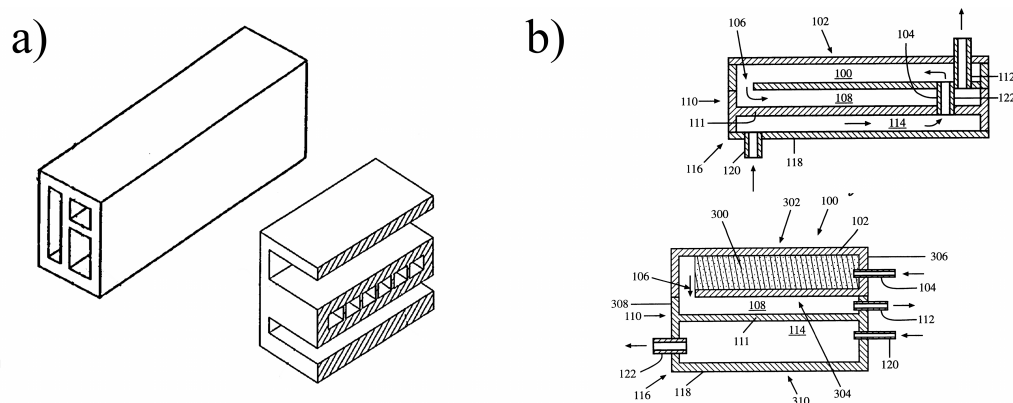


Figure 5.2: Microreactor concepts by Mathias et al. [144] (a) including heat transfer between three fluid streams at the same time; it can be used for evaporation cooling of the methanation. A similar reactor concept is patented by Tonkovich et al. [145] which consists of three chambers allowing heat exchange between three fluid streams (b).

metal felt impregnated with the catalyst. The cooling channels are placed in the metal housing and are operated with cooling oil.

Mathias et al. [144] suggest a multi-stream microchannel device (Fig. 5.2 a)), which could be used as a pure heat exchanger between at least 3 fluid streams but also in combination with chemical reaction, e.g. methanation of CO and CO₂. The invention includes a phase transition of the fluid in general, e.g. evaporation/condensation but also physical processes like ab- and adsorption. The inner dimensions of the structures are in the range 0.1-2 mm. The catalyst could be integrated by known methods, e.g. wash-coating, packed bed, monoliths etc.

An invention by Tonkovich et al. [145] comprises a reactive microchannel heat exchanger consisting of 3 zones. The exothermic reaction chamber is filled with the catalyst material and provides heat due to the reaction. The exhaust gas is directed to an exhaust chamber while pre-heating or evaporating the working fluid.

Another invention of microstructured device comprises a ceramic microreactor consisting of multiple ceramic layers and at least three chambers, where two of them are for cooling/heating purpose, while another acts as the reaction zone [146]. The reactor is designed for extremely exothermic reactions, e.g. methanation and allowed operation temperatures up to 1000°C. The catalyst is integrated by washcoat methods.

5.2 Development of the novel microstructured reactor concept for methanation of CO and CO₂ mixtures

The design procedure for a novel reactor from scratch poses a complex multidimensional problem which requires several iterations to match all requirements to a satisfactory extent. The most significant process and reactor aspects are summarized in Tab. 5.1, which are addressed in this section in detail. The poly-tropic microreactors in this thesis encompass three domains which are cooling and reaction zones and reactor housing. All domains interact with each other regarding mass and heat transport phenomena, so that a simultaneous consideration of every physical/chemical process in each zone is required. Theoretical considerations are used to support the design process where possible.

Catalyst amount & catalyst deployment method

The design starts with the determination of the catalyst mass required to convert 1 Nm³/h of syngas, according to the MINERVE project. Depending on catalyst activity and degradation, its amount governs the size of the reactor housing and determines the catalyst deployment method. The necessary catalyst amount can be calculated either from experimental results given in Chapter 4 or using simulation. The latter method is presented here, since the kinetic rate given by Kopyscinski et al. [58] reflects the behavior of the used commercial catalyst precisely. Thus, a deeper insight into the reactor can be gained. For this reason, a differential equation for 1-dimensional isothermal plug-flow model (see Eq. 4.2) is evaluated for the assumed MINERVE gas composition with 10% CO, 7% CO₂, H₂/C=3, rest N₂, the total throughput of 1 Nm³/h at 400°C and a total reactor pressure of 6 bar. Due to deactivation of the catalyst at all reaction conditions, as observed experimentally in Chapter 4, the excess amount of catalyst is necessary to allow longer operation times of the reactor. The corresponding conversion profiles from

Table 5.1: Requirements and challenges encountered in the course of the design of the microstructured reactor.

Requirements		Challenges
Process level	Reactor & catalyst level	Reactor level
Throughput >1 Nm ³ /h	Long-term catalyst stability	Catalyst deactivation/Blockage by coke
Superheated steam generation for supplying the SOEC	Quick and easy catalyst replacement	Hot spot formation / Reaction extinguishment Fluid maldistribution
Feasibility of dynamic operation	Defined temperature control	
	Uniform fluid distribution Application of transient load changes	

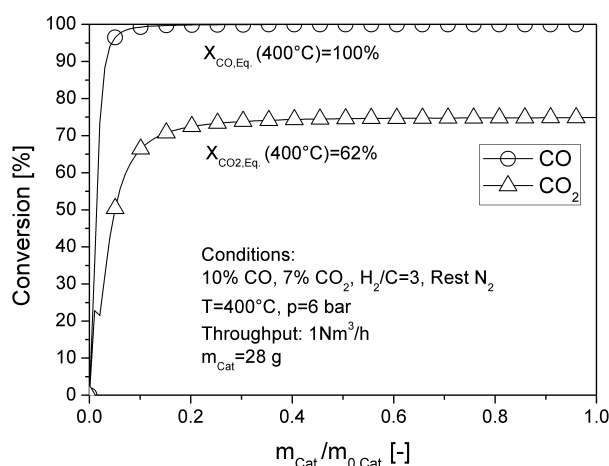


Figure 5.3: Conversion of CO/CO₂ mixture as a function of the normalized catalyst amount at 400°C for 1 Nm³/h of syngas with the gas composition 10% CO, 7% CO₂, H₂/C=3, rest N₂, reactor pressure of 6 bar and the total catalyst amount of 28 g.

simulation are depicted in Fig. 5.3 using the catalyst amount of 28 g. The surplus of catalyst provides maximum possible conversion of CO and CO₂ at around 5% and 15% of the applied catalyst mass already, i.e. the reactor output composition is governed by thermodynamics. The downtime of the microstructured reactor using 28 g of the commercial Ni catalyst, with information from Chapter 4, is estimated to exceed 6 months at elevated temperatures beyond 400°C and on particles larger than 400 μm in diameter. This time span is considered sufficient for testing the unit regarding the performance and possible degradation of the catalyst. The simulation shows an inconsistency in respect to CO₂ conversion overestimation by around 10 p.p. compared to the thermodynamic equilibrium, which is attributed to the kinetic rate expression and is discussed in Chapter 2.3.2. This issue is insignificant here. Taking the catalyst amount into account, the catalyst deployment method and the geometry of the reaction zone are addressed. The common catalyst integration method in microstructures involving wall coating is ruled out due to a low catalyst per reactor volume ratio and the difficulty of replacement. These problems are solved by integrating the catalyst in the form of a packed bed similar to the catalyst study in Chapter 2.3. With a typical catalyst bulk density of around 1400 kg/m³ [86], the previously estimated amount of catalyst of 28 g can be integrated in a compact reaction zone of approx. 20 cm³, additionally providing long downtimes of the reactor. Technically, the reaction zone is designed in both prototypes as two rectangular ducts with 2 mm in height, 50 mm in width and 100 mm in length yielding 20 cm³ of the effective reaction volume (see Fig. 5.5, 5.6). The catalyst is fixed by a frit at the in- and outlet which also functions as a reaction fluid distributor. Due to simple geometry, the reaction duct can be filled with catalyst or emptied quickly.

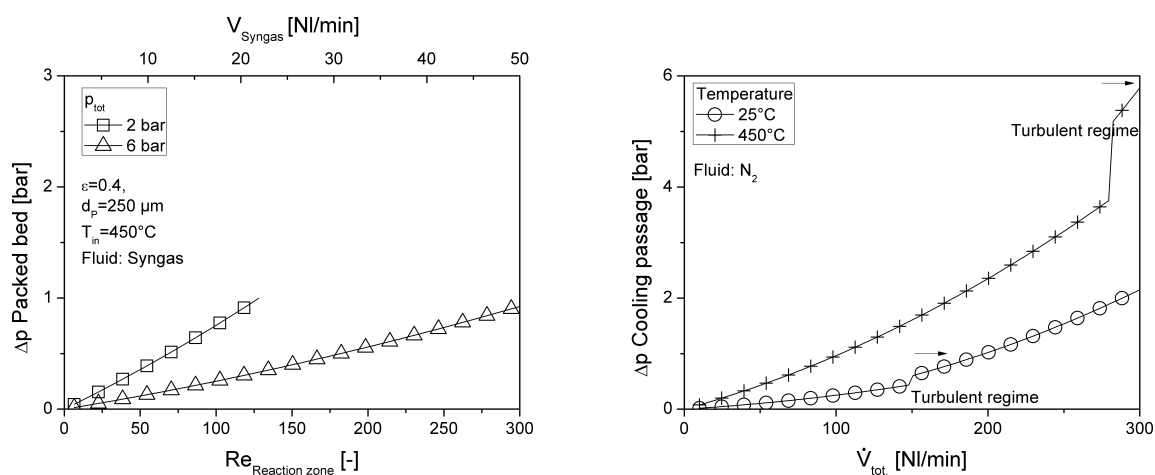


Figure 5.4: Pressure drop in the packed bed as a function of the Reynolds number at 2 and 6 bar reactor pressure, 450°C , $\varepsilon=0.4$, $d_p=250 \mu\text{m}$, MINERVE gas composition (left). Pressure drop in the 0.15 m long cooling zone of the Prototype 1 as a function of the coolant volumetric flow for two temperatures of 25 and 450°C (right).

Pressure drop and heat transfer in the packed bed

To account for the pressure drop in the packed bed, which reduces the driving force for flow, the Ergun Eq. 7.8 [147] is evaluated for the 0.1 m long reaction zone as a function of the total syngas flow for two different pressures of 2 and 6 bar ($T=450^\circ\text{C}$, MINERVE gas composition) in Fig. 5.4 on the left. A particle diameter of $250 \mu\text{m}$ and a porosity of 0.4 are used for the estimation. Fluid parameters like specific heat capacity and dynamic viscosity for the given gas composition is computed according to [148; 149]. As depicted in Fig. 5.4 on the left, the pressure drop becomes pronounced at higher Reynolds numbers and diminishes with increasing total pressure due to fluid compression and lower gas velocities. At 6 bar reactor pressure, around 250 mbar of pressure drop are expected in the packed bed at 450°C for $1 \text{ Nm}^3/\text{h}$ ($16.7 \text{ NI}/\text{min}$), which is negligible. Since the methanation reaction is strongly exothermic, the packed bed height in combination with low heat conductivity of the packed bed could potentially lead to heat transport resistance. This issue is not studied prior to the manufacturing procedure but results from previous knowledge on reactor design. The heat transport bottleneck of the manufactured reactor is examined in Chapter 6.

Cooling potential and pressure drop in the cooling passage

The design of the cooling passage starts with the estimation of the released heat amount at methanation conditions given by MINERVE (throughput $1 \text{ Nm}^3/\text{h}$, 10% CO , 7% CO_2 , $\text{H}_2/\text{C}=3$, rest N_2) and the required mass flow of the coolant. Water is the preferred cooling medium, since it may provide effective heat removal due to evaporation in the reactor and the steam could be fed into the SOE-cell directly for electrolyzing purposes without the necessity of an external evaporation unit. In addition, superheating

of the steam above 350°C in the methanation unit is desired. According to Eq. 5.1, the required mass flow \dot{m} of the coolant to remove the reaction heat of 400 W can be calculated. Here, nitrogen is used as a representative for gaseous coolants with the specific heat capacity $\bar{C}_{p,m}$ [J/(kgK)] and the overheating of the fluid ΔT of 150 K.

$$\dot{Q} = \dot{m} \cdot \bar{C}_{p,m} \cdot \Delta T \quad (5.1)$$

The resulting mass flow of nitrogen is calculated to 2.4 g/s which corresponds to approx. 130 NI/min. In comparison to water, where around 10 g/min of water can already remove the generated heat of 400 W due to high evaporation enthalpy (only evaporation), high volumetric flows of gas, e.g air or steam may lead to high pressure drops. The pressure drop for the design of the cooling passage is estimated according to Darcy-Weisbach Eq. 5.2 using nitrogen.

$$\Delta p = \frac{\rho u^2}{2} (K_{fric} \cdot \frac{l}{d_h} + \sum \xi) \quad (5.2)$$

Here, ρ is the fluid density in kg/m³, u is the superficial gas velocity in m/s, l is the length of the tube in m, d_h is the hydraulic diameter in m, and ξ is the pressure loss coefficient. The friction coefficient K_{fric} is calculated according to Hagen-Poiseuille at $Re < 2320$ with $K_{fric} = 64/Re$ and according to Blasius $K_{fric} = \frac{0.3164}{Re^{0.25}}$ in the turbulent regime with $Re > 2320$ [150]. The pressure loss coefficient ξ is 1.1 for 90° redirection of the flow [150]. Nitrogen with temperature dependent dynamic viscosity is taken from [148] for Re evaluation.

Since the coolant flow is constrained by the heat amount due to the reaction release, the only design variables remain the length and diameter of the channel and the flow restricting fixtures like narrowings or elbows. In this work, the optimized cooling zone above each reaction zone in both prototypes consists of 69 rectangular channels of 500 x 500 μm in width and height. Fins of 300 μm separate the channels to support the heat removal by heat conductivity. To ensure an uniform fluid distribution in the cooling zone, the flow is redirected several times in both prototypes. The length of the entire cooling passage is around 15 cm for Prototype 1 and around 8 cm longer in Prototype 2. Fig. 5.4 on the right shows the pressure loss along the cooling passage as a function of the total volumetric flow fed into two symmetrically positioned cooling inlets for Prototype 1 for 25 and 450°C using nitrogen as the heat transfer medium. As can be seen, the volumetric flow rate of 130 NI/min can be used without exceeding pressure drop of 1.5 bar at 450°C and remains negligible at 25°C. For the Prototype 2, the pressure drop increases to 1.9 bar at 450°C and 130 NI/min gas flow, which is tolerable. Below 150 NI/min of coolant flow, laminar regime is present at $T < 450^\circ\text{C}$ for both prototypes. At 450°C, the

turbulent regime is shifted to higher flows due to temperature dependence of kinematic viscosity. In the second reactor prototype, two coolant inlets are realized with a single outlet. The benefit compared to the first prototype is that evaporation occurs in greater distance. In addition, variation in coolant flows between the two inlets is expected to provide an improved handling of hot spot temperatures to the reaction ducts, reducing the possible extinguishment of the reaction in the presence of water boiling at low temperatures. Further designs and operation modes are provided in the patent application [151].

Dynamic operation and heat management in the reactor

The methanation unit is expected to operate under load changes due to possible fluctuations of the renewable energy, i.e. syngas fluctuation provided by the SOE-cell should occur frequently. To allow the reactor to heat up fast, both reactor prototypes are equipped with five heating cartridges at the symmetry axis. This feature allows defined start-up and shut-down cycles and could be used to adjust the axial gradients for improved reactor performance. Additionally, five holes for temperature measurements are designed to monitor temperature along the reaction slit.

5.3 Prototype specifications and manufacturing

The Prototype 1 and 2 are manufactured according to CAD drawings shown in Fig. 5.5-5.6. Each reactor unit is made from several machined metal sheets which are stacked and bonded together via diffusion welding. Each reactor exhibits two reaction slits with 2 mm in height, 50 mm in width and 100 mm in length yielding 20 cm³ of the effective reaction volume. The adjacent cooling chamber above/below each reaction slit consists of 69 rectangular channels of 500 x 500 μm in width and height. Perforated frits in the in- and outlet hold the catalyst in place. Reactants are supplied into the reaction slit via flanges which are fixed to the reactor body via screws. Graphite sealings provide leak tightness. The coolant is supplied/removed into/from the cooling zone via Swagelok VCR connectors. Highly alloyed stainless steel, Nicrofer[®] 3220, is used with approx. 32% of Ni and 21% of Cr content. This kind of steel guarantees high resistance against oxidation and carburization [152] and delays possible metal dusting processes.

The devices are manufactured at IMVT (KIT) and the final units are presented in Fig. 5.7. The comparison with literature devices reveals several novelties. The first feature concerns the flow management of the heat transfer medium. Redirection of the fluid allow for an improved flow distribution uniformity. The second feature concerns the heat management using the heat transfer fluid and electrical heating at the same time, allowing adjustable gradients. In this particular case, the low reactor weight allowed rapid heating >300°C within approx. five minutes. This could be advantageous during the start-up from cold or hot standby which are likely in the MINERVE concept. The third feature includes the pressurized operation of the reaction and cooling zones.

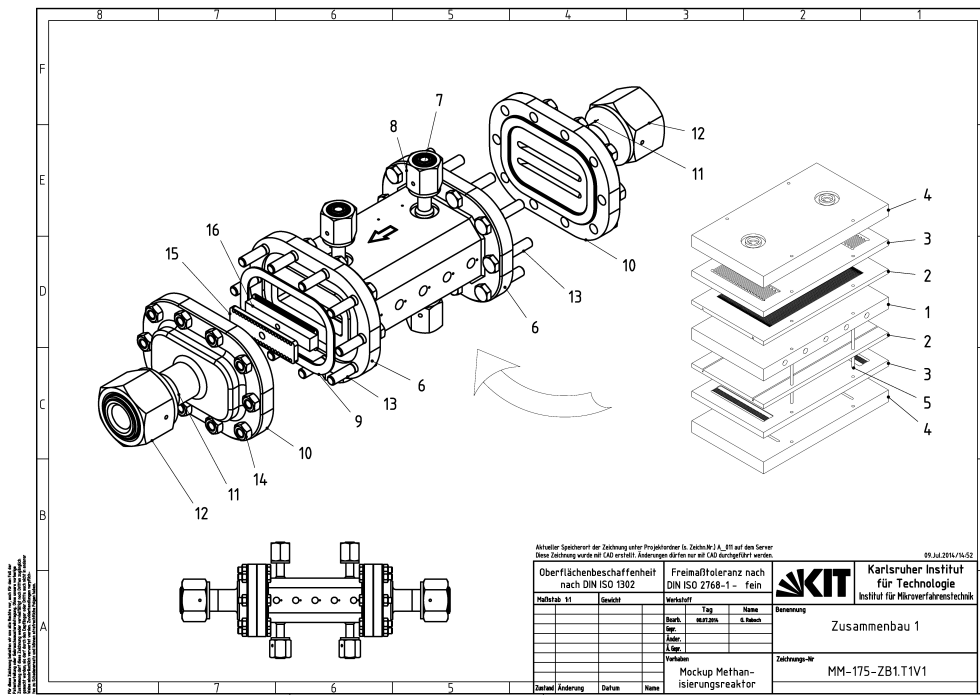


Figure 5.5: Technical drawing of the methanation unit according to Prototype 1.

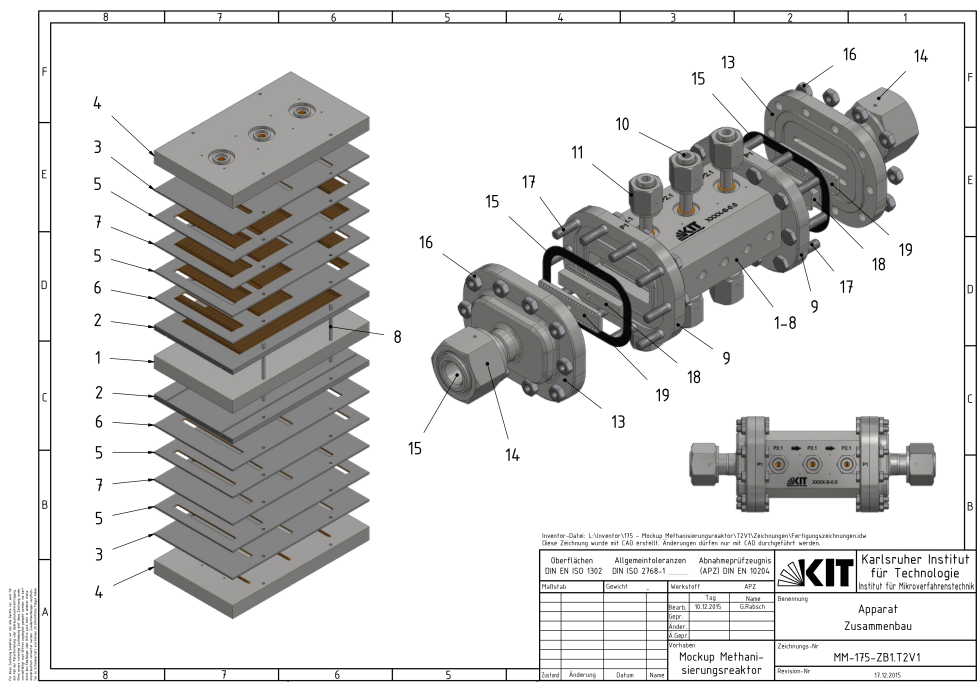


Figure 5.6: Technical drawing of the methanation unit according to Prototype 2.



Figure 5.7: Manufactured reactor devices according to Prototype 1 (left) and Prototype 2 (right) at IMVT (KIT) for the MINERVE project.

5.4 Experimental procedure and equipment

Test rig & reactor integration

The test rig for prototype testing is slightly modified compared to that for kinetic measurements. Reactants supply and GC analytics are equal (see Chapter 4.2). A PC with LabView® is used for control and saving of temperature and pressure data. Two additional Knauer K-1800 pumps are installed for evaporation experiments using demineralized water as coolant feed. In case liquid water or air is used as a coolant, a microstructured heat exchanger from IMVT equipped with 15 heating cartridges (HORST GmbH) 225 W each is used for preheating the cooling fluid. For steam generation, two micro heat exchangers are operated in parallel with a total electrical power of 6.75 kW_{el}.

The integration in the setup of both reactor prototypes is explained according to Fig. 5.8 on the left in terms of Prototype 2. Along the symmetry axis, the reactor is equipped with 5 heating elements (225 W, HORST GmbH) which are controlled separately. Each heating element is regulated by an adjacently inserted thermocouple and is referred to as Pos. 1 to 5. The distance between Pos. 1 and 5 corresponds to 85% of the axial reaction zone length. Additional thermocouples are inserted into the metal top plate measuring the temperature 1 mm above the cooling zone. For monitoring temperature in the packed bed, a flexible 40 cm thermocouple with 0.5 mm i.d. is inserted through the reaction inlet. For Prototype 1, the tip of the thermocouple is placed at the same axial position as Pos. 2, for Prototype 2 between Pos. 1 and 2.

Since the Prototype 2 is designed with two inlets, the inlet connection close to the flange is labeled as Outer and the inlet in the center as Inner cooling passage.

The reactor is operated in a metal box which is filled with the insulation powder Microtherm Freeflow®-1000X provided by PROMAT GmbH. The Prototype 1 is always operated horizontally as shown in Fig. 5.8 on the right with cooling inlet connections pointing to the side. Prototype 2 is always operated with inlet connections pointing to the top and bottom. In addition, the reaction flow is directed 45 degrees upward for evaporation experiments in co-flow.

Heat transfer experiments in absence of reaction using Prototype 1

Examination of the heat transfer behavior with air, steam and evaporation of water is done by simulating reaction heat occurrence via heating cartridges. Thereby, the reaction slits are empty and filled with nitrogen. In case of air, 40, 60, 80 and 100 NI/min are preheated to 150°C with a heating wire and fed into the cooling zones of the reactor. In case of steam as coolant, demineralized water in the range 15-65 g/min is evaporated and superheated to 150°C prior to feeding into the two individual cooling zones. In case of water, 8 and 12 g/min water are fed to the electric heat exchangers and preheated to 95-99°C before feeding into the cooling zones.

Reaction experiments

In the Prototype 1, the reaction is conducted with two different syngas flows of 15 and 23 NI/min with a gas composition of 10% CO, 7% CO₂, 72% H₂ and N₂ (remainder) as internal standard for the GC analytics. The reactor is filled with 5 g of a commercial Ni catalyst, diluted with silicon carbide. The particle size of the catalyst is adjusted to 400-500 μm, while the size of the silicon carbide is adjusted to 300-400 μm. This allows the separation of catalyst and inert material after reaction and also to lower pressure drop alongside with better catalyst stability in presence of CO (see Chapter 2.3). Prior to experiments, the catalyst is reduced in-situ in nitrogen-hydrogen 1:1 flow for 4 h at 450°C. For cooling purposes, air steam and water are used accordingly to the heat transfer experiments described above.

In the Prototype 2, CO/CO₂ mixture with a throughput of 17.15 NI/min is fed into the reaction zone with the gas composition of 11.7% CO, 6.7% CO₂, 70% H₂ and N₂ (remainder). Alternatively, methanation of CO₂ is conducted in the reactor using a throughput of 19.7 NI/min with the gas composition of 18.7% CO₂, 71% H₂ and nitrogen as a remainder. Particle size distribution and reduction procedure of the catalyst is identical to Prototype 1. All studies in the Prototype 2 are performed on a commercial Ni

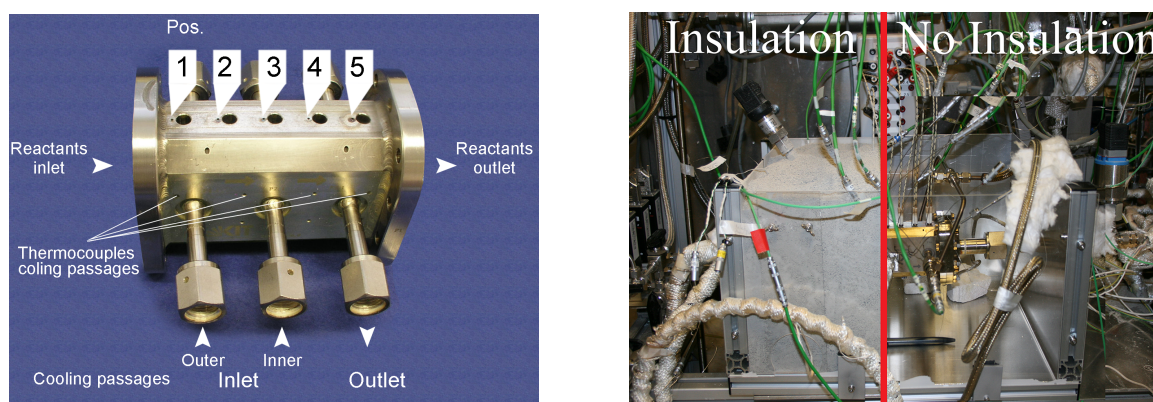


Figure 5.8: Labeling of thermocouple, heating element and inlet/outlet positions (left) and integrated reactor (prototype 1) into the test rig including insulation material (right).

catalyst (2.5 g) which was filled into one reaction slit. The second reaction slit was blocked intentionally as its cooling zone was damaged during the fabrication. The variation of the input concentrations was done during the MINERVE project because of new input data provided by the project partners. It should also be noted that the flow rate in Prototype 2 is almost double that in Prototype 1 due to improved control of the temperature.

5.5 Characterization of the Prototype 1

This section covers the aspects of heat generation and removal in the Prototype 1. First, the reactor is examined as a pure heat exchanger using heating cartridges as the heat source and air steam and water as the heat transfer media. Based on the collected data, the reactor is analyzed regarding heat removal and temperature control using methanation of CO/CO₂ mixtures.

5.5.1 Heat transfer experiments in absence of reaction

The heat transfer with air and steam is examined in the microstructured reactor at a constant reactor temperature of 300 and 450°C using electrical heating cartridges. Fig. 5.9 on the left shows the electrical power consumption $Q_{el.,HC}$ of the heating cartridges (HC) as a function of the mass flow multiplied with the heat capacity $\dot{m} \cdot C_p$ [W/K] of air and steam. The offset of $Q_{el.,HC}$ ($\dot{m} \cdot C_p = 0$) provides the heat loss to environment while keeping the reactor at desired temperature niveau. It is found that the insulation with the Freeflow[®] powder reduces the heat loss while other insulation approaches such as glass-wool fail. The heat loss is in the range 30-50 W at 300-450°C, respectively. The increase of the coolant mass flow leads to a higher power consumption of the heating elements due to higher heat removal. At $\dot{m} \cdot C_p < 0.75$, a nearly linear relation between $Q_{el.,HC}$ and $\dot{m} \cdot C_p$ is obvious using air and steam. At higher mass flows, the gradient of the curves decreases indicating possible heat transfer limitations. The comparison of the two fluids shows that 30% more heat can be extracted by steam at the examined temperature levels. Since the heat conductivity and thus the heat transfer coefficient differ by approx. 10%, the deviation could only be explained with non-complete evaporation of water during steam generation despite overheating. This allows additional heat removal by evaporation of water droplets. Calculating backwards, the hypothetical evaporation degree of water in the electric heat exchangers is around 90%. This is consistent with the

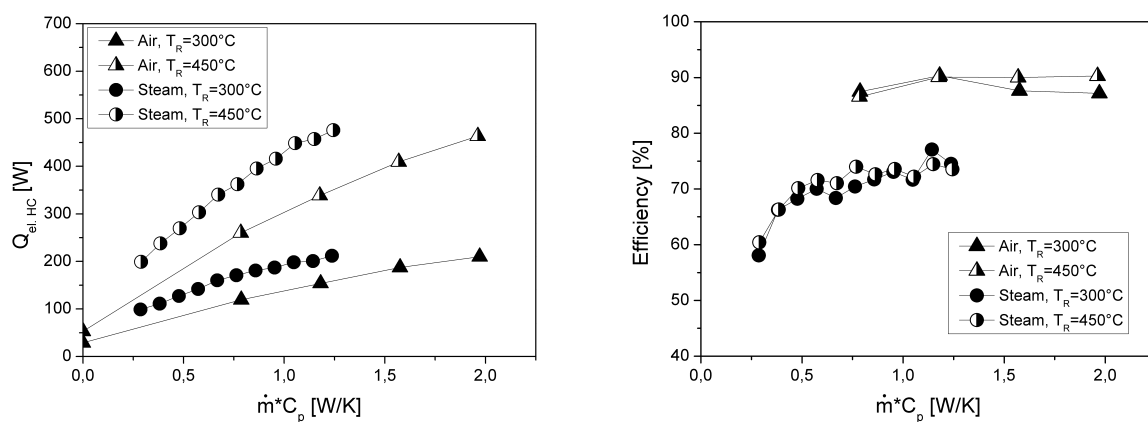


Figure 5.9: Power consumption of the heating cartridges while flushing the reactor Prototype 1 with air and steam with different mass flows at a constant reactor temperature of 300 and 450°C (left). Heat transfer efficiency at different heat capacities using air and steam as heat transfer fluids (right).

literature at the applied evaporation conditions [153].

Since small-scale devices suffer from heat losses in general, the heat recovery is examined. The heat transfer efficiency is calculated according to $(\dot{m} \cdot C_p \cdot \Delta T) / Q_{el.,HC}$ which is the ratio of the absorbed heat by the cooling fluid and the electrical power introduced into the system by the heating elements. Fig. 5.9 on the right shows the heat recovery efficiency as a function of $\dot{m} \cdot C_p$ for air and steam as heat transfer fluids for the different reactor temperatures. Around 90% of the released heat in the reactor could be removed with air, independent of the volumetric flow and reactor temperature. In case of steam, lower efficiencies of around 70% are calculated. This supports the assumption that the generated steam contains liquid water droplets.

The heat transfer via air or steam could show insufficient cooling potential at higher syngas throughputs due to low specific heat capacities. For this reason, evaporation of water is tested for removal of heat at a high level of process intensification. Fig. 5.10 on the left shows the electrical power consumption of heating cartridges while flushing the cooling zone with water between 1-10 g/min, compared to air and steam. Evidently, water exhibits an enormous cooling potential which exceeds that of air by a factor of 20 at reactor temperatures of 300 and 450°C. This value is close to the ratio of evaporation heat and the product of the specific heat of air and the mean temperature difference $h_{v,m} / (C_{p,m,AIR} \cdot \Delta T) = 22$, while neglecting the overheating of steam. The calculated heat transfer efficiencies are shown in Fig. 5.10 on the right. The efficiency obtained using water is comparable to that of steam. The lower values could be attributed to either incomplete evaporation or possible condensation of steam at the thermocouple located at the somewhat colder outlet pipe.

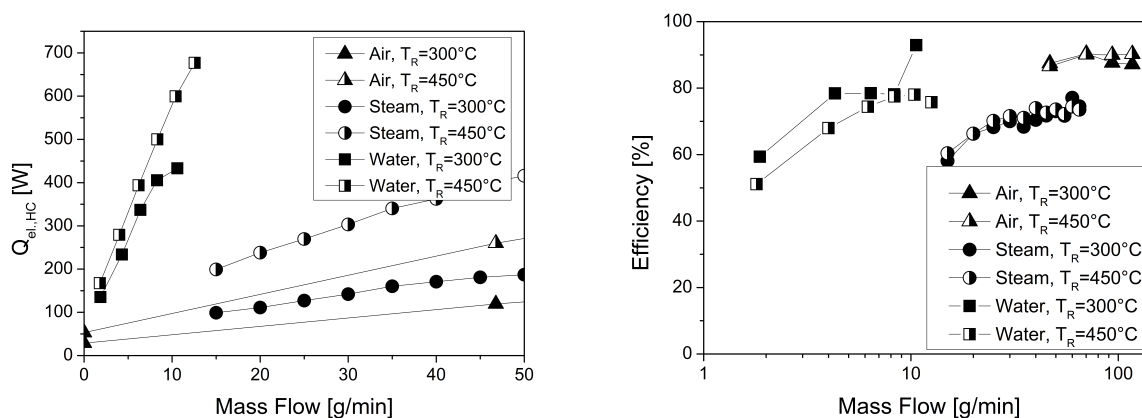


Figure 5.10: Power consumption of the heating cartridges while flushing the cooling zone of the reactor Prototype 1 with water ($T_{c,in}=99^{\circ}\text{C}$) at reactor temperature of 300 and 450°C, compared to air and steam (left). Heat transfer efficiency at different mass flows using air, steam and water as heat transfer fluids (right).

5.5.2 Reaction experiments

5.5.2.1 Dynamic behavior of the reaction system

Start-up of the reactor

The start-up of the reactor is always done in absence of cooling and similar temperature development schemes as in Fig. 5.11 are observed. After initial completion of the catalyst reduction, the reactor temperature is set to 300°C with the help of heating cartridges. When dosage of H₂ and N₂ is established, the introduction of CO and CO₂ begins, and the first temperature rise can be observed at the rear part of the reactor. The temperature rise of the reactor happens quickly with around 50 K/min due to reaction heat release (in the 4th to 5th minute), while the hot spot temperature moves towards the inlet of the reactor. After 7 minutes, the hot spot arrives near the reactor inlet and achieves up to 500°C. To prevent run-away, the coolant dosage is initiated during this time. In the specific case of Fig. 5.11 on the left, air flow is turned on. With the inlet temperature of 50°C and volumetric flow of 50 NI/min a quasi steady-state temperature profile is reached after approximately 30 min. The temperatures at Pos. 3, 4 and 5 are held within 450 to 500°C. Fresh catalyst always induces the reaction at around 300°C. After conduction of several experiments, the ignition temperature increases up to 340°C, which is an indication of the catalyst change. This phenomenon is also observed by Brooks et al. [120]. They conclude that this is not equivalent to a considerable catalyst deactivation. The thermocouple inserted into the front part of the catalyst bed allows to monitor the temperature progression in the catalyst bulk in comparison with the metal bulk (level of the heating cartridge at Pos. 2). Fig. 5.11 on the right shows the comparison of these two temperatures at identical axial position during the start-up of the reactor. After

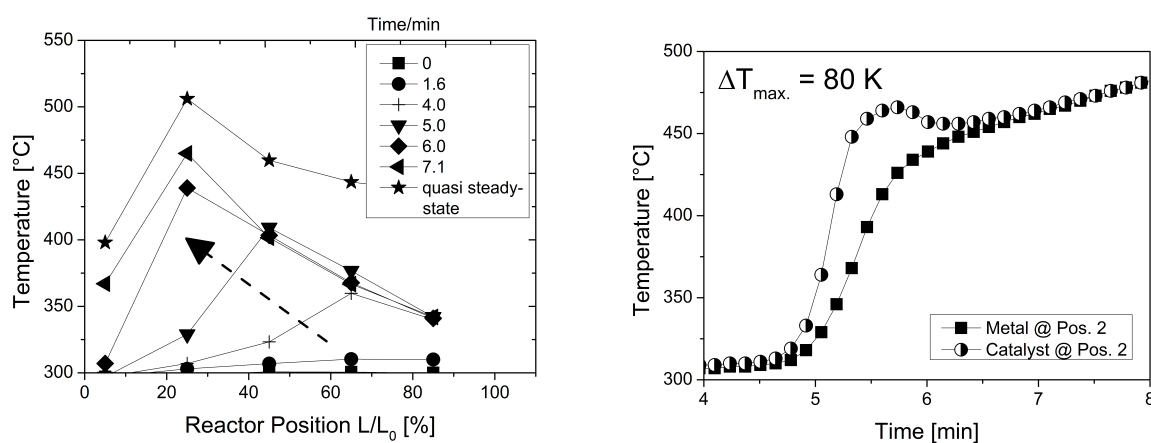


Figure 5.11: Temperature development in the reactor Prototype 1 during the start-up in absence of cooling; quasi steady state is obtained with cooling of 50 NI/min air at 50°C inlet temperature (left). Temperature development in the catalyst bed and in the metal bulk during the start-up of the reactor in absence of cooling (right).

5 minutes, the hot spot reaches Pos. 2 inside the catalyst and a quick temperature rise in the catalyst bed can be observed with a maximum rate of around 280 K/min. The temperature of the metal follows with approx. 30-60 sec. delay and a lower rate of 163 K/min. The maximum temperature difference between the reactor and catalyst is calculated to around 80 K. After 6 minutes, the two temperature profiles align in a quasi steady state.

Extinguishment of the reaction at higher cooling flows

In the course of the experiments, it became obvious that stable operation points of the reactor could only be achieved by the right set of cooling flow and inlet temperature as well as syngas flow and inlet temperature. Removing less heat from the reactor results in potential overheating of the reactor, while too harsh cooling leads to extinguishment of the reaction. Fig. 5.12 on the left shows different temperature profiles along the reactor while cooling the reaction (syngas flow 23 NI/min) with different air flows at $T_{c,in}$ of 50°C. To prevent a premature extinguishment of the reaction while analyzing the outlet composition of the product gas, the volumetric flow of the air as a coolant is increased stepwise to approach a steady state at the individual settings. The first increase of the coolant flow by 18% (65 NI/min in total) leads to a great temperature drop at Pos. 1 of around 100 K. In contrast, the temperature of the hot spot (Pos. 2) and subsequent temperatures in the reactor (Pos. 3-5) barely change. This behavior is attributed to the co-flow cooling regime. The greatest local heat transfer occurs at the first contact of the coolant and the reaction zone due to the maximum possible temperature difference. With the temperature increase of the coolant, less heat can be removed at Pos. 2-5. A further increase of air to 70 NI/min would cause a temperature drop at Pos. 1 to below 200°C. To prevent catalyst damage by nickel carbonyl formation, the minimum reactor temperature is stabilized to 275°C at each point using

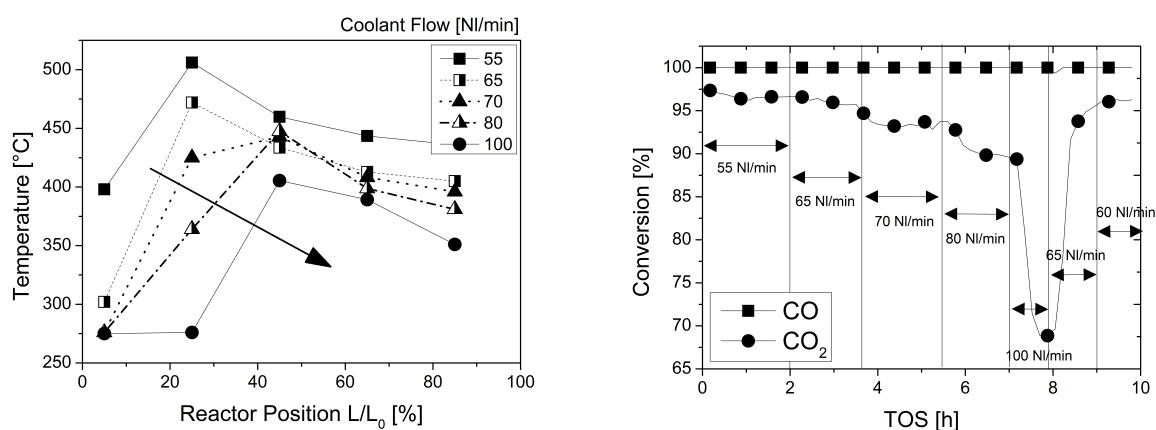


Figure 5.12: Extinguishment of the reaction (syngas 23 NI/min in reactor Prototype 1) at excessive cooling rates of air ($T_{c,in}$ 50°C) (left) and influence of the air flow ($T_{c,in}$ 50°C) on the overall conversion of CO and CO₂ (syngas flow 23 NI/min) (right).

the electric heating cartridges. The temperature at Pos. 2 drops by around 50 K compared to 55 NI/min air flow and the local position of the hot spot shifts towards the mid of the reactor. The temperature drop can be explained with better heat removal at higher mass flows of air, while the local movement could be attributed to a partial extinguishment of the reaction which occurs when the temperature drops below 330°C. The volumetric flow of 100 NI/min of air diminishes the hot spot by approx. 100 K and shifts it to the rear part of the reactor. The lower hot spot temperature, however, increases the demand of electrical heating to keep the system stable. As shown in Chapter 2.4, lower temperatures favor the thermodynamically possible conversion of CO and especially CO₂. Fig. 5.12 on the right shows the effect of the coolant flow on the reactor outlet gas composition in the corresponding experiment series of Fig. 5.12 on the left. Carbon monoxide is fully converted during the entire experiment series, while CO₂ conversion starts at around 97% at 55 NI/min coolant flow. A slight decrease of CO₂ conversion by up to 5% is observed at 70 NI/min of coolant flow despite a noticeable change of the temperature profile in the front part of the reactor. A considerable drop of CO₂ conversion, i.e. more than 20%, is evident using 100 NI/min of coolant flow. This is clearly attributed to the decrease of the reactive catalyst zone length due to extinguishment. Diminishing the coolant amount to 65 and 60 NI/min of air, reverses the temperature profiles and also the CO₂ conversions to the initial levels. Subsequently, no obvious catalyst damage occurs during the experiment series.

5.5.2.2 Steady-state temperature profiles in methanation of CO/CO₂ mixtures using gas cooling

In the following, the cooling potential of air, steam and water is examined under heat transfer from the reaction zone in steady state. Throughputs on the reaction gas side of 15 and 23 NI/min with a total released reaction heat of approx. 340 and 560 W are investigated. The inlet temperature for air and steam is always 150°C.

Influence of throughput on temperature profile in the reactor at different cooling flow rates

Fig. 5.13 on the left shows temperature profiles along the reactor for the methanation of 15 NI/min of CO/CO₂ mixture while cooling with air. Using an air cooling flow rate of 55 NI/min, the hot spot with a maximum temperature of approx. 460°C occurs directly at the inlet of the bed (Pos. 1). This finding indicates that a major part of the reactants CO and CO₂ is converted in the first 30% of the reactor length and that the cooling potential is insufficient. In the rear part of the catalyst bed, less reaction heat is generated, while heat is removed by the coolant. As a consequence, the temperature at Pos. 3-5 drops steadily. As observed before, a slight increase of the coolant flow rate by 5 NI/min has a great influence

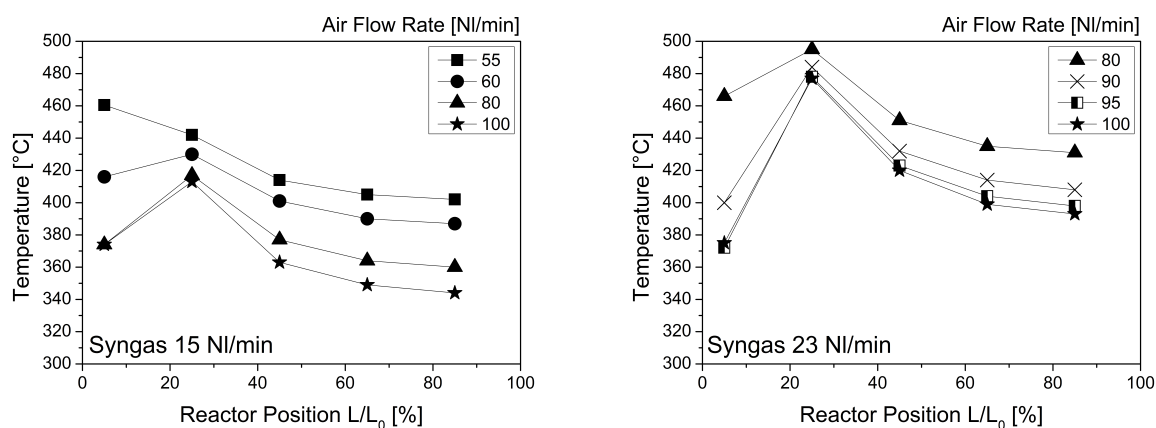


Figure 5.13: Temperature distribution along the reactor Prototype 1 during methanation of 15 NI/min (left) and 23 NI/min (right) of syngas while cooling with air ($T_{c,in}=150^{\circ}\text{C}$) at different flow rates.

on the temperature at Pos. 1. The effect is less pronounced at Pos. 2-5. To prevent the extinguishment of the reaction front at higher flow rates > 80 NI/min, the temperature at Pos. 1 is held at a constant value of 375°C . The hot spot temperature drops only around 20 K while increasing the coolant flow from 55 to 100 NI/min. The experiment is also conducted using a higher throughput of 23 NI/min of syngas. The amount of cooling air is varied between 80 and 100 NI/min to prevent a run-away of the reaction. The resulting temperature profiles are shown in Fig. 5.13 on the right. In general, the temperature profiles are similar compared to lower syngas throughput, i.e. with a hot spot at Pos. 2. The temperature at Pos. 1 is again strongly sensitive regarding the air flow rate. The rear part of the reactor shows similar temperature progression to the previous experiment series. The difference between 15 and 23 NI/min of syngas at 80 NI/min air flow is a temperature offset at positions 2-5 of around 60 K.

Comparison of cooling potential of air and steam

The cooling potential of steam and air is compared under methanation conditions at 15 and 23 NI/min of syngas with $m \cdot C_p = 1.6$ and 1.8 W/K, respectively. Fig. 5.14 shows the temperature distribution along the reactor at the two syngas throughputs and coolant flows of equal heat capacities. Independent of the syngas throughput, the temperature distribution with air cooling is nearly identical to steam cooling along the reactor axis. Steam cooling allows little reduction of the temperature, which is in accordance with the measurements from pure heat transfer experiments assuming small content of water droplets.

5.5.2.3 Evaporation cooling in the microreactor

Gas cooled reactor experiments suggest that the methanation reaction leads to an enormous local heat release. The limited heat capacity caused by cooling with air or steam either leads to extinguishment of the reaction in the first part of the reactor, or is insufficient to reduce the hot spot. Therefore, the

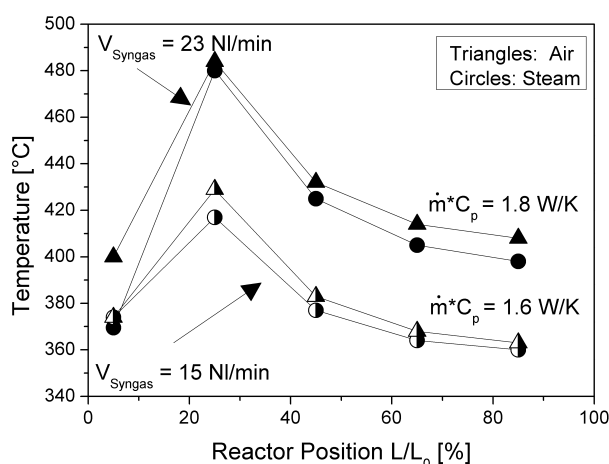


Figure 5.14: Comparison of the cooling potential of air and steam at syngas flows of 15 and 23 NI/min at similar heat capacities; reactor Prototype 1.

evaporation of water is examined for heat removal purposes. Using throughputs of 15 and 23 NI/min of syngas, a water mass flow of 8 and 12 g/min is pumped into the cooling channels with temperature between 95 and 99°C, respectively. Even though the heat removal capacity is equivalent to the air and steam flow, no stable operation point could be found in these experiments. Either overheating or extinguishment at the inlet of the reactor is observed. The problem could be solved by using the heating cartridges as anchoring points for temperature according to Case 1 and 2. In Case 1, the temperature at Pos. 1 and Pos. 4 is kept at 460°C and 350°C to support the initial state. In Case 2, the temperature of the first heating cartridge is confined to 360°C to prevent extinguishment of the reaction.

Case 1.

Fig. 5.15 on the left shows the steady-state temperature distribution along the reactor with throughputs of syngas flow of 15 and 23 NI/min pumping 8 and 12 g/min of water into the cooling channels, respectively. The hot spot occurs directly at the beginning of the reaction zone. Due to co-flow cooling, most of the water evaporation potential can be concentrated on the desired hot spot. The temperature profiles at both throughputs have a similar shape, since they are governed by the heating elements. No considerable temperature peaks could be observed and water is fully evaporated. Since the reactor is not operated autonomously, the question arises how much power is consumed by the heating elements. Using 15 NI/min of syngas, the heating cartridges at Pos. 1 ($Q_{HC,1}$) and Pos. 4 ($Q_{HC,4}$) consume around 5 and 32 W, respectively. This corresponds to around 10% of the released reaction heat. The same applies to the methanation using the throughput of 23 NI/min. The low power consumption by the heating cartridges also indicates that the water mass flow is chosen properly. The evaluation of the thermal efficiency, which is the ratio of the removed heat and the released heat plus electrical consumption, is

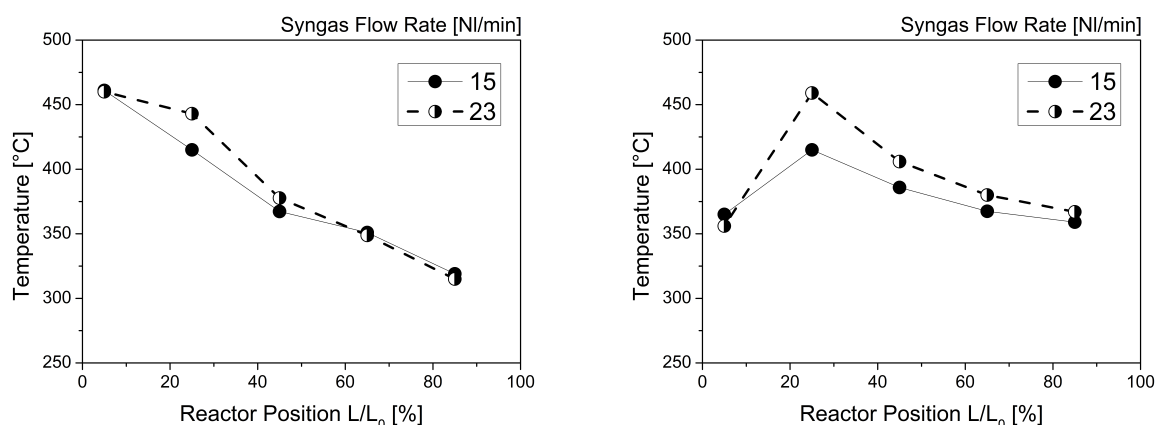


Figure 5.15: Temperature profiles in the reactor Prototype 1 for 15 and 23 NI/min of syngas while cooling with 8 and 12 g/min water mass flow at 95-99°C, respectively. Heating cartridge operation as anchoring point according to Case 1 (left) and Case 2 (right).

67% and 72% for 15 and 23 NI/min of syngas, respectively. The values are slightly lower compared to heat removal efficiencies without a chemical reaction. This is attributed to the electrical heat input. Case 1 provides valuable information for further reactor designs. First, the full cooling potential should not be concentrated on the packed bed inlet. Second, the cooling potential must be unleashed in the first reactor half. Third, the use of heating cartridge at Pos. 4 is necessary, indicating that overheating of the steam does not occur in the front part of the reactor leading to a high temperature gradient between coolant and reaction and thus subsequent extinguishment from outlet to inlet. Full evaporation must be guaranteed in an improved prototype.

Case 2

By setting the lowest allowable temperature limit at Pos. 1 to 360°C, the temperature profile transforms into a profile according to Case 2. The temperature profiles, shown in Fig. 5.15 on the right, are measured under methanation conditions of 15 and 23 NI/min of syngas while cooling with 8 and 12 g/min of water in analogy to Case 1. Hot spot formation of 400-450°C occurs in the front part of the reactor (Pos. 2) and depends mainly on the syngas throughput as was already observed during experiments with cooling using air or steam. This finding is a strong indicator for heat transfer limitation which is possibly governed by the packed bed and/or the reactor plate thickness between packed bed and the cooling channels. The main contribution to the heat transfer resistance, however, could only be answered using simulation.

The power consumption of the first heating cartridge is higher than in Case 1; 115 and 168 W are required for 15 and 23 NI/min syngas flow, respectively. The percentage of the electrical heat compared to the reaction heat is relatively high at around 32%-35%. This indicates that the heating element at Pos. 1 largely contributes to the evaporation of the water. The contribution of reaction heat to evaporation

at Pos. 1 is comparatively low due to the low reaction rate at 360°C. The occurrence and control of the hot spot must be taken into account for further reactor optimization. Case 2 explicitly supports the assumption that not all the cooling potential should be focused on the reactor inlet.

5.6 Characterization of the Prototype 2

The reactor concept according to Prototype 2, derived from the learnings with water cooling of Prototype 1, is examined regarding temperature control at methanation conditions using preheated water as the heat transfer medium. The possibility of influencing temperature distribution along the reactor under methanation conditions using the modified cooling zone is presented.

5.6.1 Methanation of CO/CO₂ mixtures

The reactor Prototype 2 is tested with a throughput of CO/CO₂ mixture of 17.15 NI/min (11.6% CO, 6.7% CO₂, H₂/C=3.8, 6 bar, N₂ as remainder) according to Scenario 1 to 3 to reveal the reactor behavior (Fig. 5.16).

Scenario 1

This scenario provides a similar temperature profile like in Case 1 obtained with the Prototype 1. However, no electrical heating is required, i.e. the reactor operated autothermally. The outer cooling entry is fed in co-flow with water of 4.9 g/min ($T_{c,in}=73^{\circ}\text{C}$) while no coolant is dosed into the inner entry. Fig. 5.16 on the left shows the semi steady-state temperature profile in the reactor along the symmetry axis (Pos. 1-5) and in the catalyst bed. The hot spot is placed directly at the inlet of the reactor pointing to fast reaction rate with conversion of most CO in the front part. The temperature at Pos. 1-5, in the metal top plate close to cooling channels (not shown here) and catalyst bed are similar pointing to weak gradients in the system. The reactor performance is evaluated in terms of CO and CO₂ conversion in Fig. 5.16 on the right. Opposite to expectation, CO is only converted to 95%. The reason for this behavior could lie in the bypass through the second reaction slit which is filled with fine SiC

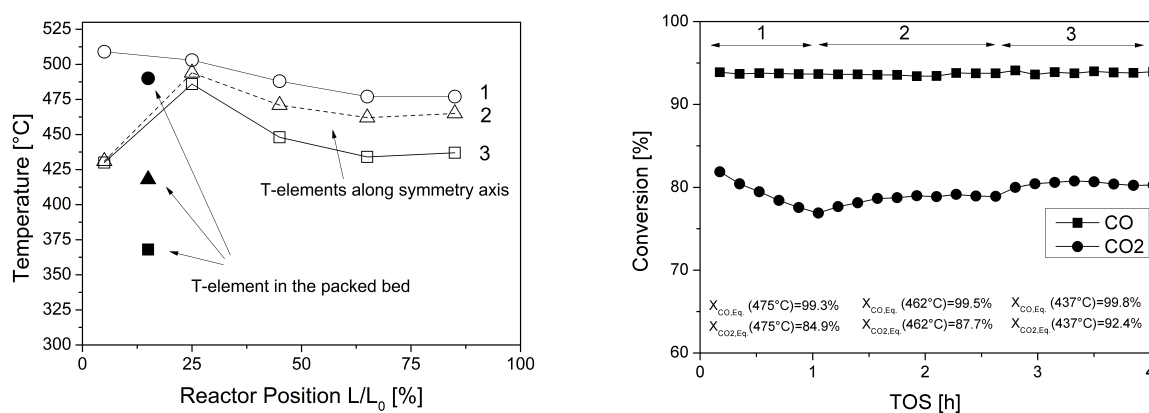


Figure 5.16: Axial temperature profiles (left) and corresponding conversions of CO and CO₂ in the water cooled reactor Prototype 2 under methanation conditions using 17.15 NI/min of syngas through one reaction passage according to scenarios 1-3.

powder ($d_p=100-200 \mu\text{m}$) to intentionally block this slit. Accordingly, the conversion of CO_2 should also be slightly higher than indicated in all scenarios.

Scenario 2

The increase of water through the outer cooling inlet to 6 g/min leads to similar behavior as in the Prototype 1. First, the metal cap of the reactor begins to cool down followed by a temperature drop in the packed bed. To prevent a complete extinguishment of the reaction front, the temperature at Pos. 1 is stabilized to 430°C using the heating cartridge (Pos. 1). Despite a higher coolant amount, hot spot formation remains around 490°C . The temperature of the thermocouple in the packed bed is representative for the metal cap of the reactor showing an average temperature of approx. 431°C . Thus, transversal gradients over the packed bed and the cooling channels could be narrowed to 20-40 K.

The electrical power consumption is determined to 25 W, which corresponds to a thermal efficiency of the reactor of approx. 73%.

Scenario 3

Evidently, the reduction of the hot spot temperature according to Scenario 2 is not possible and an additional heat sink is required. In Scenario 3, 1.4 g/min of water are additionally pumped into the inner cooling inlet. As it can be seen, the temperature of the hot spot, measured in the metal at the symmetry axis, is barely affected. However, the temperature after the hot spot decreases by around 30 K compared to Scenario 2. Both observations lead to the conclusion that in the place of the highest reaction heat production (hot spot), the heat removal is not limited by the design of the cooling channels and the coolant amount. The same observations in the Prototype 1 substantiate that either the catalyst bed or the separating metal wall are the heat transport bottleneck of the system.

A further increase of the coolant through the inner passage is not considered valuable, since the temperature of the reactor metal top plate dropped to the average temperature of approx. 385°C . This increased the radial gradient over the bed and the cooling passage to around 60-100 K in the hot spot zone.

Regarding heat supply, the electrical power consumption increases to 125 W, which corresponds to a reactor efficiency of 57%. Compared to Scenario 2, it could be stated that additional water supply through the inner inlet in the metal cap led to additional strain for the heating element at Pos. 1. The comparison of the reactor performance (Fig. 5.16) reveals that CO conversion remains unaffected as it is limited by the bypass. The conversion of CO_2 is highest for Scenario 3, as the reactor outlet temperature is the lowest of all scenarios. The usage of both cooling passages improves the CO_2 conversion by 2 p.p. However, according to thermodynamic equilibrium improvement of 6 p.p. could be expected. The

difference is potentially governed by the transversal gradients in the packed bed. Further optimization of the autothermal operation, while distributing different amounts of water is not reported here because of the damaged second cooling side. A fully operational Prototype 2 could most probably perform better due to less contribution of heat.

5.6.1.1 On the temperature control under CO₂ methanation conditions

The temperature control is further studied under methanation conditions of CO₂ using a throughput of 19.7 NI/min through one slit (18.8% CO₂, H₂/C=3.6, N₂ as remainder, 6 bar, $m_{cat}=2.5$ g). Bypass flow of approx. 5% is expected based on the previous results. Temperature profiles are examined according to three scenarios: 1) Start-up with no cooling, 2) Cooling via inner inlet and 3) Cooling via inner and outer inlets. No external heating is required in all scenarios.

Scenario 1

After the reaction mixture is fed into the reactor, a temperature rise can be observed starting in the rear part of the reactor as described previously (see Fig. 5.17 on the left). The difference compared to methanation of CO/CO₂ mixture is that the temperature develops approx. 3-4 times slower. After approx. 30 min, the peak temperature reaches 475 °C in the center of the reactor.

Scenario 2

For cooling purposes, preheated water of 4.4 g/min to 80°C is introduced into the inner cooling inlet. During this time, the hot spot moves to the inlet. At Pos. 1 and 2, the temperature in the metal along the symmetry axis does not exceed 490°C. However, the thermocouple inserted in the packed bed (filled

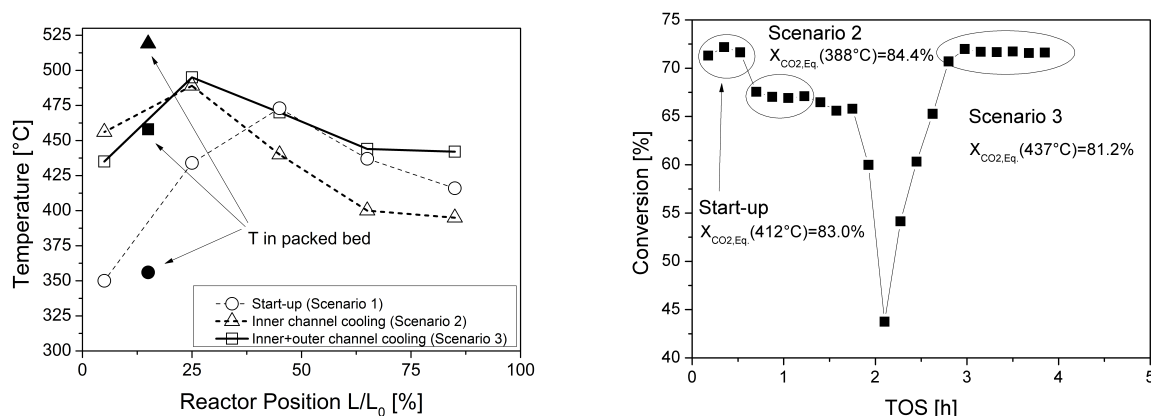


Figure 5.17: Temperature profiles in the reactor (left) and corresponding conversion of CO₂ in reactor Prototype 2 (right) under methanation conditions of CO₂ using throughput of 19.7 NI/min with 18.8% CO₂, H₂/C=3.6 and 6 bar.

trinagles in Fig. 5.17 on the left) shows temperature of 519°C. By the fact that the inner cooling channel provides heat removal beginning from Pos. 2, the hot spot position is clearly outside of the cooling zone. The temperature in the reactor top plate is around 360°C and barely changes in axial direction. The comparison with the temperatures obtained at the symmetry axis indicate transversal gradients in the packed bed and cooling channels of 100-160 K in the hot spot zone.

Scenario 3

Based on the temperature profile development in Scenario 2, it is reasonable to introduce water through the outer cooling inlet to control the hot spot in the catalyst bed. In Scenario 3, distribution of the water mass flow is 1 and 3.4 g/min for the outer and inner cooling inlets, respectively. As expected, the temperature at Pos. 1 is lowered. The hot spot shifts back to Pos. 2 and the hot spot temperature drops from 519 to around 495°C. The temperature at Pos. 3-5 (symmetry axis) is also higher by around 20-40 K. The mean temperature in the reactor top plate is 409°C.

The examination of the reactor performance shows that an improvement of around 5 p.p. in regard to CO₂ conversion could be achieved using both cooling channels. Higher temperatures at the reactor outlet help to increase the reaction rate and the thermodynamic influence is still negligible.

5.7 Summary

Prototype 1:

The characterization of the Prototype 1 concerns heat transfer behavior as pure heat exchanger and as polytropic reactor. It is found that the minimum reactor heat loss is around 30 W at 300°C and 50 W at 450°C when the reactor is submerged in Microtherm Freeflow-100X[®] insulation powder. Other insulation materials fail in regards to heat loss, so that the prototype cannot be investigated as a repetitive element of a larger reactor (upscaling by number). With increasing mass flow of air, steam and water more heat could be extracted from the reactor. Using gases, up to 500 W could be removed from the system at 450°C. In case of evaporation of water, the highest cooling potential is obtained, and up to 700 W could be removed at 450°C. The high exothermicity and reaction rate of the methanation and superior heat removal allow for a high reactor compactness leading to very fast reactor dynamics and heating up by reaction is possible in less than 5 min. Transversal temperature gradients in the catalyst bed are moderate and differed only from the reactor temperature during this start-up for less than 1 minute by up to 80 K. An excessive amount of coolant, however, leads to an extinguishment of the reaction front and subsequently, to a measurable conversion drop of CO₂. Using gases as coolants, strong sensitivity of the temperature at Pos. 1 is observed in dependence of the coolant flow which could be attributed to the co-flow operation of the reaction and the coolant. The hot spot of 420-440°C and 480-500°C at 15 and

23 NI/min of syngas, occurs close to the inlet which shows low dependence on the coolant flow. This is a strong indicator for heat transfer resistances in the reaction unit and is further analyzed using CFD in Chapter 6. Due to polytropic operation, full conversion of CO and over 95% of CO₂ can be achieved in one single step while generating superheated gas.

Steam generation from water cooling at the examined syngas flows requires temperature stabilization by the heating cartridges. Two cases are determined as feasible. In the first case, the highest temperature along the reactor is enforced at Pos. 1. This means strong overheating of the catalyst in the front part. In the second case, the temperature at Pos. 1 is kept at a minimum to prevent extinguishment of the reaction front. As a consequence, a hot spot of 415 and 460°C could occur at Pos. 2 for a syngas flow of 15 and 23 NI/min, respectively. The reactor achieves full conversion of CO and over 95% of CO₂ while generating superheated steam in both cases. The results show that, in micro structures, temperature control becomes difficult when the cooling potential impacts at the wrong axial position. As in the case of Prototype 1, heat transfer resistances, either in the metal or in the packed bed, limit the system. From an energetic point of view, the usage of heating elements lowers the thermal efficiency of the reactor. On the process level, however, certain flexibility regarding heat supply of the reactor and operation mode can be gained.

Prototype 2:

The Prototype 2 is a result of the improvement of Prototype 1, which is laid in a patent application. It is tested under methanation conditions using CO/CO₂ mixtures as feed. By feeding water through the outer cooling inlet, the reactor behaves similarly to Prototype 1. This includes the hot spot formation at the inlet of around 495°C and extinguishment of the reaction at higher water mass flows through the cooling passages. As a consequence, stabilization of the reactor using heating cartridges would be necessary with high water flow. By additionally feeding water to the inner cooling inlet, the hot spot is barely affected. Thermal resistances either in the metal or bed govern the heat transport. However, temperature in the outlet part of the reactor could be affected with success, leading to a full conversion of CO and better conversion of CO₂ compared to only cooling with feed of water to the inlet. Furthermore, under low water mass flow the Prototype 2 could be operated in autothermal mode.

Under methanation conditions converting pure CO₂/H₂ mixture, it is shown that the hot spot position could be influenced by adjusting the coolant flows through the inner and outer cooling channels. Although, the hot spot temperature could not be decreased considerably, up to 5 p.p. more CO₂ is converted by distributing the cooling potential.

Due to a fabrication error, the Prototype 2 in this work could not be operated symmetrically (only 1 reaction slit). Thus, only information about the reactor dynamics and possible heat transport limitations

could be gathered. It may be that a fully operational prototype could even perform better with regards to hot spot control and autothermal operation. An indication for this is the successful scale-up in industrial application during the defense of this thesis [154].

6 CFD analysis of the microstructured prototype

A CFD analysis of the manufactured reactor Prototype 1 is presented in the following. The chapter starts with the examination of the cooling zone, the fluid distribution quality and the influence of fins on the heat transfer capability. The reaction zone is examined regarding bed heat conductivity and hot spot formation under different cooling flow rates for identification of the observed heat transport bottleneck. Finally, the entire methanation system is simulated using the kinetic rate models from literature and the results are compared to experimental data.

6.1 Motivation

The CFD analysis is a powerful tool for examining highly complex systems including (reacting) flows, heat and mass transfer. This approach is very promising for the analysis of microstructured devices, since the intensification of processes is often based on a sophisticated reactor geometry and cannot be reflected using one-dimensional models. In addition, the CFD method allows the examination of local quantities like temperature, pressure or gas velocity which are inaccessible experimentally for several reasons. Hypothetical variation of the geometry and physical properties allows for further development of devices.

CFD is successfully used in the literature for analysis of microstructured heat exchangers [155] and reactor modules [156; 157; 158; 159; 160]. However, CFD studies on the packed bed microreactor and especially for methanation are scarce.

The goal of this chapter is a more nuanced understanding of the heat transport and fluid flow phenomena in the manufactured device according to Prototype 1. A separate examination of the cooling and reaction zones is conducted. On the cooling zone, the attention is paid to maldistribution of the fluid in microstructures, since it could potentially become a problem in such devices (see Chapter 3). Hypothetical variation of the geometry on the cooling side, the heat removal is examined. The analysis of the reaction zone is highly relevant due to complexity of the packed bed itself. Porosity and heat conductivity distribution could result in poor thermal properties of the packed bed which require attention under extreme heat release in the catalyst packing. The most important aspect is to determine the thermal bottleneck which results in hot spot formation under experimental conditions, being barely affected by the coolant flow rate (see Chapter 5). The insights are expected to provide valuable information for a further scale-up and optimization of the device.

6.2 Methodology

Simulation soft- and hardware

For CFD analysis, Ansys® V. 15 is used. The geometry and mesh is created with Design Modeler® and the Workbench Mesher®, respectively. The CFD calculations are performed with Fluent® running on an AMD XEON 8 core, each 3 GHz, and 24 GB of RAM.

Definitions and used correlations

In this work, the hydraulic diameter is used as a representative length for the rectangular channel geometry; it is defined according to Eq. 6.1.

$$d_h = \frac{4A}{P} \quad (6.1)$$

Where, A is the cross-sectional area and P is the wetted perimeter. For flow and heat transfer analysis, the non-dimensional Reynolds and Nusselt numbers are used according to definitions in Eq. 6.2 and 6.3.

$$Re = \frac{u \cdot d_h}{\nu} \quad (6.2)$$

$$Nu = \frac{\alpha \cdot d_h}{\lambda_f} \quad (6.3)$$

Here, u is the gas velocity [m/s], ν is the kinematic viscosity [m²/s], α is the heat transfer coefficient [W/(m²K)], and λ_f is the heat conductivity of the fluid [W/(mK)].

For the analysis of the hot spot formation in the packed bed, the porosity function by Giese et al. [161] is applied (Eq. 6.4).

$$\varepsilon(r) = \varepsilon_0 \left(1 + 1.36 \cdot \exp\left(-5 \cdot \frac{R-r}{d_p}\right) \right) \quad (6.4)$$

Here, ε_0 is the bulk porosity [-], r the tube radius [m], and d_p the particle diameter [m]. Due to rectangular channels in the presented device, the tube diameter is replaced by the hydraulic diameter. The implementation of the porosity function is done by a User Defined Function (UDF) which is hooked into the Porous Body® model describing the packed bed. The built-in function of the Porous Body® model calculates the heat conductivity of the packed bed by weighing the single heat conductivity values of the fluid (λ_f) and solid (λ_s) according to Eq. 6.5.

$$\lambda_{PB} = \varepsilon\lambda_f + (1 - \varepsilon)\lambda_s \quad (6.5)$$

It should be noted that the physically relevant heat conductivities of fluid and solid lead to a considerable overestimation of the packed bed heat conductivity λ_{PB} . Therefore, the Λ_r -model given by Winterberg et al. [162] (see Chapter 7.2) is used as reference.

Material properties

Heat capacity and heat conductivity of all gases are implemented in Fluent[®] as piece-wise linear functions with 6 points from 20 to 700°C. The required fluid data are taken from VDI [148]. Physical and thermal properties for the prototype material NICROFER[®] are obtained from the Wiam[®] Metallinfo database.

6.3 Results

The obtained results are discussed in the following.

6.3.1 Geometry and mesh generation

The abstracted geometry of the reactor model is shown in Fig. 6.1 on the left. Compared to the manufactured device, areas with curvature are approximated with rectangular structures to reduce the complexity of the model and to simplify the meshing procedure. This mainly concerns the outer flanges area, holes for the heating elements and the inlet piping. The dimensions of the cooling inlet zone, including redirection of the fluid areas and the geometry of the cooling/reaction channels, are kept as in the manufactured device.

The procedure for generating the model is based upon the creation of the desired amount of cooling channels and extrusion of their surfaces to volumes. In the meshing step, the sweeping method is applied to generate the structured mesh on the entire geometry. The amount of cells is controlled via the sizing function with a predefined amount of cells per edge. Each single cooling channel ($500 \times 500 \mu\text{m}$ in height \times width) is resolved with 6 cells in height and width with a cell height of around $60 \mu\text{m}$ close to the wall (non-equidistant spacing, see also Fig. 6.1 on the right). The separating metal wall and the reaction channel are resolved with 6 and 12 cells in height applying the sizing function as in the case of the cooling channels. It is found that in the laminar range, the results regarding flow characteristics and the conjugate heat transfer are almost mesh independent, which is the case for most microstructured devices (see also Chapter 7.2). Hence, rougher resolution than applied could be possible. The final mesh is created for one quarter of the reactor exploiting the symmetry of the device; 7.053 million cells are generated for the model in total.

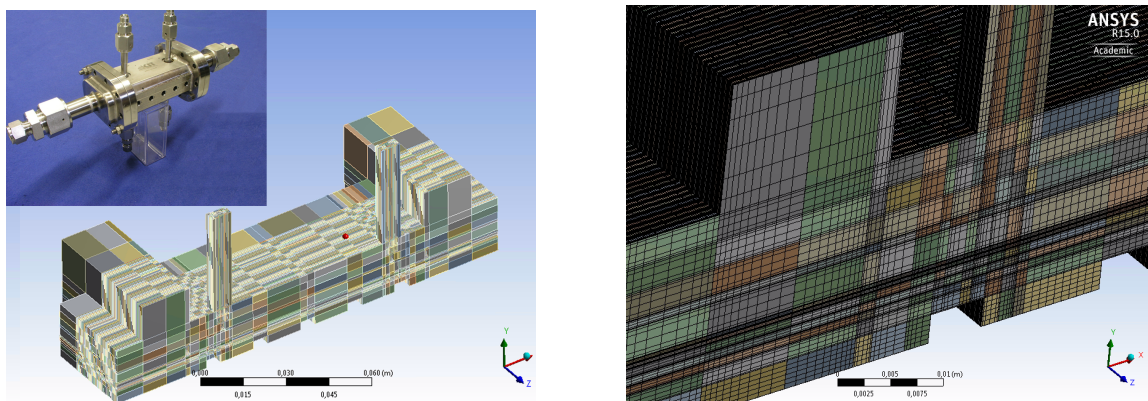


Figure 6.1: CAD-geometry (left) and generated mesh (right) for the CFD study based on specifications of the Prototype 1.

6.3.2 Validation of the model - Conjugate heat transfer

The validation of the reactor model is based on the experimental heat transfer studies. Heating elements are simulated by setting the surface interface at appropriate positions to a desired temperature. The domain of the cooling zone is assigned the heat transfer medium air. The reaction slit domain is assigned nitrogen as in the experiments. Fig. 6.2 shows the experimentally and numerically calculated heat amounts, removed by the cooling fluid air as a function of the volumetric flow of 60, 80 and 100 NI/min. The surface temperature of the heating elements interface at Pos. 1-5 is set to 300 or 450°C. Generally, the extracted heat in the experiments slightly depends on the coolant flow. The evaluation of the conventional Nu correlation at a constant wall temperature [163] shows flow independency in the examined Re range. Due to laminar conditions a constant Nu number of 3.7 is derived. The dominant driving force for heat transfer could be attributed to the temperature difference between the reactor wall and the cooling fluid, which is supported by experimental observations. The heat transfer coefficient calculated from the standard Nusselt correlation ($T=\text{const.}$) for air is approx. 300 and 400 W/(m²K) at the temperature of 300 and 450°C, respectively. The difference is a result of temperature dependence of the heat conductivity of air. Regardless of the fact that an adiabatic boundary condition is assumed in the simulation, excellent agreement with experiments can be observed in Fig. 6.2. The relative error is below 5%.

The accuracy of the obtained results is double-checked in terms of temperature distribution in the reactor housing. Fig. 6.3 on the left shows the simulated temperature profiles of the reactor in the heat transfer experiment using 80 NI/min air flow, with the inlet temperature of 110°C, while keeping the heating elements at 450°C. Thermocouples at positions denoted with T1-T11 are used to collect the experimental data and their temperature values are compared to CFD results in Fig. 6.3 on the right. The calculated temperature distribution shows that the system exhibits strong axial and transversal temperature gradi-

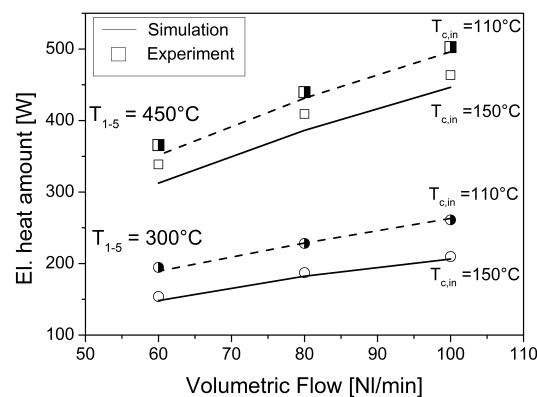


Figure 6.2: Comparison of the experimentally and numerically calculated heat amount at different flow rates of the coolant air ($T_{c,in}=110$ and 150°C) while keeping the heating cartridges (Pos. 1-5) at constant surface temperature of 300 and 450°C .

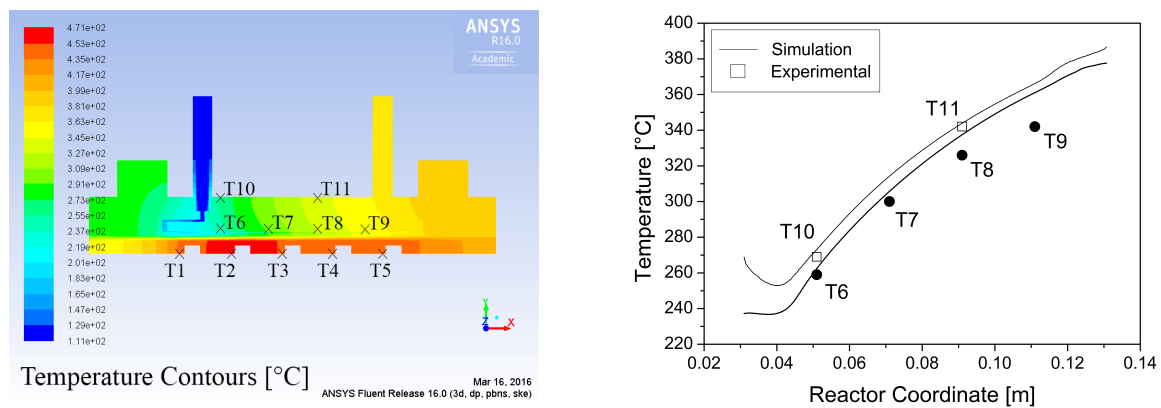


Figure 6.3: Calculated temperature distribution in the reactor Prototype 1 (left) and the comparison of the experimental and calculated results at T6-T11 (right) while keeping the heating cartridges at 450°C and flushing the cooling zone with 80 NI/min air ($T_{c,in}=110^{\circ}\text{C}$).

ents. As expected, the cooling potential is concentrated in the front part of the reactor, where, according to experimental results, the most of the reaction heat is generated. Due to co-flow and a subsequent temperature increase of the cooling fluid, less heat is removed in axial direction, which could lead to hot spot at reaction conditions. The comparison of the CFD results with experimental results is completely in agreement along the cooling channel (T6-T9) and on the reactor surface (T10-T11).

The reactor validation study can be condensed to several important findings:

- The proper reflection of the temperature distribution in the entire device is a result of the precise description of the conjugate heat and mass transport implemented in Fluent®.
- The simplifications regarding reactor geometry, e.g. substitute of curvature elements with blocks are plausible.
- The boundary conditions are posed correctly, including the adiabatic condition at the reactor surface. The insulation powder in the experiments allows the assumption of the adiabatic system.

6.3.3 CFD analysis of the cooling zone

The cooling zone is complex regarding fluid flow and geometry, which is discussed in the following.

6.3.3.1 Flow distribution

The flow distribution of the coolant in the manufactured device is based on the branching approach similar to the idea proposed by Amador et al. [164]. Fig. 6.4 on the left illustrates the pathways of the fluid through the microstructured cooling zone at 60 NI/min of air. The fluid is fed through the inlet pipe, which is orthogonal to the cooling channels. The flow is distributed in a first array of channels,

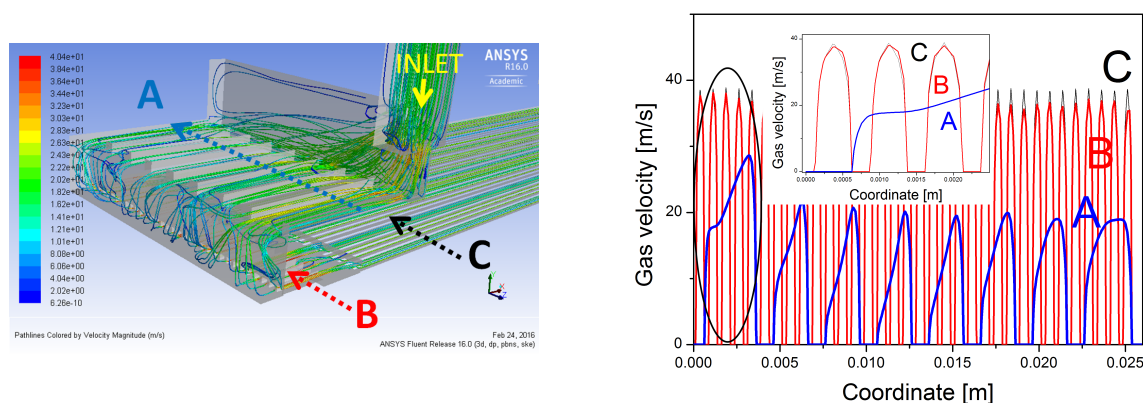


Figure 6.4: Pathlines of air colored by velocity magnitude in the microstructured cooling zone at the total air flowrate of 60 NI/min (NTP) (left) and according velocity profiles in the channels along the lines A, B and C (right).

which is in direct alignment to the reaction zone. The quality of the fluid distribution is visualized in terms of velocity profiles in the microstructured channel arrays along the line A, B and C in Fig. 6.4 on the right. Apparently, the first array of channels (line A) provides a rough distribution of the fluid with non-uniformity of the gas velocity along the line A exhibiting up to 30% higher gas velocity close to the symmetry axis (0.0 m). The triangular shape of the velocity profile in the single channels is caused by the radial momentum. Thus, design concepts including fluid distributors with a single redirection could suffer from fluid maldistribution being worsened with temperature gradients. According to the simulation, the fluid is perfectly distributed after the second and third redirection (line B and C), showing a parabolic velocity profile in each channel. Despite high gas velocities of 40-65 m/s (60 and 100 NI/min in total), laminar flow regime with Re numbers between 900-1500 prevails. According to the simulation, the pressure drop is relatively low with around 80-300 mbar at 60 and 100 NI/min, respectively (p_{out} ambient).

6.3.3.2 Influence of fins on heat transfer capability

The enhancement of the surface area in microstructured devices is realized by surface textures like pins or fins. The effect of fins on the heat transfer is therefore studied by modifying the geometry of the cooling zone. The analysis is performed using heat transfer oil instead of air for two main reasons. First, the usage of air is not considered an option for cooling of the methanation unit with high syngas throughput due to the low specific heat capacity. Second, the application of thermal oil offers high heat transfer coefficients in the order of 1500 W/(m²K), serving as reference for evaporation cooling.

The presence/absence of fins has a direct impact on the fluid velocity as exemplarily shown for both systems at the total mass flow rate of 0.12 kg/s in in Fig. 6.5 on the left. In absence of fins, a uniform velocity profile is calculated in the entire cooling passage with a variation of 2.8-3 m/s. In case of fins,

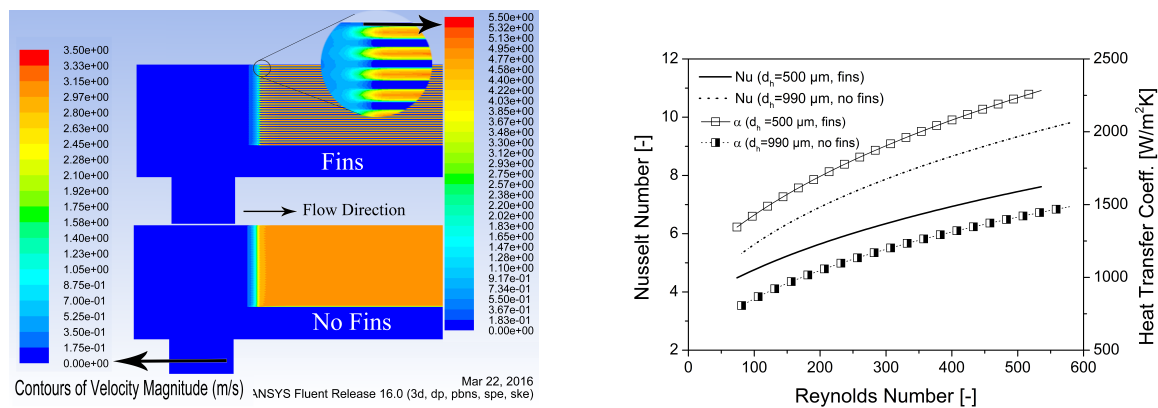


Figure 6.5: Velocity profiles in the cooling channels of reactor Prototype 1 in presence and absence of fins at a total oil mass flow of 0.12 kg/s (left) and according Nusselt number ($Pr=45=const.$) and heat transfer coefficient as a function of Re (right).

the fluid velocity is 30% higher due to the change of the cross section area. A parabolic velocity profile in each channel is present. Compared to air, a significant improvement of the Nu number, see Fig. 6.5 on the right, could be obtained at higher Re numbers even at low velocities less than 5 m/s. This is due to the long hydrodynamic run-up length influenced by the high Pr number (45). The system without fins ($d_n=990 \mu\text{m}$) leads to Nu numbers between 5 and 10, whereas 4-8 is obtained with fins ($d_n=500 \mu\text{m}$). The corresponding heat transfer coefficients are relatively high and range between 800-1500 and 1300-2300 $\text{W}/(\text{m}^2\text{K})$, accordingly.

Independent of the fact that the system with fins is advantageous with regards to the heat transfer coefficient, it still encounters limitations which are discussed in the following. The upper wall of the reaction slit is set to a constant temperature of 300 and 450°C in a simulation. The heat flux passes through the separation wall of 1 mm thickness and is removed by the coolant. Fig. 6.6 on the left shows the benefit of the fins computed by normalizing the transferred amount of heat to the value obtained in absence of fins as a function of the oil mass flow at temperatures of 300 and 450°C. Since both systems showed different Reynolds numbers, the Re numbers for the system with fins is provided in the graph. The number at each data point is the total transferred heat amount at the particular temperature. The improved heat transfer, caused by fins at lower Reynolds numbers less than 70, is relatively low with less than 10 p.p.. This is due to large residence times which consequently lead to a quick heat-up of the coolant to the pre-defined wall temperature. The benefit of the fins is more evident at Reynolds numbers larger than 100 and leads to improvement of the total heat transfer by up to 25 p.p.. A further increase of thermal oil mass flow beyond $Re>280$ yields no further improvement. In contrast to the operation at low Re numbers, where the fluid adapts the surface temperature due to the long residence time, the system is likely limited by heat transfer through the separating wall. The extent of the heat transfer limitation is exemplarily presented in Fig. 6.6 on the right on the basis of the temperature distribution in the cooling zone at $z/L=5\%$

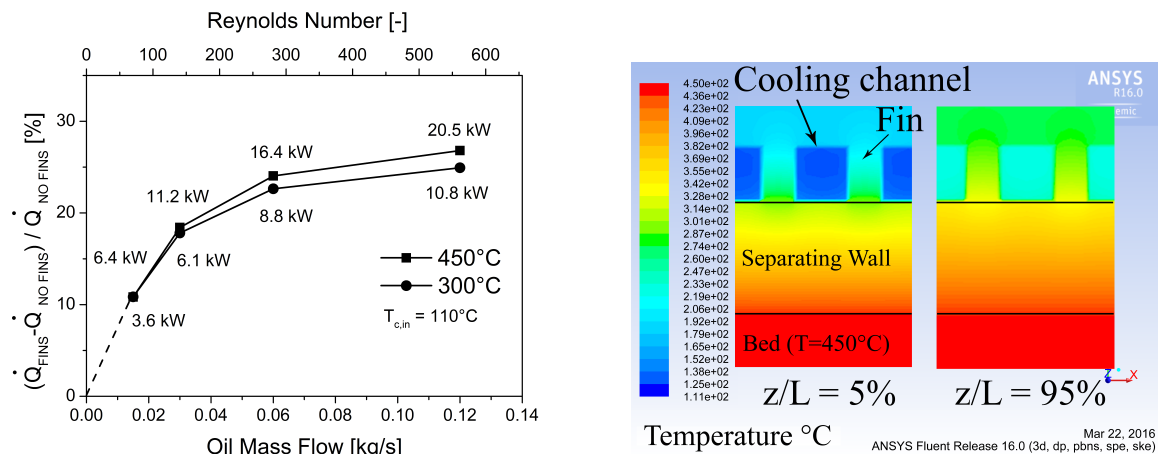


Figure 6.6: Improvement of the total transferred heat in the Prototype 1 with fins at different temperatures and oil mass flows (left), and temperature distribution in a transversal cross-section of the reactor at 5% and 95% of the reaction zone length (0.12 kg/s) (right).

(corresponds to Pos. 1) and at the end ($z/L=95\%$, Pos. 5) at the Reynolds number of 535 (0.12 kg/s) for the system with fins. At $z/L=5\%$, a large temperature gradient of around 120 K is caused in the 1 mm thick separating metal wall despite a quite good heat conductivity of approx. 18 W/(mK). The temperature at the bottom of the fin is around 290°C and at the top 200°C, which is a temperature gradient of 90 K per 500 μm length. At the outlet of the cooling zone ($z/L=95\%$), the temperature gradient in the separating wall decreases to 100 K due to axial heat exchange. Thermal resistances in the thermal oil can be neglected, since no considerable temperature gradients are apparent.

6.3.4 CFD analysis of the reaction zone

The reaction zone is represented by a catalytic packed bed and is highly complex in nature (see Chapter 7.2). The dependency between porosity, heat conductivity and heat release on the hot spot formation is discussed and the potential of the reactor design is highlighted.

6.3.4.1 Influence of the packed bed heat conductivity on the hot spot formation

Since packed beds exhibit a transversal porosity and consequently a heat conductivity function, it is of interest to examine their impact on the hot spot formation in the reactor slits.

The implementation of the heat conductivity function according to Λ_R -model would be desired. However, due to the complexity and restricted modification possibilities in the used commercial software, a built-in function for the heat conductivity has to be used in order to investigate the impact of the local packed bed heat conductivity on the hot spot formation. Both models are compared to their applicability. In Fig. 6.7 on the left, at reaction conditions similar to the experimental ($T=300^\circ\text{C}$, $d_p=350 \mu\text{m}$, $d_t=2$

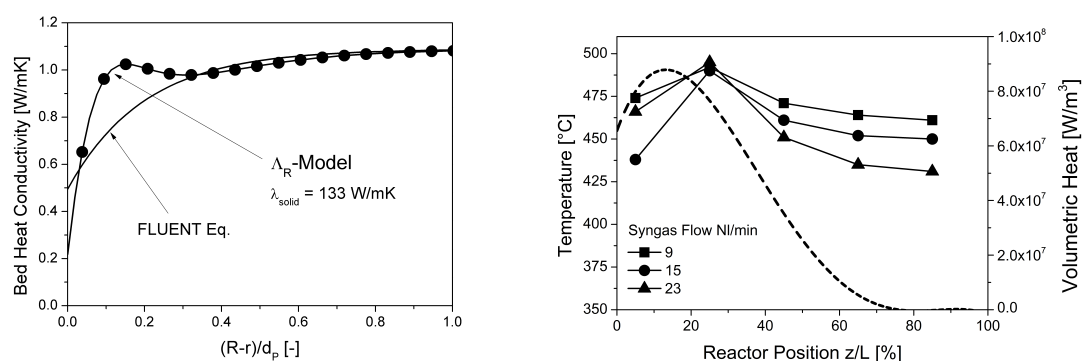


Figure 6.7: Radial heat conductivity distribution according to Λ_R -model ($d_t=2$ mm, $d_p=350$ μ m, $\epsilon_0=0.3$, $Re_p=13$, $T=300^\circ\text{C}$) and of adapted Eq. 6.5 (Fluent[®] built-in function) for the solid heat conductivity of the catalyst particles (left, abscissa range from 0 to 2.86 is confined to 0-1 to better visualize the near-wall behavior) and the profile of the designed heat source function (dashed line, only axial dependence) used to describe experimental temperature profiles (right).

mm, $V_{syn.}=23$ NL/min, $p=6$ bar), the Λ_R -model by Winterberg et al. [162] is evaluated exemplarily for the heat conductivity of SiC, which takes around 82 vol.% of the packed bed in the microreactor. It yields a nearly constant λ value in the particle-particle bulk which drops to the heat conductivity value of the gas phase due to increasing porosity near the wall. The usage of highly heat conductive particles (SiC, 133 W/(mK) at 300°C [165]) corresponds to a bulk heat conductivity of approx. 1.1 W/(mK).

Due to the extreme overestimation of the effective packed bed conductivity in the built-in function in Fluent[®] the λ_s in Fluent[®] has been adapted to match the bulk heat conductivity of the Λ_R -model. The resulting bulk heat conductivity and the trend towards the wall is therefore reflected sufficiently (see Fig. 6.7 on the left). Since the effect of the fluid flow is neglected in Fluent[®], the λ values close to the wall region are underestimated. Thus, the model is the worst-case scenario (stagnant conditions). At the wall, the heat conductivity of the adapted Fluent[®] model could not exactly match the gas phase value (0.07 W/(mK)), which is attributed to mathematical nature of the equation. However, this issue is less critical due to the discretization error of the packed bed. Summarized, the adapted built-in function in Fluent[®] could be applied to determine the heat transfer resistances.

With regards to investigate the heat transport resistance in the catalytic packed bed along the reactor axis, the heat generation due to reaction heat is required. Besides the implementation of the kinetic models from the literature (see Chapter 2.3), the tailored heat source mimicking the reaction heat release is advantageous. No additional transport and energy equations need to be solved for reactants, which allows for faster computation. Such approach also eliminates possible dynamic processes, e.g. extinguishment of the reaction front observed experimentally. The axial heat distribution of the heat source is shown in Fig. 6.7 on the right and the design procedure is briefly explained in the following. Based on the experimental temperature profiles, a polynomial function of 4th order is selected and

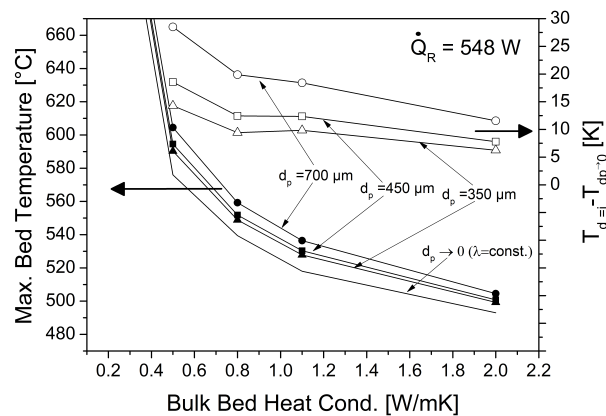


Figure 6.8: Hot spot temperature and packed bed overheating as a function of the bulk heat conductivity and particle size while releasing around 548 W in the packed bed and air cooling the reactor with 80 NI/min ($T_{c,in}=150^{\circ}\text{C}$).

hooked into the reaction zone as heat source via a UDF. The integral value of the heat source function is adjusted to the heat amount according to the heat release in experiments. Since there is no obvious relation between the hot spot position and the syngas throughput (see Fig. 6.7), the designed heat source could approximate experimental temperature profiles by varying a prefactor, only governing the integral heat release.

The adapted built-in function of Fluent[®] describing the transversal heat conductivity and the designed heat source allows the analysis of the thermal aspects of the packed bed on the hot spot formation along the bed length. Fig. 6.8 shows the maximum packed bed temperature resulting from heat release (artificial heat source) as a function of the bulk heat conductivity and particle size. The assumed heat of 548 W, which corresponds to a methanation in reactor Prototype 1 with a syngas throughput of 23 NI/min, is removed with air of 80 NI/min ($T_{c,in}=150^{\circ}\text{C}$ in the simulation). The hot spot temperature at constant packed bed heat conductivity (no transversal distribution) is plotted as a reference.

In general, the hot spot temperature shows an exponential character regarding bulk heat conductivity. Its sensitivity increases at values below 0.6 W/(mK), whereas only a slight hot spot temperature change is obtained at $\lambda_{Bulk} > 0.6$. The examination of temperature profiles in the reactor reveals that, at lower bulk heat conductivities, the packed bed overheats considerably and represents the limiting factor in the overall heat transfer. With increasing λ_{Bulk} , the dominant heat transfer limitation shifts to the cooling side due to the low heat transfer coefficient $< 400 \text{ W}/(\text{m}^2\text{K})$ applying air as coolant.

The calculation also shows the overheating of the packed bed with increasing particle size, which is attributed to the decline of the heat conductivity at the wall (second ordinate in Fig. 6.8). The extent is a slight function of the bulk value λ_{Bulk} . The overheating is less than 20 K for $\lambda_{Bulk} > 0.4$ and a particle size of 450 μm .

From these results, several conclusions regarding design aspects & operation of the reactor unit and

packed bed could be given:

- The heat transfer coefficient of cooling gas becomes the limiting factor at $\lambda_{Bulk} > 0.6$, which means that the total cooling potential of the microstructured methanation unit cannot be reached using air as a coolant.
- The overheating of the packed bed due to particle size can be neglected if 20 K difference at $\lambda_{Bulk} > 0.6$ is tolerated in industrial application. This is in-line with the experiment.
- The application of small particles will not improve the bulk heat conductivity and is only slightly dependent on the solid heat conductivity. Small particles would only increase the pressure drop.
- Improvement of the bulk heat conductivity using, e.g. highly conductive metal foams becomes irrelevant in air cooled devices, since the heat removal is governed by the heat transfer on the cooling side.

6.3.4.2 Determination of the effective packed bed heat conductivity by comparing CFD simulation and reaction experiments

One of the most critical and important parameters for the heat transfer assessment in the packed bed is the effective packed bed heat conductivity value. It is dependent on many parameters which are hardly accessible experimentally and theoretically. In the following, results from the determination of the effective heat conductivity of the packed bed by comparison of CFD simulation and reaction experiments are provided. For a broad validity, several reaction experiments were consulted at different syngas throughputs with different heat release amounts. The reaction heat release in the simulation

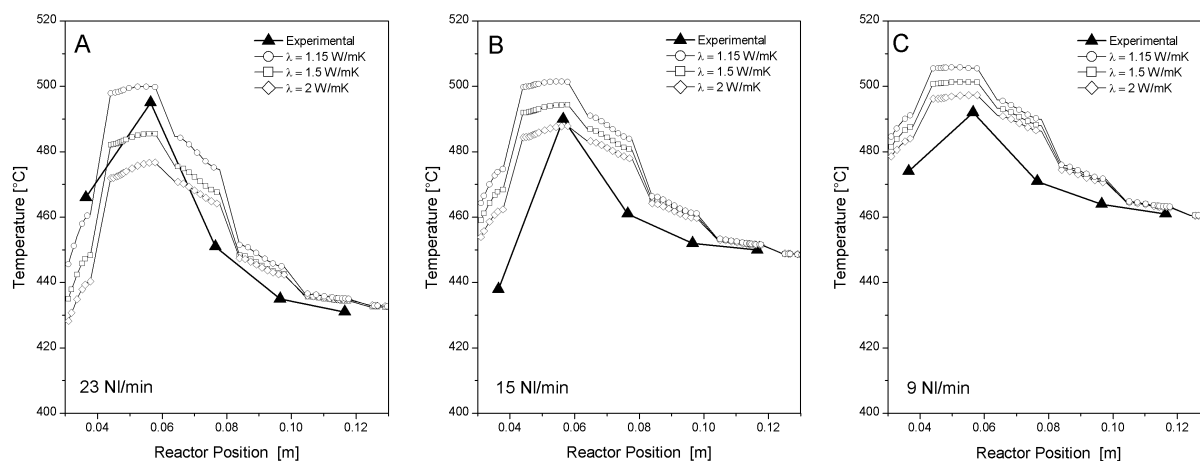


Figure 6.9: Approximation of the experimental temperature profiles under methanation conditions using 23 (A), 15 (B) and 9 (C) NI/min of syngas applying the artificial heat source and different packed heat conductivities.

is calculated according to the artificial heat source (see Chapter 6.3.4.1). The heat conductivity of the porous packed bed (λ_{PB}) is assumed as transversally constant ($\epsilon=\text{const.}$) and is varied until the experimental and simulated temperature profiles match. Fig. 6.9 A-C shows measured T-profiles under methanation conditions of 23, 15 and 9 NI/min (reaction heat 565, 356 and 211 W) of syngas compared to the calculated temperature distribution using different packed bed heat conductivities. The results show that the polynomial heat source function mimics the axial reaction heat release well and the resulting temperature profiles are in good agreement with all experimental observations. This is apparent from the properly calculated hot spot position and the temperature drop due to heat exchange in axial direction. The variation of the λ_{PB} results in an offset of the profile by keeping the original shape. As can be seen, the most accurate representation of the experimental result is achieved by using the heat conductivities between 1.15 and 1.5 W/(mK) for the syngas flow of 23 NI/min. The validity of the determined λ_{PB} is checked by repeating the simulation with lower heat generation rates, which correspond to 15 and 9 NI/min of syngas using air as coolant with 45 ($T_{c,in}=168^{\circ}\text{C}$) and 24 NI/min ($T_{c,in}=170^{\circ}\text{C}$) of total flow (Fig. 6.9 B and C). Also in this case, the computed temperature profiles fit to the experimental results. A slight overheating of 10-20 K is calculated in the front part of the reactor and approx. 13 K at the hot spot using λ_{PB} of 1.15 W/(mK) in both cases.

One should note that this method is very simplistic, yet allows for rough estimation of λ_{PB} , which is a key parameter in the packed bed reactor system. All relevant aspects of the packed bed and of the reactor are taken into account. By comparing the obtained packed bed heat conductivity of 1.15 W/(mK) with thermal properties of common materials on catalysis from the literature, it turns out that the high amount of silicon carbide (82 vol.%) governs the packed bed heat conductivity in the experiments following the relation $\lambda_{SiC} = 611/(T-115)*1E2$ [W/(mK)] [165].

6.3.4.3 Identification of the heat transfer bottleneck

The idea behind the presented reactor prototype is the upscale by multiplication of the structure and industrialization of the application which requires evaporation of water for feeding the SOEC. As presented in Chapter 5, both reactor prototypes possess some heat transfer limitations leading to a hot spot. By overcoming such limitations, the performance of future devices could be extended on the catalyst, reactor and process levels.

In this computer experiment, the heat transfer limitations are assessed in the 3D CFD model by variation of the coolant throughput and the heat conductivity of the packed bed and metal housing domain. The artificial heat source is used as the reaction heat substitute with 336 W and 1 kW in total. The already estimated packed bed heat conductivity is applied where necessary.

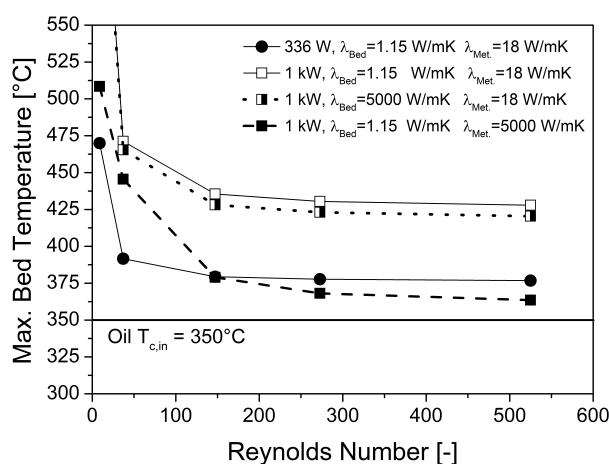


Figure 6.10: Maximum packed bed temperature in the oil-cooled reactor Prototype 1 ($T_{c,in}=350^{\circ}\text{C}$) at varied heat conductivities of the packed bed and metal.

The thermal oil throughput variation is used to reveal possible heat transfer limitations on the cooling side. Due to the high heat transfer coefficients in the range of $2500 \text{ W}/(\text{m}^2\text{K})$, the heat removal potential of thermal oil is comparable to that of water evaporation. The inlet temperature of the coolant is set to 350°C to counteract the extinguishment of the reaction as was observed experimentally. The variation of the heat conductivity of the construction material accounts for thermal resistances in the reactor geometry. And by changing the heat conductivity of the packed bed, the possible heat transfer issues could be exposed.

Three cases are considered to identify the thermal bottleneck of the system:

Scenario 1:

This scenario represents the “realistic case”. The heat conductivities of the metal bulk and the packed bed are set to approx. 18 (piece-wise linear, T-dependent) and $1.15 \text{ W}/(\text{mK})$, respectively. The generated heat is varied between 336 W and 1 kW. The resulting maximum temperature in the packed bed is shown as a function of Reynolds numbers in Fig. 6.10. Two regions dominate the system. At lower Reynolds numbers, the heat removal is insufficient due to the coolant flow heat capacity leading to a hot spot. With increasing Reynolds numbers, the packed bed temperature becomes coolant flow independent. An isothermal operation of the reactor, even at low reaction heat release of 336 W and a maximum Reynolds number of 550 is not possible; an overheating in the packed bed of 25 K occurs.

As expected, the increase of the heat production from 336 W to 1 kW results in a higher packed bed overheating of approx. 77 K. This fact could be already considered as a lack of temperature control.

Scenario 2:

This scenario represents a hypothetical case where the possible heat transfer resistance in the packed bed is eliminated by setting the heat conductivity to 5000 W/(mK). The heat conductivity of the metal housing is kept to approx. 18 W/(mK). The comparison of the maximum packed bed temperature at 1 kW reaction heat reveals no significant difference in the entire Reynolds range compared to Scenario 1. Based on this, the packed bed heat conductivity in the range of 1.15 W/(mK) does not seem to be the bottleneck of the system regarding heat transfer.

Scenario 3:

The elimination of the heat transfer resistance in the metal and separating wall is realized in Scenario 3 by increasing the metal heat conductivity to 5000 W/(mK), while maintaining the packed bed heat conductivity of 1.15 W/(mK). At higher Reynolds numbers, a convergence of the hot spot temperature towards the inlet coolant seems to be possible. Thus, the occurrence of the hot spot may dominantly be attributed to the metal separating wall (1 mm thickness) and reactor material. This finding is in-line with the reaction experiments in Chapter 5, which reveal that the extent of the hot spot formation is barely affected by the choice of the heat transfer medium or its throughput. Consequently, the improvement of the device is potentially a geometry modification with regards to the thickness of the separating wall. However, mechanical stability at higher temperatures and elevated pressures should be taken into account.

6.3.4.4 Simulation of the reactor using CFD with kinetic reaction models

The simulation of the reactor Prototype 1 is attempted by using the kinetic model given by Xu and Froment [67]. The CFD reactor simulation using the kinetic model by Kopyscinski et al. [58] is not presented here, since extinguishment of the reaction front is calculated in all cases.

The comparison is made to methanation experiments with 23 NI/min of syngas (10.3% CO, 7.2% CO₂, 72.2% H₂, rest N₂) while applying air cooling with 90 NI/min ($T_{c,in}=150^{\circ}\text{C}$). To improve the accuracy of the numerical model, the heat loss to environment is set to 66 W (in total), as determined in the experiments. The heat conductivity of the packed bed is set to 1.15 W/(mK). Further relevant parameters are summarized in Tab. 6.1.

The first general observation is that the reaction rate of methanation is very fast, which leads to a hot spot directly at the packed bed inlet. This finding contradicts the experimental result, where the hot spot arises around 1-2 cm further away from the inlet. Since the modification of the kinetic rate is undesired to maintain consistency with Chapter 2.3.2, the consensus of the CFD simulation with the experimental

Table 6.1: Summary of important material properties, parameters and boundary conditions required for evaluation of the reactor simulation via CFD.

Name	Variable	Value	SI Unit	Additional Information
Porous Body				
Porosity	ϵ	0.3	-	physical velocity, equilibrium
Viscous resistance	-	7e9	1/m ²	
Gas/Solid properties				
Heat conductivity gas mixture	λ_{gas}	0.07	W/(mK)	no temperature dependence
Specific heat capacity of component i	$C_{p,i}$	piecewise linear	J/(kgK)	VDI [148]
Heat conductivity of solid bed material	λ_{solid}	1.6	W/(mK)	no temperature dependence
Heat conductivity of reactor steel	λ_{metal}	piecewise linear	W/(mK)	11.5 (@293 K) - 22.8 (@973 K)
Specific heat capacity of reactor steel	$C_{p,metal}$	piecewise linear	J/(kgK)	472 (@293 K) - 551 (@973 K)
Reaction conditions				
Inlet mass flow of reactants	$\dot{m}_{R,in}$	1.6269e-04	kg/s	in total
Molar fraction CO; CO ₂ ; H ₂ ; N ₂	x_i	10.3; 7.2; 72.2; rest N ₂	%	
Reactants inlet temperature	$T_{R,in}$	295	°C	
Reactor pressure (absolute)	p	6	bar	
Catalyst mass	$m_{Cat.}$	5e-3	kg	particle size 400-500 μ m
Diluent mass (Silicon carbide)	m_{SiC}	22e-3	kg	particle size 300-400 μ m
Inlet mass flow of cooling air	$\dot{m}_{C,in}$	1.7758e-3	kg/s	in total, near ambient pressure

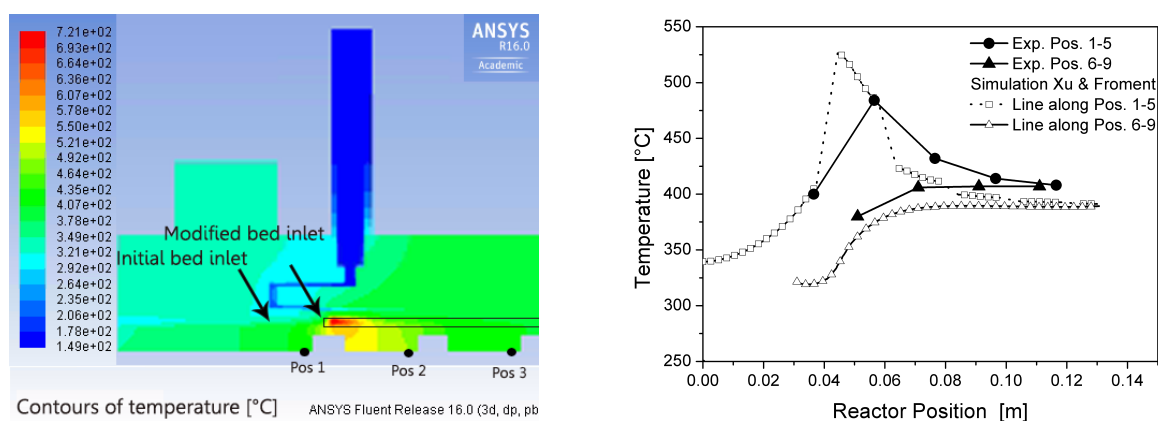


Figure 6.11: CFD temperature contours in the reactor (left) and temperature distribution along the symmetry axis (CFD vs. experiment, Pos. 1-5) (right) at the axial reaction zone offset of 1 cm.

result is attempted by accounting for deactivation of the catalyst or packed bed movement under flow conditions. For this reason, the reaction zone in the packed bed is shifted 1 cm towards the reactor mid axially (see Fig. 6.11 on the left) to match experimentally observed temperature profiles. This assumption may be valid, since the reactor has been in operation for several days already and deactivation occurs as shown in in Chapter 4, at all temperatures and syngas compositions.

The calculated temperature profiles along the symmetry axis (Pos. 1-5) in the reactor and in the metal top plate (Pos. 6-9) are compared to experimental results in Fig. 6.11 on the right. A satisfying agreement is given, which could support the made assumptions. However, the model still lacks consistency for several reasons.

- Although the predicted temperature in the metal is comparable to experiments, the predicted hot spot in the catalyst is around 700°C (see Fig. 6.11 on the left), exceeding that along the symmetry axis by 200 K, which is unlikely since the highest temperatures occur at the symmetry axis.
- The model predicts full conversion of CO and CO₂ within few millimeters (not shown here) when the gas contacts the catalyst, while full conversion of CO and only 95% of CO₂ is measured experimentally. This also explains the observation in a).

The inconsistency could be attributed to the following uncertainties

- The kinetic rate provided by Xu and Froment [67] is not sufficiently accurate in respect to CO and CO₂ conversion as shown in Chapter 4.5.
- The Porous Body model in Fluent[®] calculates an uniform gas flow profile, whereas real packed beds exhibit complex flow pattern in the entire packing (see Chapter 7.1.2).
- The Porous Body model in Fluent[®] assumes homogeneous catalyst distribution in the packed bed

and the reaction is calculated in each cell. Experimentally, the packed bed is diluted with approx. 82 vol.% inert SiC material, which could lead to uncertainties regarding the catalyst distribution inside the particle mixture

Based on these findings, the applied Porous Body model in Fluent[®], in combination with known uncertainties, is not sufficient for examination of the particular reactor unit. A better approach would be to resolve the packed bed and to calculate heat and mass transport on each particle. A possible method is developed in Chapter 7.2.

6.4 Summary

In this work, an extensive CFD study of the microstructured reaction unit according to the Prototype 1 concept, developed in the course of the MINERVE project, is performed. The results provide valuable insights into macroscopic heat and mass transport phenomena, being not accessible experimentally, and give further suggestions for optimization of the reactor geometry and performance.

Prior to the detailed examination of the relevant aspects, the correctness of the meshed model is validated in terms of heat transfer experiments and temperature distribution in the reactor. The results show exceptional agreement of both experimental and numerical heat transfer amounts and temperature distribution in the reactor as well, pointing to the properly generated geometry and mesh, well posed boundary conditions and CFD being an excellent tool for the description of such complex systems.

The further analysis encompasses the most important aspects of the cooling and reaction zones. On the cooling side, uniform distribution of the liquid and gaseous heat transfer media in the channels, due to several redirections, can be achieved indicating the correct design of the relevant zone. By using gas as a heat transfer medium, relatively high gas velocities in the microstructured zone in the range 40-65 m/s at 60-100 NI/min evolve. Nevertheless, laminar regime prevailed ($Re < 1500$) limiting the Nusselt number to a constant value of 3.7, which corresponds to heat transfer coefficients less than 400 W/(m²K) at the examined conditions. The impact of fins on the cooling side on the overall heat transfer is found as beneficial. However, the effect becomes pronounced by using liquids as coolant only. The improvement of the heat transfer in presence of fins is limited to max. 25% (Re 500-600, α 2000-2500 W/(m²K), due to heat transfer limitation caused in the separating metal wall at higher Re numbers.

The focus on the reaction zone is paid to the influence of the packed bed heat conductivity on the hot spot formation and the determination of the dominant heat transfer resistance. The first study concerns the effect of radial heat conductivity distribution, arising in packed beds, on the magnitude of the hot spot temperature. It is found that the transversal dispersion of λ contributes to the increase of the hot spot. However, at examined conditions (23 NI/min syngas, 80 NI/min air), the difference to λ with no

transversal dispersion is below 30 K at particle diameters below 700 μm . This is a clear indicator that the influence of the increased porosity at the wall has a negligible effect on the packed bed overheating. In the subsequent study, the CFD model is successfully used for parameter estimation, the effective packed bed heat conductivity, which could not be determined theoretically due to scarce information on the used materials and the characteristics of the packed bed. By applying a carefully designed heat source, being representative for the system, all experimental temperature profiles could be reproduced with the effective bed heat conductivity of 1.15 W/(mK). Based on this information, the packed bed heat conductivity is found to be governed by the highly conductive silicon carbide with λ_{SiC} of approx. 133 W/(mK) at the given conditions.

The most interesting aspect regarding the heat transport bottleneck of the system is uncovered by varying the thermal conductivity of the packed bed and the metal, while flushing the reactor with excessive amounts of cooling oil. The first study reveals that the release of even low reaction heat amounts of approx. 336 W leads to ΔT of approx. 25 K which increases to 77 K at 1 kW reaction heat generation. By increasing the packed bed conductivity to 5000 W/(mK), while maintaining that of the metal (approx. 18 W/(mK)), the system results in similar overheating at different Re numbers as using the packed bed heat conductivity of 1.15 W/(mK). However, the overheating becomes less than 10 K at larger Re numbers after eliminating the heat transfer resistance by setting the metal property to 5000 W/(mK) and maintaining that of the packed bed (1.15 W/(mK)). Consequently, the system is found to suffer from extremely fast reaction heat generation being limited by heat transport through the metal separating wall.

Finally, the reaction system is simulated using the kinetic model given by Xu and Froment [67]. Experimental temperature profiles can be recreated by adjusting the axial position of the reaction zone. Despite the properly calculated temperature profiles in the reactor, the results still lack consistency on the chemistry level, which is attributed to the accuracy of the kinetic rate model and the simplicity of the used Porous Body model in Fluent®.

7 Understanding the micro packed bed

The packed bed is one of the most widely used reactor concepts in the chemical industry and has been investigated for decades. The literature spectrum of mathematical models on packed beds ranges from simple correlations to very complex partial differential equations for describing fluid flow as well as heat and mass transport. In addition, contradictory results of several research groups lead to uncertainties in the proper application of the proposed models.

This chapter aims to uncover the most striking attributes and phenomena in the applied micro packed bed accompanied with models and correlations which are widely accepted. Finally, an advanced method for generation and characterization of the packed structures via CFD is described in detail and validated using correlations from the literature.

7.1 Fundamentals

In general, the packed bed can be defined as a collective of solid particles which are settled according to interior and exterior forces and fixed in their local position. In chemical engineering, packed beds are often realized by filling powder or granules into a reaction chamber, e.g. a tube, or, like in the case of the prototypes developed in this thesis, rectangular duct. The material is fixed via a frit or grid. The procedure is relatively simple, which makes the packed bed one of the widest spread concepts. Although easy to generate and to use, packed beds exhibit several issues which are discussed in the following.

7.1.1 Porosity

The porosity is defined as the ratio between the void (V_{void}) and total (V_{tot}) volumes according to Eq. 7.1 and has the value range between 0 and 1. The total volume can also be expressed in terms of the solid (V_s) and void (V_{void}) spaces.

$$\varepsilon = \frac{V_{void}}{V_{tot}} = \frac{V_{void}}{V_{void} + V_s} \quad (7.1)$$

For several configurations, e.g. cubic packings of equal spheres, the porosity can be derived theoretically. The most dense packing can be achieved with cubic or hexagonal tightest packings yielding a porosity of 0.26 [166]. However, in engineering applications, random structures prevail with higher porosities of around 0.36-0.42 [167]. Besides randomness, the volumetric porosity can be strongly influenced by additional factors, e.g. particle shape, particle size and size distribution. For example, cylindrically- or

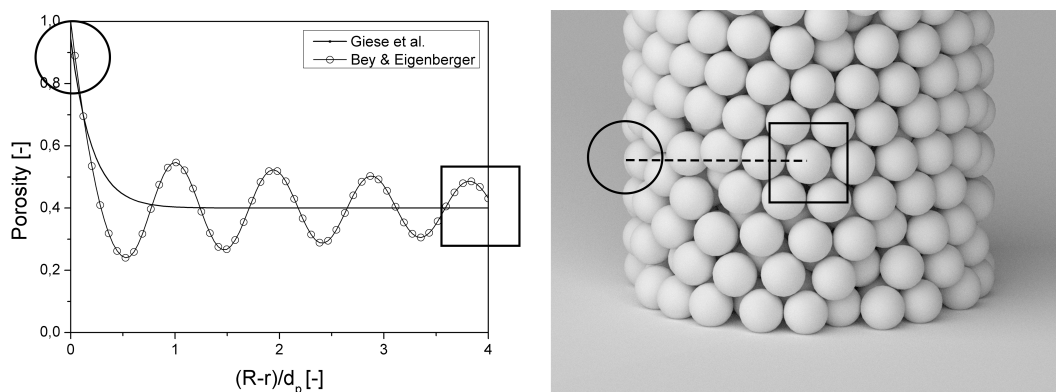


Figure 7.1: Porosity distribution as a function of the normalized tube radius at the constant d_t/d_p -ratio of 8 according to equations by Giese et al. [168] and Bey and Eigenberger [169] (left), and packed bed geometry for elucidation purposes with the same d_t/d_p -ratio (right).

plate-shaped particles tend to decrease the overall porosity. The same applies for poly-dispersed particle distribution due to void filling with the smaller particles. On the contrary, in packings with particle size $<100 \mu\text{m}$, the porosity can be dramatically increased up to 0.6-0.9 according to material and particle size [166]. This is attributed to interparticle repulsion effects based on electrostatic forces compensating the gravity effect.

The porosity can be calculated either for the entire volume (integral value) or for a differential element. Differential consideration is needed for detailed understanding of macroscopic phenomena, e.g. flow field. Giese [168] proposed an empirical expression which describes the radial porosity distribution in a tube (Eq. 7.2).

$$\varepsilon(r) = \varepsilon_0 \left(1 + a_G \cdot \exp\left(-b_G \frac{R-r}{d_p}\right) \right) \quad (7.2)$$

Thereby, ε_0 is the bulk porosity [-], $a_G = 1.36$ and $b_G=5$ are constants. A more detailed expression is proposed by Bey and Eigenberger [169] in Eq. 7.3.

$$\begin{aligned} \varepsilon &= \varepsilon_0 + (\varepsilon_{min} - \varepsilon_0) \exp\left(-\frac{r'}{c}\right) \cos\left(\frac{\pi}{b} r'\right) \quad \text{for } r' \geq 0, \\ \varepsilon_{wall} &= \varepsilon_{min} + (1 - \varepsilon_{min})(r')^2 \quad \text{for } r' < 0, \\ x_{min} &= 0.5(d_t - ((d_t - d_p)^2 - d_p^2)^{0.5}), \\ r' &= \frac{0.5d_t - r}{x_{min}} - 1. \end{aligned} \quad (7.3)$$

Values of the constants are: $\varepsilon_{min} = 0.24$, $b = 0.876$ and $c = 10$. Both equations are plotted for a constant tube to a particle diameter ratio (d_t/d_p) of 8 in Fig. 7.1. Evidently, the porosity description in the packed bed exhibits radial non-uniformity. At the wall, both correlations reach a value close to unity and an averaged value of 0.4 in the bulk. The expression given by Bey and Eigenberger [169] oscillates and

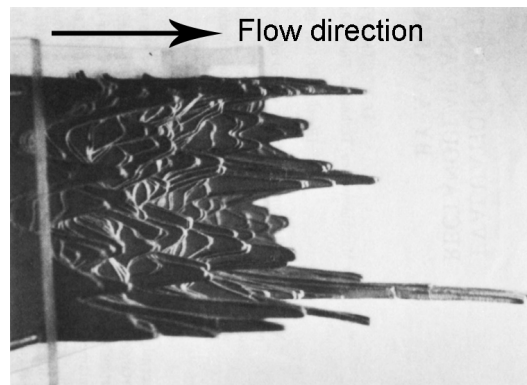


Figure 7.2: Averaged flow profile in a rectangular duct at Reynolds number of 4955 based on approx. 200 experiments [173].

reflects the nature of the packing. Thereby, interparticle voids alternate with the solid of the particles. The expression suggested by Giese [168] could be considered as the averaged form of the Bey and Eigenberger [169] correlation. The evaluation of the correlations at other d_t/d_p -ratios shows no impact on the shape of the porosity curve. For low d_t/d_p -ratios, however, the averaged porosity over the entire geometry increases due to wall proximity. This fact is captured by the correlation of Jeschar [170].

7.1.2 Flow distribution

In the 1950s, it was suggested that velocity in a packed bed might not be uniform, especially at low tube to particle diameter ratios [171]. Since then, extensive analysis of flow distribution in fixed beds has been performed including methods like Laser-Doppler Anemometry, Particle Image Velocimetry, Magnetic Resonance Tomography and Magnetic Resonance Imaging [172]. Fig. 7.2 shows an exemplarily flow profile which is obtained with Laser-Doppler-Anemometry in a rectangular duct at the Reynolds number of 4955 by averaging 200 experiments [173]. Non-uniformity of the flow is clearly present, showing increased fluid velocity in the vicinity of the wall. This effect becomes of importance, especially in tubes with low d_t/d_p -ratios as in the rectangular duct of the prototype reactors applied in this thesis.

The flow condition in the packed bed is reflected via the Reynolds number. In this work, the particle Reynolds number for all the following correlations is defined according to Eq. 7.4.

$$Re_p = \frac{\bar{u}d_p}{\nu_f} \quad (7.4)$$

With the superficial fluid velocity \bar{u} [m/s], the particle diameter d_p [m] and the kinematic viscosity ν_f [m²/s].

The fluid flow profile in porous structures can be successfully described by the modified Brinkman-

Equation [173]. The momentum balance for a tubular system is formulated as follows (Eq. 7.5):

$$\frac{dp}{dz} = -f_1 u - f_2 u^2 + \frac{\eta_{eff}}{r} \frac{\partial}{\partial r} \left(r \frac{\partial u}{\partial r} \right) \quad (7.5)$$

The first two terms on the right side are attributed to the head loss of pressure and are referred to as D'Arcy and Forchheimer terms. The third term on the right accounts for the viscous friction in the vicinity of the wall. The coefficients f_1 and f_2 , listed in Eq. 7.6, are formulated as functions of the packed bed porosity ε [-], particle size d_p [m], fluid density ρ_f [m³/kg] and the effective fluid viscosity η_{eff} [Pa s]:

$$f_1 = 150 \frac{(1 - \varepsilon(r))^2 \eta_{eff}}{\varepsilon^3 d_p^2} \quad (7.6)$$

$$f_2 = 1.75 \frac{(1 - \varepsilon(r)) \rho_f}{\varepsilon^3 d_p}$$

Besides constant porosity values, radially distributed porosity functions proposed by Giese [168] or Bey and Eigenberger [169] could also be used for calculation of f_1 and f_2 . An expression for the effective viscosity η_{eff} is proposed by Giese et al. [161]. With their expression, given in Eq. 7.7, experimental flow profiles in packed beds with spherical particles could be described. A set of parameters is also available for cylinders and Raschig rings.

$$\frac{\eta_{eff}}{\eta_f} = 2.0 \cdot \exp(2 \cdot 10^{-3} Re_p) \quad (7.7)$$

Finally, the pressure drop along the packed bed $\frac{dp}{dz}$ proposed by Ergun (Eq. 7.8) [147] can be applied.

$$\frac{dp}{dz} = 150 \frac{(1 - \bar{\varepsilon})^2 \eta_f \bar{u}}{(\bar{\varepsilon})^3 d_p} + 1.75 \frac{(1 - \bar{\varepsilon}) \rho_f \bar{u}^2}{\bar{\varepsilon}^3 d_p} \quad (7.8)$$

Thereby, the averaged porosity over the entire bed $\bar{\varepsilon}$ [-] and superficial velocity \bar{u} [m/s] are required.

Plugging Eq. 7.6-7.8 into Eq. 7.5 finally yields an ordinary differential equation of the form $0=f(r, u, \frac{\partial u}{\partial r})$ under the prerequisite of negligible pressure drop in the fixed bed.

To solve the differential equation, the boundary conditions are formulated in a straight forward way. The velocity gradient becomes zero ($\frac{\partial u}{\partial r} = 0$) at the symmetry line ($r = 0$) and the no-slip condition ($u = 0$) holds at the wall ($r = R$).

An example of the derived model is presented in the following. MATLAB[®] is used to solve the obtained equation system by using the `bvp4c`-solver. Fig. 7.3 shows the normalized velocity at different Reynolds numbers and a constant d_t/d_p -ratio of 8 using the porosity function by Giese [168] ($\varepsilon_0=0.4$, 1 bar, 25 °C, air). The abscissa is confined to a maximum value of 1.4 for better visibility of the effects in the

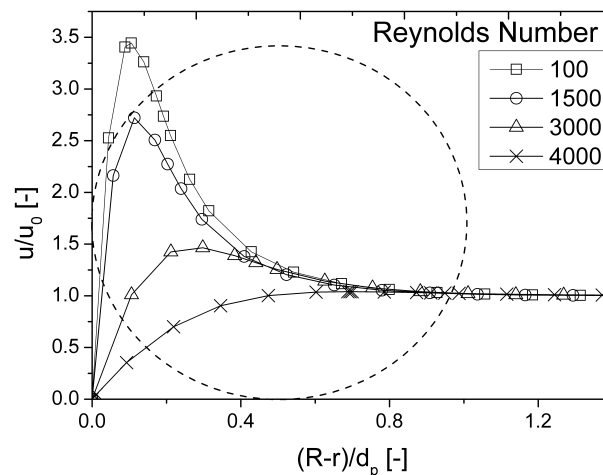


Figure 7.3: Normalized flow velocity profile at different Reynolds numbers calculated using the extended Brinkman-Equation (Eq. 7.5) as a function of the normalized tube radius. Air, $T_{in}=25^{\circ}\text{C}$, 1 bar, $\varepsilon_0=0.4$, $d_t/d_p = 8$.

underlying parameter variation. By a factor 3-4, increased gas velocities in the vicinity of the wall, are calculated at low Reynolds numbers ($\text{Re}<220$). This issue is clearly attributed to the increased porosity at the wall region. With the transition to the turbulent regime at Reynolds numbers above 3000, the bypass effect is diminished. However, this near plug-flow profile requires high superficial velocities which are barely achievable in micro packed beds. As a consequence, flow distribution in wall regions at low Reynolds numbers may become an issue in (micro) packed beds and requires further analysis (see Chapter 7.2).

7.1.3 Heat transfer

The heat transport in general, takes place via radiation, conduction and convection. In the packed bed, all types occur simultaneously. The situation is complicated by the complex fluid flow which explains the large amount of studies on heat transfer in packed beds.

The typical modeling approach, which is applied in practice, is based on the combination of all relevant heat transport phenomena in a “lumped” fixed bed heat transfer coefficient α_i (Eq. 7.9). De Wash and Froment [174] could show that the internal packed bed heat transfer resistance could be split into a flow independent and flow dependent part. The so-called static contribution α_i^0 is calculated from the overall stagnant radial heat conductivity λ_{eff}^0 of the packed bed and the tube diameter d_t . The flow dependent part is formulated as a function of the flow conditions taking into account the throughput of the fluid (G [kg/m^2]) and its thermal/physical properties (C_p , η_f). The relevant parameters for Eq. 7.9 can be found

in [174].

$$\frac{\alpha_i d_p}{\lambda_f} = \frac{\alpha_i^0 d_p}{\lambda_f} + 0.033 \left(\frac{C_p \eta_f}{\lambda_f} \right) \left(\frac{d_p G}{\eta_f} \right) \quad (7.9)$$

$$\alpha_i^0 = \frac{2.44 \lambda_{eff}^0}{d_t^{4/3}}$$

In more advanced models, the non-uniformity of porosity and flow are considered, accounting for radial and axial distribution of heat and mass. Besides CFD, the model of Winterberg et al. [162] can be considered as the most advanced amongst others. Based on the momentum balance in Eq. 7.5 and on the radial porosity distribution functions in Eq. 7.2 and Eq. 7.3, the energy balance in steady state could be written according to Eq. 7.10. The benefit of this model compared to other approaches is the formulation of the boundary conditions according to Dirichlet and Neumann without the need for additional correlations.

$$0 = \frac{1}{r} \frac{\partial}{\partial r} \left[\Lambda_r(r) r \frac{\partial T}{\partial r} \right] + \Lambda_{ax}(r) \frac{\partial^2 T}{\partial z^2} - u_0(r) \rho_f C_f \frac{\partial T}{\partial z} \quad (7.10)$$

with boundary conditions :

$$T \Big|_{r=R} = T_{wall}, \quad \frac{\partial T}{\partial z} \Big|_{z=L} = 0 \quad \text{and} \quad \frac{\partial^2 T}{\partial z^2} \Big|_{z=L} = 0$$

Furthermore, the model provides heat conductivities $\Lambda_r(r)$ and $\Lambda_{ax}(r)$ accounting for radial and axial dispersion. The radial heat conductivity dispersion coefficient in Eq. 7.11 is the most significant variable giving the model its name.

$$\Lambda_r(r) = \lambda_{static}(r) + K_1 Pe_0 \frac{u_{0,c}}{u_0(r)} f(R-r) \lambda_f$$

with

$$0 < R-r \leq K_2 d_t \rightarrow f(R-r) = \left(\frac{R-r}{K_2 d_t} \right)^n \quad (7.11)$$

$$K_2 d_t < R-r \leq R \rightarrow f(R-r) = 1$$

$$K_1 = 1/8$$

$$K_2 = 0.44 + 4 \exp(-Re/70)$$

$$n = 2$$

The entire expression covers the static and dynamic contributions as suggested by De Wash and Froment [174]. The static part, given in Eq. 7.12 is provided by Zehner and Schlunder [175] and is greatly acknowledged in the packed bed community. It is influenced primarily by the porosity, heat conductivity of the solid particles λ_s [W/mK] and the fluid phase in between the particles λ_f [W/mK].

$$\lambda_{static} = \lambda_f \left(1 - \sqrt{1 - \varepsilon} + k_c \sqrt{1 - \varepsilon} \right)$$

with

$$k_c = \frac{2}{N} \left(\frac{B}{N^2} \frac{\lambda_s - 1}{\lambda_s} \log \frac{\lambda_s}{B} - \frac{B+1}{2} - \frac{B-1}{N} \right) \quad (7.12)$$

and

$$N = 1 - \frac{B}{\lambda_s}$$

For a better understanding, the static contribution is evaluated at different solid heat conductivity values in Fig. 7.4 on the left using the porosity function proposed by Giese [168]. As in the case of porosity, the heat conductivity of the fixed bed varies locally. Near the wall, the local heat conductivity is governed by the thermal properties of the fluid phase. The thickness of the transition region is approximately half the particle diameter. Hence, the “insulation effect” is more pronounced in packed beds with larger particle sizes and could be neglected using particles in the micron range (see Chapter 6.3.4). At a distance of one particle diameter away from the wall, the local packed bed heat conductivity reaches the packed bed bulk value.

In packed beds, the bulk thermal conductivity is found to suffer substantially from the fluid presence. Highly heat conductive materials like silicon carbide with a heat conductivity larger than 300 W/(mK) at normal conditions lead to static packed bed heat conductivities of around 0.3 W/(mK). Typical porous oxide catalysts which possess pellet solid heat conductivity of around 0.5 W/(mK) [176] lead to static packed bed heat conductivities similar to that of the gas phase. Zehner and Schluender [175] suggest that the porosity and the heat conductivity of the solid material are the primary factors. The influence of

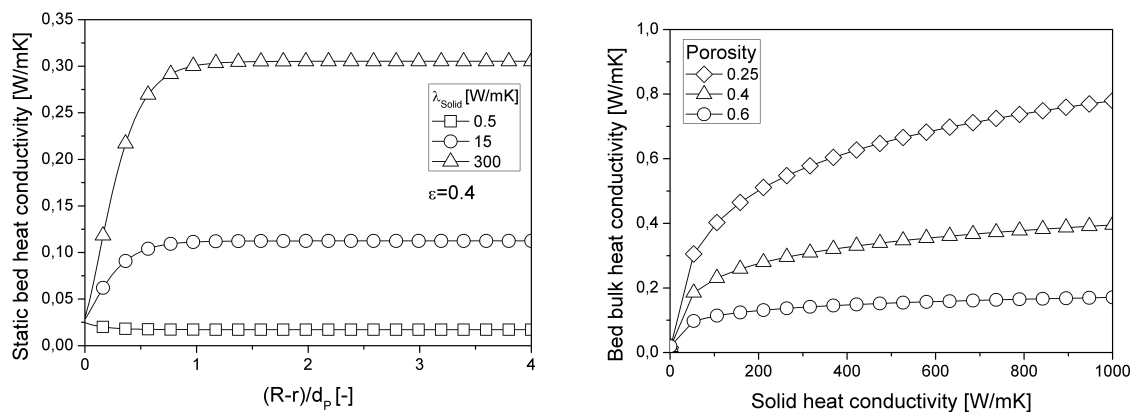


Figure 7.4: Static packed bed heat conductivity for different solid heat conductivities as a function of the normalized tube radius (left) and static packed bed bulk heat conductivity as a function of solid heat conductivity at different packed bed bulk porosities according to Zehner and Schluender (right). Air, $T_{in}=25^{\circ}\text{C}$, $p=1$ bar, $d_t/d_p=8$.

these factors on the static packed bed bulk heat conductivity of is depicted in Fig. 7.4 on the right. By a hypothetical increase of the heat conductivity of the solid material to 1000 W/(mK), the bulk bed heat conductivity function shows first a steep increase and reaches a plateau at the highest value. This implies that highly conductive particles do not lead to a significantly improved heat transfer due to the solid void fraction. Reduced porosities increase the static bed heat conductivity considerably. For example, the reduction of the porosity by half enhances the bed heat conductivity by a factor of 4 almost in the entire λ_s range. Regardless of the porosity and λ_s , the realistic static bed bulk heat conductivity value is limited to values below 0.8 W/(mK) at normal conditions.

The equation by Schluender can be extended by secondary parameters which include the effect of heat transfer by radiation, particle size distribution, pressure influence and non sphericity of the particles. More information can be found in the original research article [175].

Since the packed bed is operated under flow conditions, the effect of fluid velocity on the packed bed heat conductivity is examined. The dynamic contribution in the Λ_r -model includes parameters K_1 , particle Peclet number Pe_0 , gas phase conductivity λ_f and most importantly, the radial flow profile. Fig. 7.5 on the left shows a radial heat conductivity profile at different Reynolds numbers. The comparison to the static profile ($Re=0$) shows that the fluid flow promotes the heat transfer capability in the vicinity of the wall. The extent of the improvement is velocity dependent and improves at higher Reynolds numbers. At the wall, however, the total heat conductivity is equal to that of the pure gas phase due to the no-slip condition.

Fig. 7.5 on the right shows the bed bulk heat conductivity of the Λ_r -model as a function of the particle Reynolds number. The correlation by De Wash and Froment [174] for a two dimensional pseudo-homogeneous model is used as reference. The bulk heat conductivity increases linearly with the Reynolds

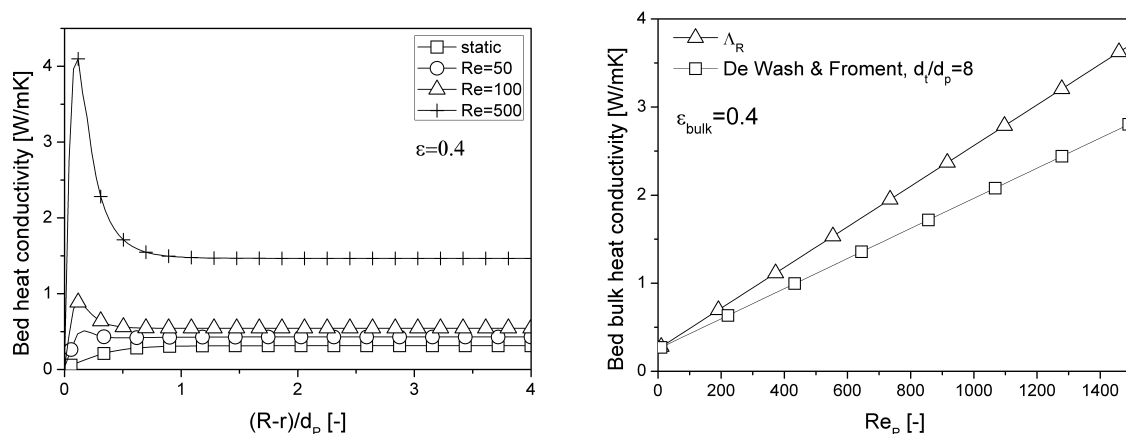


Figure 7.5: The effect of fluid velocity on the packed bed heat conductivity as a function of the normalized tube radius (left) and the bulk heat conductivity as a function of the particle Reynolds number (right) according to the Λ_r -model for $d_t/d_p=8$, Air, $T_{in}=25^\circ\text{C}$, 1 bar.

number in both models. Since the static heat conductivity is limited to 0.8 W/(mK), a considerable improvement in turbulent regimes at particle Reynolds numbers above 220 [177] could be obtained. The application of flow for improvement of the packed bed heat conductivity in microstructures could be challenging due to small particle sizes leading to considerable pressure drop. For mass transfer characteristics using the Λ_r -model, the reader is advised to read the original source in [162] or the VDI topic M7 [178].

7.2 CFD study of a resolved packed bed

In Chapter 7.1, the Λ_r -model is presented as a reference description for radial porosity, flow and heat conductivity profile. Although, the model is successfully applied even in reacting flow systems, limits could be encountered. This especially concerns the validity of empirically determined constants in the equations.

A more sophisticated approach to describe the relevant phenomena in the packed bed involves the resolution of the three dimensional space and solution of coupled mass and energy balances using Navier-Stokes equations.

Recent studies apply models which are dominantly based on unstructured meshes. The mesh generation process is time consuming and yields an immense amount of cells for low numbers of particles. In this study, a packed bed is resolved using a structured grid. The developed method is quick, yields high cell quality and allows an accurate description of flow, pressure drop and heat transfer in fixed bed structures with more than several hundreds of particles, while keeping the total cell amount relatively low.

7.2.1 Introduction

The CFD simulation of fully resolved packed bed structures is a relatively young discipline, having its origin in the late 90s and early 2000s. Initially, the research has focused on the generation of randomly packed bed geometries and validation of the resulting local porosity, flow profiles, heat and mass transfer [179; 180; 181; 182; 183]. In later studies, groups, e.g. [184; 185; 186; 187] integrated kinetic models. Dominantly, unstructured grids are applied. The interparticle voids and the particles themselves are meshed with tetrahedral cells. Often, several prism layers are introduced on the particle surface to take the boundary layer into account. The greatest challenge is, however, the meshing of contact points between the spheres, which require distorted cell shapes and therefore results in a low cell quality. Three approaches are accepted in the community: In the first approach the radius of the particles is reduced to produce a larger interparticle gap. The second approach involves the overlapping of the spheres or introduction of a solid bridge to circumvent the resolution of the contact point. The third method includes the flattening of the spheres in the contact area. The study on contact point methods conducted by Dixon et al. [188] shows that the particle shrinkage decreases the particle drag coefficient and underestimates the heat transfer, while bridging produced an overestimation of both. The flattening method is reported as the most appropriate approach accounting for both, drag coefficient and heat transfer. Furthermore, useful recommendations for the bridging technique are provided. With regard to flow distribution for $Re < 2000$ the interparticle bridge radius to particle diameter ratio should be lower than 10% for bulk particles and lower than 15% for near-wall particles. For the heat transfer, the bridge radius to particle diameter ratio

should be lower than 10% for $Re < 2000$ and lower than 5% for $Re > 2000$. In addition, it is recommended to modify the thermal properties of the bridges to gain better control over the interparticle heat transfer. Another challenge in using unstructured grids is the large amount of cells. This leads to more computation effort and requires powerful hardware. Most of the research is focused on low tube to particle diameter ratios and on low amount of particle spheres (less than 400) for examination of the porosity function or flow description [184; 187].

However, consideration of higher tube to particle diameter ratios and full length reactor scales would be also of interest, since a better insight into the transport phenomena, e.g. dispersion and chemical reactions can be gained. Furthermore, micro packed beds can easily exceed several thousand of particles as in the case of the developed reactor prototypes. For this reason, a method for resolving large amounts of particles would allow to connect experimental and theoretical work and provide further insight into the observed phenomena.

Other meshing techniques for packed beds using polyhedral [186] or Cartesian [189] meshes are relatively rare, despite several benefits compared to tetrahedral meshes. In the following, an alternative Mark and Separate Meshing approach (MSM) for resolving packed bed structures using a structured mesh is presented. It allows:

- Extremely fast packed bed generation
- Low simulation effort
- Good convergency of continuity and turbulence models
- Relatively low cell amount for a high amount of particle spheres

7.2.2 Methodology

A literature survey shows that well-known empirical correlations for a single particle or its collective, e.g. Ranz-Marshall or Ergun-Equation, can be perfectly reproduced with CFD methods and are used as a benchmark. The strategy is similar to other works which includes validation of the heat transfer on a single sphere first, before moving to the fixed bed at its full complexity.

Fluid flow and heat transfer on a single sphere

The validation of the fluid flow around a single sphere is done by other groups by evaluating and comparing the drag coefficient to experimental/empirical data. Jones and Clarke [190] show that Fluent[®] software predicts the drag coefficient of the sphere in the laminar regime with great accuracy and is mesh independent. Gunjal et al. [177] come to the same conclusion using an idealized cell

geometry and the Fluent® CFD code.

Assuming the correctness of the laminar model, the validation of the developed meshing method is done via the heat transfer capability.

For definition, the particle Reynolds number is used to describe the flow conditions around a single sphere and in the packed bed (see Eq. 7.4). The particle Nusselt number is defined as the ratio between the heat transfer by convection and conduction in the fluid phase (Eq. 7.13). The calculation of this parameter at constant particle surface temperature from simulation data requires substitution of the averaged heat transfer coefficient α_p [W/(m²K)] with the heat flux \dot{Q}_p [W] through the particle surface A_p [m²] due to driving force caused by the temperature difference between the particle surface $T_{p,surf}$ [°C] and fluid bulk temperature $T_{0,f}$ [°C].

$$Nu_p = \alpha_p \frac{d_p}{\lambda_f} = \frac{\dot{Q}_p}{A_p(T_{p,surf} - T_{0,f})} \frac{d_p}{\lambda_f} \quad (7.13)$$

In the literature, the heat transfer from the surface of a single sphere into the fluid flow is given by an empirical function including Reynolds and Prandtl numbers. In this thesis Ranz-Marshall [191] (Eq. 7.14) and Whitaker [192] (Eq. 7.15) correlations are used:

$$Nu_p = 2 + 0.66Re^{0.5}Pr^{0.33} \quad (7.14)$$

$$10 < Re < 10^4, Pr > 0.7, Pe \gg 1$$

and

$$Nu_p = 2 + (0.4Re^{0.5} + 0.06Re^{0.67})Pr^{0.4} \quad (7.15)$$

$$3.5 < Re < 7.6 \cdot 10^4, 0.7 < Pr < 380$$

At very low Reynolds numbers, the correlations provide a constant value of 2, implying that the heat transfer by convection is two times higher than by conduction.

Fluid flow and heat transfer in the packed bed

The flow distribution in the packed bed is described by the extended Brinkman equation in Eq. 7.5. The pressure drop according to Ergun (Eq. 7.8) is used. Since the geometry is resolved on the particle level, the porosity function given by Bey and Eigenberger [169] in Eq. 7.3 is calculated for reference (refer to Chapter 7.1.1).

For heat transfer validation in the packed bed, the empirical Nu-Re correlation is used (Eq. 7.16) which

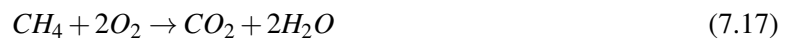
is valid for typical porosity values around 0.4, particle Reynolds numbers between 30-3000 and Prandtl numbers greater than 1 [129].

$$Nu_p = (1.8 \pm 0.3)Re^{0.5}Pr^{0.33} \quad (7.16)$$

Unlike to the Nusselt correlation on a single sphere, the improvement of the heat transfer capability by convection (due to the flow in the packed bed) is lower at very low Reynolds numbers due to packing structure. Compared to Eq. 7.14-7.15, the factor 2 is omitted.

Chemical reaction in the packed bed

Finally, a chemical surface reaction on the particles is implemented. The combustion of methane with air is chosen as a simple reaction (Eq. 7.17) with a hypothetical reaction rate according to Eq. 7.18.



$$r_i = kC_{CH_4}^2 C_{CO_2} \quad (7.18)$$

The consistency of the result is compared to a simple 1D plug-flow model based on the mass balance according to Eq. 7.19.

$$\frac{dC_i}{dz} = \frac{A_p}{L_{PB}\dot{V}_{in}}v_iR_i \quad (7.19)$$

Thereby, C_i is the concentration of the component i [kmol/m^3], z the reactor coordinate [m], A_p the particle surface [m^2], L_{PB} the total bed length [m], \dot{V}_{in} the total volumetric flow of reactants in [m^3/s], v_i the stoichiometric coefficient of the component i and R_i the reaction rate of the component i in [$\text{kmol}/\text{m}^2\text{s}$]. To account for physical relevant velocity in the packed bed, the superficial velocity must be divided by the porosity $u=u_0/\varepsilon$. For additional parameters, refer to Table 7.1.

Evaluation of the results in the resolved packed bed

Porosity (Eq. 7.20) and flow distribution (Eq. 7.21) in the packed bed geometry are averaged circumferentially with a predefined radius interval Δr (approx. 50-100 intervals). The thickness of a slice (axial coordinate) is restricted to 3-4 particle diameters.

Table 7.1: Parameters and boundary conditions used in the simulation of complete combustion of methane.

Name	Value
Tube length	0.102 m
Tube diameter	0.035 m
Packed bed porosity	0.4
Reaction conditions	
Inlet velocity	0.5 m/s
Rate constant k	1000 m ⁷ /kmol ² s
Inlet mole fraction CH_4	0.05
Inlet mole fraction O_2	0.2
Inlet mole fraction CO_2	0
Inlet mole fraction H_2O	0

$$\varepsilon(\Delta r) = \frac{\sum_r^{r+\Delta r} V_{cell,f}(r)}{\sum_r^{r+\Delta r} (V_{cell,f}(r) + V_{cell,s}(r))} \quad (7.20)$$

Here, $\varepsilon(\Delta r)$ is the averaged porosity and $V_{cell,f}$ and $V_{cell,s}$ are cell volumes of fluid and solid material, respectively.

The averaging of velocity in radial direction requires weighing the value of a cell with appropriate cell volume as shown in Eq. 7.21

$$u(\Delta r) = \frac{1}{u_0} \frac{\sum_r^{r+\Delta r} u(r) V_{cell,f}(r)}{\sum_r^{r+\Delta r} (V_{cell,f}(r) + V_{cell,s}(r))} \quad (7.21)$$

Where $u(\Delta r)$ is the averaged velocity in the radial interval and u_0 is the inlet gas velocity. The evaluation procedure is coded as User Defined Function in Fluent[®] and allows fast evaluation of several million cells within a few minutes.

7.2.3 The Mark and Separate Meshing approach (MSM) for packed bed description

The proposed approach consists of three essential steps.

- (a) Calculation of particle position in an empty reaction chamber
- (b) Mesh generation of the empty reaction chamber
- (c) Mark cells in the chamber according to information on particle position and separate phases in Fluent[®]

a) Position of the spheres in the empty reaction chamber using BLENDER

The position of the single spheres in the packed structure is calculated using the Bullet physics engine embedded in the open source 3D content-creation program BLENDER. The procedure is shown in Fig. 7.6. First, a cylinder with a specified diameter and length is generated (not shown) and filled with a desired amount of spherical particles using the Python[™] language. After the simulation is started, the particles fall according to rigid body dynamics, gravity and specified parameters, e.g. friction or rotation (Fig. 7.6, t_2 and t_3). After the convergency of the solver is reached, the middle part of the packing is used as a representative for the fixed bed bulk. The center coordinates of the spheres are extracted using Python[™] script and transferred to the CFD software.

The Bullet Physics engine expects multiple parameters to describe the physical behavior of the particles. The important and applied parameters are density (glass spheres, $\rho = 2500 \text{ kg/m}^3$), surface friction (0.01), particle translation (0.05) and particle rotation (0.1) coefficients. The most important parameter is particle-particle and particle-wall surface friction. High parameters result in very high porosity packings with non-realistic particle arrangement, whereas lower values (approx. 0.01) yield physically realistic results.

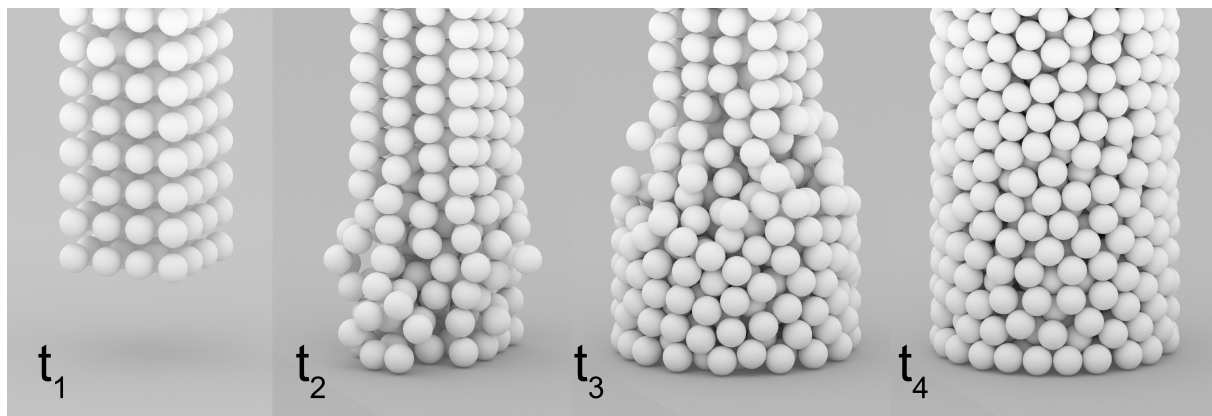


Figure 7.6: Packed bed generation using Bullet physics engine: t_1) Initial state, t_2)- t_4) Begin of the settlement process and arrangement of the particles according to interparticle forces, friction and gravity.

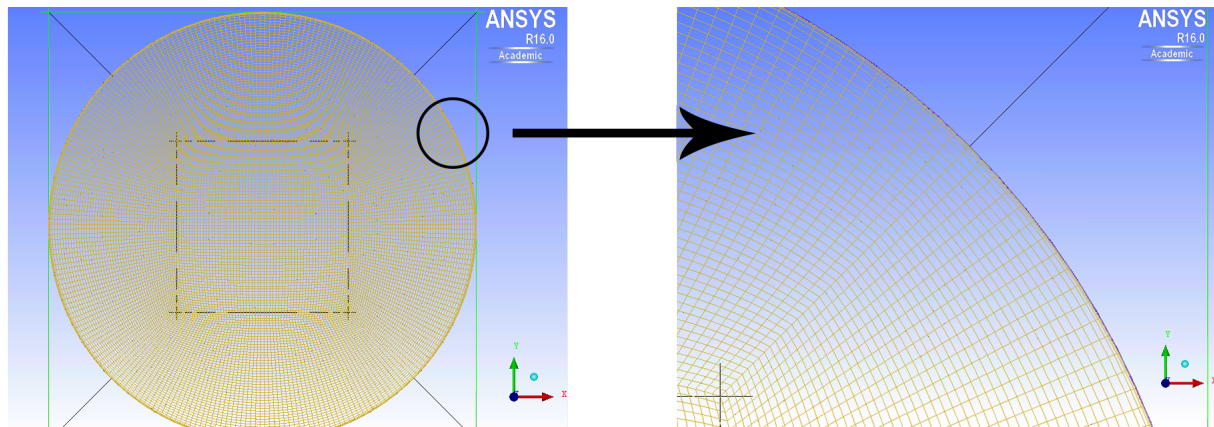


Figure 7.7: Structured mesh for a tubular reaction chamber geometry which is used for the MSM-approach. Full domain (left) and outer wall region (right).

b) Mesh generation of the empty reaction chamber

A tubular geometry with specifications in a), e.g. diameter and length is created in ICEM CFD®. The meshing is done using a structured O-grid as it is shown in Fig. 7.7. For rectangular ducts, the procedure becomes much simpler, since the structured meshing procedure is straight-forward, and perfect cubic cells can be applied. The size of a single mesh element in the tube is governed by cells per sphere ratio which is varied from 10-40. At the wall, smaller spacing is applied to reduce the aspect ratio of the cells which allows to take the wall effects into account. The time consumption for the tube meshing is less than 5 min (<20 mio. cells) since a straight-forward sweeping procedure is used.

c) Mark cells and phase separation

The final step consists of marking the spheres in the tubular domain and separate the phases to obtain

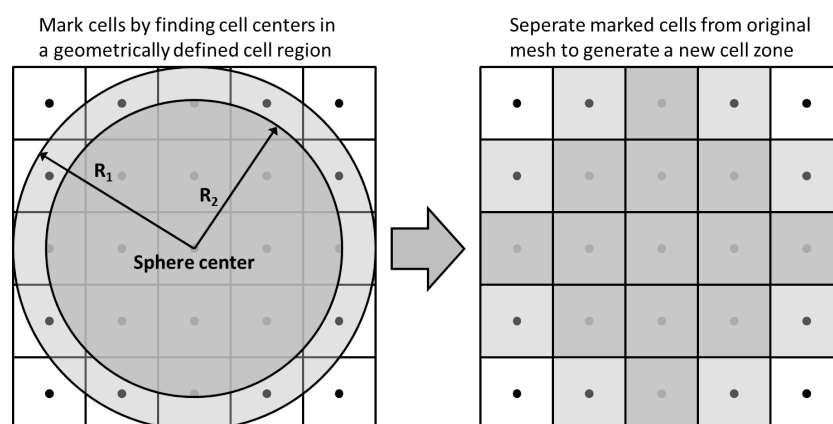


Figure 7.8: Visualization of cell scanning, marking and separation based on a sphere center with example of two different radii R_1 and R_2 for a two dimensional quadratic grid.

the final mesh structure. First, the tubular mesh from step b) is loaded into FLUENT®. Sphere center coordinates are transferred from step a). With this information, the cells in the structured mesh are scanned using the DEFINE-ON-DEMAND macro in a programmed routine to find cells with a cell center coordinate within a distance smaller or equal to the radius of the sphere from the sphere center coordinates. Afterwards, the found cells could be easily separated from the original mesh with a meshing tool in order to generate a separate cell zone for the particles. The procedure is visualized in Fig. 7.8. The resolution strongly depends on the cells per particle ratio and defines the surface roughness.

7.2.4 Results obtained with the MSM approach

7.2.4.1 Heat transfer on a single sphere

The first question to answer, using the MSM-approach, is the appropriate number of cubic cells required to resolve one sphere with an acceptable error tolerance for CFD calculations. Cell per sphere diameter ratios of 40, 20, 15 and 10 are considered in this work (see Fig. 7.9). Obviously, a high cell per sphere diameter ratio, e.g. case a) describes the shape of the sphere more accurately compared to case d) which degrades the particle to a cube shape. A characteristic of the spheres presented in Fig. 7.9 is the increased surface area compared to ideal sphere of the same diameter by a factor of 1.49. This value is found to be independent of the cells per sphere ratio and is used as a correction factor for the sphere surface in all simulations. Data are provided as a function of the real sphere diameter in the following.

The mesh dependence is checked by considering the heat transfer from the sphere surface into the fluid bulk. Ranz-Marshall [191] and Whitaker [192] correlations are considered as a benchmark. Fig. 7.10 on the left shows the calculated Nusselt number as a function of Reynolds from 4.7 to 376 ($u=0.25-20$ m/s) on a $300\ \mu\text{m}$ particle applying different sphere resolution ratios. For Reynolds numbers below 210 laminar regime could be assumed, whereas the transition regime starts at Reynolds numbers greater than 210 [177; 190]. The results from CFD simulation reproduce the values given by Ranz-Marshall and Whitaker well. The obtained results agree with Ranz-Marshall with an error of $<5\%$ at $\text{Re}<30$, $<15\%$ at $\text{Re}<200$ and $15-20\%$ in the transition regime at $\text{Re}>210$. The overestimation of heat transfer rates on a fully resolved sphere is also observed by Romkes et al. [129]; however the error reported is $<5\%$ for $\text{Re}<1000$. The most interesting aspect, however, is that the heat transfer is independent of the cells per sphere ratio in the laminar regime. This finding is supported by several groups using unstructured meshes for a single sphere [183; 190; 193]. In the laminar range, the $k - \varepsilon$ turbulence model is used in

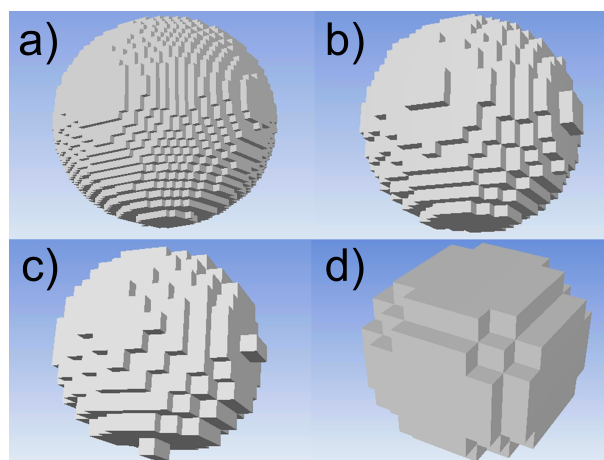


Figure 7.9: Resolution of a single sphere with a) 40, b) 20, c) 15 and d) 10 cells per sphere diameter using the MSM-approach.

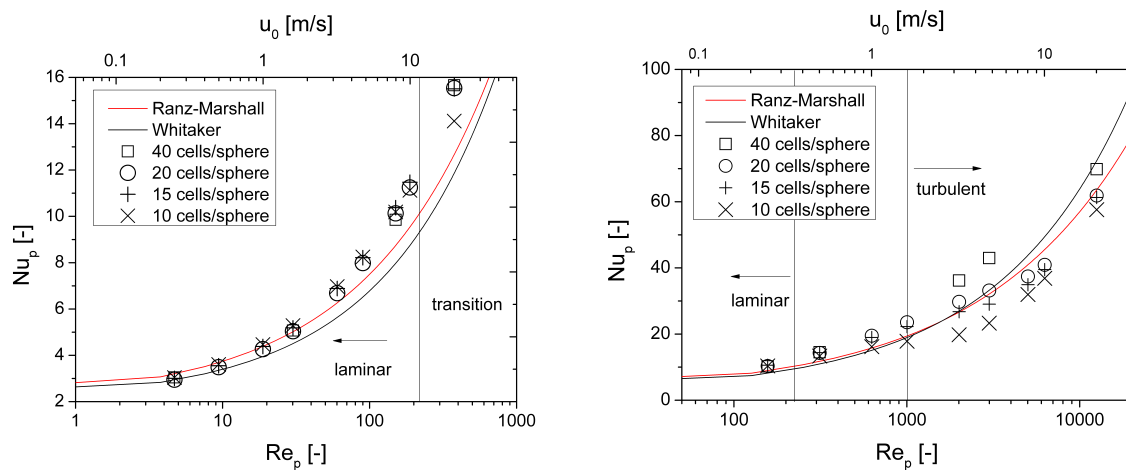


Figure 7.10: Particle Nusselt number as function of particle Reynolds number at different cells per sphere ratios for a 300 μm (left) and 1 cm (right) diameter of particle. Fluid air, $T_{in}=25^\circ\text{C}$, 1 bar.

this thesis. The results don't deviate to the laminar model, which is also found by Kuroki et al. [193].

To reach turbulent regime, the particle diameter is set to 1 cm. Fig. 7.10 on the right shows the particle Nusselt as a function of the particle Reynolds number on the larger particle at different cells per sphere ratios. In the laminar range ($Re < 210$), the calculated Nusselt numbers coincide with the correlations as in the case of the 300 μm particle diameter. At Reynolds numbers larger than 1000, the cells per sphere ratio starts to gain importance and a scattering of the particle Nusselt numbers occurs. Lowest sphere resolution (10 cells per sphere diameter) yields an underestimation of the Nusselt number by up to 25% compared to the Ranz-Marshall correlation. In contrast to that, the highest resolution with 40 cells per sphere diameter overestimates the Nusselt number by up to 35%. At Reynolds numbers greater 6000, the deviation of the correlations decreases for all sphere resolution ratios to a value below 10%.

To examine the correctness of the results as a function of the sphere resolution, the boundary layer theory is considered. The theory provides a rule for the non-dimensional boundary layer thickness y^+ . In the literature, recommended y^+ values for resolved packed bed values scatter from 1-1000 [129]. However, values below 1 seem to be more appropriate and produce accurate results [129; 186]. Transferred to this case, only the highest resolution of 40 cells per sphere diameter would be valid for Reynolds below 500, if $y^+=1$ could be taken as a limit. By taking a less conservative value of $y^+=10$, it could be stated that all applied resolutions would be valid for Reynolds numbers < 2000 . Despite this limitation, the prediction of the heat transfer on a single sphere is still tolerable in the higher Reynolds range.

7.2.4.2 Packed bed meshes for the CFD study

The validation of the CFD results using the MSM-approach is done in the following subchapters on five levels including verification of 1) Porosity, 2) Flow, 3) Pressure drop, 4) Heat transfer and 5) Chemical

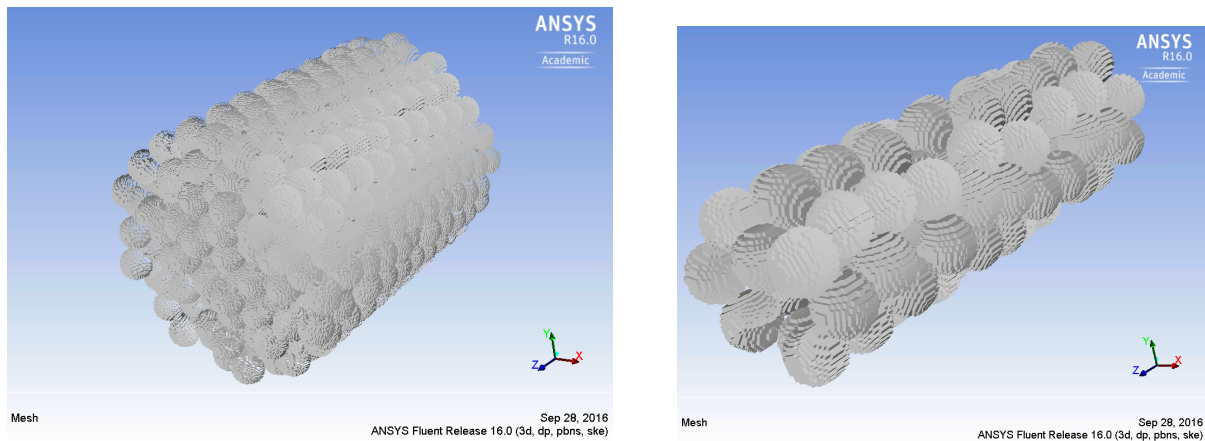


Figure 7.11: Two representative packed bed geometries used in this work. Left: Geometry with the tube to particle diameter ratio of 8.3 (sphere diameter 6 mm) consisting of 660 spheres; total amount of cells 5.02 mio.. Right: Geometry with the tube to particle diameter ratio of 3.5 (sphere diameter 1 cm) holding 99 spheres and resolved with the total amount of cells of 0.68 mio.

reaction. Two geometries are selected as representatives for fixed beds with different tube to particle ratios. Fig. 7.11 shows the mesh of these two geometries generated for Fluent[®]. The geometry in Fig. 7.11 on the left has a tube to particle ratio of 8.3 (particle diameter 0.6 cm) with the total length of the bed of around 7 cm. The number of spheres is 660 with the resolution of 20 cells per sphere diameter. The near-wall tube region is resolved with 0.5 μm cell thickness. The mesh in Fig. 7.11 on the right has a different tube to particle ratio of 3.5 (particle diameter 1 cm) with a total bed length of about 10 cm. The total number of spheres is 99 which is also resolved with a cells per sphere diameter ratio of 20. The near-wall region was resolved with 10 μm cell thickness. The time consumption for marking all the spheres depends strongly on the initial mesh size and the number of spheres. For example, case a) requires around 5 min on an AMD XEON 8 core a 3 GHz and 24 GB of RAM.

7.2.4.3 Contact points

As already mentioned in the introduction, the contact points lead to several problems during the meshing with unstructured meshes and require special attention. In the presented method, no further adaptation of the meshing is required at the contact points, since the initial mesh is generated first and not modified in the next steps. However, depending on the radius of the spheres and their position, bridging of the spheres occurs in the MSM approach. Fig. 7.12 shows contact regions between spheres at a cell per sphere ratio of 20. A bridge radius to particle diameter ratio of 20% is calculated. The variation of the cell to particle ratio from 10 to 40 shows that this value is independent of the resolution. Following the recommendations given by Dixon, that value should be below 10%. Thus, an overestimation of particle to particle heat conductivity could be expected.

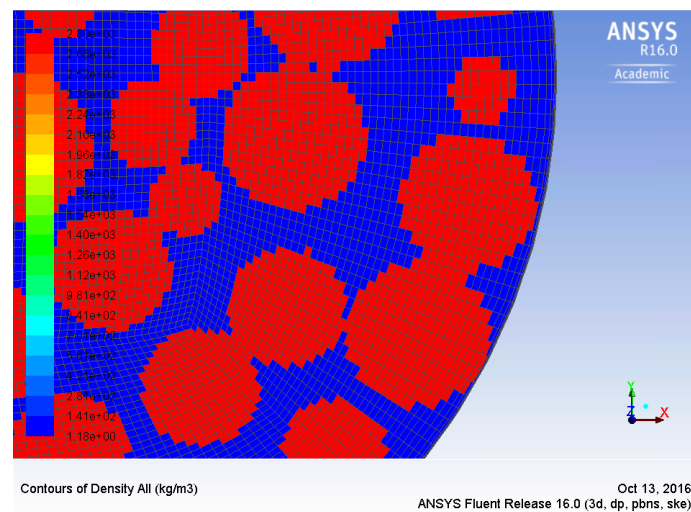


Figure 7.12: Visualization of the contact points between the particles in the packed bed mesh using a cell per sphere diameter ratio of 20 (arbitrary axial cut).

7.2.4.4 Local porosity

The local porosity profile in the two bed structures is analyzed regarding the different tube to particle diameter ratio using the correlation of Bey and Eigenberger [169]. The resulting porosity over normalized tube radius is shown in Fig. 7.13. Generally, the local porosity extracted from the packed bed geometries agrees closely with the correlation of Bey and Eigenberger in the vicinity of the tube wall and the bed bulk.

7.2.4.5 Fluid flow profile

Fig. 7.14 shows axial cuts through the packed bed for the two geometries for the inlet velocity of 0.5

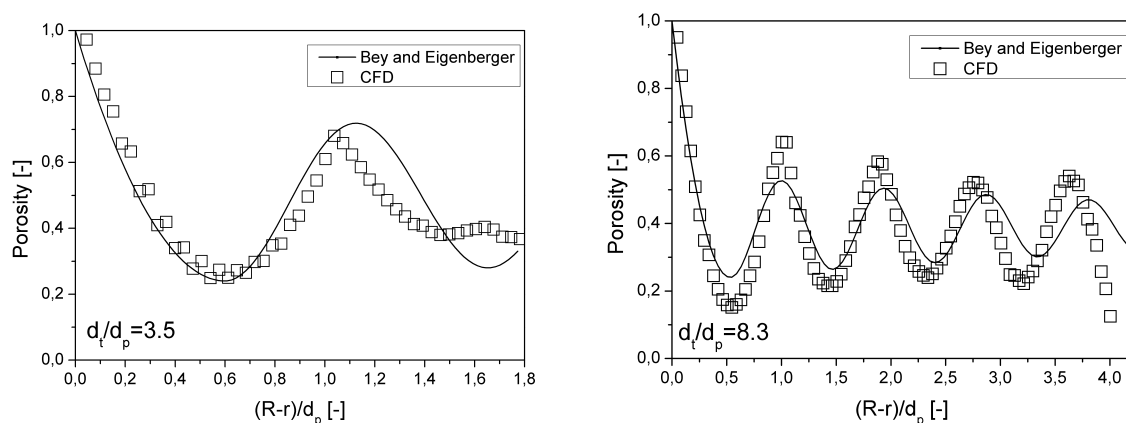


Figure 7.13: Porosity profile as a function of the particle normalized tube radius for the packed bed geometries with d_t/d_p -ratio of 3.5 (left) and 8.3 (right). Comparison of CFD results and correlation according to Bey and Eigenberger [169].

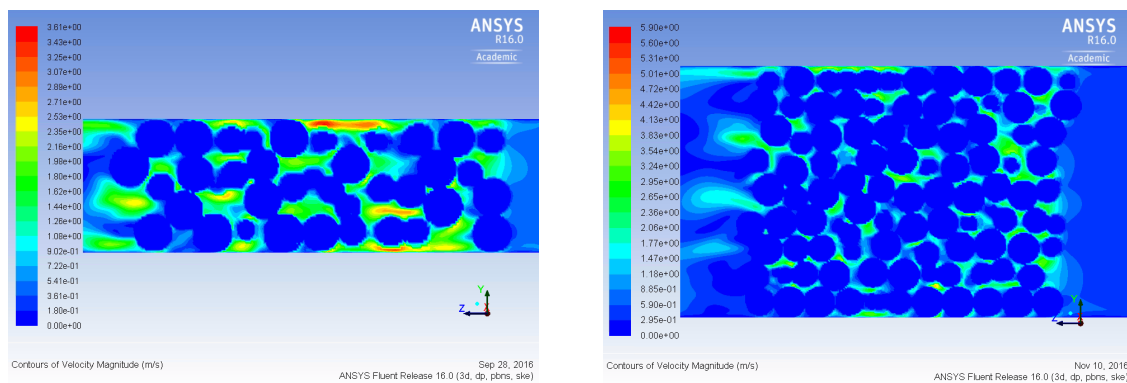


Figure 7.14: Velocity distribution in the two bed geometries with d_t/d_p -ratio of 3.5 (left) and 8.3 (right) for an air inlet velocity of 0.5 m/s, $T_{in}=25^\circ\text{C}$, p_{out} ambient.

m/s. At first glance, the gas flow through the packing structure does not show any remarkable anomalies. The velocity increases in the bulk up to 5-10 times, compared to the empty tube. For further analysis, the gas velocity is averaged circumferentially. Fig. 7.15 shows the normalized flow profile for the two geometries, compared to the flow profile obtained with the Brinkman-Equation. First, the flow characteristics are similar in both geometries. The velocity distribution in the bulk of the packed bed is of oscillating character similar to the porosity profile. Close to the wall, the gas velocity doubles for the tube to particle diameter ratio of 8.3 due to the value of porosity of near 1. At the wall, the velocity is zero due to the no-slip condition. For the lower tube to particle diameter ratio of 3.5, the peak gas velocity close to the wall is similar to that close to the packed bed center. A direct comparison of the calculated velocity with the profile of the extended Brinkman-Equation reveals good agreement for both geometries. A slightly higher velocity amplitude of approx. 20% in CFD is calculated in case of a tube to particle diameter ratio of 8.3 in the packed bed bulk compared to the Brinkman model. This, however,

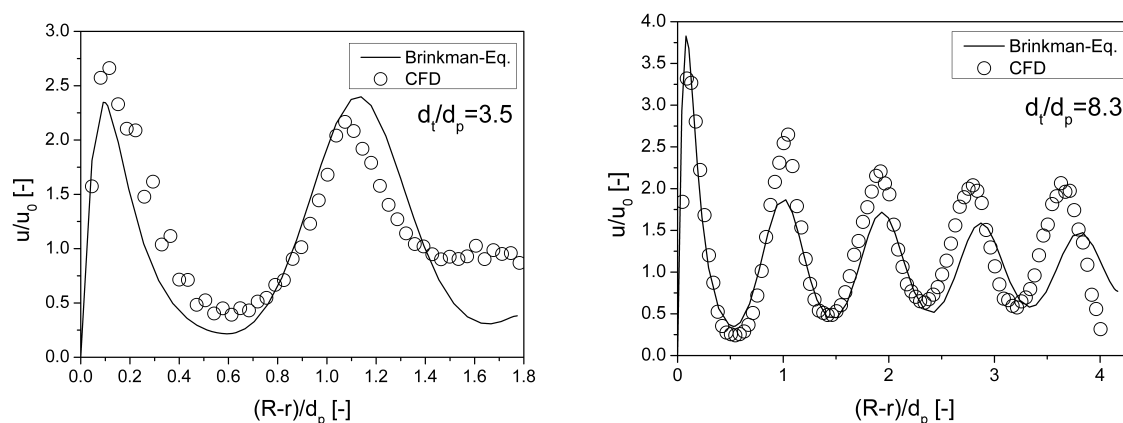


Figure 7.15: Normalized and averaged velocity profile in the two packed bed geometries with d_t/d_p -ratio of 3.5 (left) and 8.3 (right) for the inlet velocity of 0.5 m/s. Comparison of CFD with Brinkman results for air, $T_{in}=25^\circ\text{C}$, p_{out} ambient.

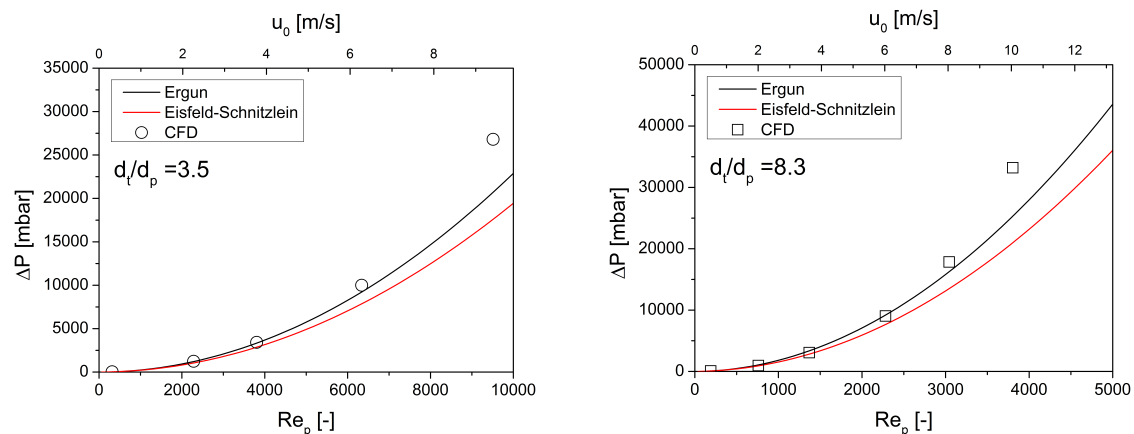


Figure 7.16: CFD calculated pressure drop in the two packed bed geometries as a function of the particle Reynolds number in comparison with the correlations given by Ergun [147] and Einfeld-Schnitzlein [194]. Left: $d_t/d_p=3.5$; Right: $d_t/d_p=8.3$; Fluid air, $T_{in}=25^\circ\text{C}$, p_{out} ambient.

could be attributed to the influence of randomness of the packing generation in CFD.

7.2.4.6 Pressure drop

The verification of the pressure drop is completed, as in the case of fluid flow, for the two geometries by comparing the numerical results to the correlations of Ergun (Eq. 7.8) and Einfeld-Schnitzlein [194] in the Reynolds range up to 10000 (see Fig. 7.16). In both cases, a satisfactory agreement is achieved at Reynolds numbers below 3000 for a tube to particle diameter ratio of 8.3 and at Reynolds numbers below 6000 for a tube to particle diameter ratio of 3.5. The relative deviation is calculated to be less than 10% compared to Ergun [147]. For higher velocities, a greater deviation occurs for both geometries with an error of about 30%. This could be attributed to the insufficient resolution of the sphere according to the boundary layer theory which limits the validity of the simulation for particle Reynolds numbers to maximum 3000 for both ratios with y^+ of 10 as limit (see heat transfer on a single sphere).

7.2.4.7 Heat transfer

Unlike the previous subchapters, the heat transfer in the packed bed is examined for different particle sizes of 6 mm and 300 μm using a geometry with a tube to particle diameter ratio of 8.3. The examples are selected because a similar particle diameter range is used in the experiments with the reactor prototypes. For computer simulation, two spheres, one in the packed bed center and another one near the wall, are selected. The surface temperature of these two spheres is set to 370 K and the inlet temperature of the gas phase is set to 300 K (air). Fig. 7.17 visualizes the position of the spheres and temperature distribution in the fixed bed. No overlapping of the temperature fields occurs and therefore, thermal interaction can be excluded widely. The particle Nusselt number is examined as a function of the Reynolds

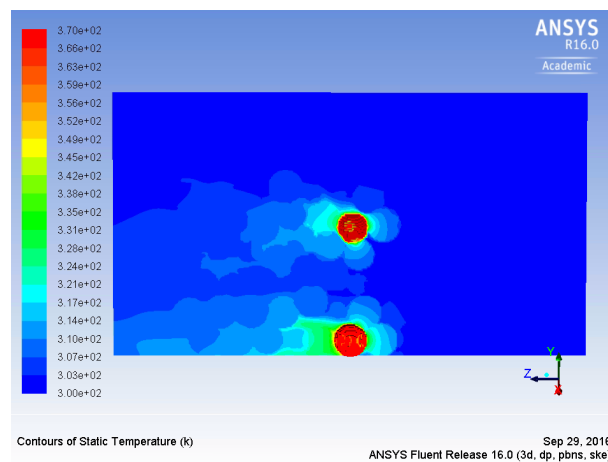


Figure 7.17: CFD temperature contours in the packed bed geometry with a tube to particle diameter ratio of 8.3, where one sphere in the center and one near the wall have a surface temperature of 370 K while the entire bed is flushed with air (300 K) with the inlet velocity of 0.5 m/s. p_{out} ambient.

number in Fig. 7.18. The Ranz-Marshall [191] correlation for a single sphere and the Nu-Re correlation for the heat transfer in packed beds are taken as a reference. In the packed bed, the heat transfer from a sphere surface to the fluid becomes more pronounced with higher Reynolds numbers compared to a stand-alone single sphere in the Reynolds region >1 . The computed particle Nusselt numbers for both spheres closely follows the empirical Nu-Re correlation for the packed bed. The deviation between the CFD calculated Nusselt number for the center sphere and the empirical correlation is less than 11% in the laminar flow regime ($Re < 210$).

According to CFD results, there is a deviation in heat transfer capability between the sphere in the bulk and the sphere close to the wall. The highest difference in Nusselt numbers between the two spheres oc-

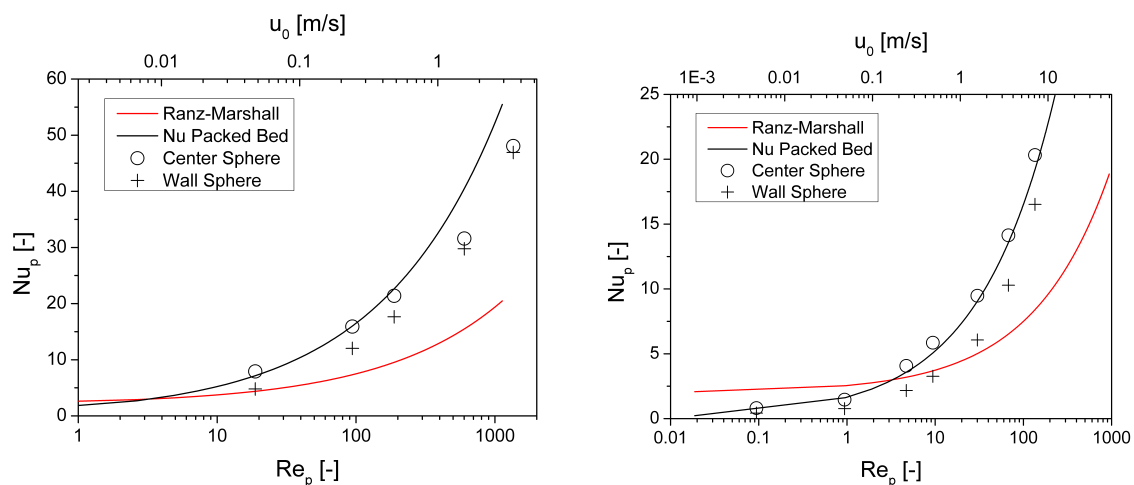


Figure 7.18: Heat transfer from a single particle into the gas phase in the packed bed as function of the Reynolds number. The packed bed consists of 6 mm (left) and 300 μm spheres in diameter (right). One sphere in the center and one in the vicinity of the wall are considered, $d_t/d_p=8.3$.

curs in the laminar flow regime ($Re < 210$). The difference progressively diminishes with higher Reynolds numbers and drops below 6% in the transition regime ($210 < Re < 1000$). A possible explanation for this could be the static contribution of the heat conductivity at lower flow rates and an increased radial heat dispersion by flow at higher velocities.

Since Reynolds numbers lower than unity could occur especially in micro packed bed structures, the packed bed geometry is scaled down to account for Reynolds numbers lower than one while still preserving feasible superficial gas velocities greater than 0.001 m/s. Fig. 7.18 on the right shows that at very low Reynolds numbers less than one, the heat transfer rate of a single sphere in the packed bed converges towards zero, while the minimum Nusselt number for a stand-alone sphere is two (Ranz-Marshall). The deviation in Nusselt number between the wall and the center particle in the CFD simulation is the highest with up to 50% in the Reynolds range less than one.

One major conclusion is that micro packed beds with Reynolds numbers less than approx. 100 require careful consideration in respect to heat transfer on particles in wall regions. In this work, the Reynolds number is approx. 500 for all conducted experiments and conditions. Therefore, the heat transfer in the packed bed is expected to be similar on all particles.

7.2.4.8 Chemical reaction

In the final validation step of the proposed meshing technique for packed beds, the Chemical reaction module of Fluent[®] software is utilized. Besides mass and momentum balances, which are correctly calculated by Fluent[®] in the proposed geometries (see previous sections), the chemical reaction requires for additional transport equations for each reactant as well as their conversion according to the specified kinetic rate equation.

The isothermal methane combustion is simulated in the packed bed geometry with a low tube to particle diameter ratio of 3.5. The reaction is set as "Surface Reaction" in Fluent[®], i.e. without assuming porosity of the particles. The kinetic constant is corrected by a surface factor of 1.49 to account for the increased surface area of the resolved particles. Fig. 7.19 on the left shows the molar concentration of the chemical reactants involved in the reaction as a function of the dimensionless reactor length z/L for one-dimensional plug-flow and CFD. The inlet and outlet concentration as well as the consumption/production of the reactants along the packed bed axis agree closely for both models, from which several conclusions can be drawn.

Regarding the MSM-approach, the transport of chemical species and their local reaction rates are properly calculated by CFD code at given conditions ($Re=315$, $p_{out}=1$ bar) on the proposed packed bed meshes, which adds to the validity and robustness of the utilized meshing technique.

Future studies may focus on, e.g. reaction in the catalytic packed beds in the laminar and turbulent flow

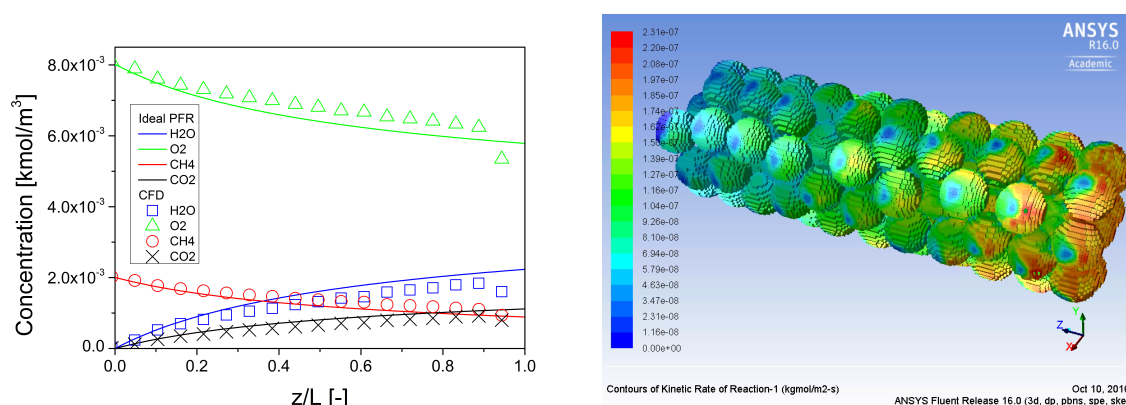


Figure 7.19: Comparison of the concentration profiles obtained in the resolved packed bed by CFD versus an ideal plug-flow model on the example of combustion of methane at isothermal conditions (left) and according contour plot of surface reaction rate in the packed bed provided by the CFD simulation (right).

regimes and the determination of the required mesh resolution.

Another insight regarding packed bed systems is revealed by analyzing the local reaction rate, as shown in Fig. 7.19 on the right, which shows non-uniformity on the particle surface in the pinch points. Between wall-particle and particle-particle surfaces, the reaction rate is significantly lower than on the surfaces, which are exposed to fluid flow. Therefore, catalytic packed beds with the low amount of pinch points are clearly beneficial regarding the overall reaction rate. However, by adjusting the lower d_t/d_p -ratio as one possible option to reduce the number of contact points, the heat transfer capability begins to suffer with increasing porosity, which can lead to a potential overheating of the catalyst bed.

Nonetheless, despite the non-uniformity of the reaction rates on the particle surface, the axially averaged CFD results accurately predict the concentration profiles of the one-dimensional plug-flow reactor.

Summarized, the influence of the effects in the wall region, i.e. higher porosity, increased flow at the wall and the non-uniformity of the reaction rate, even at low d_t/d_p -ratio of 3.5, do not have a considerable negative impact on the overall mass transport and the overall reaction rate.

Hence, microreactors in this work, which show larger d_t/d_p -ratios larger than 4 and exhibit Reynolds numbers beyond 500 can be treated as nearly ideal plug-flow reactors.

7.3 Summary

The intention of this chapter is to give a brief insight into the local phenomena in the packed bed of the applied prototype reactors. Thus, this chapter covers the analysis of existing correlations and their comparison to the CFD simulation. For the latter, the meshing method with structured grids is applied to examine packed beds.

The most important attributes of a packed bed are local porosity and flow distribution. The porosity has a singularity at the wall reaching a value close to 1. The bulk porosity value, on the contrary, is governed by parameters such as particle form and size distribution.

The fluid flow is affected considerably by the porosity distribution. For simple tube or ducts, the extended Brinkman-Equation can be used for a flow examination based on the description of the radial porosity profile. Generally, the velocity in the packed bed in the wall region exhibits higher values than in the packed bed bulk due to increased porosity. With increasing Reynolds numbers the velocity at the wall diminishes and the flow profile strives towards an ideal plug-flow.

Regarding heat transfer, the extended Brinkman-Equation with energy balance and heat dispersion coefficients proposed by Winterberg et al. [162] is analyzed with the focus on the packed bed heat conductivity. The value of the packed bed heat conductivity depends strongly on porosity and fluid flow conditions. Near the wall, the heat transfer is governed by the fluid due to increased porosity, whereas the bulk heat transfer is governed by the solid material. It is found that despite extremely high heat conductivity of the solid material, the stagnant packed bed heat conductivity is typically limited to values below 0.8 W/(mK) at ambient conditions. Fluid flow positively contributes to the average heat conductivity with increasing Reynolds number and enhances the thermal transfer up to 10 times at Reynolds numbers of around 10,000. Since this operation is not feasible in micro packed beds, they typically suffer from overall low packed bed heat conductivity in the laminar regime. Pressure drop restricts the Reynolds number.

The correlations from the literature are limited to simplified geometries and lumping of the local phenomena. For this reason, a CFD method is applied to study the local effects. Compared to available meshing approaches using unstructured grids, an alternative meshing strategy using a structured mesh is presented. The procedure of meshing is very fast, yields good cell quality and leads to faster computation times. Besides, several hundreds to thousands of spheres can be resolved with a relatively low amount of cells.

Due to particular characteristics, e.g. increased surface/roughness of spheres resulting from the particular approach, validation of the meshing strategy is performed regarding heat transfer on a single sphere and regarding pressure drop, porosity, flow distribution, heat transfer and chemical reaction. The correlations from literature serve as a benchmark in the validation of the code. The results from flow around a single sphere show no mesh dependence of the particle Nusselt number as a function of the particle Reynolds

number in the laminar flow regime. This is the first requirement to analyze the local phenomena in a micro packed bed. In the comparison of CFD, porosity is found to be in accordance with the correlation of Bey and Eigenberger [169] for the examined bed geometries with tube to particle diameter ratios of 8.3 and 3.5. Fluid flow, heat transfer and pressure drop are found to match the literature correlations/models in the laminar regime well. Deviations occur only in the transition and turbulent regime. Furthermore, differences between heat transfer on spheres in the wall region and in the “bulk” become pronounced with lower Reynolds numbers and disappear towards the transition flow range ($Re > 210$).

Chemical reaction on the particle surface in the packed bed is analyzed under isothermal conditions by comparison of the resolved geometry in CFD with an ideal plug-flow model. The agreement of both models points to the exact calculation of the fluid flow, transport equations for the individual chemical species and the local reaction rates by the CFD code on the proposed packed bed meshes. The detected local non-uniformities of the reaction rate on the particle surface are found to not significantly contribute to the overall reactor performance, even at low d_t/d_p -ratio of 3.5 ($Re = 315$). As a result, the proposed microreactor prototypes can be treated as nearly ideal plug-flow reactors at examined conditions. The presented meshing strategy for packed beds in combination with CFD methods is able to accurately describe the most relevant phenomena in micro packed beds. Consequently, this technique can be exploited for further studies to obtain a deeper understanding of complex interactions between local mass, heat transfer and reactions in the geometries of microreactors.

8 Summary

Microstructured methanation reactor prototypes for conversion of CO/CO₂/H₂ mixtures are successfully developed in the scope of the MINERVE PtG project from 2012-2015 and are extensively characterized on the experimental and theoretical level in this thesis. The entire work is subdivided in six thematic chapters, whereby each contributes to a complete understanding of the devices.

Fundamentals of the reaction system

The most significant aspects of the methanation system are presented in the first chapter. The choice of the catalyst system is mainly limited to Ni based catalysts for economical reasons. Hydrogenation mechanisms of CO and CO₂ are discussed regarding the Carbide theory and the model given by Solymosi et al. [40]. The results from other research groups regarding kinetics on methanation catalyst are summarized including the retarding effect of CO, enhancing effect of temperature, H₂ and pressure. The influence of further relevant factors like water and support material are summarized as well. Few LHHW kinetic rate expressions are carefully selected from the literature, potentially being suitable for the MINERVE feed composition. These are given by Xu and Froment [67], Kopyscinski et al. [58], Zhang et al. [56] and Koshany et al. [68]. A thermodynamic consideration is conducted with respect to the MINERVE objective. The study reveals best conversions of both CO and CO₂ in the temperature range 300-450°C. The examination of the H₂/C-ratio, pressure and water shows that hydrogen is the most effective parameter for improving the methane yield. Both CO₂ and CO contribute potentially to carbon formation which can be formed at lower and higher temperature regions, respectively. Besides hydrogen, water in the range of few vol.% is found to inhibit coke occurrence effectively.

The chapter also addresses the deactivation mechanisms discussed in the literature on methanation. The main focus is paid to fouling processes caused by coke and the morphology of the carbonaceous species. Regeneration and preventive methods are provided.

Conventional vs microstructured reactor technology

Conventional technology for methane production on an industrial level is examined and adiabatic packed bed reactors are identified as the dominant technology. The main drawbacks of the adiabatic operation are elucidated: low methane yield, increased byproduct formation and catalyst damage due to fouling/sintering phenomena as well as metal dusting. On the process level, the technology is found to require multiple reactor units with interstage cooling and additional periphery. Microstructured reactor technology is introduced, allowing a high degree of process intensification with regard to temperature control. This fact is found promising in respect to high CO and CO₂ conversions, less byproduct formation and catalyst damage due to thermal effects. In addition, transportability of compact

reactors and decentralized methane production are valued as the key aspects for the application of a microreactor in the framework of conversion of renewable energy into methane like in the MINERVE project. Drawbacks of the new technology are examined in detail, which include improper design and fluid maldistribution, improvement of reaction rates and hot spot formation despite miniaturization and frequent catalyst replacement due activity loss of the catalyst.

Catalyst performance

A commercial Ni-based catalyst is tested under methanation conditions using CO, CO₂ and their mixtures as feed in the range between 300 and 450°C at 6 bar. Carbon monoxide (9.1 vol. %) causes harsh deactivation of the catalyst at all examined conditions limiting the life-time to several hours. Worst catalyst stability is obtained in the low temperature range between 360-400°C which improves above 400°C. According to the literature, a change in reaction pathway seems as a feasible explanation leading to less coke accumulation on the catalyst. Hydrogen improves the catalyst stability with a higher H₂/C-ratio which is in-line with the literature. Observed quicker deactivation of smaller catalyst particles could partially be explained by mass transfer resistances, however, unknown processes could not be excluded. Post-analysis of representative catalyst samples confirm the formation of carbonaceous species via WDS, which is supported by the drastic decrease of the BET surface by a factor of 3.

Three catalyst systems are tested under CO₂ methanation conditions for comparison reasons: a commercial (Ni-based), a self-prepared (Ni-based) and a bimetallic Ni₃Fe catalyst. All catalysts show very good long-term stability in over 100 h TOS experiment. At temperatures above 350°C, all catalysts show better selectivity towards methane which decreases at temperatures below 320°C due to CO production. At the same time, higher degradation rates are observed giving hint to the deactivation by CO. The best performance is obtained from a bimetallic Ni₃Fe catalyst above 350°C in terms of conversion and selectivity towards methane. However, it suffers from extremely high CO production and quick deactivation at lower temperatures. Satisfying overall performance is obtained from commercial and self-prepared Ni catalysts in the entire temperature range. The post-analysis of the commercial catalyst sample via WDS reveals the formation of surface carbon which is likely the main deactivation cause. The carbon surface concentration is by a factor of 5 lower compared to the catalyst aged under CO methanation conditions, which is also supported by a relatively low BET surface change.

By using CO/CO₂/H₂ mixtures as feed, preferential conversion of CO is observed. CO conversion is unaffected with further CO₂ addition. According to the deactivation experiments, fast activity loss is primarily attributed to the CO presence.

The obtained initial activity of the commercial catalyst could be successfully compared with literature models. Methanation of CO/H₂, CO₂/H₂ and their mixtures is reflected with very good accuracy by

the Kopyscinski model [58]. However, its validity is given only below 400°C due to the absence of the thermodynamic consideration of the RWGS reaction. The models of Zhang et al. [56] and Xu and Froment [67] lack in accuracy regarding conversion of both species, but are thermodynamically consistent in the entire temperature range. For CO₂ methanation, the model of Koshany et al. [68] provides the most accurate results and is thermodynamically consistent.

Reactor development & performance tests

Based on the knowledge of the literature, thermodynamic study and catalytic activity tests, the design procedure for two microreactor prototypes is illustrated paying attention to lateral dimensions of the cooling and reaction zone, while optimizing in respect to pressure drop, catalyst mass and possible heat transfer phenomena. The microstructured reactors for methanation of CO/CO₂ mixtures are manufactured and tested in the lab-scale using syngas throughputs <1.4 Nm³/h. The reactor design according to Prototype 1 is characterized as a pure heat exchanger prior to reaction experiments. Up to 700 W could be removed with heat transfer media, while reducing the heat losses to the environment effectively with Freeflow-100X[®]. Under reaction conditions, characteristics of the reactor and catalyst system are investigated. This includes overheating of the packed bed inlet in absence/lack of heat removal and extinguishment of the reaction front by excessive coolant flows. By applying gases and water as a heat transfer media, an adiabatic temperature rise could be successfully suppressed. Nevertheless, an overheating of the catalyst of approx. 100-200°C, depending on syngas throughput, occurs. The peak temperature is barely coolant flow and medium dependent, which could be explained with possible heat transfer resistances in the metal or the catalyst bed. At high cooling flows, stabilization of the system via heating elements is required. Due to polytropic operation, the manufactured device allows full conversion of CO and over 95% of CO₂ in one single step, which makes the system superior to all known conventional devices. Compared to known patented microstructured units for exothermic reactions, the presented reactor exhibits some novelties: easy maintenance (quick catalyst replacement), heat management due to integrated heating elements in combination with fluid passages and pressurized operation of the cooling zone.

The Prototype 2 reactor exhibits much better flexibility regarding the temperature control, since it allows a defined dosage of coolant according to the heat release from reaction without extinguishment of the reaction under well optimized cooling by evaporating water. This reactor concept is laid down in a patent application and is meanwhile successfully applied in industrial application.

CFD analysis of the microstructured prototype

A 3D CFD model of the manufactured device (Prototype 1) is created and verified in terms of heat

transfer experiments and temperature distribution in the reactor. On the cooling side, uniform distribution of the fluid is calculated due to several redirections. Laminar regime ($Re < 1500$) using air (100 Nl/min) yields a constant Nusselt number of 3.7 which corresponds to a heat transfer coefficient up to $400 \text{ W}/(\text{m}^2\text{K})$ at the given conditions. Fins are found to improve the heat transfer from the packed bed by up to 30%. Further improvement is limited by the separating metal wall.

On the reaction zone, the heat transfer resistance from the packed bed to the wall could be neglected in industrial applications using particles of $450 \mu\text{m}$ in the air cooled reactor. 20 K overheating is found as the maximum temperature gradient in transversal direction. The model could be successfully used for parameter estimation, i.e. to determine the effective packed bed heat conductivity based on the observed temperature profiles from experiments with the help of an artificial heat source mimicking the reaction heat release. The bottleneck of the system regarding heat transport under methanation conditions could be identified by varying the thermal properties of the packed and the metal housing. The metal wall is identified as the main heat transport resistance in an oil cooled reactor. Due to the high heat transfer coefficients of oil as coolant in CFD calculation studies, the results can be transferred to the evaporation cooling experiments.

The entire reaction system is also simulated using the kinetic models of Xu and Froment [67]. Experimental temperature profiles could be recreated by adjusting the axial position of the reaction zone. Despite properly calculated temperature profiles in the reactor, the results still lack consistency on the chemical level, which is attributed to the accuracy of the kinetic rate model and the simplicity of the used Porous Body model in Fluent®.

Understanding the micro packed bed

The main characteristics of the packed bed, e.g. porosity, flow and heat conductivity distribution are elucidated and correlations and models in the literature are summarized.

An alternative meshing strategy for packed beds based on structured meshes for CFD analysis is presented and validated using the literature correlations in terms of the porosity, flow distribution, pressure drop, heat transfer and chemical reaction.

Regarding catalysis, local non-uniformities of the reaction rate on the particle surface in the packed in the pinch points are found to not significantly contribute to the overall reactor performance even at low d_t/d_p -ratio of 3.5 ($Re < 315$). Heat transfer issues on the particles at the wall are detected for the particle Reynolds number less than 100, which become negligible at higher Reynolds numbers greater than 210. Thus, the microreactors in this work, which are operated at Reynolds numbers of approx. 500, can be considered, according to CFD results, as ideal plug-flow reactors.

9 Zusammenfassung

Die vorliegende Arbeit war motiviert durch das MINERVE PtG Projekt (2012 bis 2015) und beinhaltet die Entwicklung von zwei mikrostrukturierten Reaktorprototypen für die Methanherstellung aus CO/CO₂/H₂ Gemischen, die auf der theoretischen sowie experimentellen Ebene detailliert untersucht wurden. Die Arbeit ist in sechs thematische Kapitel gegliedert, die zu einem ganzheitlichen Verständnis der Aufgabenstellung beitragen.

Grundlagen des Reaktionssystems

In den Grundlagen wurde die Katalysatorauswahl für die Methansynthese diskutiert, die jedoch aufgrund des Wirtschaftlichkeitsaspekts auf Ni-basierte Systeme reduziert werden kann. Der Methanisierungsmechanismus von CO und CO₂ basierend auf der Carbide-Theorie sowie auf dem Modell von Solymosi et al. [40] wurden näher beleuchtet und erklärt. Hinsichtlich Kinetik wurden Befunde von unterschiedlichen Gruppen zusammengetragen, die die inhibierende Wirkung von CO und den positiven Einfluss von Temperatur und H₂-Konzentration auf die Reaktionsrate unterstreichen. Der Einfluss weiterer relevanter Faktoren wie Wasserdampf und Katalysatorträgermaterial wurde ebenfalls diskutiert. Einige LHHW Kinetikausdrücke aus der Literatur wurden ausgewählt, die hinsichtlich ihrer Eignung zur Beschreibung von CO und CO₂-Methanisierung geprüft werden sollten. Darunter fallen die Arbeiten von Xu and Froment [67], Kopyscinski et al. [58], Zhang et al. [56] and Koshany et al. [68].

Eine thermodynamische Gleichgewichtsstudie unter Berücksichtigung der MINERVE Prozessbedingungen wurde durchgeführt. Daraus ergab sich ein optimales Prozessfenster im Hinblick auf CO und CO₂ Umsätze zwischen 300 und 450°C. Die Variation des H₂/C-Verhältnisses, sowie des Gesamtdrucks und des Wassergehalts zeigte, dass Wasserstoff die effektivste Strategie für die Erhöhung der Methan- ausbeute ist. Sowohl CO als auch CO₂ tragen zur Koksablagung bei, wobei die Spezies CO₂ eher im Nieder- und CO im Hochtemperaturbereich Kohlenstoff bilden. Neben Wasserstoff trägt Wasserdampf im Bereich weniger Volumenprozent zu einer effizienten Unterdrückung der Koksablagerungen bei.

Des Weiteren wurden einige Desaktivierungsmechanismen des Katalysators aus der Literatur beleuchtet. Dabei lag der Fokus auf den Fouling-Prozessen, die durch Koks verursacht werden, auf der Morphologie des Kohlenstoffs, sowie auf Regenerierungsmethoden des desaktivierten Katalysators.

Vergleich der konventionellen und mikrostrukturierten Technologien für die Methanherstellung

Die Literaturrecherche der konventionellen Reaktortechnik für die Methansynthese brachte die Erkenntnis, dass der adiabate Festbettreaktor der verbreitetste Reaktortyp in der Industrie ist. Die wesentlichen Nachteile der adiabaten Betriebsweise wurden erklärt, die z.B. geringe Methan- ausbeute, erhöhte Nebenproduktbildung, schnelle Katalysatordesaktivierung aufgrund der Fouling- bzw. Sinterphänomene,

sowie Metal-Dusting beinhalten. Zudem werden auf der Prozess-Ebene mehrere Reaktorstufen mit Zwischenkühlung und zusätzlicher Peripherie benötigt. Mikrostrukturierte Reaktortechnologie bietet dagegen einen hohen Grad der Prozessintensivierung im Hinblick auf Temperaturkontrolle. Dies bedeutet hohe CO und CO₂ Umsätze, weniger Nebenproduktbildung und verringerte Katalysatordeaktivierung aufgrund thermischer Effekte. Zudem sind kompakte Mikroreaktoren und die dezentrale Methansynthese ein wesentlicher Aspekt bei der Umwandlung erneuerbarer Energie in Methan, wie z.B. im MINERVE-Projekt. Die Herausforderungen der Mikrostrukturtechnologie wurden diskutiert, die sich auf die Herstellung und Fluid-Gleichverteilung, Beschleunigung der Reaktionsrate, Temperaturführung sowie Strategie zum Katalysatorwechsel im Falle der Desaktivierung beziehen.

Katalysatorstudien

Ein kommerzieller Ni-basierter Katalysator wurde auf Methanbildungsaktivität sowohl ausgehend von CO, CO₂, als auch deren Gemisch in einem Temperaturbereich zwischen 300 und 450°C bei 6 bar untersucht. Kohlenstoffmonoxid (9.1 Vol. %) führte zu einem schnellen Aktivitätsverlust innerhalb weniger Stunden bei allen untersuchten Bedingungen. Der schnellste Aktivitätsabfall wurde im Nieder-temperaturbereich zwischen 360-400°C festgestellt. Dies widerspricht vielen Studien aus der Literatur; gleichzeitig argumentieren einige Gruppen mit einer Änderung im Reaktionsweg, die zu weniger Koksblidung bei hoher Temperatur beitragen kann. Der Wasserstoffanteil verbesserte die Katalysatorstabilität, was der Erwartungshaltung anhand der Literaturstudie entspricht. Die beobachtete schnelle Desaktivierung von kleinen Katalysatorpartikeln kann eventuell mit Stofftransportlimitierung erklärt werden, jedoch konnten weitere Prozesse nicht ausgeschlossen werden. Die Analyse repräsentativer verbrauchten Katalysatorproben mittels WDS stützte die These, dass kohlenstoffhaltige Spezies zur Desaktivierung beitragen. Diese Vermutung wurde mit BET-Daten untermauert; eine Abnahme der spezifischen Oberfläche um den Faktor 3 wurde festgestellt.

Drei Katalysatorsysteme wurden unter CO₂-Methanisierungsbedingungen untersucht und verglichen: kommerzieller Ni-basierter, selbst hergestellter sowie bimetallischer Ni₃Fe Katalysator. Alle Systeme zeigten gute Langzeitstabilität über 100 h. Bei Temperaturen oberhalb 350°C zeigten alle Katalysatorsysteme bessere Selektivität zu Methan. Darüber hinaus wurde ein stetiger Aktivitätsverlust beobachtet, der auf Desaktivierung durch CO zurückgeführt wurde. Beste Stabilität zeigte der bimetallische Ni₃Fe Katalysator oberhalb von 350°C gepaart mit höchsten Umsätzen und Selektivitäten zu Methan. Bei niedriger Temperatur führte die hohe Selektivität zu CO zur schnellen Katalysatordeaktivierung bei diesem Katalysator. Bei der Analyse des gebrauchten kommerziellen Katalysators via WDS wurden Kohlenstoffablagerungen auf der Oberfläche festgestellt, die mit großer Wahrscheinlichkeit zur Katalysatordeaktivierung beitragen. Die Konzentration des Oberflächenkohlenstoffs war um den Faktor 5

geringer als bei den Methanisierungsexperimenten mit CO. Dies spiegelte sich auch in der spezifischen BET-Oberfläche wider, die sich kaum durch den Gebrauch reduziert hat. Bei der Methanisierung von CO/CO₂/H₂ Mischungen konnte bevorzugte Umsetzung von CO beobachtet werden. Zusätzliche Zugabe von CO₂ hatte keinen Einfluss auf den CO Umsatz. Entsprechend den Ergebnissen aus der CO-Methanisierung konnte die Desaktivierung der CO-Konzentration zugeschrieben werden.

Die Anfangsaktivität des kommerziellen Katalysators konnte fast mit allen ausgewählten Literaturkinetiken hinreichend gut beschrieben werden. Die Methanisierung von CO, CO₂ und deren Gemisch wurde mit der Kinetik von Kopyscinski et al. [58] mit hoher Genauigkeit beschrieben; jedoch ist das Modell aufgrund fehlender Betrachtung der RWGS Reaktion nur unterhalb von 400°C gültig. Die Kinetiken von Zhang et al. [56] and Xu and Froment [67] zeigten deutliche Abweichungen hinsichtlich Umsatz beider Spezies, waren jedoch im gesamten Temperaturbereich thermodynamisch konsistent. Für die reine Methanisierung von CO₂ zeigte die Kinetik von Koshany et al. [68] sehr gute Übereinstimmung und war zudem im betreffenden Temperaturbereich thermodynamisch konsistent.

Reaktorentwicklung

Ausgehend von Literatur-, Thermodynamik- und Katalysatorstudien, wurde ein Design für zwei Mikroreaktorprototypen im Hinblick auf die lateralen Abmessungen der Kühl- und Reaktionszonen unter Beachtung des Druckverlusts, benötigter Katalysatormasse und Wärmetransporteigenschaften entwickelt. Die gefertigten Prototypen für Methanisierung von CO/CO₂ Gemischen wurden im Technikum mit Durchsätzen bis 1.4 Nm³/h ausgiebig untersucht. Das Reaktordesign entsprechend dem Prototyp 1 wurde zunächst als reiner Wärmeübertrager charakterisiert. Durch gute Isolation des Reaktors mit dem Pulver Freeflow-100X[®] konnten bis zu 700 W mit verschiedenen Wärmeübertragungsmedien aus dem Reaktor extrahiert werden. Unter Reaktionsbedingungen wurden bestimmte Charakteristika des Reaktors und des Katalysatorsystems untersucht. Darunter fallen die Hot-Spot Bildung sowie das Erlöschen der Reaktionsfront bei exzessiver Kühlung. Bei Verwendung von Gase und Wasser als Wärmeübertragungsmedien konnte eine adiabate Temperaturerhöhung erfolgreich vermieden werden. Die zugelassene Überhitzung von ca. 100-200°C war abhängig vom Syngasdurchsatz. Der beobachtete Temperaturhöchstwert war kaum abhängig vom Kühlmediumdurchsatz, was auf einen möglichen Wärmetransportwiderstand entweder im Festbett oder im Metallgehäuse hindeutete. Bei hohen Kühlraten war entgegen der sonst autothermen Fahrweise ein Stabilisierung des Reaktors mittels Heizpatronen notwendig. Aufgrund des polytropen Temperaturverlaufs im Reaktor war bereits im Prototyp 1 vollständiger Umsatz von CO und über 95% Umsatz von CO₂ in einem Schritt möglich. Diese Tatsache machte dieses System der konventionellen Technik weit überlegen. Im Vergleich zu bereits patentierten Mikrostrukturreaktoren für exotherme Reaktionen, zeigte der in dieser Arbeit vorgestellte

Mikroreaktor bereits Neuerungen, die z.B. einen schnellen Katalysatorwechsel, Wärmemanagement aufgrund integrierter Heizpatronen in Kombination mit Kühlpassagen, sowie die Möglichkeit die Kühlpassagen mit Druck zu beaufschlagen betreffen.

Das Design entsprechend dem Prototyp 2 zeigte eine deutlich bessere Flexibilität der Temperaturkontrolle, da durch den zweiten Kühlmittelzugang eine gezielte Dosierung des Kühlmediums entsprechend der Wärmeerzeugung durch Reaktion erlaubte. Die zudem optimierten Kühlzonen erlaubten die Aufrechterhaltung der Reaktion, selbst wenn aus Kühlwasser überhitzter Dampf generiert wurde. Das Konzept wurde in einem Patent niedergelegt und findet mittlerweile Anwendung in industriellem Einsatz.

CFD-Studie des mikrostrukturierten Reaktors

Ein 3D Modell des Prototyps 1 wurde für CFD Studien angefertigt und anhand der Wärmeübertragungsexperimente hinsichtlich der übertragenen Wärmemengen und der Temperaturverteilung im Reaktor validiert. Die Simulation zeigte einheitliche Verteilung des Kühlfluids aufgrund der mehrfachen Umlenkung in der Kühlzone. Bei Verwendung von Gas als Kühlmedium mit Durchsätzen bis 100 NI/min liegt laminare Strömung ($Re < 1500$) vor, die zu einer konstanten Nusselt-Zahl von 3.7 führt. Dies entspricht einem Wärmeübergangskoeffizient von ca. $400 \text{ W}/(\text{m}^2\text{K})$ bei gegebenen Bedingungen. Stege in der Kühlzone verbesserten die Wärmeabfuhr bis zu 30%, wobei der Hauptwärmtransportwiderstand durch die Trennwand zwischen Kühl- und Reaktionszone verursacht wurde.

Auf der Reaktionsseite konnte der Wärmtransportwiderstand von der Festbettmitte bis zur Reaktorwand als limitierend ausgeschlossen werden, wenn Partikeldurchmesser $< 450 \mu\text{m}$ in einem luftgekühlten Reaktor verwendet werden. Eine maximale Temperaturerhöhung von ca. 20 K wurde zur Strömungsrichtung berechnet. Das Simulationsmodell konnte für die Bestimmung der effektiven Wärmeleitfähigkeit des Festbetts unter Berücksichtigung der Temperaturprofile aus den Experimenten und einer künstlichen Wärmequelle, die die Reaktionswärme nachahmt, genutzt werden. Der Wärmtransportwiderstand des Reaktorsystems unter Methanisierungsbedingungen konnte durch Variation der effektiven Wärmeleitfähigkeit des Festbetts und der Wärmeleitfähigkeit des Reaktorwerkstoff auf die Metalltrennwand als Hauptwärmtransportwiderstand reduziert werden. Eine Reaktorsimulation unter Einbindung der Reaktionskinetik von Xu and Froment [67] wurde durchgeführt. Experimentell beobachtete Temperaturprofile konnten unter Anpassung der axialen Festbettposition reproduziert werden. Trotz der guten Übereinstimmung der Temperaturprofile im Reaktorgehäuse, konnte der Umsatz der Kohlenstoffspezies nicht richtig abgebildet werden. Dies kann eventuell auf die mangelnde Genauigkeit des Kinetikmodells sowie die vereinfachten Annahmen mittels Porous-Body Modells in Fluent[®] zurückgeführt werden.

Simulation des Festbetts

Die wesentlichen Charakteristika des Festbetts wie z.B. die Porosität, Strömungs- und Wärmeleitfähigkeitsverteilung wurden beleuchtet und passende Korrelationen/Modelle für die Anwendung auf das Mikrofestbett zusammengefasst. Eine alternative Vernetzungsstrategie für eine Festbettgeometrie basierend auf strukturierten Netzen wurde vorgestellt, die sehr schnell ist und eine sehr gute Genauigkeit bei der Berechnung der Strömungs- und Wärmeverteilung im laminaren- und Übergangsströmungsbereich liefert.

Die Herangehensweise der Geometrieerstellung samt CFD Ergebnissen wurde im Hinblick auf Porositäts- und Strömungsverteilung, Druckverlust, Wärmetransport und Katalyse, mit den ausgewählten Korrelationen validiert.

Die Simulation der Reaktion auf den Partikeln in der Schüttung zeigte eine verminderte Reaktionsgeschwindigkeit an den Berührungspunkten zwischen den einzelnen Partikeln und der Partikel-Wand, die sich jedoch sogar bei geringem Rohr-zu-Partikel-Verhältnis von 3.5 kaum auf die Konzentrationsverläufe der einzelnen Komponenten auswirkte. Die Studien bezüglich des Wärmetransportverhaltens auf Partikeln führten zur Schlussfolgerung, dass es im unteren Reynoldsbereich zu einer starken Abweichung der Nusselt-Zahl zwischen den Partikeln an der Wand und im Schüttungsinnen kommen kann. Ab einer Reynolds-Zahl größer als 210, kann jedoch der Wärmetransporteffekt vernachlässigt werden. Die vorgestellten Mikroreaktorprototypen in dieser Arbeit, die im Reynoldsbereich größer als 500 betrieben wurden und ein Rohr-zu-Partikel-Verhältnis von mindestens 4 aufwiesen, können daher laut den Erkenntnissen aus der CFD Studie als "ideale" Rohrreaktoren aufgefasst werden.

Symbols and abbreviations

Latin symbols	Description	SI units
A	Surface area	$m^2 \cdot m^{-3}$
a_V	Volume related surface area	$m^2 \cdot m^{-3}$
a_i	Activity of the comp. i	—
C_i	Molar concentration of the comp. i	$mol \cdot m^{-3}$
$C_{p,i}$	Specific heat capacity of the comp. i	$J \cdot kg^{-3} K^{-1}$
$D_{i,(eff)}$	(Effective) diffusion coefficient of the comp. i	$m^2 \cdot s^{-1}$
d	Diameter	m
E_A	Activation energy	$J \cdot mol^{-1}$
F_i	Mole of the comp. i	mol
\dot{F}_i	Molar flow of the comp. i	$mol \cdot s^{-1}$
G	Specific throughput	$kg \cdot m^{-2}$
G_R	Molar Gibbs energy	$J \cdot mol^{-1}$
H_R	Molar reaction enthalpy	$J \cdot mol^{-1}$
h	Height	m
h_V	Evaporation heat	$J \cdot kg^{-1}$
K	Equilibrium constant	—
K_i	Adsorption constant	<i>a.u.</i>
k_G	Overall mass transfer coefficient	$m \cdot s^{-1}$
k_i	Reaction rate constant	<i>a.u.</i>
L	Length	m
m	Mass	kg
n_i	Mole amount of the comp. i	mol
$p^{(i)}$	(Partial) pressure	Pa
P	Perimeter	m
\dot{q}_V	Volumetric heat density	$W \cdot m^{-3}$
R, r	Radius, radial coordinate	m
\dot{Q}	Heat amount	W
R	Universal gas constant	$J \cdot mol^{-1} K^{-1}$
R_i	Net reaction rate of the comp. i	$mol \cdot s^{-1} kg^{-1}$
r_{eff}	Observable reaction rate	$mol \cdot s^{-1} m^{-3}$
S_R	Molar reaction entropy	$J \cdot mol^{-1}$
$S_{i,k}$	Selectivity from the comp. i to k	—

T	Temperature	K
t	Time	s
u	Gas velocity	$m \cdot s^{-1}$
V	Volume	m^3
$\dot{V}_{(i)}$	Volumetric flow (of the comp. i)	$m^3 \cdot s^{-1}$
w	Width	m
X_i	Conversion of the comp. i	—
x	Lateral length	m
x_i	Molar fraction of the comp. i	—
Y_i	Yield of the comp. i	—
z	Axial coordiante	m

Greek symbols	Description	SI units
α	Heat transfer coefficient	$W \cdot m^{-2} K^{-1}$
Δ	Difference	—
ε	Porosity	—
$\eta_{Cat.}$	Catalyst effectiveness factor	—
ρ	Density	$kg \cdot m^{-3}$
λ_i	Heat conductivity of the species i	$W \cdot m^{-1} K^{-1}$
$\tau_{mod,i}$	Modified residence time in terms of vol. flow of the comp. i	$m^3 \cdot kg^{-1} s^{-1}$
Θ	Angle	—
Λ_r	Model parameter by Winterberg et al. [162]	$W \cdot m^{-1} K^{-1}$
μ_i	Chemical potential of the component i	$J \cdot mol^{-1}$
ν	Kinematic viscosity	$m^2 \cdot s^{-1}$
ξ	Pressure loss coefficient	—
Π	Product	—
Φ	Weisz-modulus	—

Abbreviations

BET	Brunauer-Emmett-Teller
BJH	Barrett-Joyner-Halenda
Ca	Carberry Number
CAPEX	Capital Expenditure
CAD	Computer Aided Design

CFD	Computational Fluid Dynamics
DAE	Dissociative Adsorption Energy
DFT	Density-Functional Theory
FB	Fixed Bed
FIC	Flow Indication Control
FL	Fluidized Bed
GC	Gas Chromatograph
GHSV	Gas Hourly Space Velocity
HC	Heating Cartridge
IMVT	Institut für Mikroverfahrenstechnik
KIT	Karlsruhe Institute of Technology
LHHW	Langmuir-Hinshelwood-Hougen-Watson
MFC	Mass Flow Controller
MSM	Mark and Separate Meshing approach
NTP	Normal Temperature and Pressure
$Nu_{(P)}$	(Particle) Nusselt Number
p.p.	Percentage Point
PB	Packed Bed
Pe	Peclet Number
PI	Pressure Indication
PIC	Pressure Indication and Control
Pr	Prandtl Number
PtG	Power-to-Gas
$Re_{(P)}$	(Particle) Reynolds Number
RLS/RDS	Rate-Limiting/Determining Step
RWGS	Reverse Water-Gas Shift
Sc	Schmidt Number
SEM	Scanning Electron Microscopy
Sh	Sherwood Number
SiC	Silicon Carbide
SNG	Synthetic Natural Gas
SOEC	Solid Oxide Electrolysis Cell
STP	Standard Temperature and Pressure
TIC	Temperature Indicator Control

TOS	Time On Stream
TON	Turnover Number
TPH	Temperature Programmed Hydrogenation
TR	Tubular Reactor
UDF	User Defined Function
VDI	Verband Deutscher Ingenieure
WDS	Wavelength-Dispersive Spectroscopy
WGS	Water-Gas Shift
XRD	X-Ray Diffraction

Sub- and superscripts

0	Standard/Reference/Initial
*	Adsorbed state
A	Activation
ax	Axial
bulk	Bulk, center of the bed
c	Coolant
cat	Catalyst
cell	Cell element
el.	Electrical
eff	Effective
Eq	Equilibrium state
f/g/s	Fluid/gas/solid
film	Film
fric	Friction
h	Hydraulic
in	Inlet
mod	Modified
N	Normal
out	Outlet
p	Particle
r	Radial
ref	Reference
R	Reactor/Reaction

s	Solid
static	Static contribution of the heat conductivity
surf	Surface
syn	Syngas
sys	System
t	Tube
tot	Total
V	Volume
void	Void space
wall	Wall region

References

- [1] BUNDESMINISTERIUM FÜR WIRTSCHAFT UND ENERGIE: <http://www.erneuerbare-energien.de>. Online, accessed: March 9, 2017.
- [2] ZUKUNFT ERDGAS E.V.: <https://www.zukunft-erdgas.info/markt/absatzmaerkte/stromerzeugung>. Online, accessed: March 9, 2017.
- [3] SABATIER P, SENDERENS J B: *Comptes Rendus Des Séances De L'Académie Des Sciences. Chimie*, 6, 1902.
- [4] ROSTRUP-NIELSEN J R: *Industrial relevance of coking*. *Catalysis Today*, 37:225–232, 1997.
- [5] FISCHER F, TROPSCH H, DILTNEY P. *Brennst.-Chem.*, 6:265, 1925.
- [6] VANNICE M A: *The Catalytic Synthesis of Hydrocarbons from H₂/CO Mixtures over the Group VIII Metals*. *Journal of Catalysis*, 37:462–473, 1974.
- [7] BLIGAARD T, NORSKOV J K, DAHL S, MATHIESEN J, CHRISTENSEN C H, SEHSTEDT J: *The Bronsted-Evans-Polanyi relation and the volcano curve in heterogeneous catalysis*. *Journal of Catalysis*, 224:206–217, 2004.
- [8] BOUDART M, BRENNER H: *Kinetics of Chemical Processes: Butterworth-Heinemann Series in Chemical Engineering*. Butterworth-Heinemann, Stoneham, USA, 1991.
- [9] SEGLIN L, GEOSITIS R, FRANKO B R GRUBER G: *Survey of Methanation Chemistry and Processes*, chapter 1, pages 1–30. American Chemical Society, Washington, D.C., 1975.
- [10] BARTHOLOMEW C H: *Carbon Deposition in Steam Reforming and Methanation*. *Catalysis Reviews*, 24:67–112, 1982.
- [11] LUNDE P J, KESTER F: *Rates of methane Formation from Carbon Dioxide and Hydrogen Over a Ruthenium Catalyst*. *Journal of Catalysis*, 30:423–429, 1973.
- [12] KOWALCZYK Z, STOLECKI K, RARNG-PILECKA W, MISKIEWICZ E, WILCZKOWSKA E KARPINSKI Z: *Supported ruthenium catalysts for selective methanation of carbon oxides a very low CO_x/H₂ ratios*. *Applied Catalysis A: General*, 342:35–39, 2008.
- [13] KARN F S, SHULTZ J F, ANDERSON R B: *Hydrogenation of carbon monoxide and carbon dioxide on supported ruthenium catalysts at moderate pressures*. *Industrial Engineering Chemistry Product Research and Development*, 4:265–269, 1965.

- [14] PONEC V: *Some Aspects of the Mechanism of Methanation and Fischer-Tropsch Synthesis*. Catalysis Reviews, 18:151–171, 1978.
- [15] LOC L C, NGUYEN M H, NGUYEN K D, NGUYEN H H P, THOANG H S: *A study on methanation of carbon monoxide over catalysts NiO/TiO₂ and NiO/ γ -Al₂O₃*. Advances in Natural Sciences, 7:91–105, 2006.
- [16] MILLS A G, STEFFGEN F W: *Catalytic Methanation*. Catalysis Reviews: Science and Engineering, 8:159–210, 1974.
- [17] PANAGIOTOPOULOU P, KONDARIDES D, VERYKIOS X: *Selective methanation of CO over supported Ru catalysts*. Applied Catalysis B: Environmental, 88:470–478, 2009.
- [18] VANNICE M A, GARTEN R L: *Metal-Support Effects on the Activity and Selectivity of Ni Catalysts in CO/H₂ Synthesis Reactions*. Journal of Catalysis, 56:236–248, 1979.
- [19] ROSS J R H: *Metal catalysed methanation and steam reforming*. In BOND G C, WEBB G (editor): *Catalysis*., volume 7, pages 1–45. The Royal Society of Chemistry, 1985.
- [20] STORCH H H, GOLUMBIC N, ANDERSON R B: *The Fischer-Tropsch and Related Syntheses*. John Wiley & Sons, New York, 1951.
- [21] CRAXFORD S R, RIDEAL E K: *The Mechanism of the Synthesis of Hydrocarbons from Water Gas*. Journal of the Chemical Society, pages 1604–1617, 1939.
- [22] KUMMER J T, EMMETT P H: *Fischer-Tropsch Synthesis Mechanism Studies. The Addition of radioactive Alcohols to the Synthesis Gas*. Journal of the American Chemical Society, 75:5177–5183, 1953.
- [23] ARAKI M, PONEC V: *Methanation of Carbon Monoxide on Nickel and Nickel-Copper Alloys*. Journal of Catalysis, 44:439–448, 1976.
- [24] BLYHOLDER G, NEFF L D: *Infrared study of the interaction of carbon monoxide and hydrogen on silica-supported iron*. The Journal of Physical Chemistry, 66:1664–1667, 1962.
- [25] GOODMAN D W, KELLEY R D, MADEY T E, YATES J T JR.: *Kinetics of the Hydrogenation of CO over a Single Crystal Nickel Catalyst*. Journal of Catalysis, 63:226–234, 1979.
- [26] EIDUS Y T: *The mechanism of the Fischer-Tropsch reaction and the initiated hydrolymerisation of alkenes, from radiochemical and kinetic data*. Russian Chemical Reviews, 36:338–351, 1967.

- [27] HAPPEL J, CHEH H Y, OTAROD M, OZAWA S, SEVERDIA A J, YOSHIDA T, FTHENAKIS V: *Multiple Isotope Tracing of Methanation over Nickel Catalysts*. *Journal of Catalysis*, 75:314–328, 1982.
- [28] CANT N W, BELL A T: *Studies of Carbon Monoxide Hydrogenation over Ruthenium Using Transient Response Techniques*. *Journal of Catalysis*, 73:257–271, 1981.
- [29] VLASENKO V M, YUZEFOVICH G E: *Mechanism of the Catalytic Hydrogenation of Oxides of Carbon to Methane*. *Russian Chemical Reviews*, 38:728–739, 1969.
- [30] DARENSBOURG D J, BAUCH C G, OVALLES C: *Mechanistic aspects of catalytic carbon dioxide methanation*. *Reviews in Inorganic Chemistry*, 7:315–340, 1985.
- [31] BALDWIN V H JR., HUDSON J B: *Coadsorption of hydrogen and carbon monoxide on (111) platinum*. *Journal of Vacuum Science & Technology*, 8:49–52, 1971.
- [32] FUJITA S, TERUNUMA H, NAKAMURA M, TAKEZAWA N: *Mechanisms of Methanation of CO and CO₂ over Ni*. *Industrial & Engineering Chemistry Research*, 30:1146–1151, 1991.
- [33] ALSTRUP I: *On the Kinetics of CO Methanation on Nickel Surfaces*. *Journal of Catalysis*, 151:216–225, 1994.
- [34] OTAROD M, HAPPEL J, WALTER E: *Transient isotopic tracing of methanation kinetics with parallel paths*. *Applied Catalysis A: General*, 160:3–11, 1997.
- [35] ANDERSSON M P, ABILD-PEDERSEN F, REMEDIKIS I N, BLIGAARD T, JONES G, ENGBAEK J, LYTKEN O, HORCH S, NIELSEN J H, SEHSTEDT J, ROSTRUP-NIELSEN J R, NORSKOV J K, CHORKENDORFF I: *Structure sensitivity of the methanation reaction: H₂-induced CO dissociation on nickel surfaces*. *Journal of Catalysis*, 255:6–19, 2008.
- [36] COENEN J W E, VAN NISSELROOY P F M T, DE CROON M H J M, VAN DOOREN P F H A, VAN MEERTEN R Z C: *The dynamics of methanation of carbon monoxide on nickel catalyst*. *Applied Catalysis*, 25:1–8, 1986.
- [37] FALCONER J.L., ZAĞLI A.: *Adsorption and Methanation of Carbon Dioxide on Nickel/Silica Catalyst*. *J. Cat.*, 62:280–285, 1980.
- [38] IIZUKA T, TANAKA Y, TANABE K: *Hydrogenation of CO and CO₂ over Rhodium catalysts supported on various metal oxides*. *Journal of Catalysis*, 76:1–8, 1982.

- [39] BEULS A, SWALUS C, JACQUEMIN M, HEYEN G, KARELOVIC A, RUIZ P: *Methanation of CO₂: Further insight into the mechanism over Rh/γ-Al₂O₃ catalyst*. Applied Catalysis B: Environmental, 113-114:2–10, 2012.
- [40] SOLYMOSI F, ERDOEHELYI A, KOCSIS M: *Methanation of CO₂ on Supported Ru Catalysts*. Journal of the Chemical Society, 77:1003–1012, 1981.
- [41] MEDSFORTH S: *CLXIX.-Promotion of catalytic reactions. Part I*. Journal of the Chemical Society, Transactions, 123:1452–1469, 1923.
- [42] WEATHERBEE G D, BARTHOLOMEW C H: *Hydrogenation of CO₂ on group VIII Metals. II Kinetics and Mechanism of CO₂ Hydrogenation on Nickel*. Journal of Catalysis, 77:460–472, 1982.
- [43] PEEBLES D, GOODMAN D: *Methanation of Carbon Dioxide on Ni(100) and the Effects of Surface Modifiers*. Journal of Physical Chemistry, 87:4378–4387, 1983.
- [44] HENDERSON M A, WORLEY S D: *An Infrared Study of the Hydrogenation of Carbon Dioxide on Supported Rhodium Catalysts*. Journal of Physical Chemistry, 89:1417–1423, 1984.
- [45] PRAIRIE M, RENKEN A, HIGHFIELD J, THAMPI K, GRAETZEL M: *A Fourier Transform Infrared Spectroscopic Study of CO₂ Methanation on Supported Ruthenium*. Catalysis Today, 129:130–144, 1991.
- [46] GUPTA N, KAMBLE V, KARTHA V, IYER R, THAMPI K, GRATZEL M: *FTIR spectroscopic study of the interaction of CO₂ and CO₂ + H₂ over partially oxidized Ru/TiO₂ catalyst*. Journal of Catalysis, 146:173–184, 1994.
- [47] LIOTTA L, MARTIN G, DEGANELLO G: *The Influence of Alkali Metal Ions in the Chemisorption of CO and CO₂ on Supported Palladium Catalysts: A Fourier Transform Infrared Spectroscopic Study*. Journal of Catalysis, 164:322–333, 1996.
- [48] MARWOOD M, DOEPPER R, RENKEN A: *In-situ surface and gas phase analysis for kinetic studies under transient conditions: The catalytic hydrogenation of CO₂*. Applied Catalysis A: General, 151:223–246, 1997.
- [49] LAPIDUS A, GAIDAI N, NEKRASOV N, TISHKOVA L, AGAFONOV Y, MYSHENKOVA T: *The Mechanism of Carbon Dioxide Hydrogenation on Copper and Nickel Catalysts*. Petroleum Chemistry, 47:75–82, 2007.
- [50] JACQUEMIN M, BEULS A, RUIZ P: *Catalytic production of methane from CO₂ and H₂ at low temperature: Insight on the reaction mechanism*. Catalysis Today, 157:462–466, 2010.

- [51] WESTERMANN A, AZAMBRE B, BACARIZA M C, GRACA I, RIBEIRO M F, LOPES J M, HENRIQUES C: *Insight into CO₂ methanation mechanism over NiUSY zeolites: An operando IR study*. Applied Catalysis B: Environmental, 174-175:120–125, 2015.
- [52] GOODMAN D W, RYE R R: *Hydrogen dissociation on transitional metal surfaces: The effects of surface impurities*. Materials Science, 18:93–104, 1986.
- [53] JOHNSON J L: *Fundamentals of coal gasification*. In: *Chemistry of coal utilization*. Wiley, New York, 1981.
- [54] VAN HERWIJNEN T, VAN DOESBURG H, DE JONG W: *Kinetics of the Methanation of CO and CO₂ on a Nickel Catalyst*. Journal of Catalysis, 28:391–402, 1973.
- [55] KLOSE J, BAERNS M: *Kinetics of the Methanation of Carbon Monoxide on an Alumina-Supported Nickel Catalyst*. Journal of Catalysis, 85:105–116, 1983.
- [56] ZHANG J, FATAH N, CAPELA S, KARA Y, GUERRINI O, KHODAKOV A: *Kinetic investigation of carbon monoxide hydrogenation under realistic conditions of methanation of biomass derived syngas*. Fuel, 111:845–854, 2013.
- [57] SCHOUBYE P: *Methanation of CO on Some Ni Catalysts*. Journal of Catalysis, 14:238–246, 1969.
- [58] KOPYSCINSKI J, SCHILDHAUER T J, VOGEL F, BIOLLAZ S, WOKAUN A: *Applying spatially resolved concentration and temperature measurements in a catalytic plate reactor for the kinetic study of CO methanation*. Journal of Catalysis, 271:262–279, 2010.
- [59] HABAZAKI H, YAMASAKI M, ZHANG B P, KAWASHIMA A, KOHNO S, TAKAI T, HASHIMOTO K: *CO-methanation of carbon monoxide and carbon dioxide on supported nickel and cobalt catalysts prepared from amorphous alloys*. Journal of Catalysis, 172:131–140, 1998.
- [60] PANAGIOTOPOULOU P, KONDARIDES D, VERYKIOS X: *Mechanistic Study of the Selective Methanation of CO over Ru/TiO₂ Catalyst: identification of Active Surface Species and Reaction Pathways*. Applied Catalysis B: Environmental, 88:470–478, 2010.
- [61] KAPTEIJN F, BERGER R J, MOULIJIN J A: *Handbook of Heterogeneous Catalysis*. Wiley VCH, Weinheim, Germany, 2008.
- [62] LEE C B: *Methanation of Carbon Monoxide and Carbon Dioxide on Raney Nickel, and Computer Simulation of Chain Growth in the Fischer-Tropsch Synthesis*. PhD thesis, Ontario McMaster University, 1982.

- [63] GOETZ M: *Methanisierung im Dreiphasen-Reaktor*. PhD thesis, Karlsruhe Institute of Technology, 2014.
- [64] SCHLERETH D: *Kinetic and Reactor Modeling for the Methanation of Carbon Dioxide*. PhD thesis, Technische Universität München, 2015.
- [65] KOPYSCINSKI J: *Production of synthetic natural gas in a fluidized bed reactor*. PhD thesis, ETH Zurich, 2010.
- [66] SLAUGHTER M D: *The methanation reaction on ruthenium thin films: a mechanistic investigation*. PhD thesis, Iowa State University, 1979.
- [67] XU J, FROMENT G F: *Methane steam reforming, methanation and water-gas shift: I. Intrinsic kinetics*. *AIChE Journal*, 35:88–96, 2004.
- [68] KOSCHANY F, SCHLERETH D, HINRICHSSEN O: *On the kinetics of the methanation of carbon dioxide on coprecipitated NiAl(O)_x*. *Applied Catalysis B: Environmental*, 181:504–516, 2016.
- [69] LI X, GRACE J R, WATKINSON A P, LIM C J, ERGÜNDENLER A: *Equilibrium modeling of gasification: a free energy minimization approach and its application to a circulating fluidized bed coal gasifier*. *Fuel*, 80:195–207, 2001.
- [70] JARUNGTHAMMACHOTE S, DUTTA A: *Equilibrium modeling of gasification: Gibbs free energy minimization approach and its application to spouted bed and spout-fluid bed gasifiers*. *Energy Conversion and Management*, 49:1345–1356, 2008.
- [71] GAO J, WANG Y, PING Y, HU D, XU G, GU F, SU F: *A thermodynamic analysis of methanation reactions of carbon oxides for the production of synthetic natural gas*. *RSC Advances*, 2:2358–2368, 2012.
- [72] GAUTAM R, SEIDER W: *Computation of Phase and Chemical Equilibrium*. *AIChE Journal*, 25:991–999, 1979.
- [73] LIDE D R: *CRC Handbook of Chemistry and Physics*. CRC Press, Boca Raton, 2003.
- [74] KOPYSCINSKI J, SCHILDHAUER J, BIOLLAZ S: *Production of synthetic natural gas (SNG) from coal and dry biomass A technology review from 1950 to 2009*. *Fuel*, 89:1763–1783, 2010.
- [75] HARMS H, HÖHLEIN B, SKOV A: *Methanisierung kohlenmonoxidreicher Gase beim Energie-Transport*. *Chemie Ingenieur Technik*, 52:504–515, 1980.
- [76] TRIMM D L: *The Formation and Removal of Coke from Nickel Catalyst*. *Catalysis Reviews*, 16:155–189, 1977.

- [77] MOULIJN J A, VAN DIEPEN A E, KAPEIJN F: *Catalyst deactivation: is it predictable? What to do?* Applied Catalysis A: General, 212:3–16, 2001.
- [78] RÖNSCH S, SCHNEIDER J, MATTHISCHKE J, SCHLÜTER M, GÖTZ M, LEFEBVRE J, PRABHAKARAN P, BAJOHR S: *Review on methanation From fundamentals to current projects.* Fuel, 166:276–296, 2016.
- [79] GARDENER D C, BARTHOLOMEW C H: *Gravimetric Study of Adsorbed Intermediates in Methanation of Carbon Monoxide.* Industrial & Engineering Chemistry Fundamentals, 20:229–234, 1981.
- [80] FORZATTI P, LIETTI L: *Catalyst deactivation.* Catalysis Today, 52:165–181, 1999.
- [81] BARTHOLOMEW C H, SORENSEN W L: *Sintering Kinetics of Silica- and Alumina-Supported Nickel in Hydrogen Atmosphere.* Journal of Catalysis, 81:131–141, 1983.
- [82] BARTHOLOMEW C H, PANNELL R B, FOWLER R W: *Sintering of Alumina-Supported Nickel and Nickel Bimetallic Methanation Catalysts in H₂/H₂O Atmospheres.* Journal of Catalysis, 79:34–46, 1983.
- [83] BARTHOLOMEW C H, FARRAUTO R J: *Fundamentals of industrial catalytic processes.* John Wiley & Sons, New York, 2006.
- [84] GOLDBERGER W M, OTHMER D F: *The Kinetics of Nickel Carbonyl Formation.* I&EC Process Design and Development, 2:202–209, 1963.
- [85] SHEN W M, DUMESIC J A, HILL C H JR: *Criteria for Stable Ni Particle Size under Methanation Reaction Conditions: Nickel Transport and Particle size Growth via Nickel Carbonyl.* Journal of Catalysis, 68:152–165, 1981.
- [86] FROMENT G F, BISCHOFF K B, DE WILDE J: *Chemical Reactor Analysis and Design.* John Wiley & Sons, Hoboken, 2010.
- [87] MEILLE V: *Review on methods to deposit catalysts on structured surfaces.* Applied Catalysis A: General, 315:1–17, 2006.
- [88] MCCARTHY J G, WISE H: *Hydrogenation of Surface carbon on Alumina-Supported Nickel.* Journal of Catalysis, 57:406–416, 1979.
- [89] REILLY P, WHITTEN W: *The role of free radical condensates in the production of carbon nanotubes during the hydrocarbon CVD process.* Carbon, 44:1653–1660, 2006.

- [90] CHUN C M, BHARGAVA G, RAMANARAYANAN T A: *Metal dusting Corrosion of Nickel-Based Alloys*. Journal of the Electrochemical Society, 154:C231–C240, 2007.
- [91] RAMANARAYANAN T A, CHUN C M: *Developments in high-temperature corrosion and protection of materials*. Woodhead Publishing, England, 2006.
- [92] BAKER R T K: *Catalytic growth of carbon filaments*. Carbon, 27:315–323, 1989.
- [93] NOLAN P E, SCHABEL M J, LYNCH D: *Hydrogen control of carbon deposit morphology*. Carbon, 33:79–85, 1995.
- [94] SEHSTEDT J: *Four challenges for nickel steam-reforming catalysts*. Catalysis Today, 111:103–110, 2006.
- [95] GUINOT J, AUDIER M, COULON M, BONNETAIN L: *Formation and characterization of catalytic carbons obtained from CO disproportionation over an iron nickel catalyst-I: Fragmentation and rates of carbon deposition*. Carbon, 19:95–98, 1981.
- [96] CHEN I, CHEN F L: *Effect of Alkali and Alkaline-Earth Metals on the Resistivity to Coke Formation and Sintering of Nickel-Alumina Catalysts*. American Chemical Society, 29:534–539, 1990.
- [97] HUANG C P, RICHARDSON J T: *Alkali Promotion of Nickel Catalysts for Carbon Monoxide Methanation*. Journal of Catalysis, 51:1–8, 1977.
- [98] BARTHOLOMEW C H, WEATHERBEE G D, JARVI G A: *Effects of carbon deposits on the specific activity of nickel and nickel bimetallic catalysts*. Chemical Engineering Communications, 5:125–134, 1980.
- [99] MOELLER A D, BARTHOLOMEW C H: *Deactivation by Carbon of Nickel, Nickel-Ruthenium, and Nickel-Molybdenum Methanation Catalysts*. American Chemical Society, 21:390–397, 1982.
- [100] VAN STIPHOUT P C M, GEUS J W: *Platinum-Nickel Catalysts: Characterization, methanation and carbon deposition*. Applied Catalysis, 25:19–26, 1986.
- [101] MUNNIK P, VELTHOEN M E Z, DE JONGH P E, DE JONG K P, GOMMES C J: *Nanoparticle Growth in Supported Nickel Catalysts during Methanation Reaction Larger is Better*. Angewandte Chemie, 126:1–6, 2014.
- [102] FIGUEIREDO J L, TRIMM D L: *Gasification of carbon deposits on nickel catalysts*. Journal of Catalysis, 40:154–159, 1975.
- [103] SCHILDHAUER T J, BIOLLAZ S M A: *Synthetic Natural Gas: From Coal, Dry Biomass, and Power-to-Gas Applications*. John Wiley and Sons, Hoboken, New Jersey, 2016.

- [104] S, RIEKE: *Erste industrielle power-to-gas-anlage mit 6 megawatt*. Erdgas in der Energiewende, pages 660–664, 2013.
- [105] LEHNER M, TICHLER R, STEINMÜLLER H, KOPPE M: *Power-to-Gas: Technology and Business Models*. Springer, Heidelberg, 2014.
- [106] HALDOR TOPSOE: *From solid fuels to substitute natural gas (SNG) using TREMP™*. <https://www.netl.doe.gov/File%20Library/research/coal/energy%20systems/gasification/gasifipedia/tremp-2009.pdf>. Online, accessed November 14, 2016.
- [107] LOHMÜLLER R L. *Berichte aus Technik und Wissenschaft*, 41:3–11, 1977.
- [108] LEFEBVRE J, GÖTZ M, BAJOHR S, REIMERT R, KOLB T: *Improvement of three-phase methanation reactor performance for steady-state and transient operation*. Fuel Processing Technology, 132:83–90, 2015.
- [109] CHEMSYSTEM: *Liquid phase methanation/shift, Technical report*. Chem System Inc., prepared for US Energy Research and Development Administration, NO. E-(49-18)-1505, 1976.
- [110] GOETZ M, BAJOHR S, GRAF F REIMERT R KOLB T: *Einsatz eines Blasensauulenreaktors zur Methansynthese*. Chemie Ingenieur Technik, 85(7):1146–1151, 2013.
- [111] KARLSRUHE INSTITUTE OF TECHNOLOGY: https://www.kit.edu/kit/pi2014_15859.php. Accessed : 01.15.2020.
- [112] KOCKMANN N: *Transport Phenomena in Micro Process Engineering*. Springer-Verlag Berlin Heidelberg, 2008.
- [113] WIRTH T: *Microreactors in Organic Chemistry and Catalysis*. John Wiley & Sons, Weinheim, 2013.
- [114] HESSEL V, HARDT S, LÖWE H: *Chemical Micro Process Engineering*. Wiley-VCH Verlag GmbH & Co., Weinheim, 2004.
- [115] REBROV E, SCHOUTEN J C, DE CROON M H J M: *Single-phase fluid flow distribution and heat transfer in microstructured reactors*. Chemical Engineering Science, 66:1374–1393, 2011.
- [116] DELSMAN E R, PIERIK A, DE CROON M H J M, KRAMER G J, SCHOUTEN J C: *Microchannel plate geometry optimization for even flow distribution at high flow rates*. Trans IChemE, Part A, 82:267–273, 2004.
- [117] BALAJI S, LAKSHMINARAYANAN S: *Improved design of microchannel plate geometry for uniform flow distribution*. The Canadian Journal of Chemical Engineering, 84:715–721, 2006.

-
- [118] GOERKE O, PFEIFER P, SCHUBERT K: *Highly selective methanation by the use of a microchannel reactor*. Catalysis Today, 110:132–139, 2005.
- [119] LIU Z, CHU B, ZHAI X, JIN Y, CHENG Y: *Total methanation of syngas to synthetic natural gas over Ni catalyst in a micro-channel reactor*. Fuel, 95:599–605, 2012.
- [120] BROOKS K P, HU J, ZHU H, KEE R: *Methanation of carbon dioxide by hydrogen reduction using the Sabatier process in microchannel reactors*. Chemical Engineering Science, 62:1161–1170, 2006.
- [121] REBROV E V, DE CROON M H J M, SCHOUTEN J C: *Design of a microstructured reactor with integrated heat-exchanger for optimum performance of a highly exothermic reaction*. Catalysis Today, 69:183–192, 2001.
- [122] KAI T, FURUSAKI S, YAMAMOTO K: *Methanation of carbon monoxide by a fluidized catalyst bed*. Journal of Chemical Engineering of Japan, 17:280–285, 1984.
- [123] BARRIENTOS J, LUALDI M, SUAREZ PARIS R, MONTES V, BOUTONNET M, JÄRAS S: *CO methanation over TiO₂-supported nickle catalysts: A carbon formation study*. Journal of Catalysis A: General, 502:276–286, 2015.
- [124] BARRIENTOS J B: *Deactivation on methanation catalysts*. PhD thesis, KTH - Royal Institute of Technology, 2001.
- [125] SEHSTEDT J, DAHL S, JACOBES J, ROSTRUP-NIELSEN J: *Methanation of CO over Nickel: Mechanism and Kinetics at High H₂/CO Ratios*. Journal of Physical Chemistry, 109:2432–2438, 2005.
- [126] LUALDI M, BOUTONNET M, JÄRAS S: *Process development of co-production of synthetic natural gas (Green SNG) and Fischer-Tropsch diesel*. SGC Rapport 2013:272.
- [127] WAKAO N, KAGUEI S, FUNAZKRI T: *Effect of fluid dispersion coefficients on particle-to-fluid heat-transfer coefficients in packed-beds Correlation of Nusselt numbers*. Chemical Engineering Science, 34:325–336, 1979.
- [128] BERGER R: *EUROKIN, Spreadsheet on requirements for measurement of intrinsic kinetics in the gas-solid fixed-bed reactor*. 2012.
- [129] ROMKES S J P, DAUTZENBERG F M, VAN DE BLEEK C M, CALIS H P A: *CFD modelling and experimental validation of particle-to-fluid mass and heat transfer in a packed bed at very low channel to particle diameter ratio*. Chemical Engineering Journal, 96:3–13, 2003.

- [130] BUTT J B, PETERSEN E E: *Activation, Deactivation and Poisoning of Catalysts*. Academic Press Inc., New York, 1988.
- [131] GARDENER D C, BARTHOLOMEW C H: *Kinetics of Carbon Deposition during Methanation of CO*. *Industrial & Engineering Chemistry Product Research and Development*, 20:80–87, 1981.
- [132] TOTTRUP P: *Kinetics of Decomposition of carbon Monoxide on a Supported Nickel Catalyst*. *Journal of Catalysis*, 42:29–36, 2010.
- [133] PANAGIOTOPOULOU P, KONDARIDES D I, VERYKIOS X E: *Mechanistic aspects of the selective methanation of CO over Ru/TiO₂ catalyst*. *Catalysis Today*, 181:138–147, 2012.
- [134] SACHTLER J W A, KOOL J M, PONEC V: *The role of carbon in methanation by cobalt and ruthenium*. *Journal of Catalysis*, 56:284–286, 1979.
- [135] OHYA H, FUN J, KAWAMURA H, ITOH K, OHASHI H, AIHARA M, TANISHO S, NEGESHI Y: *Methanation of carbon dioxide by using membrane reactor integrated with water vapor permselective membrane and its analysis*. *Journal of Membrane Science*, 131:237–247, 1997.
- [136] CHIANG J H, HOPPER J R: *Kinetics of the Hydrogenation of carbon dioxide over Supported Nickel*. *Industrial & Engineering Chemistry Research*, 22:225–228, 1983.
- [137] DU G, LIM S, YANG Y, WANG Y, PFEFFERLE L, HALLER G L: *Methanation of carbon dioxide on Ni-incorporated MCM-41 catalysts: The influence of catalyst pretreatment and study of steady-state reaction*. *Journal of Catalysis*, 249:370–379, 2007.
- [138] SHARMA S, HU Z, ZHANG P, MCFARLAND E W, METIU H: *CO₂ methanation on Ru-doped ceria*. *Journal of Catalysis*, 278:297–309, 2011.
- [139] TIAN D, LIU Z, LI D, SHI H, PAN W, CHENG Y: *Bimetallic NiFe total-methanation catalyst for the production of substitute natural gas under high pressure*. *Fuel*, 104:224–229, 2013.
- [140] HWANG S, LEE J, HONG U G, BAIK J H, KOH D J: *Methanation of carbon dioxide over mesoporous NiFeRuAl₂O₃ xerogel catalysts: Effect of ruthenium content*. *Journal of Industrial and Engineering Chemistry*, 19:698–703, 2013.
- [141] MUTZ B, BELIMOV M, WANG W SPRENGER P SERRER M A WANG D PFEIFER P KLEIST W GRUNWALDT J D: *Potential of an Alumina-Supported Ni₃Fe Catalyst in the Methanation of CO₂: Impact of Alloy Formation on Activity and Stability*. *American Chemical Society*, 7:6802–6814, 2017.

- [142] MUTZ B: *Methanation of CO₂: Insight into deactivation mechanisms and catalyst stability under dynamic reaction conditions*. PhD thesis, Karlsruhe Institute of Technology, 2017.
- [143] TEGROTENHUIS W E, KING D L, WHYATT G A, FISCHER C M, WEGENG R S, BROOKS K P: *Microchannel reactors with temperature control*, 2007. U.S. Patent US7297324 B2.
- [144] MATHIAS J A, CHADWELL G B, QUI D, TONKOVICH A L, PERRY S T, SCHMIDT M B, FITZGERALD S P, HESSE D J, YUSCHAK T D, YANG B: *Multi-Stream Microchannel Device*, 2010. U.S. Patent US20100300550 A1.
- [145] TONKOVICH A L, ROBERTS G L, CALL C J, WEGENG R S, WANG Y: *Active microchannel heat exchanger*, 1997. U.S. Patent US6200536 B1.
- [146] SCHMITT C, AGAR D, PLATTE F, PAWLOWSKI B, ROTHE P, REITZ H G, DUISBERG M: *Keramischer Mikroreaktor*, 2005. Ger. Patent DE102005004075 B4.
- [147] ERGUN S: *Fluid Flow through Packed Columns*. Chemical Engineering and Processing, 48:89, 1952.
- [148] WAGNER W, KRETZSCHMAR H J: *VDI, D2 Stoffwerte von bedeutenden reinen Fluiden*. Springer Verlag Berlin Heidelberg, 2013.
- [149] POLING B E, PRAUSNITZ J M, O'CONNEL J P: *The Properties of Gases and Liquids*. McGraw-Hill, 2001.
- [150] CHRISTEN D S: *Praxiswissen der chemischen Verfahrenstechnik*. Springer Verlag Berlin Heidelberg, 2005.
- [151] PFEIFER P, BELIMOV M: *MICRO-REACTOR AND METHOD IMPLEMENTATION FOR METHANATION*, 2017. International Patent WO2017211864 A1.
- [152] NICROFER DATA SHEET: <http://woite-edelstahl.com/14959en.html>. Online, accessed: February 2, 2017.
- [153] ZHOU S, KONG R, PAN M, YUAN Q, HOU T: *Effects of microstructure types on the evaporation efficiency of electrically heated micro evaporator*. Advanced Materials Research, 655:1123–1126, 2013.
- [154] NATURGY: <https://prensa.naturgy.com/en/gas-natural-fenosa-launches-pilot-project-to-produce-renewable-gas-in-catalonia>. Accessed: 09.01.2020.
- [155] BHUTTA M M A, HAYAT N, BASHIR M H, KHAN A R: *CFD applications in various heat exchangers design: A review*. Applied Thermal Engineering, 32:1–12, 2012.

- [156] ZHAI X, DING S, CHENG Y, JIN Y, CHENG Y: *CFD simulation with detailed chemistry of steam reforming of methane for hydrogen production in an integrated micro-reactor*. International Journal of Hydrogen Energy, 35:5383–5392, 2010.
- [157] ARZAMENDI G, DIEGUEZ P M, MONTES M, CENTENO M A, ODRIOZOLA J A, GANDIA L M: *Integration of methanol steam reforming and combustion in a microchannel reactor for H₂ production: A CFD simulation study*. Catalysis Today, 143:25–31, 2009.
- [158] SHIN D Y, HA K S, PARK M J, KWAK G, LEE Y J, JUN K W: *CFD modeling of a modular reactor for the FischerTropsch synthesis: Effectiveness of a micro-scale cross-current cooling channel*. Fuel, 158:826–834, 2015.
- [159] AN H, LI A, SASMITO A, KURNIA J, JANGAM S, MUJUDMAR A: *Computational fluid dynamics (CFD) analysis of micro-reactor performance: Effect of various configurations*. Chemical Engineering Science, 75:85–95, 2012.
- [160] STUTZ M J, POULIKAKOS D: *Effects of microreactor wall heatconduction on the reforming process of methane*. Chemical Engineering Science, 60:6983–6997, 2005.
- [161] GIESE M, ROTTSCHÄFER K, VORTMEYER D: *Measured and Modeled Superficial Flow Profiles in Packed Beds with Liquid Flow*. AIChE Journal, 44:484–490, 1998.
- [162] WINTERBERG M, TSOTSAS E, KRISCHKE A, VORTMEYER D: *A simple and coherent set of coefficients for modelling of heat and mass transport with and without chemical reaction in tubes filled with spheres*. Chemical Engineering Science, 55:967–979, 2000.
- [163] GNIELINSKI V: *Zur Waermeuebertragung bei laminarer Rohrstroemung und konstanter Wandtemperatur*. Chemie Ingenieur Technik, 61:160–161, 1989.
- [164] AMADOR C, GAVRIILIDIS A, ANGELI P: *Flow distribution in different microreactor scale-out geometries and the effect of manufacturing tolerances and channel blockage*. Chemical Engineering Journal, 101:379–390, 2004.
- [165] NILSSON O, MEHLING H, HORN R, FRICKE J, HOFMANN R, MULLER S G, ECKSTEIN R, HOFMANN D. High Temperatures-High Pressures, 29:73–79, 1997.
- [166] STIESS M: *Mechanische Verfahrenstechnik-Partikeltechnologie I*. Springer Verlag, Heidelberg, 2009.
- [167] TSOTSAS: *VDI, M7 Wärmeleitung und Dispersion in durchströmten Schüttungen*. Springer Verlag Berlin Heidelberg, 2013.

-
- [168] GIESE M: *Strömung in porösen Medien unter Berücksichtigung effektiver Viskositäten*. PhD thesis, TU München, 1998.
- [169] BEY O, EIGENBERGER E: *Gas flow and heat transfer through catalyst filled tubes*. International Journal of Thermal Sciences, 40:152–164, 2001.
- [170] JESCHAR R: *Druckverlust in Mehrkornschüttungen aus Kugeln*. Archiv für das Eisenhüttenwesen, 35:1155–1159, 1964.
- [171] SCHWARTZ C E, SMITH J M: *Flow Distribution in Packed Beds*. Industrial and Engineering Chemistry, 45:1209–1218, 1953.
- [172] SUEKANE T, YOKOUCHI Y, HIRAI S: *Inertial Flow Structures in a Simple-Packed Bed of Spheres*. Fluid Mechanics and Transport Phenomena, 49:10–17, 2003.
- [173] VORTMEYER D, SCHUSTER J: *Evaluation of steady flow profiles in rectangular and circular packed beds by a variational method*. Chemical Engineering Science, 38:1691–1699, 1983.
- [174] FROMENT G F, BISCHOFF K B: *Chemical Reactor Analysis and Design*. Wiley, 1979.
- [175] ZEHNER P, SCHLUENDER E U: *Waermeleitfähigkeit von Schuettungen bei maessigen Temperaturen*. Chemie Ingenieur Technik, 42:933–941, 1970.
- [176] WIJNGAARDEN R I, WESTERTERP K R, KRONBERG A: *Industrial Catalysis: Optimizing Catalysts & Processes*. Wiley-VCH, 1998.
- [177] GUNJAL P R, RANADE V V, CHAUDHARI R V: *Computational Study of a Single-Phase Flow in Packed Beds of Spheres*. AiChe Journal, 51:365–378, 2005.
- [178] TSOTSAS E: *M7 Waermeleitung und Dispersion in durchstroemten Schuettungen*. Springer-Verlag Berlin Heidelberg, page 1519, 2007.
- [179] DIXON A G, NIJEMEISLAND M: *CFD as a Design Tool for Fixed-Bed Reactors*. Industrial & Engineering Chemistry Research, 40:5246–5254, 2001.
- [180] NIJEMEISLAND M, DIXON A G: *Comparison of CFD simulations to experiment for convective heat transfer in a gas-solid fixed bed*. Chemical Engineering Journal, 82:231–246, 2001.
- [181] NIJEMEISLAND M, DIXON A G: *CFD Study of Fluid Flow and Wall Heat Transfer in a Fixed Bed of Spheres*. Chemical Engineering Journal, 50:906–921, 2004.

-
- [182] FREUND H, ZEISER T, HUBER F, KLEMM E, BRENNER G, DURST F, EMIG G: *Numerical simulations of single phase reacting flow in randomly packed fixed-bed reactors and experimental validation*. Chemical Engineering Science, 58:903–910, 2003.
- [183] GUARDO A, COUSSIRAT M, RECASENS F, LARRAYOZ M A, ESCALER X: *Convective heat transfer at low and high pressure*. Chemical Engineering Science, 61:4341–4353, 2006.
- [184] GUARDO A, COUSSIRAT M, RECASENS F, LARRAYOZ M A, ESCALER X: *Convective heat transfer at low and high pressure*. Chemical Engineering Science, 61:4341–4353, 2006.
- [185] TASKIN M E, TROUPEL A, DIXON A, NIJEMEISLAND M, STITT H: *Flow, Transport, and Reaction Interactions for Cylindrical Particles With strongly Endothermic Reactions*. Industrial & Engineering Chemistry Research, 49:9026–9037, 2010.
- [186] WEHINGER G, EPPINGER T, KRAUME M: *Detailed numerical simulations of catalytic fixed-bed reactors: Heterogeneous dry reforming of methane*. Chemical Engineering Science, 122:197–209, 2015.
- [187] PENG W, XU M, HUAI X, LIU Z: *3D CFD simulations of acetone hydrogenation in randomly packed beds for an isopropanol-acetone-hydrogen chemical heat pump*. Applied Thermal Engineering, 94:238–248, 2016.
- [188] DIXON A, NIJEMEISLAND M, STITT E H: *Systematic mesh development for 3D CFD simulation of fixed beds: Contact points study*. Computers and Chemical Engineering, 48:135–153, 2013.
- [189] KEYSER M J, CONRADIE M, COERTZEN M, VAN DYK J C: *Effect of coal particle size distribution on packed bed pressure drop and gas flow distribution*. Fuel, 85:1439–1445, 2006.
- [190] JONES D A, CLARKE D B: *Simulation of Flow Past a Sphere using the Fluent Code*. Defence Science and Technology Organisation, 2008.
- [191] RANZ W E, MARSHALL W R: *Evaporation from drops*. Chemical Engineering Progress, 48:141–146, 1952.
- [192] WHITAKER S: *Forced convection heat transfer correlations for flow in pipes, past flat plates, single cylinders, single spheres, and for flow in packed beds and tube bundles*. AIChE Journal, 18:361–371, 1952.
- [193] KUROKI M, OOKAWARA S, STREET D, OGAWA K: *High-fidelity CFD modeling of particle-to-fluid heat transfer in packed bed reactors*. Proceedings of European Congress of Chemical Engineering, Copenhagen, 16-20 September, 2007.

-
- [194] EISFELD B, SCHNITZLEIN K: *The influence of confining walls on the pressure drop in packed beds*. Chemical Engineering Science, 56:4321–4329, 2001.

List of Figures

1.1	Schematic representation of the MINERVE PtG project (2012-2015).	1
1.2	“Microreactor Development” as major goal of this thesis and the spectrum of further research fields required for accomplishment.	3
2.1	Activity of different supported transition metals as a function of the reaction energy for dissociative CO chemisorption [7].	6
2.2	Number of CH ₄ and CO ₂ molecules formed during CO disproportionation in presence of H ₂ as a function of time (H ₂ /C=5, 250°C).	10
2.3	Methane and CO ₂ formation after presaturation of Ni film with ¹³ C and flushing the reaction chamber with ¹² CO/H ₂ syngas as a function of time.	10
2.4	Hydrogenation model of CO ₂ to CH ₄ according to Solymosi et al. (adapted from [40]). .	13
2.5	Conversion of CO as a function of W/F _{CO} (x _{CO} =0.0065 %) (left) and initial rate of methanation of CO (right) on Ni/Al ₂ O ₃ at different temperatures [54].	15
2.6	Rate of methane formation at 496 K as a function of CO and H ₂ partial pressures (left) [55] and dependence of the reaction rate on the partial pressure of H ₂ O at 220°C and p _{H₂} =200 hPa and p _{CO} = 6 hPa on different catalysts: 1) Ni/TiO ₂ , 2) Ni/Al ₂ O ₃ , 3) Ni-CaO/Al ₂ O ₃ and 4) Ni-Ce ₂ O ₃ /Al ₂ O ₃ (right) [15].	16
2.7	Conversion of CO and CO ₂ as function of temperature and space velocity on a Ru/Al ₂ O ₃ catalyst [17].	18
2.8	Equilibrium constants (left) and Gibbs energy (right) for possible reaction set R1-R6 as a function of temperature in the range 25-1000°C.	26
2.9	Thermodynamic equilibrium composition as a function of temperature (A) and conversion/selectivity as function of temperature for CO (B) and CO ₂ (C) in the mixture containing 10% CO, 7% CO ₂ , H ₂ /C=3.4 at 1 bar (N ₂ as remainder).	27
2.10	Influence of H ₂ /C-ratio A), pressure B) and addition of water and methane C) to the mixture containing initially 9% CO and 6% CO ₂ (N ₂ as remainder).	29
2.11	The effect of H ₂ /C-ratio A), steam content B) and pressure C) on the coke formation (10% CO, 7% CO ₂ , N ₂ as remainder)	30
2.12	Five deactivation mechanisms: 1a) Selective poisoning, 1b) Non-selective poisoning, 2) Sintering 3) Leaching/Corrosion 4) Fouling 5) Attrition (adapted from [77]).	32
2.13	TEM images of carbon deposition on a Ni/MgAl ₂ O ₄ catalyst via encapsulation of the catalyst A), whisker formation on the catalyst B) [94] and whisker formation on the reactor material Inconel 693 at 650°C C) [90].	36

3.1	Picture of one semi-commercial reactor stage in the TREMP™ process for 200 Nm ³ /h of SNG product [106] (left). Linde reactor concept for isothermal operation including submerged piping coil for cooling purposes [107] (right).	39
3.2	Temperature profile in the first reactor stage of the TREMP™ process as a function of the reactor length and operation time ($H/C=6$, 30 bar). The catalyst bed with the length of 2.5 m is filled with the MCR-2X catalyst which is regenerated two times after (2) 2013 h and (3) 4034 h.	40
3.3	Cross-sectional SEM image of the Inconel 693 after 160h at 650°C (left) and metal dusting rate on the Ni-alloys as a function of temperature in a H ₂ :CO-rich environment (50:50 vol.%) (right) [90].	41
3.4	Flow diagram of the TREMP™ process as designed during the NFE-Project in the 1980s.	42
3.5	COMFLUX pilot plant for up to 20 MW _{SNG} erected by Ruhrchemie Oberhausen (Ger) [74] (left) and schematic visualization of the three-phase slurry reactor for methanation [108] (right).	43
3.6	Microstructured reactor element (left) and polytropic reactor of 290 kg in weight with the total throughput capability of approx. 1700 kg/h of liquid chemicals built by KIT. . .	44
3.7	Visualization of the methanation process conducted in a conventional technology using 3 adiabatic reactors with interstage cooling and in a polytropic microstructured reactor (left). The optimum temperature regime is characterized in terms of yield of CH ₄ and byproduct formation (solid carbon) (right). Initial equilibrium conditions: 10% CO, 7% CO ₂ , N ₂ as remainder, H ₂ /C=3, 1 bar.	46
3.8	Pressure (left) [116] and velocity profile (right) [117] distribution examination in two microstructured heat exchanger geometries.	47
4.1	Conversion as a function of time during the aging process of the NiAlO _x catalyst under CO ₂ methanation conditions [68] (left) and observed decline of reaction rate on alumina supported Ni catalyst under CO methanation conditions at 485 K (H ₂ /CO=48) [55] (right).	50
4.2	Influence of the H ₂ /CO-ratio (left) and temperature (H ₂ /CO=3) (right) at 583 K and 1 bar and different GHSV on conversion over TiO ₂ supported Ni catalyst [123].	51
4.3	General flow chart of the test rig used for kinetic studies of the methanation reaction. . .	52
4.4	Visualization of the reactor architecture (left) and the manufactured device (right) for kinetic measurements.	53
4.5	Influence of particle size on the conversion of CO at 450°C, $\tau_{mod,CO}=7329=const.$ ml/(g min) (left) and 380°C, $\tau_{mod,CO}=3665=const.$ ml/(g min) (right) at the constant H ₂ /CO-ratio of 6 and pressure of 6 bar.	57

4.6	Temperature dependence of the conversion loss (left) and corresponding selectivity to CO ₂ for particle size of 200-300 μm at 450, 380 and 360°C and $\tau_{mod,CO}$ of 7557, 3715 and 2438 ml/(g min) as a function of TOS, respectively (H ₂ /C=6, 6 bar).	59
4.7	Influence of the H ₂ /CO-ratio on the catalytic loss of the commercial Ni/Al ₂ O ₃ catalyst (left) and according selectivities towards methane and CO ₂ for T=360°C, $\tau_{mod,CO}$ =1166 ml/(g min), p=6 bar, d _p =200-300 μm (right).	60
4.8	Catalytic activity after the shut-down/restart cycles under CO methanation conditions at 360 ($\tau_{mod,CO}$ =1166 ml/(g min)) and 450°C ($\tau_{mod,CO}$ =4448 ml/(g min)) as a function of different particle sizes.	61
4.9	Long-term stability of the commercial Ni catalyst under methanation conditions of CO ₂ in the temperature range between 328-371°C using initial gas composition of 9% CO ₂ , H ₂ /C=4 at 6 bar and τ_{mod,CO_2} =1237 ml/(g min).	63
4.10	Long-term stability of the self-prepared Ni catalyst under methanation of CO ₂ in the temperature range between 331-370°C using initial gas composition of 9% CO ₂ , H ₂ /C=4 at 6 bar and τ_{mod,CO_2} =1237 ml/(g min).	65
4.11	Long-term stability of the Ni-Fe bimetallic catalyst under CO ₂ methanation conditions in the temperature range between 305 and 382°C using initial gas composition of 9% CO ₂ , H ₂ /C=4 at 6 bar and τ_{mod,CO_2} =1237 ml/(g min).	66
4.12	Stability test of the commercial Ni catalyst under CO ₂ methanation conditions at different temperatures and H ₂ /CO ₂ -ratios at equal τ_{mod,CO_2} =1283 ml/(g min) and 6 bar.	67
4.13	Deactivation of the commercial Ni catalyst under methanation conditions of CO/ CO ₂ mixtures at H ₂ /C-ratios of 3 and 4 compared to activity loss under CO methanation conditions at H ₂ /C-ratios of 3, 4 and 6 ($\tau_{mod,CO}$ =1191 ml/(g min), τ_{mod,CO_2} =varied and 6 bar).	68
4.14	SEM images of the fresh surface of the commercial Ni catalyst at 100 (left) and 5000-fold (right) magnification.	69
4.15	SEM images of the spent commercial Ni catalyst deactivated under CO methanation conditions at 360°C and H ₂ /CO=4 for approx. 4 h. Surface topology at 5000-fold magnification (left) and measuring points for WDS analysis (right).	70
4.16	Pore size distribution (left) and XRD (right) of the fresh and spent commercial Ni catalysts.	71
4.17	Parity plot showing experimental and simulated conversions for A) Methanation of CO, B) Methanation of CO ₂ and C) Parallel methanation of CO and CO ₂ . For simulation, original kinetic models with according parameters are used.	74

4.18	Thermodynamic consistency of the models given by Kopyscinski et al. [58], Xu and Froment [67] and Zhang et al. [56] (10% CO, 7% CO ₂ , H ₂ /C=4, 6 bar) (left) and the model by Koshany et al. [68] (7% and 15% CO ₂ , H ₂ /C=4 and 9.7) (right).	76
5.1	Microreactor concepts by Tegrotenhuis et al. [143] (a) and Brooks et al. [120] (b) for highly exothermic equilibrium reactions.	79
5.2	Microreactor concepts by Mathias et al. [144] (a) including heat transfer between three fluid streams at the same time; it can be used for evaporation cooling of the methanation. A similar reactor concept is patented by Tonkovich et al. [145] which consists of three chambers allowing heat exchange between three fluid streams (b).	80
5.3	Conversion of CO/CO ₂ mixture as a function of the normalized catalyst amount at 400°C for 1 Nm ³ /h of syngas with the gas composition 10% CO, 7% CO ₂ , H ₂ /C=3, rest N ₂ , reactor pressure of 6 bar and the total catalyst amount of 28 g.	82
5.4	Pressure drop in the packed bed as a function of the Reynolds number at 2 and 6 bar reactor pressure, 450°C, ε=0.4, d _p =250 μm, MINERVE gas composition (left). Pressure drop in the 0.15 m long cooling zone of the Prototype 1 as a function of the coolant volumetric flow for two temperatures of 25 and 450°C (right).	83
5.5	Technical drawing of the methanation unit according to Prototype 1.	86
5.6	Technical drawing of the methanation unit according to Prototype 2.	86
5.7	Manufactured reactor devices according to Prototype 1 (left) and Prototype 2 (right) at IMVT (KIT) for the MINERVE project.	87
5.8	Labeling of thermocouple, heating element and inlet/outlet positions (left) and integrated reactor (prototype 1) into the test rig including insulation material (right).	88
5.9	Power consumption of the heating cartridges while flushing the reactor Prototype 1 with air and steam with different mass flows at a constant reactor temperature of 300 and 450°C (left). Heat transfer efficiency at different heat capacities using air and steam as heat transfer fluids (right).	90
5.10	Power consumption of the heating cartridges while flushing the cooling zone of the reactor Prototype 1 with water (T _{c,in} =99°C) at reactor temperature of 300 and 450°C, compared to air and steam (left). Heat transfer efficiency at different mass flows using air, steam and water as heat transfer fluids (right).	91
5.11	Temperature development in the reactor Prototype 1 during the start-up in absence of cooling; quasi steady state is obtained with cooling of 50 NI/min air at 50°C inlet temperature (left). Temperature development in the catalyst bed and in the metal bulk during the start-up of the reactor in absence of cooling (right).	92

5.12	Extinguishment of the reaction (syngas 23 NI/min in reactor Prototype 1) at excessive cooling rates of air ($T_{c,in}$ 50°C) (left) and influence of the air flow ($T_{c,in}$ 50°C) on the overall conversion of CO and CO ₂ (syngas flow 23 NI/min) (right).	93
5.13	Temperature distribution along the reactor Prototype 1 during methanation of 15 NI/min (left) and 23 NI/min (right) of syngas while cooling with air ($T_{c,in}$ =150°C) at different flow rates.	95
5.14	Comparison of the cooling potential of air and steam at syngas flows of 15 and 23 NI/min at similar heat capacities; reactor Prototype 1.	96
5.15	Temperature profiles in the reactor Prototype 1 for 15 and 23 NI/min of syngas while cooling with 8 and 12 g/min water mass flow at 95-99°C, respectively. Heating cartridge operation as anchoring point according to Case 1 (left) and Case 2 (right).	97
5.16	Axial temperature profiles (left) and corresponding conversions of CO and CO ₂ in the water cooled reactor Prototype 2 under methanation conditions using 17.15 NI/min of syngas through one reaction passage according to scenarios 1-3.	99
5.17	Temperature profiles in the reactor (left) and corresponding conversion of CO ₂ in reactor Prototype 2 (right) under methanation conditions of CO ₂ using throughput of 19.7 NI/min with 18.8% CO ₂ , H ₂ /C=3.6 and 6 bar.	101
6.1	CAD-geometry (left) and generated mesh (right) for the CFD study based on specifications of the Prototype 1.	108
6.2	Comparison of the experimentally and numerically calculated heat amount at different flow rates of the coolant air ($T_{c,in}$ =110 and 150°C) while keeping the heating cartridges (Pos. 1-5) at constant surface temperature of 300 and 450°C.	109
6.3	Calculated temperature distribution in the reactor Prototype 1 (left) and the comparison of the experimental and calculated results at T6-T11 (right) while keeping the heating cartridges at 450°C and flushing the cooling zone with 80 NI/min air ($T_{c,in}$ =110°C).	110
6.4	Pathlines of air colored by velocity magnitude in the microstructured cooling zone at the total air flowrate of 60 NI/min (NTP) (left) and according velocity profiles in the channels along the lines A, B and C (right).	111
6.5	Velocity profiles in the cooling channels of reactor Prototype 1 in presence and absence of fins at a total oil mass flow of 0.12 kg/s (left) and according Nusselt number ($Pr=45=const.$) and heat transfer coefficient as a function of Re (right).	112
6.6	Improvement of the total transferred heat in the Prototype 1 with fins at different temperatures and oil mass flows (left), and temperature distribution in a transversal cross-section of the reactor at 5% and 95% of the reaction zone length (0.12 kg/s) (right).	113

6.7	Radial heat conductivity distribution according to Λ_R -model ($d_t=2$ mm, $d_p=350$ μm , $\varepsilon_0=0.3$, $\text{Re}_p=13$, $T=300^\circ\text{C}$) and of adapted Eq. 6.5 (Fluent [®] built-in function) for the solid heat conductivity of the catalyst particles (left, abscissa range from 0 to 2.86 is confined to 0-1 to better visualize the near-wall behavior) and the profile of the designed heat source function (dashed line, only axial dependence) used to describe experimental temperature profiles (right).	114
6.8	Hot spot temperature and packed bed overheating as a function of the bulk heat conductivity and particle size while releasing around 548 W in the packed bed and air cooling the reactor with 80 NI/min ($T_{c,in}=150^\circ\text{C}$).	115
6.9	Approximation of the experimental temperature profiles under methanation conditions using 23 (A), 15 (B) and 9 (C) NI/min of syngas applying the artificial heat source and different packed heat conductivities.	116
6.10	Maximum packed bed temperature in the oil-cooled reactor Prototype 1 ($T_{c,in}=350^\circ\text{C}$) at varied heat conductivities of the packed bed and metal.	118
6.11	CFD temperature contours in the reactor (left) and temperature distribution along the symmetry axis (CFD vs. experiment, Pos. 1-5) (right) at the axial reaction zone offset of 1 cm.	121
7.1	Porosity distribution as a function of the normalized tube radius at the constant d_t/d_p -ratio of 8 according to equations by Giese et al. [168] and Bey and Eigenberger [169] (left), and packed bed geometry for elucidation purposes with the same d_t/d_p -ratio (right).	125
7.2	Averaged flow profile in a rectangular duct at Reynolds number of 4955 based on approx. 200 experiments [173].	126
7.3	Normalized flow velocity profile at different Reynolds numbers calculated using the extended Brinkman-Equation (Eq. 7.5) as a function of the normalized tube radius. Air, $T_{in}=25^\circ\text{C}$, 1 bar, $\varepsilon_0=0.4$, $d_t/d_p = 8$	128
7.4	Static packed bed heat conductivity for different solid heat conductivities as a function of the normalized tube radius (left) and static packed bed bulk heat conductivity as a function of solid heat conductivity at different packed bed bulk porosities according to Zehner and Schlunder (right). Air, $T_{in}=25^\circ\text{C}$, $p=1$ bar, $d_t/d_p=8$	130
7.5	The effect of fluid velocity on the packed bed heat conductivity as a function of the normalized tube radius (left) and the bulk heat conductivity as a function of the particle Reynolds number (right) according to the Λ_r -model for $d_t/d_p=8$, Air, $T_{in}=25^\circ\text{C}$, 1 bar.	131

7.6	Packed bed generation using Bullet physics engine: t_1) Initial state, t_2)- t_4) Begin of the settlement process and arrangement of the particles according to interparticle forces, friction and gravity.	138
7.7	Structured mesh for a tubular reaction chamber geometry which is used for the MSM-approach. Full domain (left) and outer wall region (right).	139
7.8	Visualization of cell scanning, marking and separation based on a sphere center with example of two different radii R_1 and R_2 for a two dimensional quadratic grid.	139
7.9	Resolution of a single sphere with a) 40, b) 20, c) 15 and d) 10 cells per sphere diameter using the MSM-approach.	141
7.10	Particle Nusselt number as function of particle Reynolds number at different cells per sphere ratios for a 300 μm (left) and 1 cm (right) diameter of particle. Fluid air, $T_{in}=25^\circ\text{C}$, 1 bar.	142
7.11	Two representative packed bed geometries used in this work. Left: Geometry with the tube to particle diameter ratio of 8.3 (sphere diameter 6 mm) consisting of 660 spheres; total amount of cells 5.02 mio.. Right: Geometry with the tube to particle diameter ratio of 3.5 (sphere diameter 1 cm) holding 99 spheres and resolved with the total amount of cells of 0.68 mio.	143
7.12	Visualization of the contact points between the particles in the packed bed mesh using a cell per sphere diameter ratio of 20 (arbitrary axial cut).	144
7.13	Porosity profile as a function of the particle normalized tube radius for the packed bed geometries with d_t/d_p -ratio of 3.5 (left) and 8.3 (right). Comparison of CFD results and correlation according to Bey and Eigenberger [169].	144
7.14	Velocity distribution in the two bed geometries with d_t/d_p -ratio of 3.5 (left) and 8.3 (right) for an air inlet velocity of 0.5 m/s, $T_{in}=25^\circ\text{C}$, p_{out} ambient.	145
7.15	Normalized and averaged velocity profile in the two packed bed geometries with d_t/d_p -ratio of 3.5 (left) and 8.3 (right) for the inlet velocity of 0.5 m/s. Comparison of CFD with Brinkman results for air, $T_{in}=25^\circ\text{C}$, p_{out} ambient.	145
7.16	CFD calculated pressure drop in the two packed bed geometries as a function of the particle Reynolds number in comparison with the correlations given by Ergun [147] and Einfeld-Schnitzlein [194]. Left: $d_t/d_p=3.5$; Right: $d_t/d_p=8.3$; Fluid air, $T_{in}=25^\circ\text{C}$, p_{out} ambient.	146

-
- 7.17 CFD temperature contours in the packed bed geometry with a tube to particle diameter ratio of 8.3, where one sphere in the center and one near the wall have a surface temperature of 370 K while the entire bed is flushed with air (300 K) with the inlet velocity of 0.5 m/s. p_{out} ambient. 147
- 7.18 Heat transfer from a single particle into the gas phase in the packed bed as function of the Reynolds number. The packed bed consists of 6 mm (left) and 300 μ m spheres in diameter (right). One sphere in the center and one in the vicinity of the wall are considered, $d_t/d_p=8.3$ 147
- 7.19 Comparison of the concentration profiles obtained in the resolved packed bed by CFD versus an ideal plug-flow model on the example of combustion of methane at isothermal conditions (left) and according contour plot of surface reaction rate in the packed bed provided by the CFD simulation (right). 149